Understanding and Modelling Damage and Fracture in Nuclear Grade Graphite

Thorsten Hermann Becker

This thesis is submitted for the degree of Doctor of Philosophy
In the Department of Mechanical Engineering
Univesity of Cape Town

January 2011

Abstract

This thesis studied the crack initiation and propagation characteristics of Nuclear Block Graphite 10 (NBG10) and Gilsocarbon (IM1-24), using the Double Torsion (DT) technique. The DT technique allows for stable crack propagation in such brittle materials where a modification, with the use of a graphical analysis, enabled the ability to measure the non-linear fracture characteristics as a J-integral parameter. The full field surface displacement measurement techniques of electronic speckle pattern interferometry (ESPI) and digital image correlation (DIC) were used to observe and measure crack initiation and propagation. In addition, an experimental-numerical method for the calculation of the J-integral from a DIC measured displacement field in cracked test specimens was proposed, which enabled the direct calculation of the J-integral during crack initiation and propagation of the graphite material.

Since the DT is not a standardised test methodology, the thesis first presents a critical review of the technique and its proposed corrections through an experimental analysis using the proposed corrections, a Finite Element model of the geometry and the use of Digital Image Correlation to measure out-of-plane surface deformations. It focuses on the validity of the assumed constant stress intensity regime and the independence of crack length in a critical evaluation using Polymethylmethacrylate test specimens. A small but clear dependence of the stress intensity on crack length was observed in all specimen configurations. This dependence is attributable to significant load-point deflections and out-of plane deformations that are not accounted for in the DT analysis. Revisions of the proposed analysis methodologies show that a crack length independent specimen geometry can be achieved, but at the cost of less accurate data. Reliable and accurate data can be achieved with a DT testing configuration using an optimum specimen configuration. As such, the DT technique was deemed suitable for the investigations of graphite fracture.

The analysis showed that graphite fracture is associated with significant micro-cracking in the fracture process zone (FPZ) prior and during macro-cracking as well as crack bridging in the wake of the crack tip, which contributes up to 50% of the irreversible energy dissipation in both graphites. Micro-cracks tended to nucleate at pores, causing deflection of the crack path. Rising R-curve behaviour was observed, which is attributed to the formation of the FPZ, while crack bridging and distributed micro-cracks are responsible for the increase in fracture resistance. The R-curve analysis of the two materials has shown the typical quasi-brittle R-curve behaviour.

A comparison of the R-curve data with other data available in literature, suggests a geometry dependent fracture behaviour, where the non-linearity due to the FPZ and the wake effects result in variations of the apparent fracture toughness. It was found that the reported FPZ size varies significantly between various geometries, showing a relationship between the non-linear fracture behaviour and the FPZ and wake region size. It was identified that the observed and measured behaviour is very similar to that of other quasi-brittle materials. In these a clear size effect on geometry has been established and fracture cannot be categorised by conventional elastic plastic fracture mechanics.

As such, the common fracture characteristics of quasi-brittle fracture were compared to those observed in graphite fracture. Subsequently, a failure model was proposed which is an adaption of an existing non-local damage plasticity model for concrete and other brittle materials. The model allowed for the observed degradation and non-linearity of the graphite material and was shown to correlate well with experimental data.

List of Publications

This project produced the the following publications:

Submitted Journal Publications

1. Becker, T. H., Marrow, T. J. and Tait, R. B. (submitted September 2010, accepted January 2011). An Evaluation of the Double Torsion Technique, Journal of Experimental Mechanics.

2. Becker, T. H., Mostafavi, M., Tait, R. B. and Marrow, T.J. (submitted April 2011). A Novel Approach to Calculate the J-Integral by Digital Image Correlation, Fatigue and Fracture of Engineering Materials and Structures.

3. Becker, T. H., Marrow, T. J. and Tait, R. B. (submitted September 2010, accepted April 2011). Damage, crack growth and fracture characteristics of nuclear grade graphite using the double torsion technique, Journal of Nuclear Materials.

Conference Papers

1. Becker, T. H. and Tait, R. B. (2009). Fracture and slow crack characteristics of nuclear grade graphite using the double torsion beam technique. ICF, Ottawa, Canada.

2. Becker, T. H., Mostafavi, M., Tait, R. B. and Marrow, T.J. (2010). Damage,, Crack Growth and Fracture Characteristics of Nuclear Grade Graphite using the Double Torsion Technique IYNC 2010, Cape Town, South Africa.

3. Becker, T. H., Mostafavi, M., Tait, R. B. and Marrow, T.J. (2011). An Approach To Calculate The J-Integral Using Digital Image Correlation Displacement Field Data, ICF, Luxor, Egypt.

Declaration

I hereby

1. grant the University free license to reproduce the above thesis in whole or in part, for the purpose of research;

2. declare that:

   (a) the above thesis is my own unaided work, both in conception and execution, and that apart from the normal guidance of my supervisor, I have received no assistance apart from that stated below;

   (b) except as stated below, neither the substance or any part of the thesis has been submitted in the past, or is being, or is to be submitted for a degree in the University or any other University.

   (c) I am now presenting the thesis for examination for the Degree of PhD.

Word count: 72073

Thorsten Hermann Becker

Date

Acknowledgements

The author would like to express his sincere appreciation to his supervisors, Professor R.B. Tait at the University of Cape Town and Professor T.J. Marrow at the University of Manchester for their continued efforts, encouragement and guidance. In particular, a special thanks to Professor Tait for enabling this PhD and the academic year at the University of Manchester. I am also particularly grateful to colleagues for their kind assistance, discussions and encouragement.

In addition, thanks to University of Cape Town and the people involved for facilitating this PhD. Special thanks go to Penny Park-Ross the laboratory assistant at the University of Cape Town, Glen Newins for the manufacture of testing fixture and specimens and Kathryn Rosie for dealing with the paperwork while in the UK.

The author would also like to express his gratitude towards the University of Manchester for providing the required experimental equipment, such as digital image correlation and mechanical testing apparatuses as well as for the use of the server cluster, office space and a desktop PC. Special mentions go to Barry Marsden, Jonathan Duff, Stewart Morse, Hui Dai, and Freyja Peters. The technical assistance of Dr. Mahmoud Mostafavi is especially acknowledged; his technical discussions were invaluable.

The sponsorship of the PBMR Company, the University of Cape Town and the Harry Crossly Foundation, which made this wonderful opportunity possible, is gratefully acknowledged.

Finally, I would like to express my appreciation to family and close fiends, too numerous to mention, for their support and understanding during this work. Special mentions go to the wonderful Danielle de Kock for proof reading this thesis and her tireless support, my immediate family (Reinhard, Ursula, Martin and Tavish), the de Kock family for their generous support and Andrew Wasylyk for making coffee when it was needed most.

It is worth mentioning that the views expressed are those of the author, and not necessarily those of his collaborators and sponsors.

Contents

List of Figures

List of Tables

List of Abbreviations and Symbols

Abbreviations

AGR	Advanced gas-cooled reactor
CSD	Centrally slotted disc
CN	Chevron notched
CT	Compact tension
COD	Crack opening displacement
CTOD	Crack tip opening displacement
BS	Cylindrical bend specimen
DIC	Digital image correlation
DCT	Disc compact tension
DT	Double torsion
EPFM	Elastic plastic fracture mechanics
ESPI	Electronic speckle pattern interferometry
FE	Finite element
FPZ	Fracture process zone
GP	The number of Gauss points
IM1-24	Gilsocarbon
LDC	Large deflection correction
LEFM	Linear elastic fracture mechanics
MS	Mean Stress
NBG10	Nuclear block graphite 10
PBMR	Pebble-bed modular reactor
PGA	Polygranular graphite grade A
PMMA	Polymethylmethacrylate (perspex)
SR	Short rod
SENB	Single edge notched beam
SIF	Stress intensity factor

3PB	Three-point bend
RV-BD	V-notched Brazilian disc
RV-SCB	V-notched semi-circular bend
VK	Slow crack growth data

Symbols

ΔW	Rate of change of work input
ΔU_{el}	Rate of change of internal elastic energy
ΔU_{pl}	Rate of change of internal "plastic" energy
ΔU_{λ}	Rate of change in surface energy
ε	Strain
ε	Tensor of strain
$\tilde{\varepsilon}_t^{pl}$	Tensile plastic strain
$\tilde{\varepsilon}_t^{ck}$	Tensile cracking strain
$\tilde{\varepsilon}_c^{pl}$	Compression plastic strain
$\tilde{\varepsilon}_c^{ck}$	Compression cracking strain
ϵ_{cc}	Eccentricity
λ_{wof}	Work of fracture
ψ	Dilation angle
$\psi(w,d)$	Thickness correction
Γ	A contour encompassing the crack tip
δ	Kronecker delta
μ	Shear modulus
σ	Stress
σ_t	Stress in tension
σ_c	Stress in compression
σ	Tensor of stress
σ_r	Remote stress
ν	Poisson's ratio
ξ	Ciccotti's correction factor
η	Ciccotti's correction factor
η_1, η_2	Local coordinate for an element
a	Nominal crack length (measured on the tensile surface in the DT specimen)

$\dot{a}$	Measured crack velocity on the tensile surface
$a_{i,f}$	Initial or final crack lengths during load relaxation tests
a_n	Specimen notch length
a_{off}	Crack offset length, measured at $3/4L$
a_p	Pre-crack length
A	Crack surface area
$\mathbf{B}$	strain-displacement matrix
B_A	Compliance relationship slope (analytically determined)
B_E	Compliance relationship slope (experimentally determined)
c	Crack-front inclination
C	Compliance relationship
d	Specimen thickness
d_n	Specimen thickness with side grooves
da, Δa	small increment in crack extension
dA, ΔA	small increment in Area
ds	Small increment on a contour encompassing the crack tip
d_t	scalar tensile damage variable
d_c	scalar compression damage variable
D	Structure size (understood as the dimension of the with crack cross-section)
$\mathbf{D}$	Material matrix
D_E	Compliance relationship y-intercept (experimentally determined)
E	Young's modulus
E_0	Young's modulus (undamaged)
E'	Equivalent elastic modulus for plane stress or plane strain conditions
f_{c0}	direct local compressive strength
f_{cu}	direct local compressive yield
f_{tu}	direct local tensile strength
f_{t0}	direct local tensile yield

F	Yield function
$\mathbf{F}$	Tensor Matrix of force acting on a node
F_{ty}	Tensile Yield strength
G	Flow rule
G_I, G_{III}	Shear strain energy release rate (in mode I, Mode II and Mode III respectively)
G_I^P	Shear strain energy release rate (in mode I) under the constant load assumption
G_I^y	Shear strain energy release rate (in mode I) under the constant displacment assumption
G_{Ic}	Critical shear strain energy release rate (Mode I, fracture toughness under LEFM)
G_f	Energy associated with the formation of two new crack surfaces
G_F	Total energy dissipated during fracture
I_p	Second moment of area
J, J_R	J integral
J_{el}	Elastic contribution to the J integral
J_{pl}	Non-linear contribution to the J integral
k	Chevalier's correction constant
K_I, K_{III}	Stress intensity (Mode I, Mode II and Mode III respectively)
K_{Ic}	Fracture toughness or critical stress intensity (Mode I)
$log(B)$	Slow crack growth data, linear log-log y-intercept
ℓ_{ch}, ℓ_1	Characteristic lengths
L	Specimen length
m	Chevalier's correction constant
n	Slow crack growth data, linear log-log slope
$\hat{n}$	Unit vector normal to a contour at an increment
p	Integration point number
P	Load/force at the load points
P_c	Critical load/force at the load points
$P_{i,f}$	Initial or final load during load relaxation tests

q, Q	Smooth function ranging from 1 at the inner and 0 at the outer contour
r	Distance through specimen thickness ($r = d$ at upper tensile surface)
r_y	Radius of plastic zone
R	Crack resistance
$\mathbf{S}$	Global stiffness matrix
t	time
T	Applied torque
u	displacement
u_t^{pl}	Tensile plastic displacement
u_t^{ck}	Compression cracking displacement
u_c^{pl}	Compression plastic displacement
u_c^{ck}	Tensile cracking displacement
V	Average crack velocity
W	Specimen width
w_m	Moment arm (Figure 3.1)
w_m^{LDC}	Corrected moment arm (large deflection correction)
y	Load point displacement
y_o	Zero load point displacement
y_{fail}	Load points displacement at specimen failure

Chapter 1

Introduction

This thesis concerns the characterisation and modeling of the failure mechanisms associated with graphite fracture. Although graphite is commonly assumed to be a material used in pencils to draw or write with, today graphite has been developed into an engineering material with advanced applications, such as brake linings, foundry facings and lubricants. The attraction of graphite lies in its ability to provide a variety of properties, some of which are unique, which make it suitable for numerous advanced applications. One of these is its application in the nuclear field. Special grades of synthetic polycrystalline graphite, high purity, polycrastiline graphite, find use as neutron moderators within nuclear reactors. This type of graphite is often referred to as nuclear graphite and is an important material for the construction of both historical and modern nuclear reactors.

The Pebble Bed Modular Reactor (PBMR) is such a type of nuclear reactor that uses graphite. At the this point, the future of the PBMR is somewhat unclear, however, the PBMR, a South African reactor design, was on the forefront of development within the field of nuclear energy [1] with the additional attribute of being a source of very high temperature energy for a range of applications from desalination to the hydrogen economy. One of the main distinguishing features of the PBMR is its inherently safe reactor design [1]. The PBMR is a high temperature, helium-cooled nuclear reactor. Structurally, the PBMR is made up of a 27 m vertical steel Reactor Pressure Vessel (RPV), which contains a metal core barrel, which in turn supports an annular pebble fuel core. The fuel core is positioned between inner and outer graphite reflectors. The foundation of the PBMR design is the spherical fuel elements, or "pebbles". These pebbles are tennis-ball sized graphite spheres containing thousands of micro-particles called

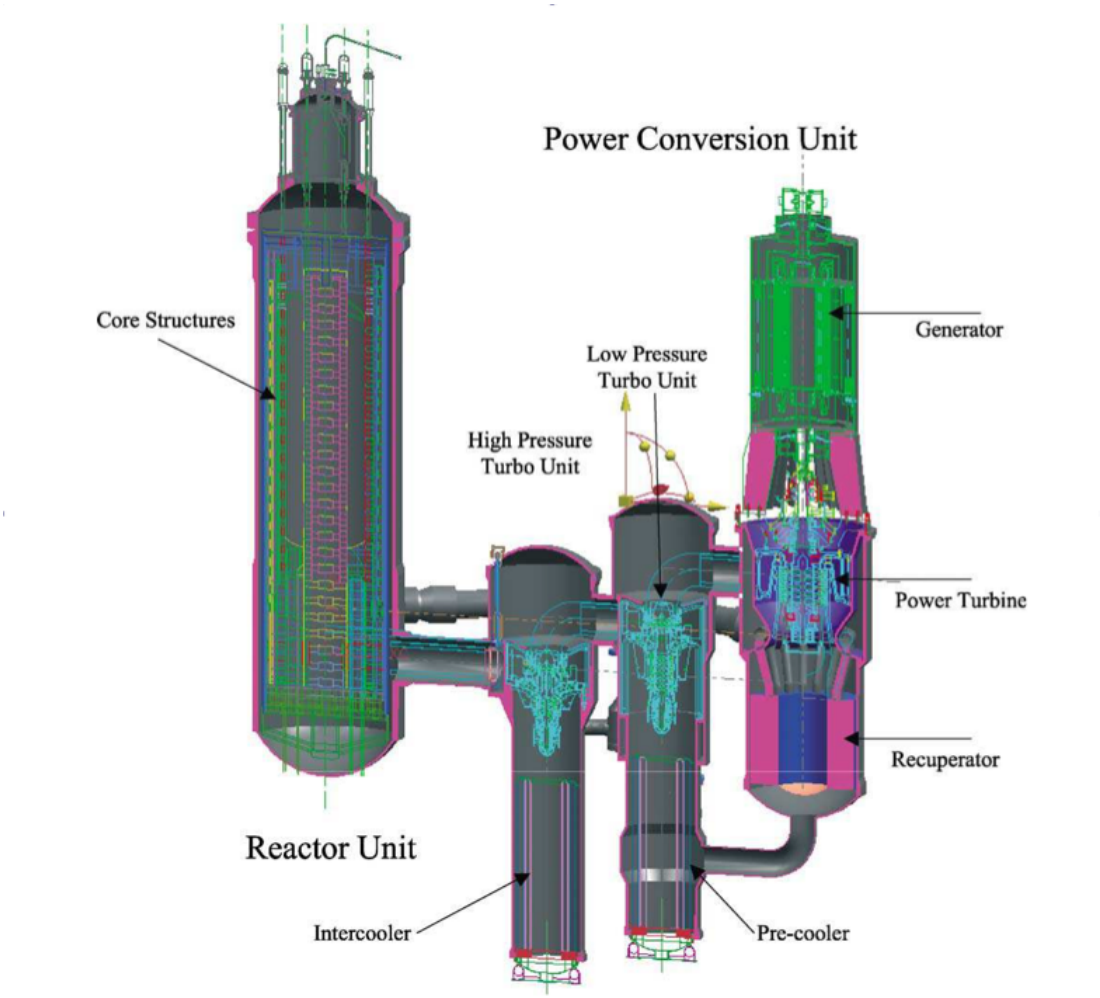

Figure 1.1 – Layout of the PBMR [1]

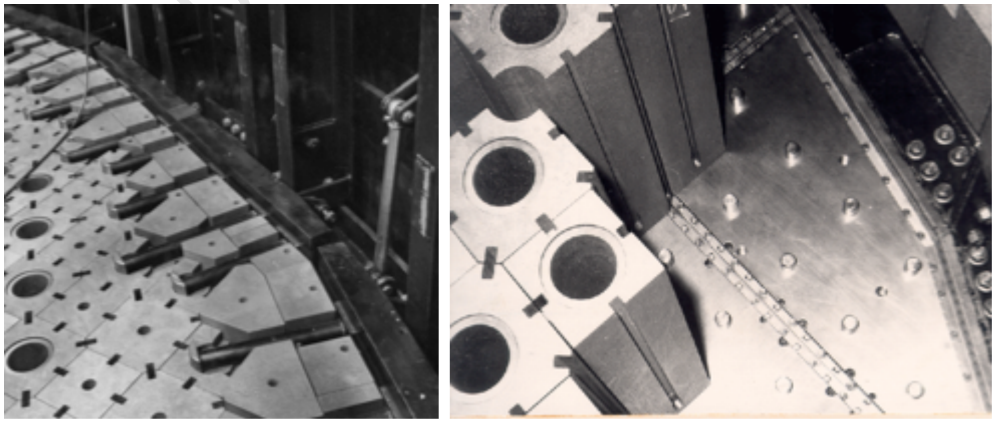

Figure 1.2 – PGA bricks in an Magnox reactor [2].

Tristructural-isotropic (TRISO) particles. TRISO-particles are uranium dioxide coated with silicon carbide, and are used to generate heat via a nuclear fission reaction. The graphite forming the outer layer of the pebble acts as a neutron moderator, effectively slowing the neutrons down. When full, the annular pebble fuel core can contain up to 450 000 pebbles [1]. The operating temperature of the pressurized gas is approximately 900^{o}C at a 9 MPa pressure. The core structures are designed to ensure sufficient passive heat removal from the reactor, so as to maintain a temperature safely below the 1600^{o}C at which the silicon carbide coating on the TRISO-particles begins to degrade. The major components of the PBMR can be seen in Figure 1.1.

Further examples of nuclear reactors that rely on graphite components are Magnox reactors and Advanced Gas-cooled Reactors (AGRs) in the United Kingdom. As with the PBMR design the AGRs use graphite to moderate the fast neutrons. Magnox reactors are pressurised carbon dioxide cooled reactors that employ natural uranium as fuel and Magnox alloy (an alloy of magnesium with small amounts of aluminium and other metals) as fuel cladding. The basic design was continuously refined throughout the 1950's and the 1960's, and, as a consequence, most Magnox reactors are unique. In the AGR design the Magnox cladding was replaced with Stainless Steel to allow for higher temperatures and greater thermal efficiency. In the AGR, fuel is enriched uranium oxide pellets embedded in a fuel rod. The carbon dioxide circulates through the core, reaching 640°C and a pressure of around 4 MPa, and then passes through boiler (steam generator) assemblies outside the core but still within the steel lined, reinforced concrete pressure vessel [4].

The need for graphite in a nuclear generator originated due to its ability to retain its properties (including strength) at high temperatures and its ability to slow neutrons to the speed required for nuclear fission to take place [6]. Graphite components in the core structures are generally in the form of bricks, which are arranged to accommodate thermal and radiation induced deformations throughout the life of the reactor. Graphite keys and dowels restrict movement during abnormal events, such as seismic activity [3]. These graphite reflectors also provide neutron reflection and, in the PBMR design, act as passive heat removers. Figure 1.2 shows the arrangement of graphite components in a MAGNOX reactor.

Due to the nature of nuclear generators, the structural integrity of any components in the power plant are of up most importance. Numerous factors need to be taken into account for a successful failure-free operation of the reactor, and one of

the key points is the sustained structural integrity of the nuclear graphite reflector material as it provides channels for control rods and fuel cooling. In the PBMR, graphite components form part of the inner core structure which supports the fuel pebbles. Thus, there is special interest in the failure mechanisms associated with graphite fracture. As nuclear graphite research stands there are many questions which still need to be answered regarding its damage development, fracture initiation and propagation, and fracture toughness. This is the aim of this thesis; to contribute to the understanding of nuclear graphite fracture.

1.1 Moderator Graphite Integrity

This project was initiated as part of an ongoing research effort in the PBMR programme in conjunction with the University of Cape Town. Its aim is it to determine the fracture characteristics of nuclear grade graphite for the development of the PBMR and its nuclear safety approval. With the future of the PBMR being somewhat unknown, this project was extended by collaboration with the University of Manchester in the United Kingdom. The issue of structural integrity of graphite components is also in its interest, since public attention was drawn in 2006 to the issue of structural integrity in the AGRs and more specifically to crack formation in AGR moderator graphite [4]. It was claimed that British Energy were unaware of the extent of the cracking in moderator bricks and that they did not know why the cracking had occurred [4]. It is worth mentioning that the project was funded by PBMR and the University of Cape Town which included a year abroad at the University of Manchester. The University of Manchester provided testing apparatus, graphite material and various other resources.

Current models to explain the fracture behaviour of graphite are based on the results of work undertaken in the UK, Japan, Russia and the USA. A range of different criteria are applied to determine when atomic bond separation will take place; stress criteria [41], strain criteria [42] and elastic strain energy criteria [43] have all been applied. Models of this type are elastic but pseudo-plastic behaviour can be obtained by assuming different strengths for each of the elements in the model. Work carried out on polygranular graphite has indicated that crack formation is preceded by damage in the most highly stressed regions of the material [13]. Whichever model is used, the understanding of the mechanisms behind failure and the fracture parameters is essential. This being said,

these parameters prove difficult to determine by conventional fracture mechanics methodologies, since graphite is a quasi-brittle material. Many researchers [14, 13, 44, 45, 46, 15, 47] have attempted various techniques to determine fracture properties, however, they report difficulty in propagating cracks controllably and obtaining valid and repeatable data. In this project an alternate method is employed, which facilitates stable crack growth using the so called Double Torsion (DT) technique. Since the DT technique achieves controlled crack propagation, it is believed to provide for more insight into the fracture behaviour and fracture mechanisms of nuclear graphite.

1.2 Fracture Mechanics and Modelling Approach

One way to asses the structural integrity, more specifically cracking, of the graphite components is through the fracture mechanics methodology. In essence, fracture mechanics concerns the study of the mechanics of the formation and propagation of cracks in materials. It uses methods of analytical solid mechanics to calculate the energetics and driving forces on a crack and those of experimentally determined fracture properties to determine whether a crack or discontinuity will propagate.

Early analyses have assumed a linear elastic hypothesis by using the critical stress intensity factor K_{Ic} and the critical strain energy release rate G_{Ic} to predict graphite failure. This however, raised some concern as large deviations in results [41] and non linearity have been reported [14]. These discrepancies have been attributed to extensive micro-cracking and irreversible slip deformation along the basal planes of graphite crystallites [48, 40]. As a result the assessment methodology has focused on a non-linear hypothesis [14]. The complexity of the graphite fracture behaviour becomes evident through the phenomenon of rising resistance to crack propagation. Furthermore the rising resistance appears to exhibit a range of different behavioural characteristics for which there is no satisfactory explanation [16].The application of the R-curve concept, i.e. a measure of the rising resistance with crack propagation, has become more common in recent years for describing the process of graphite fracture [16, 13, 4, 15].

In this study the concept of fracture mechanics is also utilised in an attempt to characterise graphite fracture. Since a different testing configuration is used, LEFM parameters, EPFM parameters and the R-curve behaviour are measured

in conjunction with optical observation techniques of the fracture process. It will be shown that the EPFM methodology does not characterise graphite fracture adequately. As a result a non-local continuum based damage plasticity approach is proposed to predict graphite failure.

1.3 Aims of the project

The purpose of this project is to develop a greater understanding of the conditions that will cause cracks to initiate and propagate in two graphite grades, namely Nuclear Block Graphite 10 (NBG10) proposed for the PBMR and Gilsocarbon (IM1-24) used in the AGRs. The research develops on the results of earlier work undertaken by Hodgkins [4] and Fazluddin [16]. Providing an explanation for the mechanisms associated with damage development and the variations in reported toughness lies at the heart of this project.

To fulfill these objectives, the thesis is split into four categories. This includes; a verification of the DT technique, the development of a novel approach to calculate the J-Integral by Digital Image Correlation (DIC) displacement field measurement, the damage, crack growth and fracture characteristics of graphite using the DT technique, and a proposed non-local continuum-based damaged plasticity model. Chapter 4 is dedicated to a complete description of the thesis objectives.

1.4 Details of Thesis Format

It was considered appropriate to include a brief section explaining the philosophy and layout of the research report in this thesis. The chapters, while consecutive, are largely self-contained.

The reader is first informed about relevant background information in Chapter 2. This includes general graphite information, how polycrystalline graphite is manufactured and some general mechanical properties. Other topics include the fracture mechanics methodology, the damage mechanics methodology and a brief introduction into plasticity theory.

Previous studies on polygranular graphite, and how these materials fracture, are considered in Chapter 3. This includes sections on the general factors affecting

static strength, Linear Elastic Fracture Mechanics (LEFM), Elastic Plastic Fracture Mechanics (EPFM), statistical approaches (Weibull) and continuum-based models. It was considered necessary to include this chapter as there are particular difficulties when attempting to identify the fracture parameters of polycrystalline graphite.

Chapter 4 summarises the aim of this research project. In this work four categories, split into the relevant chapters respectively are presented and include; a critical review of the DT technique (Chapter 5); the development of a novel approach to calculate the J-Integral by DIC displacement field measurement, called JMAN (Chapter 6); the damage, crack growth and fracture characteristics of graphite using the DT technique (Chapter 7 and 8); and a proposed non-local continuum-based damaged plasticity model (Chapter 9).

In particular Chapter 5 details the experimental techniques and system employed. This includes a discription of the material's fabrication, mechanical testing facilities, and evaluation of the DT technique and damage monitoring techniques. The latter includes descriptions of Electronic Speckle Pattern Interferometry (ESPI) and DIC techniques.

The novel approach to calculate the J-Integral by DIC displacement field measurement (called JMAN), presented in Chapter 6, enables the continuous evaluation of fracture parameters from the DIC images obtained during testing. This methodology is also proposed for the evaluation of other materials.

Chapter 7 describes the observations made during testing using the aforementioned damage monitoring techniques. The chapter focuses particularly on the crack initiation phase. DIC figures are shown, which illustrate the micro-cracking and crack wake region effects. The mechanisms of crack propagation and failure are described which include a discussion of the mechanisms of micro-cracking.

Similarly, Chapter 8 covers the LEFM and EPFM fracture parameters obtained from the graphite testing. With the use of JMAN an initiation toughness and R-curve behaviour is obtained. Conclusions are drawn on the obtained data and, combined with data available in literature, a conclusion is drawn on the fracture behaviour of graphite.

In view of the difficulty of adequately predicting the crack development and fracture toughness using EPFM, because of the abundantly micro-cracked nature of the graphite material, it was decided to propose an alternate methodology. Based on a non-local continuum-based damaged plasticity approach for quasi-brittle ma-

terials, the alternate approach was used to simulate fracture of three standard Gilsocarbon specimen configurations.

A comprehensive discussion on the research undertaken in this thesis is given in Chapter 10. This includes recommendations for future graphite fracture research. The last chapter, Chapter 11, concludes this project.

Chapter 2

Background Reading

This chapter is aimed to provide some general information on graphite; its microstructure, manufacturing process and general properties. The Chapter also intends to introduce the necessary background knowledge on fracture mechanics, damage mechanics and plasticity required for later reading of this thesis. A detailed discussion on the previous studies on the graphite fracture mechanisms and parameters can be found in Chapter 3.

2.1 Nuclear Grade Graphite

Mineral graphite is a crystalline allotropic form of carbon. Being non-metallic, it holds the distinction of being the most stable form of carbon under standard conditions and occurs in natural or synthetic forms. One of its main advantageous properties is its ability to retain its properties at high temperatures, with a high melting point of 3650^oC, and being a highly refractory and chemically non reactive material. Nuclear grade graphite is a high purity graphite used, as the name indicates, in nuclear applications. It has a low absorption coefficient for x-rays and absorption cross section for neutrons making it particularly useful material in nuclear applications [49]. Additional properties of graphite include its stability at high temperatures, where it is said to resist cracking and distortion. It is worth mentioning that graphite is a highly flamable material at high temperatures. As such, inert gases are utilised to overcome this. Table 2.1 tabulates the ranges of mechanical properties of commercially available graphites.

The nuclear graphite grades considered in this thesis are Nuclear Block Graphite 10 (NBG10) and Gilsocarbon (IM1-24). NBG10, proposed for the Pebble Bed

Property	Property value
Bulk Density	$1.3 - 1.95 g/cm^3$
Porosity	$0.7 - 53\%$
Modulus of Elasticity	$8 - 15 GPa$
Compressive Strength	$20 - 200 MPa$
Flexual Strength	$6.9 - 100 MPa$
Coefficient of Thermal Expansion	$1.2 - 8.2 \cdot 10^{-6}/^oC$
Thermal conductivity	$25 - 470 W/mK$
Specific heat capacity	$710 - 830 J/KgK$
Electrical resistivity	$5 \cdot 10^{-6} - 30 \cdot 10^{-6} Wm$

Table 2.1 – Mechanical properties of commercial graphite at ambient temperature [40]

Modular Reactor (PBMR), is an extruded, pitch coke graphite manufactured by SGL Carbon Company. The material has a maximum grain size of approximately 1.6 mm and exhibits distinct grain orientations or anisotropy due to the extrusion process of manufacture [50]. Gilsocarbon is predominantly used in Advanced Gas-cooled Reactors (AGRs). IM1- 24, also a medium grained graphite, is classed as a "near isotropic" graphite. It is manufactured from the raw material Gilsonite pitch coke, which is prepared from naturally occurring asphalt found in the Utah basin in Eastern Utah, USA. Both graphite grades form part of the internal structure in some nuclear reactors and hence are subjected to high fast neutron flux. It is noteworthy to mention that NBG10 has not been used in a nuclear reactor.

2.1.1 Graphite's crystal structure

Graphite is one of two naturally occurring, metastable allotropes of carbon at ambient temperatures and pressure [3]; the other being diamond [51]. Graphite consists of layered planes of carbon atoms bonded to three neighbour atoms at a separation, of approximately 1.415Å [3], seen in Figure 2.1a. Hexagonal rings form when this basic structure is expanded by repetition and it is from these that the basal planes are produced (Figure 2.1b) [52]. Successive planes, each a single atom thick, sit above their nearest neighbours, offset in a repeating formation (Figure 2.1c).

Nuclear graphite is an artificially produced graphite manufactured to fit the required properties (one requirement of moderator graphite is low neutron absorption properties). The control of these properties and, to some extent, the irradi-

ation behaviour of the graphite can be achieved by variation of the raw materials and by careful control of the forming and heating processes.

2.1.2 The manufacture of polycrystalline graphite

Various techniques exist for the manufacture of artificial graphite. The techniques described here are common to graphite produced in the nuclear industry. The following description of the processes by which artificial graphite is produced, has been provided by Graftech Ltd [4].

Green coke is the raw material from which all artificial graphite is made and is a slurry of carbon compounds. Prior to manufacture the green coke is calcined. In this process the impurities and moisture are removed by heating within the temperature range 1200^oC – 1350^oC. The green coke is then crushed, mixed with a liquid pitch binder and heated to approximately 165^oC – 170^oC, which is said to improve homogeneity and leads ultimately to the formation of two solid phases in the finished product. These phases are further discussed in Chapter 7. The mixture is then allowed to cool and then formed by either an extrusion or a moulding process. The extrusion process, which is the most common, involves the aggregate being extruded into long cylindrical rods, as shown in Figure 2.2. Iso-moulding uses a process by which the mixture is moulded into shape and heated in a pressurised container to 75 - 85 ^oC for several hours. Slurry moulding uses a low viscosity binder, which is poured into the mould and then vibrated to remove air bubbles, followed by a heated and pressurised treatment for several hours. During the manufacture of graphite so called "non-equiaxed isotropic coke filler particle" tend to orientate themselves along the general extrusion direction, which result in some anisotropy in graphite grades [4]. The NGB 10 grade is such an example.

Following this the formated article is cooled in water causing the liquid pitch to freeze. The material can then be safely handled for transportation to furnaces where they are baked at temperatures between 750^oC – 1000^oC. During this phase the material undergoes a number of changes and baking cycles last between 20 to 70 days. The pitch baking represents a distillation process and as a result up to 33% of its volume is lost, leaving behind characteristic interconnected porosity. Following baking the product may be immediately graphitised or, alternatively, liquid pitch can be impregnated into the pores to reduce porosity and increase mechanical strength. Some grades are subjected to three pitch impregnations

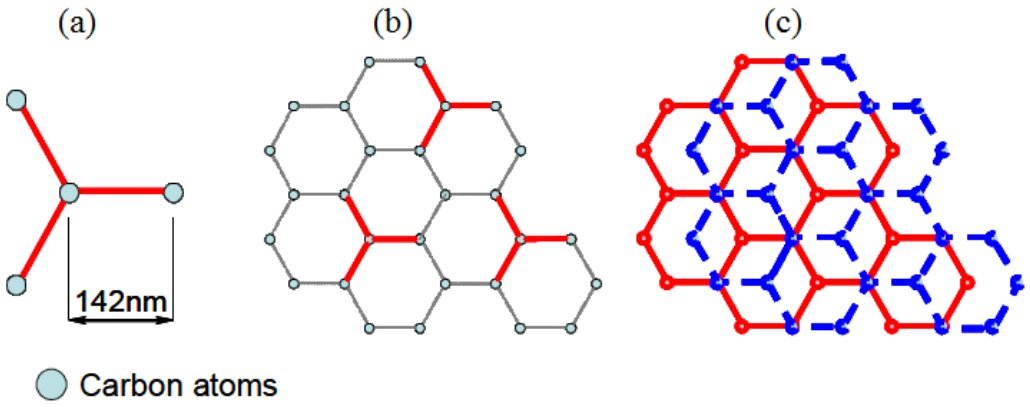

Figure 2.1 – Graphite's hexagonal ring formation [3]

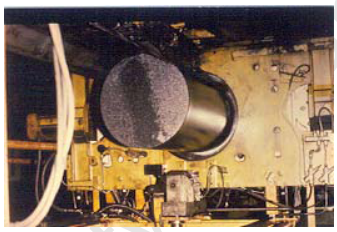

Figure 2.2 – Loading billets of extruded carbon into the furnace prior to baking [4]

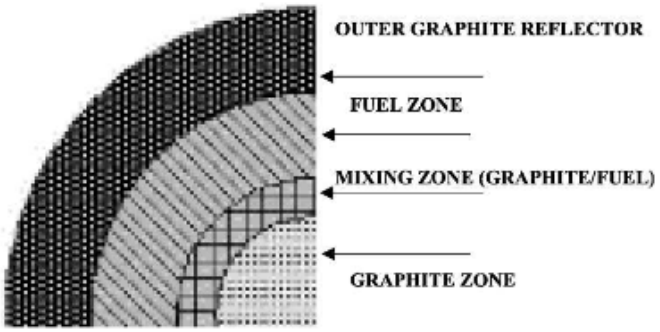

Figure 2.3 – Core structure of the PBMR [1]

followed by re-bake. The porosity in these grades can be as low as 8% as with each impregnation the reduction in porosity falls as pores become increasingly enclosed. The final step of graphite manufacture is called graphitisation and takes place in the temperature range of 2600^oC – 3000^oC. It is during this stage that the hexagonal shaped crystallites rearrange to form three dimensional crystals. Physical and mechanical properties undergo abrupt change during the process [4].

2.1.3 Graphite in a Nuclear Reactor Environment

Most graphite components in a nuclear reactor environment form part of the core structure of the reactor and comprise of reflector bricks, keys and dowels. In the PBMR design, the core structure consists of

- graphite reflectors,
- metallic components, including the core barrel and
- thermal insulation

The primary function of the core barrel is to support the graphite reflector blocks, and to bear the external loads that the graphite cannot withstand. The graphite reflectors, in the form of bricks, are arranged to accommodate thermal and radiation induced deformations throughout the life of the reactor. The graphite keys and dowels restrict movement during abnormal events, such as seismic activity [1]. These graphite reflectors also provide neutron reflection and act as passive heat removers for decay heat, which is is essential to maintaining safe operating temperatures. A schematic is shown in Figure 2.3.

2.2 The Fracture Mechanics Methodology

Throughout the life of the reactor, graphite components are subjected to radiation, temperature fluctuations and other forms of stresses. These factors result in degradation of the material and the structural integrity of graphite components may be compromised. Hence, to assess the integrity of components, it is essential to understand the failure mechanisms. Fracture Mechanics, which deals with the

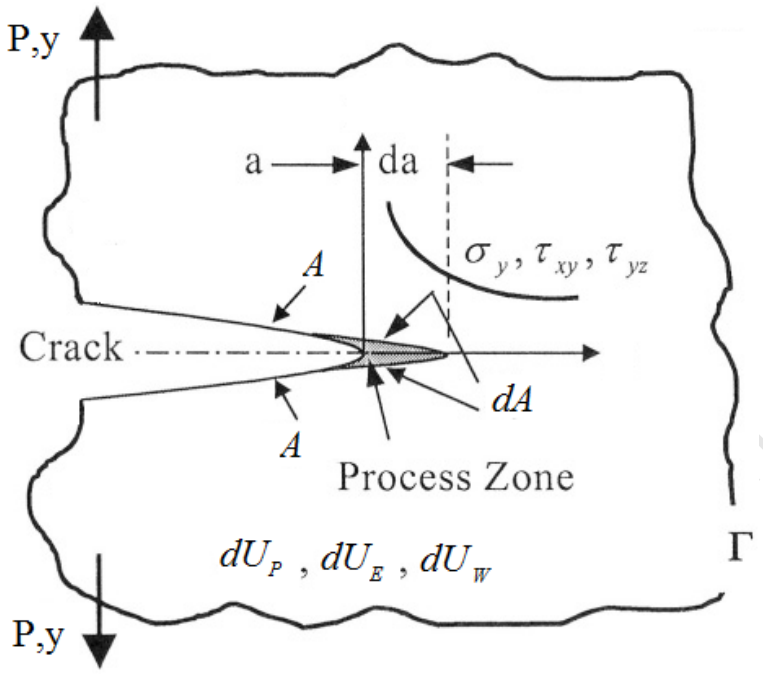

Figure 2.4 – A cracked body showing the energy changes

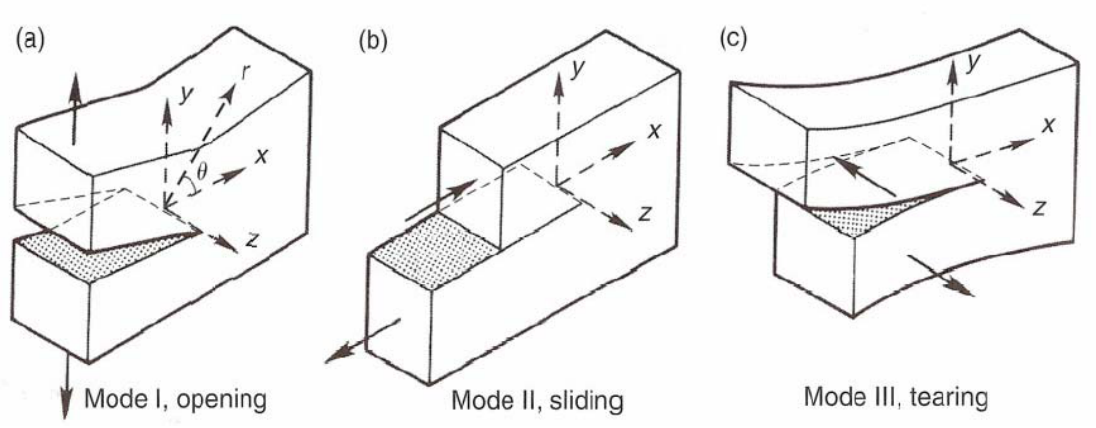

Figure 2.5 – The three basic modes of fracture surface displacement under different loading: (a) mode I, tensile or opening mode; (b) mode II, in plane shear or sliding mode; (c) mode III, anti-plane shear or tearing mode (Pollard and Fletcher [5])

study of the propagation of cracks in materials, may be used to asses the structural integrity of such a material and in turn allows for predictive capabilities.

This section briefly discusses the fracture mechanics methodology. This summary has been tailored to the thesis relevant topics, where some experimental methodologies for the fracture and growth characterisation are stated. More detailed discussions on the theory and its application can be found in books by Anderson [6], Knott [53] and Broek [54] amongst many others.

2.2.1 Background

In essence, fracture mechanics is concerned with the study of the mechanics of crack propagation in materials. It uses methods of analytical solid mechanics to calculate the energetics associated with crack propagation in combination with experimentally determined fracture properties to determine whether a crack or discontinuity will propagate. Fracture mechanics is used as an important tool in improving the mechanical performance of materials and components. It applies the physics of stress and strain, in particular the theories of elasticity and plasticity, to the microscopic crystallographic defects found in real materials in order to predict the macroscopic mechanical failure of components.

The analysis of cracked components has its roots in the attempt to understand the failure of glass extended through the fracture properties of ceramics and leading to the stability of metal engineering structures. Fracture mechanics has grown particularly because of the successful application of its relatively simple methodology in describing the failure of materials. A non-ductile material, which is not capable of relaxing peak stresses at crack-like defects, can be analysed on the basis of elastic concepts through the use of Linear Elastic Fracture Mechanics (LEFM). LEFM methodology has enabled a quantitative measure of the resistance (of a brittle material) to unstable or catastrophic crack propagation. However, if fracture is accompanied by considerable plastic deformation near the crack tip, a more complex concept known as Elastic Plastic Fracture Mechanics (EPFM) is needed. Both principles will be discussed briefly here.

2.2.2 The Energy Principle from an LEFM Perspective

One of the central concepts in fracture mechanics is the Griffith energy criterion. This concept, born out of the discrepancies and inadequacies observed in the

hypotheses on the fracture strength of elastic materials prevalent around the nineteenth and early twentieth century, was a modification of a fundamental energy theorem of classical mechanics and thermodynamics called the minimum energy theorem. According to this theorem, the equilibrium state of an elastic solid body, deformed by specified forces, is such that the potential energy of the whole system is a minimum [55]. Griffith's modification, which became widely known as the energy criterion, relates the energy associated with an incremental crack propagation of an isolated crack in a solid, to the energy absorbed to create a new surface during the fracture process.

A material is considered to have a flaw which is subjected to an external force or displacement. In the event that fracture has occurred, the crack, a, extends over an increment, da, (i.e. from a to $a + \mathrm{d}a$), resulting is a crack surface area extension dA (i.e. from A to $A+\mathrm{d}A$). During this process some energy is released to the formation of the new crack surface. This is illustrated in Figure (2.4). An elastic body containing a crack with a relatively insignificant process zone (the shaded area) is shown. The energy consumption of the system, Γ, considers only the changes of the energy within the system. During fracture (of da) the load does some work (dW), the internal potential strain energy changes somewhat (dU_E) and some energy U_γ is released due to the formation of new crack surfaces γ. Hence the energy conservation criterion reads (assuming isothermal conditions)

$$\frac{d}{dA}\left(W + U_E + U_\gamma\right) = 0 \tag{2.1}$$

which can be written as

$$\frac{d}{dA}\left(W + U_E\right) = -\frac{dU_\gamma}{dA} \tag{2.2}$$

Equation 2.2 must hold when fracture occurs, i.e. that some energy is lost to the formation of a new crack surface. Conversely when the equality does not hold, fracture does not yet take place, in which case $d(W + U_E)/dA = 0$. In turns out that the deliverable energy is always equal to the change in strain energy and instead of $d(W + U_E)/dA = 0$ one may use the absolute change of strain energy dU/dA. Hence, the deliverable energy is dU/dA and Equation (2.2) reduces to the criterion:

$$-\frac{dU}{dA} = \frac{dU_\gamma}{dA} \tag{2.3}$$

The left hand side is called the strain energy release rate G and the right hand side the fracture energy criterion or fracture resistance R . For a stationary body, the energy release rate criterion for crack tip instability is

$$G \geq R \tag{2.4}$$

Fracture will occur if, sufficient strain energy is available.

2.2.3 Crack Tip Displacement Modes

Cracking modes are subdivided into three types based on the orientation of the load relative to the plane of the initial crack (as shown in Figure 2.5). Each opening mode has their own energy requirement for crack propagation and, as such, fracture is considered to be mode dependent. Mode I or opening mode cracks are the result of tensile stresses with the displacement of the crack surfaces perpendicular to the plane of the crack. In mode II or sliding mode cracks, shear stresses acting parallel to the crack surfaces result in displacement in the crack plane, normal to the crack front. Mode III or tearing mode crack growth is caused by out of- plane-shear. It corresponds to shear stresses acting parallel to both the crack plane and the crack front.

Of the three modes of crack tip displacement, mode I is the most important to crack propagation for highly brittle solids as brittle cracks tend to orient in a configuration that minimises the shear loading [56]. In problems concerning crack loading, a combination of any of the displacement modes constitutes mixed-mode. For pure mode I (opening mode) fractures, there are no resolved remote shear stresses in the plane of the fracture. It is thus expected that propagation will be along a straight path perpendicular to the least compressive (or most tensile) principal stress direction. However, mixed-mode cracking results in crack propagation into a region where remote stresses are in different directions and as a result the crack path ceases to continue along a straight path, resulting in a fracture mechanics criterion under mixed-mode condition.

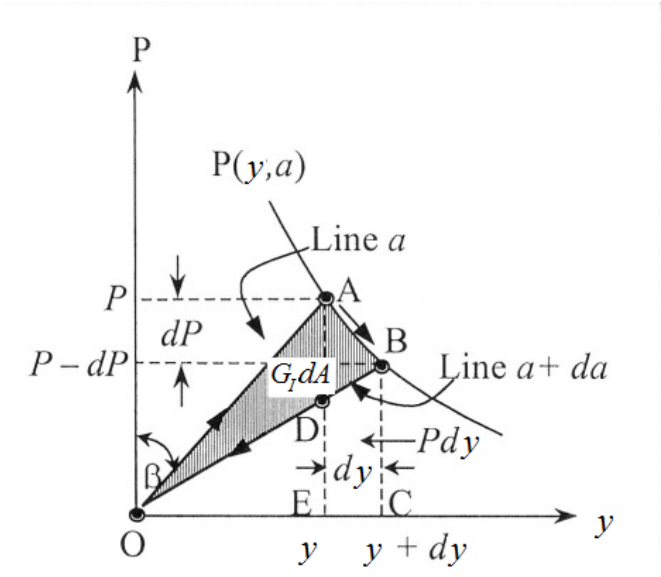

Figure 2.6 – A load vs. displacement curve during crack extension *da* (from Ref. [6])

2.2.4 Strain Energy Release Rate G

The previously discussed energy balance (Equation (2.2)) can be formally expressed with the Griffith energy concept [55]. Since Equation (2.3) simply expresses the energy balance for crack growth, G can generally be applied to any crack geometry and crack growth configuration as a global parameter. G includes contributions from all parts of the system (cracked specimen plus loading mechanism).

Consider mode I (tension) loading and the linear behaviour shown in Figure 2.6. The stored energy due to tension loading can be defined as the area under the load-displacement curve. G can be found by energy lost during the fracture process

$$G_I = \frac{1}{2}\left(P\frac{dy}{dA} - y\frac{dP}{dA}\right) \tag{2.5}$$

As for mode I fracture, it is convenient to evaluate G in terms of the compliance (or the inverse of stiffness) C of the sample. C is defined as the displacement y of the force application region divided by the applied force P. Thus, the strain energy release rate during an incremental crack extension is independent of loading configuration [56] and can be used to determine G through measuring compliance

as a function of crack length. A relationship of the compliance is obtained as a function of the crack extension area.

$$G_{I,y} = \frac{1}{2}P^2\frac{dC}{dA} \tag{2.6}$$

$$G_{I,P} = \frac{1}{2}\frac{y^2}{C^2}\frac{dC}{dA} \tag{2.7}$$

where $G_{I,y}$ denotes a constant displacement assumption and $G_{I,P}$ denotes a constant load assumption (both in mode I loading). Figure 2.6 may also be used as a graphical representation of the energy equilibrium. For instance:

- OA = Initial loading line
- AB = Unloading line, where P changed to $P - dP$, similarly y changed to $y + dy$. Consequently, the crack area changes from A to $A + dA$

This leads to:

- Area OAE = Stored energy at fracture = $Py/2$
- Area OBC = Stored energy after fracture = $(P - dP)(y + dy)/2$
- Area $ABCE$ = Work done = Pdy (if a constant load is assumed)
- Area $OAB = OAE + ABCE - OBC$ = Release of elastic energy = GdA

2.2.5 Stress Intensity Factor

Similarly an equivalent Stress Intensity Factor (SIF) can be used to predict fracture. The SIF can be seen as a more accurate prediction of the stress state ("stress intensity") near the tip of a crack caused by a remote load and aims to provide a measure of the real forces applied to the crack tip. Similarly to G, the SIF will determine whether the crack will propagate or remain stationary.

The stress distribution in the crack tip region is analysed on the assumption that classical linear theory of elasticity applies. This is valid provided that any region of non linear behaviour is small compared with the length of the crack and the dimensions of the cracked body. When non-linear effects at the crack tip become large, an alternate analysis is required such as the crack opening displacement

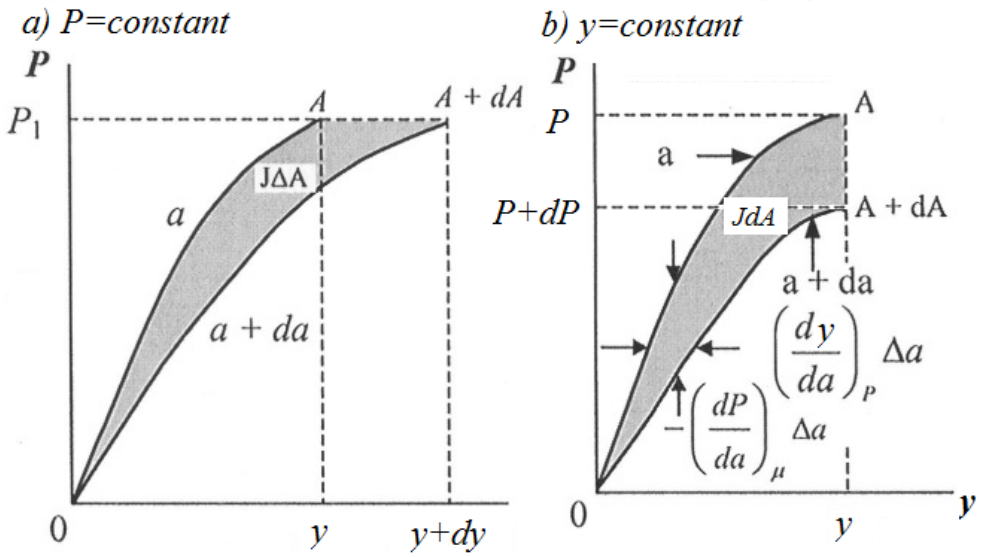

Figure 2.7 – J integral at a) $dP = 0$ and b) $dy = 0$ (from Ref. [6])

COD or the J integral. For the linear elastic SIF, the magnitude of the crack tip stress field for a particular mode in a homogeneous linear elastic material is defined by

$$K_I = \lim_{r \to 0} [\sigma \sqrt{2\pi r}] \tag{2.8}$$

where sigma σ is the tensile stress normal to the crack surface (in mode I) and r the distance measured from the crack tip to the surrounding stress field due to the crack tip. The surrounding stress field is governed by the applied load, the shape and length of the crack and the shape of the body. A common, simplified expression for the stress intensity, which assumes that a cracked body has a two dimensional stress/strain field at the crack tip, is expressed as

$$K_I = Y \sigma_r \sqrt{\pi a} \tag{2.9}$$

where σ_r is the remote applied stress, Y is a numerical modification factor to account for crack geometry, loading conditions and edge effects, and a is the crack length. It is worth mentioning that the Equation 2.9 forms the bases of fracture mechanics. The three dependent variables K_I (SIF), σ_r (stress) and a (crack length) form part of the so called "triangle of integrity" which dictates whether a structure or component is structurally sound.

2.2.6 The Energy Principle from an EPFM Perspective

Some materials undergo considerable plastic deformation before they fracture, resulting in a considerable amount of energy being lost to the formation of a Fracture Process Zone (FPZ) ahead of the crack tip. LEFM assumes that all energy is converted to the formation of new crack surfaces and thus the assumption of LEFM no longer holds true. A concept known as Elastic Plastic Fracture Mechanics (EPFM) is used and the fracture parameter often used is referred as the "J integral". J, similar to G, is the energy release rate at the onset of fracture. Another criterion used to quantify fracture is known as the Crack Opening Displacement (COD) which measures the crack tip opening at the onset of fracture. The COD will not be discussed as it is not relevant for this thesis.

Whether there is plasticity or not the energy conservation criterion must hold. Thus, an energy term is added to Equation (2.2)to account for plasticity. The fracture criterion now consists of an elastic term and an plastic term, such that

$$\frac{dU}{dA} = \frac{d}{dA}\left(U_{el} + U_{pl}\right) \tag{2.10}$$

where, $U_{el} = U_{\gamma}$, i.e. the energy used for the formation of the new surface areas, and U_{pl} the energy used due to plasticity or for the formation of a process zone. For elastic materials the energy balance is written in short hand as $G = R$, in EPFM this becomes

$$J = J_R \tag{2.11}$$

Figure 2.7 is the non-linear equivalent of Figure 2.6, from which the critical value of the J integral or fracture toughness can be determined at the onset of crack growth. Similarly, the non-linear resistance to fracture J_R now consists of two parts. An elastic contribution J_{el} with the extension of the crack tip and an plastic part, which is the energy required to form the plastic zone or process zone J_{pl} around the crack tip. Hence fracture occurs if

$$J_{el} + J_{pl} \geq J_R \tag{2.12}$$

Unlike brittle materials, where fracture is sudden and catastrophic, plastic materials often have some "stable" fracture due to the formation of the so called

process zone at the crack tip. Stable fracture is often referred to as stable crack growth, however, at sufficient loading fracture becomes uncontrollable.

2.2.7 J Integral derivation

The J-integral forms an important part of this thesis and thus it was considered essential to include the theory behind the J-integral. Chapter 6 introduces a novel technique to measure the J-integral directly from surface displacement fields obtained through the Digital Image Correlation (DIC) technique, which is based on the following derivation.

Rice [57] showed that under the assumption of a elastic plastic material the J integral, or in this case the non-linear energy release rate, is the area enclosed by the loading and unloading paths during crack extension. For the crack system shown in Figure 2.4 the J integral is defined as (in indicial notation)

$$J = \int_{\Gamma} (W n_x - n_i \sigma_{ij} \frac{\delta u_{ij}}{\delta x}) ds \qquad i, j = x, y \tag{2.13}$$

where σ_{ij} and u_{ij}, are the stress and displacement components, ds is the arc increment around the crack tip, n_i the unit normal to the contour or path of integration Γ (which begins and ends on the crack surfaces and encloses the crack tip respectively) and W the strain energy density given by

$$W = \int_0^{\varepsilon_{ij}} \sigma_{ij} d\varepsilon_{ij} \tag{2.14}$$

In essence the J-integral evaluates the energy associated with fracture by taking the net stored energy (considered by the integral) and subtracting the energy of traction forces and their respective displacements, in the crack propagation direction. For linear or non-linear elastic materials that are homogeneous the value of J is path dependent. Thus, the evaluation of J on a remote contour and on one near the crack tip enables conditions at the crack tip to be related to parameters describing the applied loads.

2.2.8 Equivalence of Fracture Mechanic Parameters

Under conditions of small scale yielding the various fracture mechanics parameters can be considered equivalent. For example, in plane-strain mode I crack

propagation

$$G = J_{el} = \frac{K_I{}^2(1-v^2)}{E} \approx CTOD \cdot F_{ty} \tag{2.15}$$

It must be emphasised, however, that this equivalence only holds if the assumption of linear elasticity is valid, i.e. any inelastic or non-linear elastic region is confined to a negligibly small zone at the crack tip, and there is no frictional loading on the crack surfaces. Under these circumstances the several parameters in Equation (2.15) are termed the fracture toughness and the material obeys linear elastic fracture mechanics. If linear elasticity is not an adequate representation of crack tip behaviour the relations in Equation (2.15) do not hold and the most appropriate single parameter is chosen as a fracture criterion.

2.2.9 Crack Extension

The energy equilibrium law specified whether a crack will extend or remain stationary. This critical point (K_c, G_c and J_c) denotes the onset of fracture. Once the critical value of K_c, G_c or J_c has been reached, crack propagation is known as fast catastrophic fracture because its speed can approach that of sound in the medium, provided that the crack is isolated and its walls are traction free. However, brittle materials often experience sub-critical crack propagation at values of fracture parameters below the critical value. The phenomenon of sub-critical crack growth was first observed in glass by Grenet [58], but has since been observed in other brittle materials such as metals, plastics and ceramics by Wiederhorn [7] and also in rocks and minerals (Atkinson [59]). Generally the crack velocity v is expressed as a function of the SIF or G

$$v = v(K, G) \tag{2.16}$$

The specific form of the crack velocity dependence on K or G depends on the precise mechanism whereby the energy barrier to crack extension is overcome. Sometimes the form of this dependence is assumed from experimental results and sometimes from physico-chemical theories regarding the assumed crack tip weakening process.

As a result of the work of Wiederhorn, three principal regions of crack growth have been identified from stress intensity factor-crack velocity vK plots (Figure 2.8). In Region I, the velocity of crack growth is controlled by the reaction rate at the crack tip. It is important because most of the slow crack growth,

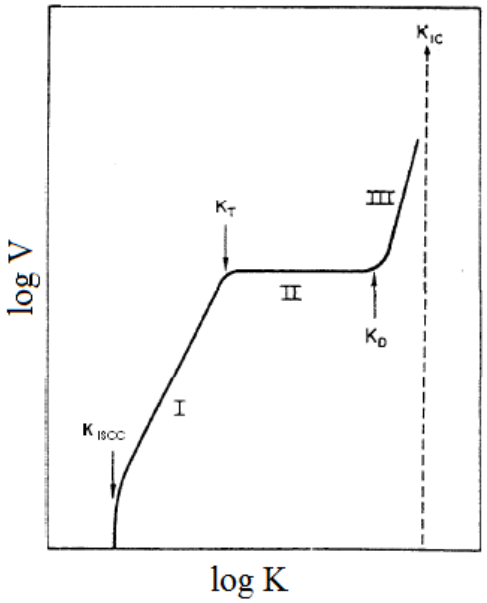

Figure 2.8 – Diagram of stress intensity factor-crack velocity VK plot showing the three identifiable regions of crack growth. Region I is stress corrosion controlled while in region II, the transport of active species control crack growth. In region III, mechanical rupture occurs. K_{ISCC} is the stress corrosion limit and K_{Ic} the fracture toughness. Sub critical crack growth takes place between these two limits. (Wiederhorn and Boltz [7])

before catastrophic rupture, occurs here. In region II, crack velocity is limited by the rate of diffusion or transport of the active species to the crack tip. Region II behavior is observed in some glasses and ceramics [7]. In region III, stress induced cracking occurs as the stress intensity approaches the critical value. Crack growth is mainly controlled by mechanical rupture and it is relatively insensitive to the chemical environment.

At very slow strain rates, the low stress intensity factor-crack velocity vK region on the vK diagram becomes more complex. It is assumed that there exists a threshold below which no significant crack extension can occur by stress corrosion, marked as K_{Iscc}. The value of this lower threshold is a function of the material's fracture properties and environmental factors [8]. Atkinson [59] calculated this limit for quartz to be about 0.2 times fracture toughness.

Other environmental factors also effect the rate of sub-critical crack growth. Temperature, for example, affects sub critical crack growth in two ways. The higher the temperature, the lower the activation energy and by implication the faster the reaction rate at the crack tip. Thus the crack velocity increases and the frac-

ture toughness and sub critical index are expected to decrease as temperature increases. However, the generation of thermal micro-cracks due to an increase in temperature can result in a toughening mechanism for very brittle materials and hence increase the fracture toughness [8]. Other factors include residual stress due to welding or quenching and the micro-structure of the material, amongst others.

In this project the concept of sub-critical crack growth is explored for the characterisation of graphite fracture. However, due to the nature of graphite the experimental data is limited. This is presented in Chapter 8.

2.2.10 Fracture Process Zone (FPZ)

Classical fracture mechanics deals with a single, ideal, atomically sharp crack. This is a suitable representation for single crystals or at a microscopic level on polycrystalline materials. In these cases extensive electron optical studies have supported the assertion that brittle cracks are atomically sharp and propagate by the sequential rupture of bonds [60]. At a macroscopic level of study, however, real polycrystalline, poly-phase materials, such as graphite, show more complex behaviour. On loading the blunt, machined notch in Figure 2.9 a few isolated micro cracks are formed, but the system behaviour remains linear.

On further loading, however, the intensity of micro cracking and behaviour in the crack tip region becomes non-linear. Finally, the macro crack extension occurs because of the linking of micro cracks in this non-linear zone, known as the FPZ. The macro-crack propagates by taking the damaged zone with it. In some materials the FPZ size becomes large, in which case non-linear fracture mechanics analysis are required, such as the J-integral. It is believed that the medium grained nuclear graphite considered in this thesis experiences this so called "micro-cracking". Thus EPFM options are investigated in the project.

2.2.11 Evaluation of Fracture Mechanics Parameters for Specific Crack Systems

Two distinct methods are used to evaluate fracture mechanics parameters for specific crack systems: (1) stress analysis, and (2) direct measurement using compliance calibrations. For stress analysis the standard approach is to define

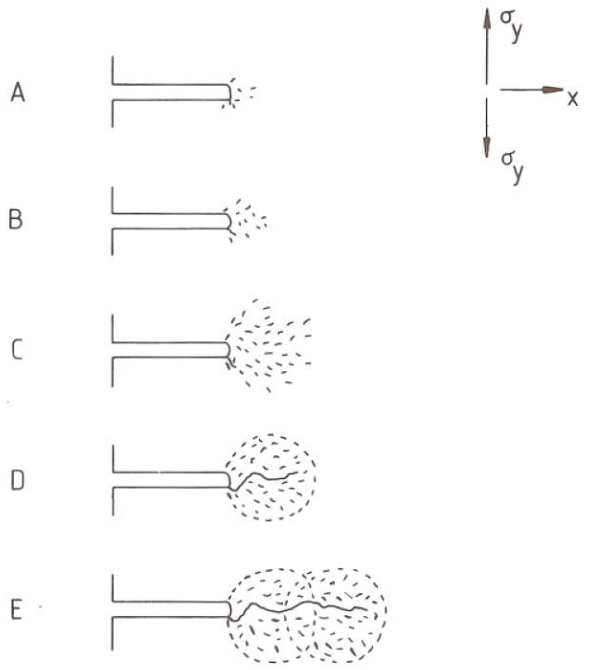

Figure 2.9 – Schematic illustration [8] of the stages of development of the fracture process zone and its influence on macro crack growth. Tensile stress increases from A to E. In (A), few isolated cracks formed around notch during preparation. (B) few more micro cracks formed but are mainly still isolated with a few forming linear cracks. Micro-cracking region exhibits linear elastic behaviour. (C) The degree of micro cracking increases with non-linear behaviour observed. (D) Micro-cracks link up to form a macro crack within the fully developed processed zone. (E) Macro-crack extends further by linking up of adjacent micro cracks in the migrated process zone ahead of the macro crack tip (from Ref [9]).

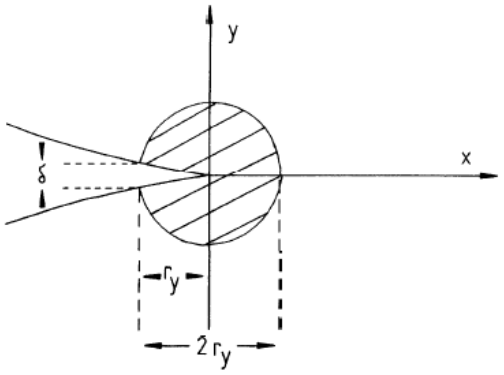

Figure 2.10 – Schematic illustration of a plastic zone, non-linear zone, or process zone size $2r_y$. For the simplicity, it is assumed that this zone is circular in the xy plane although in practise it will depend upon the stress state (from Ref [9])

a suitable stress function which satisfies the bi-harmonic equation of linear elasticity theory in accordance with the appropriate boundary conditions. This is a fourth order differential equation embodying the conditions of equilibrium, compatibility of strains, and Hooke's law. The components of stress and strain can be determined from the stress function. For complicated crack systems the analysis is formidable and simplifying analytical techniques are usually invoked, such as the sharp slit approximations of cracks, as distributed by Lawn and Wilshaw [56], or the assumption of plane stress or plane strain (for definitions see Jeager and Cook [61]). In these analyses the SIF terms are introduced to embody the essential boundary conditions of the crack systems.

G and J are usually evaluated experimentally by means of compliance calibrations. Because the strain energy release during incremental crack extension is independent of loading configuration we have a means of determining G, the energy release rate, through measuring compliance as a function of crack length to obtain dC/da as a function of a. An equivalent SIF can be obtained from Equation 2.15 when this relation is valid. Once a suitable means of calculation K, G or J for a specific crack system has been obtained and an appropriate experimental arrangement has been established, then certain key conditions need to be satisfied before experimental determination of the parameter is valid. This results from numerous simplifications in the crack analysis. For metals there are certain well defined standards, such as ASTM E399 [62], but these lack the ability to measure fracture parameters accurately for brittle or quasi-brittle materials, as shown in Chapter 3 for nuclear graphite.

2.2.12 Experimental Methods

Since the parameters that characterise fracture are said to be a material property, testing configurations must exist that can determine these fracture parameters. A wide range of experimental methods have been used to determine catastrophic crack growth parameters (K_{Ic}, G_{Ic}, J_{Ic}) for brittle materials, in contrast to only few a methods for the study of sub-critical crack growth. In part, this stems from the great difficulty experienced in determining the position with respect to time of the crack tip, especially in opaque materials. Common specimen configurations include the Three Point Bend (3PB) specimen (Figure 2.11) and the Compact Tension (CT) specimen (Figure 2.12). The 3PB has standardised techniques for the determination of SIF however, the loading configuration is unstable for short

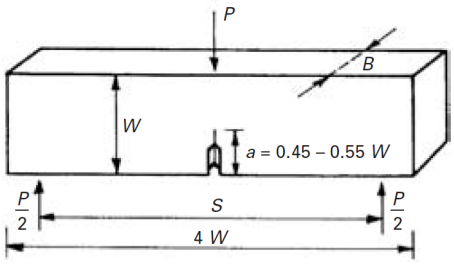

Figure 2.11 – Illustration of the Three Point Bend (3PB) configuration (from Ref. [10])

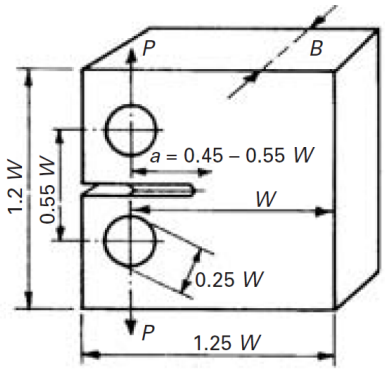

Figure 2.12 – Illustration of the Compact Tension (CT) specimen (from Ref. [10])

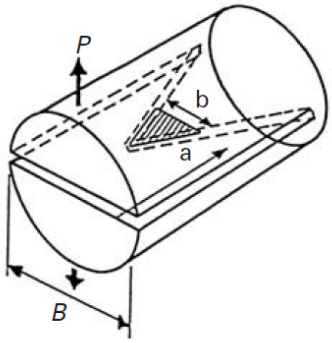

Figure 2.13 – Illustration of the Chevron Notched (CN) specimen (from Ref. [10])

cracks and inaccurate for long cracks making sub-critical crack growth tests inefficient. The CT specimen has the advantage of a straight crack front. However, the SIF calibration is a function of crack length, unless the calibration of the specimen and loading system are matched exactly.

Variations of the above mentioned techniques include chevron-notched (CN) specimens (ASTM E1304-97 [63] shown in Figure 2.13. The notch is chevron shaped and thus allows for more stable crack propagation as the crack surface area increases with crack length. However, this method does not easily allow for the observation of the crack tip and hence the suitability of a chevron-notched specimen for studying sub-critical crack growth is limited. The majority of sub-critical crack growth studies have used the so called Double Torsion (DT) testing method. The main advantage the DT technique has over other techniques is that crack velocity determinations can be made without the need for multiple crack length measurements when the crack tip driven load is applied in a particular way. The DT technique also allows for stable crack propagation at a constant driving force, which enables, unlike the other techniques, the ability to grow cracks controllably irrespective of the material's brittleness. The DT, which is the preferred technique of this project, is discussed in further detail in Chapter 5.

2.3 Damage Mechanics

Part of this thesis used an alternative methodology to predict the crack initiation (and propagation to some extent) in graphite specimens. This section intents to give the reader the necessary introduction to and understanding of the application of continuum damage mechanics in Chapter 9. This brief introduction to the damage mechanics methodology only covers the definition of a scalar damage variable from an effective stress concept and a classical thermodynamics point of view. The aim is to provide the reader with a general understanding of this methodology for the later application on quasi-brittle materials, where an elasto-plastic damage model is presented.

2.3.1 Background

In many instances and especially in quasi-brittle fracture, failure begins with a diffuse phase of damage (e.g. micro-cracking, multiple cracking and fragmentation). The fracture mechanics methodology can deal with cracking mechanisms,

however, these are defined within a framework of continuum as a single crack. Continuum damage mechanics represents a non-local tool to account for dilute distributions of voids and is not restricted to a discrete single crack, but rather considers the degradation of the bulk material as illustrated in Figure 2.14. In damage mechanics the state variables degrade as the material becomes "damaged". Often, the damage mechanics methodology is used for the crack initiation phase, however, it may also be utilised for the propagation of damage, i.e. crack growth [64].

It is worth mentioning that both damage mechanics and fracture mechanics have their distinct advantages and disadvantages. These, however, are not discussed here. Further, a distinction needs to be made between the processes of deformation, damage and crack propagation. Irreversible deformations described by the framework of continuum mechanics allow the material to be re-deformed to restore its initial shape. This is illustrated in Figure 2.15a for a tension–compression relationship. Damage corresponds to a definitive degradation of the material. Figure 2.15b shows the typical case of a quasi-brittle material whose non-linear behaviour is due to damage, observed by the drop in the elastic modulus in possible combination of small irreversible deformations. As such, damage is related to plastic or irreversible deformations, and, in the worst case scenario a fully damaged material section would represent a macro-crack.

2.3.2 Basic Concept of Damage

Like the fracture mechanics methodology, damage mechanics may be applied to a range of materials. In a ductile metal, damage may be seen as the nucleation and growth of cavities in the meso-field of plastic strains. In brittle concrete damage is seen as the micro-cracking that occurs due to a defined stress criterion. In all cases, damage can be seen as volume defects such as micro-cracks. The damage variable may thus be physically defined by a surface density of micro-cracks and the intersections of these defects of a plane cutting a representative volume of cross section δA. For the plane with normal $\bar{n}$ the damage variable becomes [11]

$$d_{\bar{n}} = \frac{\delta A_d}{\delta A} \tag{2.17}$$

Thus, damage can be seen as the ratio, where $0 \leq d_{\bar{n}} \leq 1$ depending on the severity of the damage state. If the damage is isotropic, the scalar variable does

not depend on the normal. In more advanced developments, damage may be described by second- and fourth-order tensors resulting from systematic studies of the decomposition of the stiffness or compliance tensors [23, 65].

In order to describe the impact of the damage on the macroscopic behaviour of the material, the effective stress is often used in constitutive equations. One methodology is to assume that the net stress is the average stress applied to the resistant section of the damaged specimen. The net stress is deduced from the Cauchy stress by taking into account the average section reduction due to voids and cracks. Such an approach was used for instance by Murakami [66, 67] to generalize the concept of creep damage in polycrystals directly to the anisotropic case. Another way is to assume a strain equivalence or energy equivalence[11]. This considers the same elastic energy for the actual damaged state and for the effective undamaged medium. Figure 2.16 indicates schematically the two hypotheses for the elastic tensile behaviour.

The changes in mechanical behaviour due to damage can be measured through from evolution of the damage parameters. Examples include the evolution of elastic modulus, used for ductile plastic damage (Lematre, 1985) as well as for fatigue [68]. It is also possible to use ultrasonic wave propagation velocity instead of directly measuring the elastic moduli [11].

2.3.3 Effective Stress Concept

One method, and probably the simplest concept, is to define damage using the effective stress concept. Here, for the uniaxial or multiaxial case of isotropic damage, the effective stress value can be given by a force equilibrium by using Equation 2.17 [11]

$$d_{\bar{n}} = \frac{\delta A_d}{\delta A} \rightarrow \bar{\sigma} = \frac{\sigma}{1 - d_{c,t}} \tag{2.18}$$

where d denotes the damage variable, in this case a scalar variable for compression ($_c$) or tension ($_t$). The damage due to the creation of discontinuities or micro-cracks reduces the value of the stress carrying capabilities and hence, it also decreases the elastic modulus, the yield stress before or after hardening amongst others. Some of these effects are used to evaluate the damage by inverse methods where the experimental properties of the bulk material are used to measure the degradation of the material. It is worth mentioning that the effects on mechanical

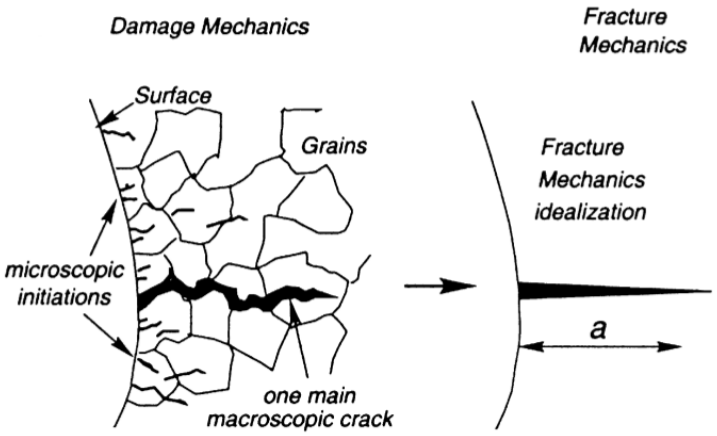

Figure 2.14 – The various defect sizes involved in fatigue and the two definitions of fatigue crack initiation (from Ref. [11])

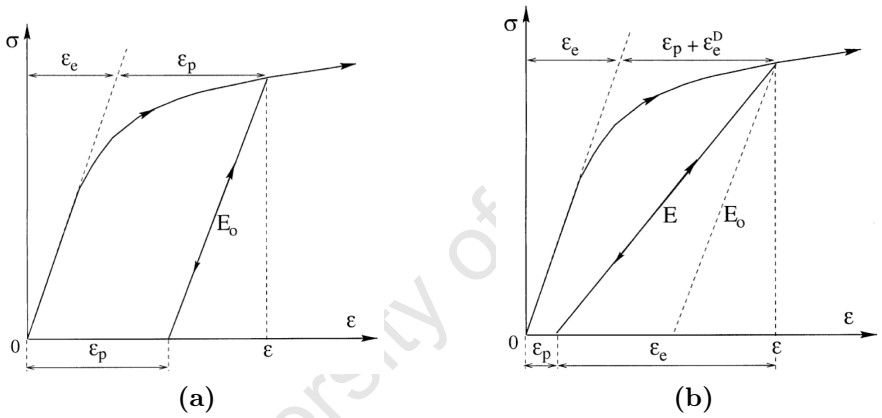

Figure 2.15 – Irreversible deformation in plasticity and brittle damage: (a) material with plasticity and (b) damageable material (from Ref [11]).

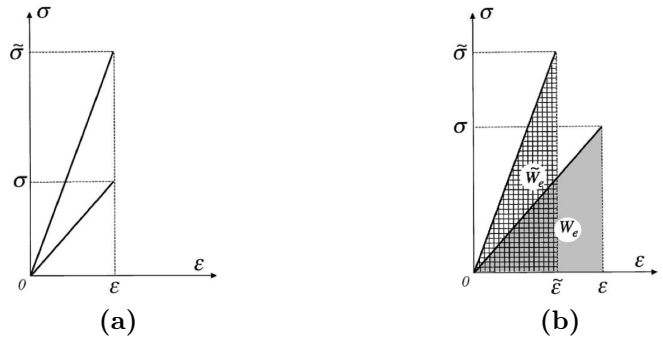

Figure 2.16 – Illustration of the two equivalence principles for the uniaxial elastic response: (a) strain equivalence and (b) energy equivalence (from Ref. [11]).

strength and stiffness are different in tension and in compression due to micro-cracks opening under tension and their closure under compression. This point becomes important in Chapter 9.

2.3.4 Thermodynamics of Damage

The energy bases damage mechanics methodology is more common in damage mechanics and is often referred to as thermodynamic damage as is adheres to an energy balance [11]. Here, the thermodynamics of irreversible processes allow for the modelling of different materials' behaviour. This is done by defining, through state variables, the present state of the corresponding failure mechanisms, the state of internal material potential and the dissipation of potential from evolution of the state variables. These three steps offer several choices for the definitions, each chosen in accordance with experimental results and purpose of use. Computationally this requires the second principle of the thermodynamics to remain balanced.

The state variables are chosen in accordance with the physical mechanisms of deformation and degradation of the material [69]. The Helmholtz specific free energy taken as the state potential of the material is a function of all the state variables. Written as $\psi(\varepsilon_{ij}, d$ (for scalar damage), r, α_{ij}, T), some qualitative experimental results have shown that the state potential (ψ) is the sum of thermo-elastic (ψ^{el}), plastic (ψ^{pl}), and purely thermal (ψ^{T}) contributions [11]. r and α_{ij} represent isotropic or kinematic hardening variables respectively. One important aspect of thermodynamic damage is that the second principle of thermodynamics has to be obeyed. The material state potential includes the damage in the elastic strain term and the hardening strain term. As such, the total energy dissipated during failure is divided into the energy stored in the material (hardening), the energy released during the damage process and possibly the energy dissipated as heat. Since the principle of thermodynamics is used, the energy dissipated during damage corresponds to the elastic energy release rate for a crack, the parameter of fracture mechanics usually denoted G [11]. For further reading on the derivation of the state variable associated with this damage model, the reader is referred to references [11, 70, 71].

Since the damage mechanics methodology relies on elastic and plastic strains, the material state needs to be defined by means of a yield and plastic flow rule. The concept of plasticity, which defines such a relationship, is presented in the

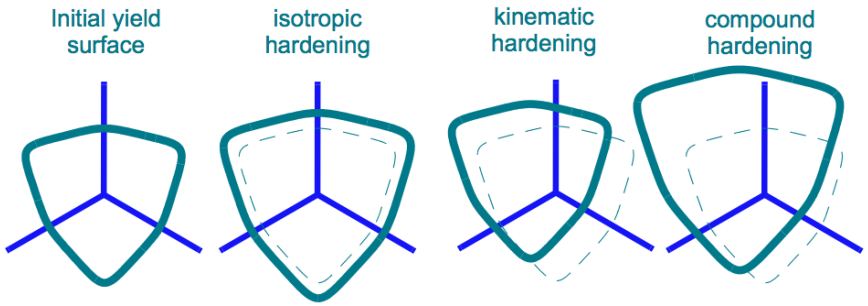

Figure 2.17 – Hardening mechanisms in the σ_1, σ_2, σ_3 space. At a given pressure, isotropic hardening entails an increase in size, kinematic hardening translates the yield surface, and compound hardening includes both mechanisms. Softening corresponds to a yield surface contraction (from Ref. [12]).

following section.

2.4 Plasticity Theory (Yield and Plastic Flow)

The term "plastic theory" defines the flow of material via dislocations and other mechanisms at the departure from elasticity. In metals, the term plasticity refers to the non-linear material response after yielding, in quasi-brittle materials plasticity refers to micro-crack growth and void collapse, amongst others. Rather than explicitly tracking each of these micro-scale failure mechanisms, the "yield" surface itself characterizes them in a phenomenological manner. The material response will be elastic to a defined limit after which the material will undergo irreversible structural changes that can be seen as inelastic strains. If continuing to apply elasticity theory, the stresses would move into regions outside the yield surface and hence plastic flow equations are required. Similarly, damage influences the plastic flow by affecting either the elastic domain or the hardening evolution.

The yield surface defines the transition from elastic to plastic behaviour and assumes various function depending on the material and its properties. For metallic materials the most common yield criterion is the Von Mises yield criterion while in quasi-brittle fracture a Drucker and Prager criterion is often assumed (these are further discussed in Chapter 9).

The elastic stress states are "inside" the yield surface. Stress states outside the yield surface are defined by a hardening evolution of the internal state variables

(r, α_{ij}) corresponding to a fundamental change of the underlying micro-structure of the material. There are two types of hardening rules; isotropic and kinematic, or both. As indicated in Figure 2.17, isotropic hardening causes a change in size of octahedral yield profiles, while kinematic hardening produces a translation of all octahedral yield profiles. Both types of hardening can occur simultaneously. These hardening evolution laws may be integrated through time, to model the time varying hardening evolution of the yield surface. The concept of plastic hardening or softening is further discussed in Chapter 9. For further information on plasticity the reader is referred to references [72, 73].

2.5 Summary

This chapter presented some general information on graphite, fracture mechanics, damage mechanics and plasticity. Its aim was to introduce these topics to the reader, as the later chapters in this thesis require the understanding of these topics. In this thesis, the characterisation of graphite fracture primarily utilised the fracture mechanics methodology. However, an additional mechanical failure model is presented in Chapter 9, where the damage mechanics, coupled with plasticity approach is utilised. The reader wishing to acquire further information on the presented topics is referred to the relevant references in the text of this chapter.

Chapter 3

Previous Studies on the Fracture of Nuclear Graphite

This chapter considers the previous studies which have been undertaken on the fracture mechanisms and behaviour of various nuclear grade graphites. An overall summary of the characteristics of fracture behaviour is given and, subsequently, the most significant studies are discussed in further detail to demonstrate the evolution of graphite fracture understanding. The purpose of studying these is to demonstrate how these have influenced each other and helped to form current understanding of graphite fracture. This is followed by a discussion on the lack of graphite fracture understanding and the need for further investigations on this topic.

It is worth mentioning that fracture mechanics methodology has prevailed in most recent studies. In addition, the two graphite grades that have been most frequently studied are Pile Grade A (PGA) and Gilsocarbon (IM1-24). This is is probably due to the fact that the PGA and IM1-24 grades are utilised in British reactors and most graphite research is undertaken in the UK. The Nuclear Block Graphite 10 (NGB10), one of the graphite grades considered by this thesis, has been researched to a very limited extend as apperent from literature.

3.1 Introduction

In Chapter 1 it was established that graphite components, in the nuclear environment, form part of the internal reactor structure. Their functionality and

integrity is thus of utmost importance. It has been reported that the failure in these graphite components is predominately due to cracking and subsequent fracture. Thus, it is important to understand the fracture and mechanical failure process. The field of fracture mechanics and damage mechanics provides useful tools in understanding and evaluating strength and durability of many materials and, in particular, fracture mechanics has frequently been used to assess the structural integrity of graphite components.

Many early fracture mechanics evaluations of artificial graphites have been conducted under the assumption of the linear elastic hypothesis (LEFM) by using the critical stress intensity factor, K_{Ic}, or the elastic strain energy release rate, G. One of the first attempts to measure the fracture toughness was undertaken by Corum on EGCR-type AGOT graphite [74]. He performed Single Edge Notched Beam (SENB) tests on extruded graphite and evaluated the critical strain energy release rates based on linear elastic fracture mechanics. His notches were placed at different depths in the specimens using a 0.24 mm thick jeweller's saw. They used both the compliance measurement method and an analytical solution for the stress intensity factor. Their results for G_{Ic} were about 70 J/m^2 and 50 J/m^2 for cracks parallel and transverse to the direction of extrusion, respectively. Their results reported that the propagation of cracks was predominantly inter-granular. Lower G_{Ic} values were observed for notch length-to-beam depth ratios (a/W) less than 0.2. The variations in his results were attributed to slow crack growth prior to unstable crack propagation and a sizable zone of inelastic deformation at the notch tip or pre-existing cracks or flaws. There were no detailed discussions on the effect of specimen geometry on the fracture toughness values of graphite.

Following various LEFM investigations, it was established that nuclear graphite experiences some non-linearity during fracture and as a result the research approach was shifted to elastic plastic fracture mechanics (EPFM) for the characterisation of graphite. Sakai et al. [14] used the compact tensile test with a chevron notch specimen on isotropic fine grain size polycrystalline graphite, IG-11. They measured the non-linear fracture parameters through the loading and unloading of a specimen. Their results included the non-linear critical strain energy release rate, the J integral, and the plastic energy dissipation rate. It was found that about 38% of the total fracture energy was consumed as plastic energy and that the fracture parameters decreased with increasing crack length for crack length to specimen width ratios between 0.6 and 0.9. They concluded that for zero plastic energy dissipation, i.e. as the crack length approaches the specimen width, the

fracture parameters converge, to give a lower limit of 73 J/m^2 which equates to a fracture toughness of 0.27 $MPa\sqrt{m}$. Sakai's research is further discussed in the later sections of this chapter. Similarly, Rose and Tucker [42] measured acoustic emissions during cracking of virgin pitch coke graphite and concluded that micro-cracking occurs prior to the main failure. In addition, they concluded that the micro-cracking decreases with increasing notch depth. In their modified solution, which is based on LEFM with analytical compliance, they added an additional 0.6 mm to the original notch depth to account for the presence of inherent flaws. An estimate of K_{Ic} was found, consistent with Corum's [74] results of values for K_{Ic} of $1.2MPa\sqrt{m}$. All tests were such that the direction of stressing was perpendicular to the extrusion direction of the graphite components.

Sakai et al [13], in a separate paper, investigated the R-curve or crack growth resistance behaviour of fine-grain polycrystalline graphite, IG-110, using the compact tensile test, ASTM E399. They showed that the fracture toughness for stable crack propagation within the plateau region for this graphite was found to be 1.2 $MPa\sqrt{m}$. They showed that the R-curves rose sharply at first, and then reached a plateau before falling off gradually for crack length to specimen width ratios of less than 0.6. On the contrary, results on fine-grain polycrystalline graphite (IG-110) including that of Fazluddin [16], who also used notched beams in three point bending, concluded that K_R changes very little over a range of crack lengths. Similar properties were also noticed by Ouagne et al [15] for PGA and IM1-24 graphite. They concluded from observations of the crack growth resistance curves for the non-linear fracture parameters that there exists a plateau region where the crack bridging zone and the frontal process zone, ahead of the crack tip, reached steady state values. Hodgkins [4] showed microscopical evidence for graphite fragments acting as crack bridges, which were much smaller than filler particles. This indicated that the graphite fragments are broken down during crack propagation. Recent studies have shown that micro-cracking can occur at a third of the peak load [17]. It was also found that the notch fracture toughness is not a constant material property and depends on the notch geometry parameters i.e. the notch angle and the notch tip radius [75].

Several additional papers may be included in this introduction on the fracture characteristics of nuclear graphite [76, 24, 41, 77, 46, 78, 79, 80, 81, 82]. These, however, show the trend that many uncertainties over the fracture characteristics of nuclear graphite remain. One may conclude that the fracture toughness of nuclear graphite is around 1 $MPa\sqrt{m}$, with the assumption that $K_R \approx K_{Ic}$.

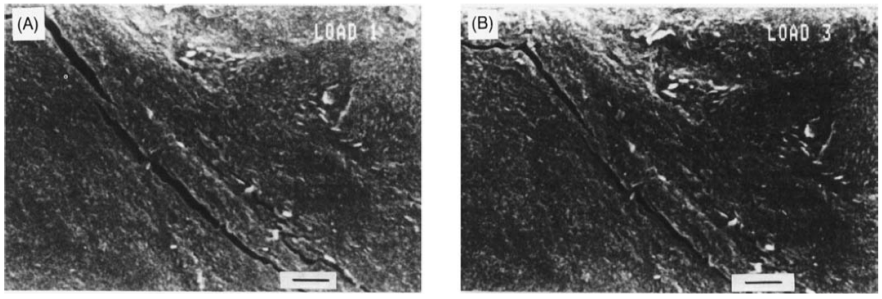

(a)

Figure 3.1 – Scanning electron micro graphs from Sakai [13] of an induced micro-crack taken (A) in the frontal process zone and (B) far downstream in the wake before and after the main crack extension, respectively (bars = 1 pm).

There seems to be a dependency of crack length, or rather the micro-cracking and crack bridging, which seems to induce plastic behaviour.

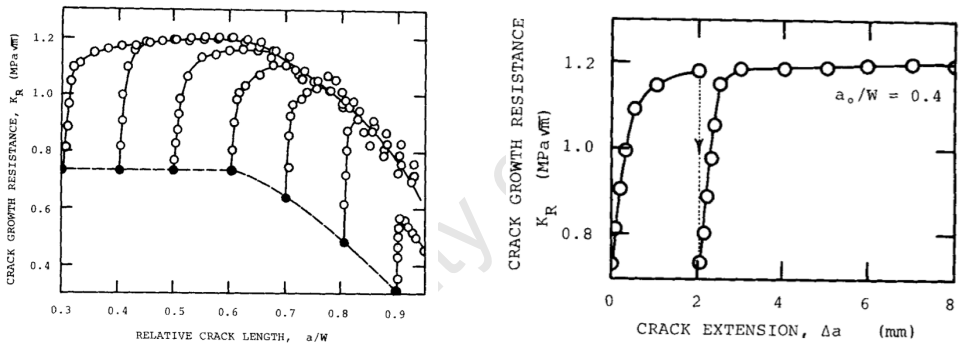

(a) **(b)**

Figure 3.2 – (a) K_R-Curve behaviours of the specimens with different initial notch lengths. Solid circles represent the critical stress intensity factor (K_c^{ini}) at crack initiation. (b) The K_R curve before and after re-notching. Re-notching was undertaken at Δa = 2mm.

An additional point worth mentioning is that standard test methods of fracture toughness measurement, which have predominantly been used for the graphite fracture characterisation, only apply to homogeneous specimens containing a sharp crack. In metals a sharp crack is typically produced by fatigue crack propagation from a machined notch. Crack branching often occurs when attempts are made to fatigue a sharp crack into brittle materials (such as graphite) which have an inhomogeneous structure. Because of this difficulty, no standard fracture toughness test for coarse grained brittle materials such as concrete and graphite

has been established.

3.2 Experimental Observations and Characterisations of Graphite Fracture

The above introduction established that many questions remain concerning the mechanisms and parameters associated with graphite fracture. It is worth pointing out that each chapter in this thesis provides a short relevant literature study of a relevant topic. As such, the aim of this chapter is to establish an historical understanding of graphite fracture. Some of the most significant contributions are considered below. Most of these are from a fracture mechanics point of view. The purpose is to demonstrate how these have influenced later work and helped to form the current understanding of graphite fracture. This project follows onto these previous projects, in an attempt to contribute to fracture understanding.

- Sakai et al. in 1983 [14] and in 1988 [13],
- Romanoski and Burchell in 1991 [78]
- Ouagne in 2001 [15],
- Fazluddin in 2002 [16],
- Hodgkins in 2006 [4],
- Ayatollahi and Torabi in 2010 [75] and
- Heard et al. in 2010 [17]

3.2.1 Sakai et al. (1983 and 1988)

It was mentioned in the introduction of this chapter, that Sakai et al. [14] utilised a specialised loading and unloading methodology to establish the non-linear parameters associated with graphite fracture. The significance of their methodology was the ability to define a range of parameters associated with stable crack propagation. The adaptation of the elastic strain energy release rate enables the definition of a series of both elastic and non-linear parameters as G and J (as J_{el}

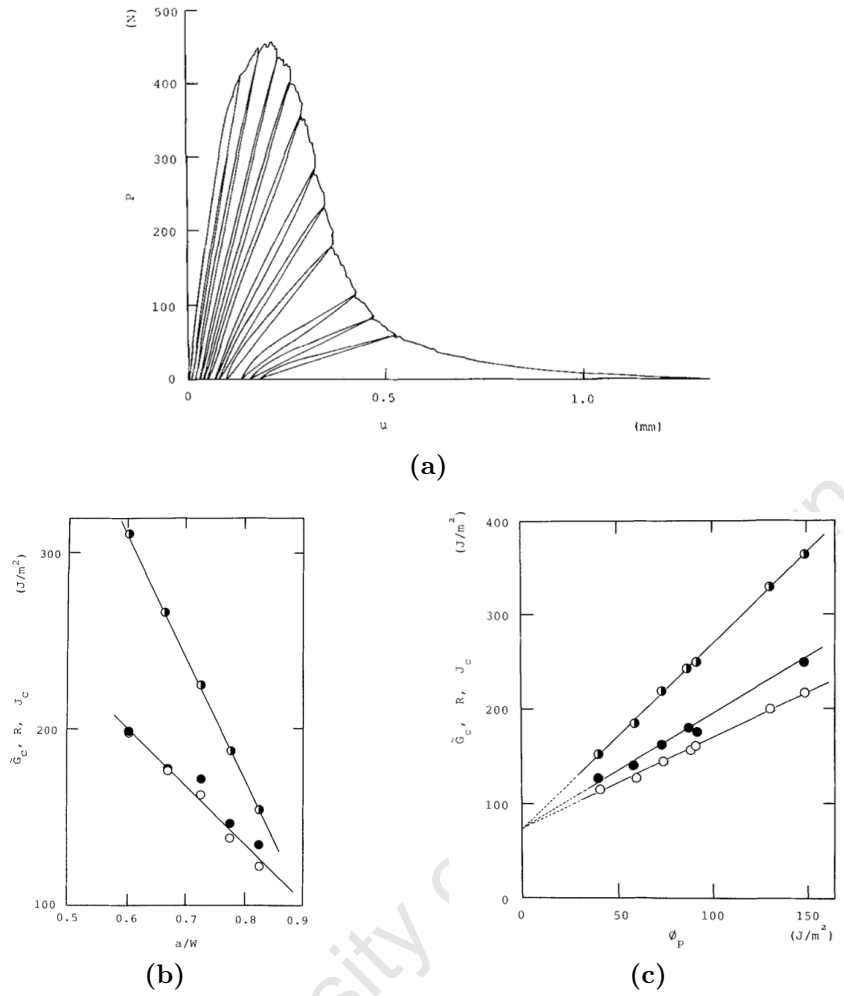

Figure 3.3 – Sakai's experimental data [14] (a) Diagram of load-displacement. Load-unload procedures were conducted repeatedly at each additional crack extension. (b) Relations between non-linear fracture toughness parameters and crack length (R-curve relationship). (c) Dependence of non-linear fracture toughness parameters on plastic energy dissipation rate.

and J_{pl}), all of which may be determined graphically (directly from the load v displacement curve for the test).

Their results, which were carried out on fine grained graphite, indicate that crack initiation occurs at the peak of the load-displacement curve following rapid load drop as the crack grows (Figure 3.3a). Subsequent analysis indicated falling crack growth resistance throughout the test (Figure 3.3b); at no point was there any evidence for a rise or a plateau crack resistance. Subsequent studies on this grade of graphite appear to confirm that there is a rise in crack growth resistance as crack length increases [16, 4, 15], but none have shown any significant fall in

resistance as exhibited by these experiments.

The approach to fracture property determination, taken in Sakai's paper, is unique. The results of the experiment contradict almost with every other test carried out on graphite, in that they show a falling crack resistance with crack length. This may be due to the unusual way in which the loading plates were attached (adhesive), which prevented the specimen from rotating about the crack tip, which clearly affects specimen compliance [4]. However, Sakai did make an important observation. They observed that fracture is associated with significant non-linear contributions and have established an elastic fracture threshold as 73 J/m^2 which equates to a fracture toughness of 0.27 $MPa\sqrt{m}$. This observation is illustrated in Figure 3.3c and signifies the understanding that graphite fracture is associated with non-linear mechanisms. It is worth mentioning that Sakai used a Chevron Notched (CN) specimen configuration as it enabled stable crack propagation. The crack front is, however, not straight making it difficult for crack tip observations.

Later in 1988, Sakai et al. [13] observed the micro-mechanical processes that leads to crack propagation in nuclear graphite . Results from earlier studies into fracture behaviour of crystalline ceramics Al_2O_3 [83, 84] and BeO [85] were used to develop a theoretical model for comparison. Sakai utilised Compact Tension (CT) specimens, which were made from isotropic IG110 nuclear graphite. Starter notches were cut to a variety of depths from 0.3 a/W – 0.9 a/W, using a razor saw, with a 10μm width estimate. Each specimen was loaded using a 'through' screw to grow cracks in a controlled fashion. For R curve behaviour, re-notching was carried out on an unloaded specimen following approximately 2 mm of crack propagation. The fracture toughness was determined using the standard test methodology ASTM E399. The formation of micro-cracks ahead of the crack tip and their closure in the wake was monitored on the flat surface using a scanning electron microscope.

Two mechanisms were highlighted as possibly being responsible for rising R-curve behaviour; micro-cracking immediately surrounding the crack tip and bridging in the wake. The onset of micro-cracks of approximately 20μm in length were observed at 60% of the fracture load. Partial micro crack closure was also observed in the wake causing some residual strain (crack closure) following the removal of the applied loads.

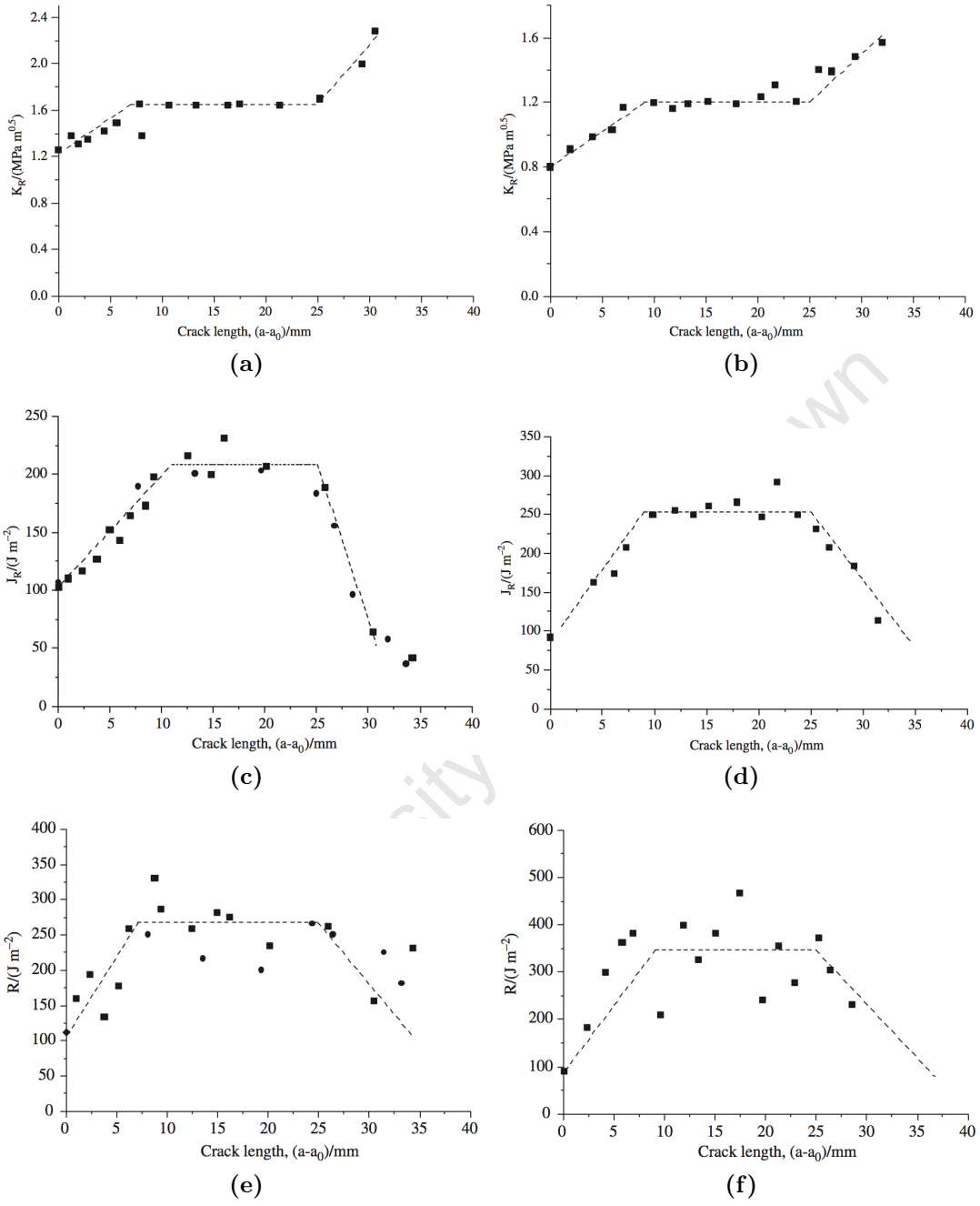

Figure 3.4 – Ouagne's R-curve analysis [15]. K_R curves for (a) IM1-24 and (b) PGA graphite. J_R curves for (c) IM1-24 (d) PGA graphite. R curves for (e) IM1-24 (f) PGA graphite. Crack lengths measured using: a video camera (square) and dye penetration (circle).

3.2.2 Romanoski and Burchell (1991)

A study at Oak Ridge National Laboratory compared various standard fracture toughness specimen configurations, using IG-110, H-451 and S2020 graphite grades, to establish specimen geometry influences on fracture toughness. The test geometries investigated were CT, disc compact tension (DCT), short rod (SR), chevron-notched short-rod (CNSR), cylindrical bend specimen (BS) and centrally slotted disc (CSD) specimens.

The analysis concluded that specimen geometries which allow for stable crack propagation, such as the CNSR and CT, yielded a higher fracture toughness than those where fracture is very rapid, e.g., the CSD. Further, it was also shown that the fracture toughness increased with increasing specimen size for all specimens and graphite grades tested. This result was attributed to the rising R-curve behaviour. No relation was draw to micro-cracking or crack bridging.

3.2.3 Ouagne et al. (2001)

Ouagne utilised Sakai's [14] graphical method and the standard ASTM E813-81 to determine the R-curve behaviour using CT specimens. Results from these R-curve experiments on IM1-24 and PGA [15] showed that the R-curves, in Figure 3.4, indicate a sharp initial rise followed by the formation of a plateau region after approximately 9-11mm of stable crack propagation. PGA appears to exhibit lower fracture toughness (1.27 vs. 0.9 $MPa\sqrt{m}$ for IM1-24 and PGA respectively) and lower critical strain energy release rate (138 vs. 79 J/m^2 for IM1-24 and PGA respectively). However, the work of fracture is higher than for the PGA graphite suggesting greater energy dissipation effects in this grade (136 vs. 170 J/m^2 for IM1-24 and PGA respectively). Further, Ouagne et al [15] showed, on a macroscopic scale, the tortuosity of the crack path (Figure 3.5). The indirect crack path results in friction planes during crack opening and hence contributes to the overall crack growth resistance, especially for large crack systems.

It was concluded that prior to crack initiation a zone of intense damage or deformation formed around the crack tip. The initial rise in resistance following initiation was due to the formation of a bridging zone in the wake. It was assumed that the distance over which the rise in resistance occurred would correspond with the length of the bridging zone, which was found to be around 9-11 mm.

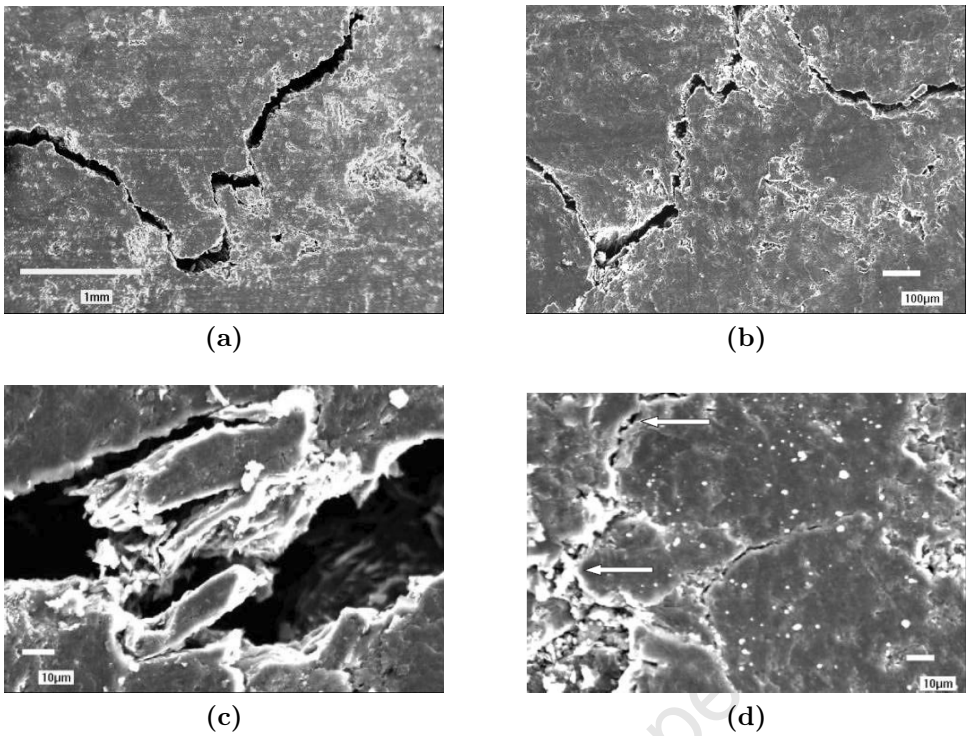

(a) **(b)**

(c) **(d)**

Figure 3.5 – Examples of cracking in PGA graphite [15]. a) and b) friction points (arrowed) and crack tortuosity; c) crack bridging particle remote from the crack tip with evidence for shear cracking; d) smaller crack bridging particles (arrowed) and crack branching closer to the crack tip.

3.2.4 Fazluddin (2002)

Fazluddin utilised Three Point Bend (3PB) and CT specimens to compare the fracture properties of a range of graphite grades used by the nuclear industry [16]. The analysis was, however, based entirely on the linear elastic assumption. The graphite grades considered included IM1-24 and Fazluddin produced a range of R-curve data from the two considered geometries. Crack length measurements were undertaken by means of a potential drop system, optical and compliance crack measurment techniques.

The curves for IM1-24 exhibit the initial sharp rise reported in earlier studies followed by continued rising resistance throughout the test. Falling resistance characterised the end of the test ($a/W \geq 0.85$). An important aspect of his results are the indication of a significant difference in the length of the bridging zone in a CT specimen, estimated at 6-7 mm, to that in a SENB specimen, estimated at 2-2.5 mm. Fazluddin reported that crack propagation in the CT

specimen undergoes several stages. This is illustrated in Figure 3.6 where during the first stage a FPZ develops at the crack tip, which initiates at the onset of the second stage. Over the middle half of the specimen, the FPZ and wake effects stabilised, resulting in the plateau R-curve phenomena. During the last stages the FPZ nears the end of the specimen and, as a result, the fracture resistance decreases.

Fazluddin's R-curves, for the two considered specimen configurations, showed a fundamentally different behaviour. The R-curve of the 3PB specimen can be identified as a typically brittle fracture, where as the the R-curve of the CT specimen can be associated with a more ductile fracture, due to the continuous rise in toughness. No explanation in this respect was provided.

3.2.5 Hodgkins (2006)

Based on the research undertaken by Sakai et al. [14, 13], Ouagne [15] and Fazluddin [16], Hodgkins [4] investigated the R-curve behaviour of IM1-24 using three dimensional X-Ray tomography. This project considered three CT specimen configurations of the IM1-24 material. Using X-Ray tomography, Hodgkins investigated the propagation of the crack tip and the micro-cracking associated with it.

He found significant evidence of micro-cracking near the crack tip, as well as in regions considerably far removed for the crack tip (of up to 45 mm). Many of his specimens exhibited non-straight crack fronts as shown in Figure 3.7. The significance of this is that conventional fracture mechanics assumes an even or continuous crack front (the reader is referred to Chapter 2) and hence results may be erroneous.

Hodgkins verified that the sharp initial rise in fracture resistance is a common feature in graphite fracture which is due to the formation of the FPZ. The shallower rise after initiation is exhibited at crack lengths greater than 10-15 mm and can be attributed to friction bridges in the crack wake (of up to 45 mm behind the nominal crack tip). This being said, Hodgkins concluded that the length of the zone can vary depending on the type of loads being applied to the specimen. He summarised by stating that graphite fracture shares common features with concrete and cementitious materials which can be characterised as quasi-brittle. As such there may be significantly less commonality with metals or glass.

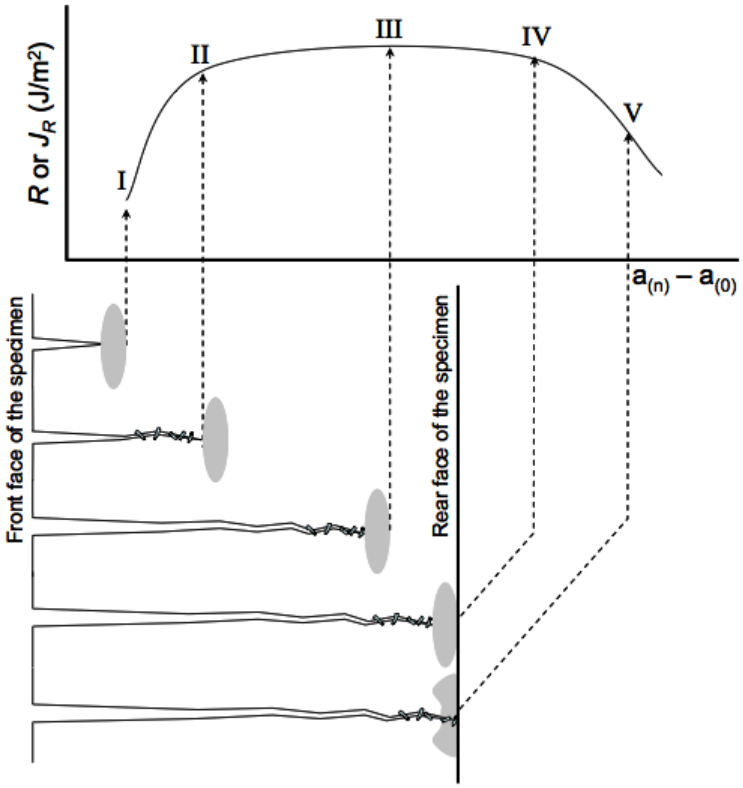

Figure 3.6 – Diagram of the R-curve and the mechanisms associated with each stage [16].

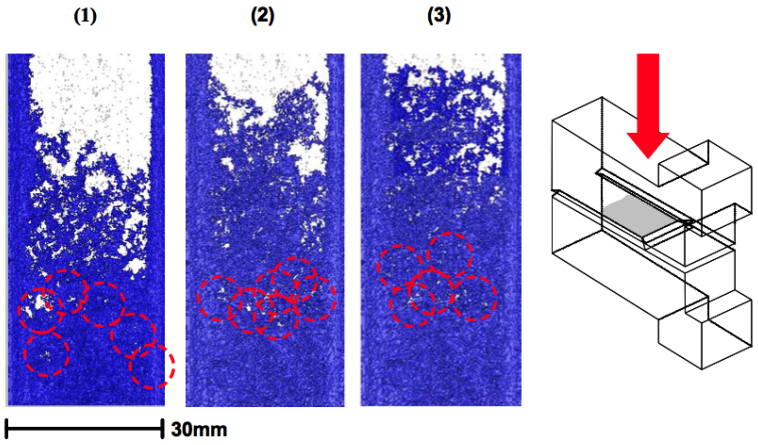

Figure 3.7 – Crack propagation (1-3) in a 30mm thick CT specimen of IM1-24 containing double side grooves [4]. Highlighted in all of the images are discontinuities in wake, at long range which may represent the location of friction bridges.

3.2.6 Ayatollahi and Torabi (2010)

Ayatollahi and Torabi [75] studied the brittle graphite fracture experimentally and theoretically using samples containing rounded-tip V-notches. They investigated three different V-notched specimens called the rounded-tip V-notched Brazilian disc (RV-BD), the rounded-tip V–notched semi- circular bend (RV-SCB) and the rounded-tip V-notched (RV-TPB) specimens. A theoretical criterion called the Mean Stress (MS) criterion was then proposed for predicting the experimental results.

The MS criterion was extended to rounded-tip V-notched domains in order to estimate the fracture toughness of notched graphite components. It was shown that the experimental results were in good agreement with the results estimated by the MS criterion. More importantly, it was found that the notch fracture toughness is not a constant material property and depends on the notch geometry parameters i.e. the notch angle and the notch tip radius.

3.2.7 Heard et al. (2010)

Heard et al. [17] used PGA cylinders (12mm in diameter and 6mm long), subjected to controlled cracking by either insertion of a needle into the material or by compressive loading, to measure the cracking mechanisms in graphite. The resultant cracking was observed using optical and focused ion beam microscopy.

Heard confirmed that micro-cracking preceded the macro-crack formation. This mechanism was consistent with the observed non-linearity in load-displacement curves prior to the peak-load. Such cracks have been observed at loads which are as low as 30% of the peak-load (as shown in Figure 3.8). Macro-cracks initiate by linking micro-cracks and follow an irregular path controlled by the direction of the applied tensile stress and the micro-structure, in particular porosity and the filler particles. These followed an irregular path controlled by the direction of the applied tensile stress and the micro-structure, in particular porosity and filler particles.

3.3 Modelling Approaches

Several studies have attempted to develop models that describe and predict failure in polycrystalline graphite, where the underlying themes of most methodologies

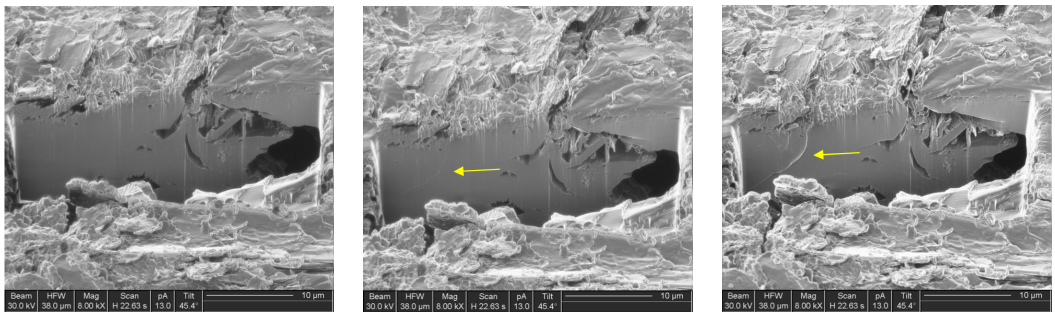

(a) **(b)** **(c)**

Figure 3.8 – FIB images of PGA specimen under (a) 497N, (b) 560N and (c) 830N compression [17]. Arrows show developing micro-crack.

are based on the fracture mechanics methodology. These include the Rose-Tucker model [86] (which is based on the probability that adjacent grains cleave to form a critical Griffith flaw leading to failure), Burchell's model which considers high aspect ratio pores that are aligned favourably to the applied stress (as sites of stress concentration, from which cracks initiate at relatively low stress levels) and more recently R-curve models by Ouagne [15], Fazluddin [16] and Hodgkins [4].

The use of the fracture mechanics methodology enables a tool for accessing flaws in materials such as graphite. If the Stress Intensity Factor (SIF), LEFM or EPFM, is higher than the predicted material property, fracture occurs. Graphite, however, experiences a rising crack resistance and hence a single parameter does not adequately describe fracture. The R-curve relates theses crack growth resistance parameters to the extent of crack growth and thus is believed to provide a more realistic view of the fracture behaviour of graphite.

It is worth mentioning that some early graphite failure models have been based on the Weibull approach. The Weibull approach is a statistical approach where failure is governed by a weakest link process. One of the main limitations of the Weibull approach, is that it assumes graphite as a homogeneous continuum material and it fails to accommodate for the non-linear stress-strain behaviour. Hence, the crack growth resistance curve or R-curve thus provides a more realistic view of the fracture behaviour.

It has, however, been shown that the use of a critical SIF (as a criterion for fracture initiation) and also R-curve behaviour to some extent varied depending on the specimen geometry [4, 16]. As such, a cohesive zone model was suggested by Zou et al. [87], which enables an alternate approach to the simulation of

crack propagation. The model, which is also founded on the fracture mechanics methodology, relates tractions to the relative displacements at an interface where a crack may occur using a constitutive law for the tractions and displacements. Based on a maximum (critical) value for the traction and the fracture energy G equivalent area under the curve, the model enabled the prediction of crack initiation and propagation for graphite structures under both regular (blunt notch) and singular (i.e. a crack tip) stress concentrations.

One of the setbacks of the model is the requirement of a predefined crack path, which has to be predicted based on a linear stress analysis before-hand. Since cracking in graphite is irregular, the assumption of a pre-defined crack path is questionable. In addition, mesh sensitivity has been reported using this technique [23, 21].

3.4 Shortcomings in the Current Graphite Failure Understanding

The current methodologies to gain understanding on the way graphite fractures utilised a range of techniques. These include standard test methods, where LEFM conditions are assumed, to more complex methodologies and measuring techniques under the EPFM assumption. Other failure models have been proposed such as the statistical Weibull approach or micro-structure based failure models. As it stands, clear evidence exists that the fracture of graphite is associated with non-linear failure mechanisms such as micro-cracking and crack wake effects. These seem to result in a rise in crack growth resistance during the first 10-12 mm of crack propagation and are said to reach a plateau region during which a steady continued rise may be observed.

One of the main problems that researchers have experienced with standard test specimens is the ability to propagate cracks in a stable manner, whilst observing the crack tip. Normally, CN specimens are utilised to obtain stable crack propagation, however these don not facilitate crack tip observations. Three Point Bend (3PB) and SENB facilitate for crack tip observations, however, fracture is highly unstable. Sandwiched SENB configurations have been used to enable stable fracture [45], but have been shown to require complex Finite Element analysis to account for friction. CT specimens have enabled, to a certain degree, stable crack propagation with crack tip monitoring capabilities, however only short crack

lengths are achievable. Modifications of the CT specimen, by Hodgkins [4], have enabled the ability to generate relatively long cracks, however, these require side grooves to enforce straight crack propagation. The effects of side grooves is not fully understood as these may act as stress concentrations. It thus appears that the need for a novel technique exists which can facilitate for stable crack propagation and crack monitoring techniques. As such, the Double Torsion (DT) technique was proposed for this project. It is believed to facilitate for stable crack propagation and easy crack tip observations. Further details about the DT technique are presented in Chapter 5.

At present there is no agreement as to which methodology models graphite failure best. The reason for such discrepancies may lie, partially, in the assumptions and limitations implied by the techniques used to characterise fracture behaviour in graphite. If fracture mechanics does provide a valid approach, then the question of whether graphite fracture is best characterised by LEFM techniques or EPFM methods remains. Therefore, perhaps it is not surprising that a wide range of results have been reported. What is understood is that the formation of damage immediately ahead of the crack tip, appears to act as a precursor to fracture. This zone was found to consist of micro-cracking, which is said to develop at approximately a third of the peak load [17]. In addition, a wake zone exists behind the damage zone in which crack bridging and friction planes can result in toughening mechanisms. Hodgkins identified these micro-flaws in front of the macro-crack tip and in regions beyond the crack tip [4]. However, the experimental evidence that the formation of the macro-crack is a function of the generation of micro-cracks, in the most highly stressed regions, remains unclear. In addition, the mechanisms in the crack wake, by irreversible slip along basal planes, crack branching and other mechanisms, remain unanswered. There also exists no understanding of the extent of this damage zone, which appears to vary in length depending on the configuration of the test specimen (6-7 mm in 3PB specimens to 15 mm in CT specimens). The studies that have reported the formation of a plateau region of fracture resistance suggest that the length of the bridging zone stabilises following approximately 9-11 mm of crack propagation.

The fracture mechanics methodology, which is based on sound understanding of the stress field and the energies associated with a crack, does provide a way to describe these mechanisms. The R-curve, which has been popularly applied in previous graphite assessments, points out that crack propagation undergoes several stages. The formation stage, notable by a sharp rise in the R-curve,

is succeeded by a steadily increasing zone, which has been attributed to the stable movement of both the deformation zone and the bridging zone ahead of the crack tip. Falling resistance is believed to take place when the deformation zone makes contact with the rear face of the specimen. The energy consumed by the deformation zone is no longer absorbed and therefore becomes available for growing the primary crack. The final stage of the crack growth process is attributed to the weakening bridging zone.

This being said, large discrepancies exist in R-curve data for the same material using different geometries. These discrepancies could be attributed to the method through which the R-curve behaviour was obtained, i.e. Sakai's energetic method, Fazluddin's potential drop system or Hodgkins X-ray tomography analysis. The question as to whether the R-curve behaviour is a true material behaviour in graphite remains.

3.5 Summary

A number of models have been proposed to simulate and predict the failure of nuclear graphite components. These are commonly based on the fracture mechanics methodology, however, few other models, such as the Weibull approach exist. With the realisation that graphite components mostly fail due to cracking, the fracture mechanics methodology is believed to provide the tools necessary to predict failure.

Nuclear graphite was shown to exhibit a rising resistance with crack propagation. The experimental evidence suggests that the mechanisms responsible is damage in the form of micro-cracking ahead of the crack tip and crack wake effects such as bridging and friction planes. The R-curve behaviour has been used to characterise these cracking mechanisms. The questions, however, remain as to what the mechanisms behind crack initiation and propagation are, and whether the R-curve behaviour is a true material behaviour.

Resolving these issues lies at the heart of this project and represents an essential precursor to developing an understanding of the corresponding graphite fracture behaviour. Questions surrounding crack growth resistance, which have been addressed experimentally, are listed below:

1. Does the DT specimen geometry facilitate for stable cracking whilst enabling easy crack tip observations? More specifically;

- How does the DT methodology compare to other standardised techniques, i.e. does the technique produce valid and repeatable experimental data?
- Does the technique facilitate for the measurement of non-linear fracture parameters?
- Can it be used for graphite?

2. Using the DT technique, what are the mechanisms of crack propagation and how do these relate to the measured and previously measure R-curve behaviour? More specifically;

   - Does a damage zone exist prior to crack initiation and at what point does a primary-crack initiate?
   - Following primary crack initiation, what are the mechanisms associated with crack propagation and how are these responsible for the initial rise in crack growth resistance?
   - What are the mechanisms of crack propagation and how do these effect the crack growth resistance?
   - Does a limit to the fracture resistance exist with respect to the reported plateau region?

   In addition to the above, it would be highly beneficial if the mechanisms attributed to the R-curve behaviour could be confirmed by means of optical measurements and observations.

3. Does fracture mechanics provide the most appropriate technique for characterising the fracture behaviour of polycrystalline graphite? More specifically;

   - Why has such a vast range of fracture mechanics based parameters been reported? Can these be attributed to the difference between the LEFM and the EPFM assumption.
   - Does the R-curve define the fundamental material property of the two considered graphite materials?
   - Is there a geometry dependency when using fracture mechanics?

4. What has been learnt, with respect to the understanding of graphite fracture behaviour, from the analysis and previous literature? More specifically;

    - Can the failure behaviour of graphite be compared to that of quasi-brittle fracture?
    - Do quasi-brittle failure models exist that can be adapted for graphite failure?
    - If so, can graphite fracture be modelled using such models?

With respect to the questions formulated above, the next chapter, Chapter 4, will discuss the aims of this project and the process of contributing to the understanding of graphite fracture.

Chapter 4

Aims and Objectives of this Thesis

This chapter intends to discuss the main aims of this research project. It introduces the problems associated with graphite fracture and gives the methods utilised to contribute to the understanding of graphite fracture. It is worth mentioning that each chapter discusses the clarification of specific problems in more detail.

4.1 Introduction

This project forms part of an ongoing research effort in determining the fracture characteristics of medium grained nuclear grade graphite. Originally initiated by the Pebble Bed Modular Reactor programme, later supported by the University of Manchester, this work aims to determine the fracture initiation and propagation characteristics of two grades of graphite, namely Nuclear Block Graphite 10 (NBG10) and Gilsocarbon (IG1-24). These properties or characteristics may then be used for life prediction models, failure probability studies or more sophisticated Finite Element studies of moderator bricks. Whichever model is used, the need for the understanding of the damage development, crack growth characteristics and parameters of the material under various loading conditions exists. This is the long term goal of this research.

The fracture toughness and crack growth properties of nuclear graphite prove difficult to determine by conventional fracture mechanics methodologies, as graphite is a quasi-brittle material. Additionally, the fracture of graphite is associated with complex mechanisms such as micro-cracking and crack bridging, which have resulted in a variety of analysis methodologies, ranging from probabilistic Weibull

failure models, to complex cohesive crack simulations (as discussed in Chapter 3). This being said, to date in literature, not one method exists that can describe and predict failure with acceptable accuracy for a variety of geometries and sizes. One of the main problems when attempting to identify the fracture parameters of graphite is in propagating cracks controllably. Another problem is the observation of the cracking mechanisms while driving a crack through graphite specimens.

In light of the above, an alternate testing method is employed in this project. The so called Double Torsion (DT) technique facilitates stable crack growth and thus it is believed to help gain more insight into the fracture behaviour and fracture mechanisms of medium grained nuclear graphite. The technique also facilitates easy crack tip observations due to the way the specimen is loaded. This enables the use of Electronic Speckle Pattern Interferometry (ESPI) and Digital Image Correlation (DIC) techniques for observations of the cracking mechanisms prior to and during macro-cracking.

4.2 Thesis Objectives

The objectives of this work can be split into four categories which themselves are divided into the relevant chapters respectively. This includes; a critical review of the DT technique, which includes an experimental analysis using the proposed corrections, a Finite Element model of the geometry and the use of Digital Image Correlation to measure out-of-plane surface deformations (Chapter 5); the development of a novel approach to calculate the J-Integral by DIC displacement field measurement, called JMAN (Chapter 6); the damage, crack growth and fracture characteristics of graphite using the DT technique (Chapter 7 and 8); and a proposed non-local continuum-based damaged plasticity model (Chapter 9). These are discussed in slightly more detail below.

4.2.1 The Double Torsion Technique

The first objective concerns the experimental development of an excellent DT experimental facility, together with the development of a rigorous understanding of its range of applicability, corrections, sensitivity to alignment parameters and consequent optimisation. To assist in this first stage, Polymethylmethacrylate (PMMA), commonly known as Perspex, was selected since it has a fracture

toughness very similar to graphite, but is user friendly and cracking is readily observed since it is transparent. Once optimised and fully understood with confidence gained in the technique, nuclear graphite was used to replace the Perspex to characterise fracture toughness. This entails the following:

- Although many publications to date are given on the DT technique, the technique is not yet standardised and some concern exists over the validity of the technique. For this reason the initial objective of this work is to develop a deep familiarity and understanding of the DT technique. For further reading, an in depth literature review is given in Appendix A and the development of the testing rig is discussed in Appendix B.

- Furthermore, several corrections are given for the DT technique. These corrections, however, are not clear in terms of their applicability, range, validity and methodology. For this reason, the major corrections were experimentally investigated in depth using PMMA specimens. Additionally a finite element analysis of the DT geometry is undertaken.

- Conclusions are drawn based on a thorough understanding of the technique with the objective of establishing an experimental methodology for the confident utilisation of the DT method for graphite testing.

4.2.2 Digital Image Correlation and the Development of JMAN

The second topic concerns the development of a novel approach to calculate the J-Integral by DIC displacement field measurement, called JMAN. The J-integral is probably the most generalised and widely used parameter to quantify the fracture behaviour of both elastic and elastic-plastic materials. It is well known that the stress, strain or displacement fields around a crack tip may be uniquely quantified by the J-integral, provided that the constraint level is high enough. Hence, if the displacement field around a crack can be measured with adequate precision, the corresponding J-integral can be extracted. Displacements can be measured, with high precision, experimentally using the full-field DIC technique. A novel combined experimental-numerical method for the calculation of the J-integral from a DIC measured displacement field in cracked test specimens is proposed. It is shown that, unlike other available methods, the technique is not limited to

elastic fields and requires little computational power. Possible errors and their magnitude are evaluated and the limitations of the method are discussed. The proposed technique may be used to measure the fracture resistance of materials in laboratory set-ups, particularly small specimens, and offers the potential for real-time, in-situ structural integrity assessments. As such the technique was utilised for the measurement of the fracture parameters, i.e. the J-integral, of NBG10 and Gilsocarbon during crack initiation and propagation. This entails the following:

- The DIC technique is introduced, together with the contour integral method commonly used to evaluate the J-integral in the finite element environment.
- The mathematical methodology for extracting the J-integral from displacement fields obtained by digital image correlation at different loads is presented (a detailed mathematical description is given in Appendix C). The displacement vectors are transformed into a finite element domain through a MATLAB implemented routine (JMAN) to obtain the J-integral as an area integral.
- The JMAN methodology is verified using an ABAQUS model, and shows excellent agreement between the standard ABAQUS and weight function calculated SIFs. JMAN is tested on three different specimen geometries for elastic-brittle, elastic-plastic and quasi-brittle materials.

4.2.3 Damage, Crack Growth and Fracture Characteristics of Nuclear Graphite

Once the DT methodology and DIC are established the focus is drawn towards nuclear graphite. The third topic concerns the crack initiation and propagation observations and characteristics of the two medium grained polygranular graphites using the DT technique. For this, the linear elastic fracture mechanics (LEFM) methodology of the DT technique is adapted for elastic-plastic fracture mechanics (EPFM) to account for the non-linearity of graphite deformation. The R-curve behaviour is measured using JMAN, enabling determination of the critical J-integral for crack propagation in both materials. The R-curve concept has the ability to capture the toughening mechanisms that contribute to crack growth resistance. The fracture and R-curve behaviours are compared to previous literature based findings and therefore attempts to improve the current understanding

of R-curve behaviour of polycrystalline, nuclear graphites. The shortcomings of the EPFM methodology for the characterisation of graphite fracture are discussed. This is split into two chapters:

- The observations of mechanisms associated with crack growth are given. The observations of two distinct phases of cracking in graphite, namely the initiation phase or damage development prior to fracture and the propagation phase, split into two categories, the FPZ and crack tip wake effects or tortuosity are presented. The full field surface displacement measurement techniques of ESPI and DIC are used to observe and measure crack initiation and propagation.

- As with the observations of mechanisms associated with crack growth, the fracture parameters are investigated. Analysis of the displacement fields ahead of the crack tip, using the JMAN method, is used to calculate the J-integral for initiation and propagation. The EPFM fracture parameters and their applicability are discussed.

4.2.4 Modeling Graphite Fracture

The last topic concerns the shortcomings of the EPFM methodology and proposes a non-local continuum-based methodology. For this the common fracture characteristics observed in quasi-brittle fracture and the models used to simulate quasi-brittle fracture are discussed. These are compared to determined graphite fracture characteristics and subsequently the adaption of an existing non-local damage plasticity model for concrete and other brittle materials for polycrystalline graphite fracture is proposed. This model allows for the degradation of the material and for so called "plasticity" or non-linearity and was shown to correlate well with experimental data. The model uses concepts of isotropic damaged elasticity in combination with isotropic tensile and compressive plasticity to represent the inelastic behaviour. In this method the failure is modeled in the finite element (FE) model and consists of a combination of non-associated multi-hardening plasticity and scalar (isotropic) damaged elasticity to describe the irreversible damage that occurs during the fracture process. The model is available in the ABAQUS/Standard environment [23]. A static, strain rate independent, model is assumed. This entails the following:

- The common observed fracture characteristics of quasi-brittle materials are discussed, followed by the appropriate methodologies to characterise fracture in such materials. Existing quasi-brittle fracture models are utilised to formulate a fracture model for IM1-24 graphite. A model definition is formulated.

- The parameters required for the proposed failure model are found experimentally or from literature.

- The model behaviour is shown together with an experimental verification using two Compact Tension specimens and a Three Point Bend specimen. A discussion is formulated.

4.3 Summary

It is believed that fully characterising the failure of nuclear graphite requires an intimate understanding of the fracture mechanisms behind crack formation as well as propagation. Current literature shows that graphite material experiences so called "plastic" behaviour, even though this material is a brittle material. Literature has suggested that micro-cracking is responsible for these irreversible "plastic" or non-linear deformations. It is believed that these micro-cracks significantly influence the crack tip formation and propagation, as these can cause crack bridging and slip formations. An understanding and measure of the irreversible energy required for crack propagation can help better characterise and predict graphite failure.

Previously used techniques for evaluating fracture characteristics in graphite material, for example three point bending specimens, prove usually very difficult as crack propagation becomes quickly unstable resulting in uncontrollable crack formation and propagation. The DT technique, however, enjoys a constant crack driving force resulting in an almost entirely constant load plateau. This enables the unique ability to propagate cracks in a highly stable and controlled manner over relatively large crack lengths (over the middle half of the specimen). In conjunction with the ability of the DT methodology, the technique was adapted to fit an elastic plastic model allowing for the measurement of irreversible deformations. Using the modified DT technique together with ESPI, DIC and JMAN systems, can enable in-depth investigations into the fracture mechanics of nuclear

graphite. The FPZ could be accurately observed allowing for the measurements of the formation and propagation of the FPZ.

The EPFM methodology, commonly utilised for materials which exhibit non-linearity, is shown to be limited and erroneous when characterising graphite fracture. Since these mechanisms are similar to those observed in other quasi-brittle materials, a non-local continuum-based damaged plasticity model for concrete and other quasi-brittle materials is proposed. It is believed that the model has the capability of describing fracture in any specimen or structure configuration.

Chapter 5

Experimental Techniques and System

The previous chapter established the need for an experimental investigation of the fracture behaviour of nuclear graphite, in particular the damage accumulation prior to and during fracture. This chapter describes the experimental techniques and systems used.

5.1 Introduction

This chapter is divided into three sections. These discuss specimen fabrication, the Double Torsion (DT) technique and damage monitoring techniques, namely Electronic Speckle Pattern Interferometry (ESPI) and Digital Image Correlation (DIC). The first section deals with the details of the graphite material used in this project, the subsequent machining of the specimens and details about the testing apparatus and environment. The second section introduces the DT technique and is specifically focused on an evaluation of the technique. The last section presents the damage monitoring techniques which were used to observe the fracture process, prior and during crack propagation, in the graphite material.

It is worth mentioning that the DT technique is not yet a standardised testing technique and, as such, several concerns exist when applying the technique. The aforementioned evaluation, undertaken in this chapter, is aimed at developing a full understanding of the technique, its concerns and proposed corrections, so that it can be applied confidently to the graphite materials. For further reading, a comprehensive literature review is presented in Appendix A.

The last section discusses the damage monitoring techniques. The nature of "damage monitoring" is in terms of the degree of micro-cracking present prior and during fracture, where the techniques presented here enable the monitoring and measurement of such damage. More specifically, the ESPI technique allows for the observation of such micro-cracking (which is invisible to the naked eye) and DIC allows for surface strain mapping of such micro-damaged fields.

5.2 Materials, Specimen Fabrication and Mechanical Testing

In this work, tests were conducted at two different locations. Part of the research was conducted in the Materials laboratory at the University of Cape Town (South Africa). These include an experimental evaluation of the DT technique, mechanical testing of DT specimens and ESPI damage monitoring. The second part was conducted at the University of Manchester (United Kingdom) and includes mechanical testing and damage monitoring using DIC. Specimens were machined at each location respectively. The details are presented below.

5.2.1 Materials

Chapter 2 presented some of the properties of nuclear graphite, that the material can have a general extrusion direction and that nuclear graphite may be regarded as a porous material. The graphite materials utilised in this work were two medium grained graphites, namely nuclear block graphite 10 (NGB10) and Gilsocarbon (IM1-24). NBG10 is a pitch coke extruded graphite manufactured by SGL Carbon Company. The material has a maximum grain size of approximately 1.6 mm [50] and exhibits distinct grain orientations or anisotropy due to the extrusion process of manufacture. Because of the anisotropy, specimens were machined so that crack propagation was either *parallel* or *perpendicular* to the dominant grain (extrusion) direction. This is sometimes also reffered to "with grain" or "against grain" direction respectivly. Mechanical material properties are reported as 10.3 GPa and 9.9 GPa for the Young's modulus and the tensile strength of 18 MPa and 21 MPa for the parallel and perpendicular directions respectively [50]. The Poisson's ratio was taken as 0.21, independent of orientation (a small effect of orientation is expected, but has been neglected). IM1-24

graphite was manufactured by a forerunner of Graftech. The material has a maximum grain size of approximately 0.5 mm and is a near isotropic material with an anisotropy factor of 1.03 [88]. The Gilsocarbon was assumed to behave as an isotropic material. Material properties are reported as 11.9 GPa for the Young's modulus with a tensile strength of 20 MPa [88]. The Poisson's ratio was taken as 0.21.

5.2.2 Sample Fabrication

All DT graphite specimens have typical dimensions of length (L) 150 mm, width (W) 50 mm and a thickness (d) of 4 mm. A starter notch (a_n), with lengths of 20, 40 and 60 mm with a crack front inclination of $c \approx 4$, was used to initiate fracture. An image of two fractured graphite specimens is shown in Figure 5.1, where a schematic of a DT specimen is shown in Figure 5.2. It is worth mentioning that the left DT specimen in Figure 5.1 did not achieve the ideal "straight" crack propagation. The consequences of this are discussed in a later DT evaluation section. Detailed drawings of the geometry can be found in Appendix Z.

The specimens were sliced from a large graphite block and machined to shape. Care was taken to stress the material minimally so as to avoid any prior damage to the specimens and ensure dimensional reliability. For the DT technique evaluation, a PMMA material of several geometry configurations was utilised.

5.2.3 Mechanical Testing

All tests were conducted as static compression tests, where compression loading resulted in a tensile mode I crack opening, due to the nature of the testing fixture. Details of the fixture design can be found in Appendix B.

The tests, which were conducted in the Materials laboratory at the University of Cape Town, utilised a 100kN (with a 5kN load cell) Zwick tensile/compressive servo-controlled, screw driven testing machine. The Zwick testing machine has large components and high inherent stiffness thus minimising background relaxation (mashine relaxation). The 5kN load cell was accurate to 0.1%. The tests which were conducted at the University of Manchester utilised a Instron 5580 tensile/compressive servo-controlled, screw driven testing machine. Similar to the Zwick, the Instron has high inherent stiffness and a load cell of 2kN.

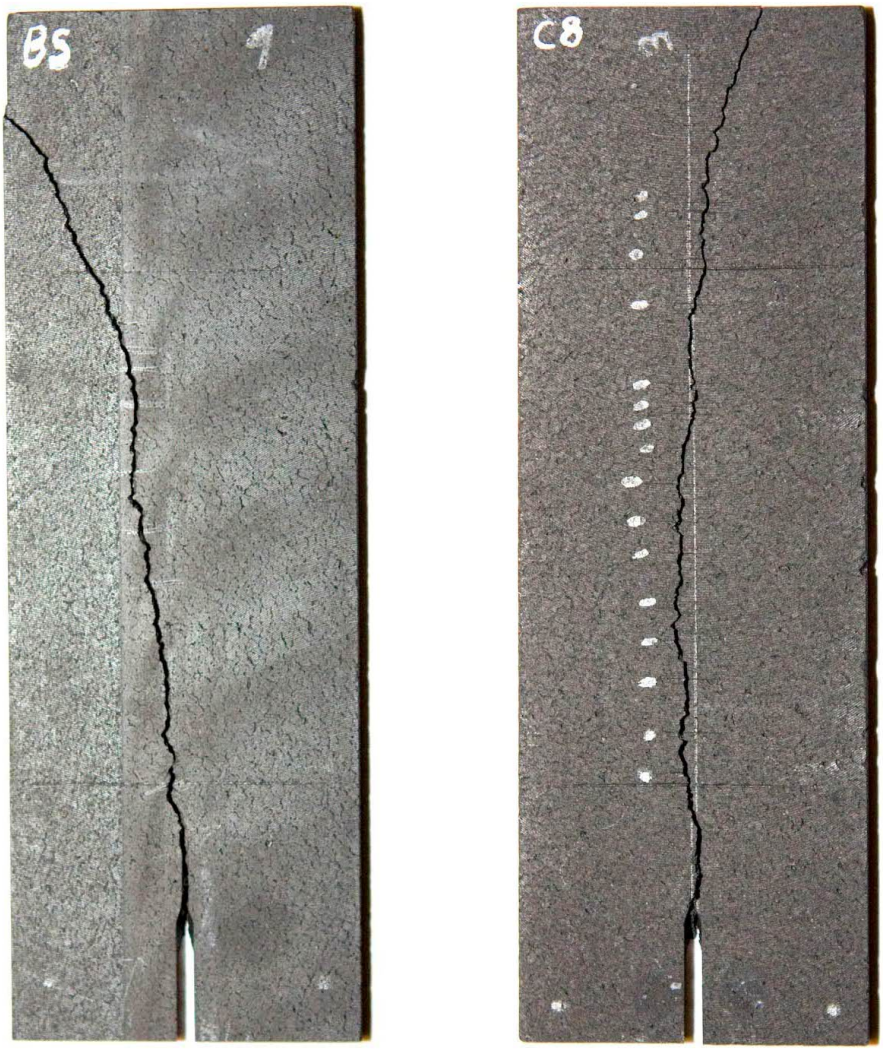

Figure 5.1 – Image of two NBG10 specimens tested

Details regarding the experimental procedures used to determine the damage and fracture characteristics of the graphite material are presented appropriately in each chapter. All tests were performed at room temperature. There was no special control over the environment, temperature or humidity, although the laboratories are air-conditioned and the temperature was typically 20 ^{o}C and the humidity 30%.

5.3 The Double Torsion Technique

The DT technique is a powerful testing configuration, which facilitates the investigation of fracture characteristics of highly brittle materials. One of the distinguishing features of this technique is that the Stress Intensity Factor (SIF) is said to be independent of crack length. This feature is especially attractive as it enables the propagation of relatively long cracks in a highly controlled manner in exceptionally brittle materials, such as ceramics [34], cements [89] and brittle polymers [31, 7]. Further, due to the way the DT specimen is loaded, the geometry allows for easy crack tip observations at a constant crack driving force. This is useful for micro-cracking observations in the fracture process zone in quasi-brittle materials [89] and is hence a desirable feature in the investigation of graphite fracture. The technique is also suitable for testing configurations where crack length measurements could be difficult to make, such as the evaluation of opaque and non-reflective materials, or in high temperature and controlled environments. Another advantage over other testing configurations, such as Single Edge Notched Bend (SENB) or Compact Tension (CT), is the ability to easily conduct slow crack growth studies (the VK relation between stress intensity factor K and crack velocity V during sub-critical crack growth).

The technique was first introduced by Outwater and Gerry [90] in the late 1960's and the main development of the DT technique may be attributed to Evans [91] and William and Evans [92]. This is described in good reviews, available in literature [32, 36]. The specimen configuration essentially comprises of a rectangular thin beam supported in a four point bend configuration at one end where the crack propagates through the specimen's length. A schematic diagram of the DT specimen is shown in Figure 5.2 where: a is the crack length, a_n the notch length, w_m the applied moment arm with applied load P and deflection y at the load points. The specimen has dimensions: length L, width W and thickness d. Grooves, aligned along the specimen length, are sometimes used to constrain the crack path. These, however, can cause substantial stress concentrations near the crack tip [36, 93, 34]. With careful alignment of the test specimen in combination with a high-quality fixture, the need for these grooves can be eliminated [36, 34].

The cornerstone of the DT methodology is the aforementioned feature of a crack length independent SIF. According to Williams and Evans [92] the strain energy release rate G, and hence an equivalent SIF (using $K = \sqrt{EG}$), is given by

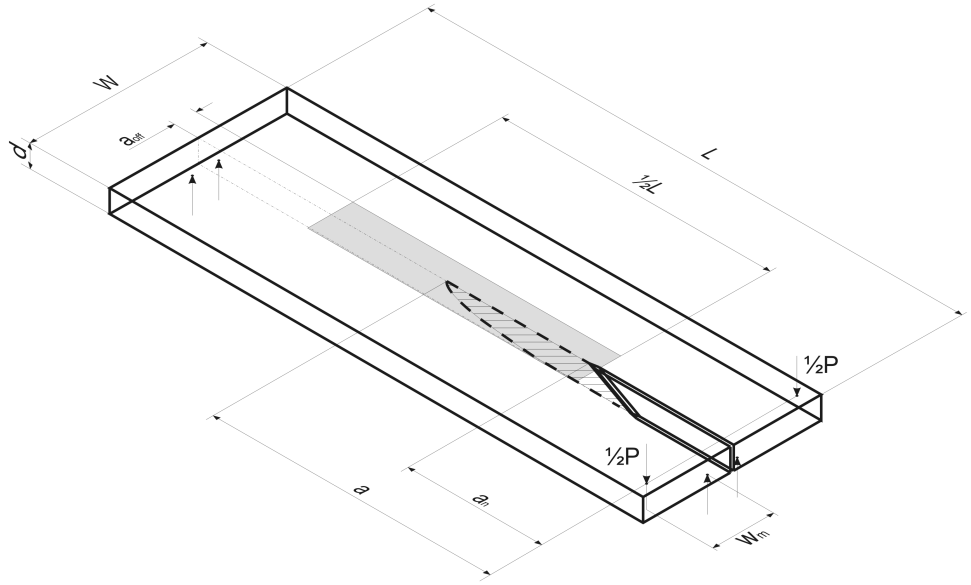

Figure 5.2 – Schematic of the Double Torsion (DT) specimen geometry. The curved crack front profile is defined by the difference in surface crack extensions as Δa.

$$G_I = -\frac{\mathrm{d}U}{\mathrm{d}A} = \frac{P^2}{2d}\frac{\mathrm{d}C}{\mathrm{d}a} = \frac{w_m^2 P^2}{2\mu W d^4 \psi} \tag{5.1}$$

where U is the total strain energy, A the crack extension surface area, C the compliance of the specimen, µ the shear modulus and ψ a thickness correction given as a function of W/d^4.

The above expression, Equation 5.1, is entirely crack length independent and has been derived with the following assumptions.

- The specimen has two symmetrical, independent halves, subjected only to torsional loading due to load P with moment arm w_m. The crack separates the two halves.

- The specimen is only subjected to small torsional deformations and the unbroken ligament remains rigid.

- The crack front or crack profile remains constant throughout crack extension.
- Fracture occurs in pure mode I.

The practical importance of these assumptions, made necessary by the analytical approach, is still unknown and concerns around the actual crack length independence have arisen independently from several different investigations [94, 95, 96, 31, 97, 98, 99, 100, 93]. It has been shown that the stress intensity factor could be a function of the crack length, which is indicated by a shift in the VK relationship data [95, 96, 31, 97, 98, 100] (discussed later). As a result various corrections have been incorporated into Evans' conventional methodology. These include Leevers et al's large deflection correction [101], Chevalier et al's crack length dependent SIF correction [95] and Ciccotti et al's finite element based correction which accounts for crack length dependencies in VK relationship data [102, 103]. These corrections, based on analytical, empirical, or Finite Element (FE) derivations, aim to force the geometry to be crack length independent.

At this point it is worth mentioning that there exists no consensus in literature on the various corrections and the reason for reported variations between laboratories. As a result, the DT technique itself provides many challenges to the user and although the DT technique offers significant advantages, due to its ability to propagate cracks controllably, there remains a concern about its inherent crack length independence and other aspects such as the optimal dimensions and test procedures. As a result, a large portion of this project was dedicated to the validation of the technique, using PMMA specimens. It is believed that this evaluation significantly contributes to the understanding of the DT methodology and, as such, has been submitted to the Journal of Experimental Mechanics.

5.4 Evaluation of the Double Torsion Technique

Given that this projects intends to utilise the DT technique for the characterisation of the damage and fracture in nuclear graphite, the need exists to use the DT technique with confidence. Since the question regarding the applicability of the crack length independent SIF remains, it is necessary to assess the DT technique and its correction factors critically. The aim of this section is to fully understand the DT methodology and to address the proposed corrections with

respect to the crack length independent SIF and to investigate the importance of the approximations made, with respect to the analytical derivation. Considering that alignment is critical in the DT configuration, the effects of misalignment are also investigated.

The evaluation is made via an experimental procedure of the various proposed corrections (Evans [91], Leevers et al. [18], Chevalier et al. [95] and Ciccotti at al. [102, 103]), a FE analysis of the full DT specimen geometry accounting for crack surface interaction, and uses measurement of the out-of-plane deflections of loaded samples by DIC. First, the analytical derivations of the DT technique and the proposed corrections are discusses. This is followed by the evaluation using the aforementioned approaches.

5.4.1 Analytical Analysis and Proposed Corrections

The DT specimen comprises a rectangular plate that is loaded in a four point bending configuration at one end across a starter notch (Figure 5.2). The specimen can essentially be considered as two halves around the cracked portion, which deform independently. Subjected only to small torsional deformations, the stiffness of each half is a function of its cross-section and length. As a result, the stiffness of each half, and thus the specimen, is a function of the specimen's crack length. If assumed that the unbroken ligament remains completely rigid, a linear compliance relationship is obtained [91]

$$C(a) = \frac{y}{P} = B_A a = \frac{3w_m^2}{Wd^3\mu}a \tag{5.2}$$

The crack front or crack profile is assumed to be straight and perpendicular to the specimen plane throughout crack extension. It is worth mentioning that this linear compliance relationship provides the crack length independent SIF. It has been shown experimentally that the compliance is indeed linear, however, a scaling constant is required to account for a shift in the compliance slope [91, 92, 31].

$$C(a) = \frac{y}{P} = B_E a + D_E \tag{5.3}$$

where, B_E is the slope and D_E is the y-axis intercept. The experimental compliance has been shown to be in agreement with the analytical compliance [31], in

which case D_E is assumed to be zero and

$$B_E \approx B_A = \frac{3w_m^2}{Wd^3\mu} \tag{5.4}$$

The actual crack profile in the DT setup is curvilinear and therefore, a crack front inclination is defined by $c = \Delta a/d$, where Δa is the crack extension difference between the upper and lower surface of the test specimen (Figure 5.2). It has been contended that the crack front geometry is material specific [104] and dependent on the slow crack growth exponent [105]. However, it has also been shown that the shape of the crack front does not vary with crack length and therefore the assumption of constant crack extension difference is valid [92, 106].

Evans' "conventional" methodology

Equation 5.1 provides the elastic strain energy release rate for the DT geometry obtained using Irwin's expression for Linear Elastic Fracture Mechanics (LEFM) in mode I rupture. For this the crack front shape is assumed to remain constant through crack propagation, so that $\mathrm{d}A = \mathrm{d}a \cdot d$. Since LEFM conditions apply, G_I may be related to the more commonly used SIF by $K_I = \sqrt{GE'}$ where, $E' = E/(1-v^2)$ and $E' = E$ in plane strain and stress conditions respectively (E being the Young's Modulus and v Poisson's ratio). The expression for K_I is given as

$$K_I^E(P) = Pw_m\sqrt{\frac{3}{Wd^4(1-v)\psi(d,W)}} \tag{5.5}$$

for plane strain conditions. Here, μ is the shear modulus and $\psi(d,W)$ a thickness correction factor, derived by Fuller [31], to account for the interaction between the crack surfaces as

$$\psi(d,W) = 1 - 0.6302\tau + 1.20\tau e^{-\pi/\tau} \tag{5.6}$$

where $\tau = 2d/W$. The validity of the thickness correction has been confirmed using tests on glass ceramics [107]. The SIF given by Equation 5.5 is a function of the applied load, the test specimen geometry and Poisson's ratio but is independent of crack length. The independence of the SIF however, is limited to a range of crack lengths due to edge effects, which can lead to a deviation from

the linear crack length-compliance relationship. Generally the middle half to a third of the specimen is regarded as crack length independent [36]. The critical strain release rate energy G_{Ic}, or fracture toughness, K_{Ic}, may be calculated by substituting P with the critical load P_c into Equation 5.5.

Crack growth analysis

One of the important characteristics of the DT methodology is the ability to measure the rate of slow crack growth without having to monitor the crack length on a continuous basis. For this, the sub-critical quasi-static crack growth or materials experiencing environment-assisted cracking is defined by the relationship

$$V = BK_I^n \tag{5.7}$$

This may be reformulated as

$$log(V) = n\, log(K_I) + log(B) \tag{5.8}$$

where, $log(B)$is a constant and n is the sub-critical crack growth index, which may be evaluated by the commonly used load relaxation technique or the constant displacement [31] technique.

According to the load relaxation technique, a pre-cracked specimen is loaded to just below the expected fracture load (i.e. 0.9 to 0.95 P_c) and the crosshead displacement is fixed (noted as subscript $_y$). The increase in test specimen compliance with crack growth relaxes the load with time and can be described by differentiating Equation 5.3 with respect to time

$$\frac{\mathrm{d}y}{\mathrm{d}t} = (B_A + D_E)\frac{\mathrm{d}P}{\mathrm{d}t} + PB_E\frac{\mathrm{d}a}{\mathrm{d}t} \tag{5.9}$$

Since the DT geometry enjoys a linear compliance and the crosshead is arrested during a load relaxation procedure, the initial and final loads may be related by

$$P_i(B_E a_i + D_E) = P_f(B_E a_f + D_E) \tag{5.10}$$

where subscripts i and f denote the initial and final during a load relaxation procedure respectively. Hence, by setting Equation 5.9 equal to zero and rearranging it with Equation 5.10 an expression for the crack velocity V is given as

$$V_y(P,t) \equiv \left(\frac{\mathrm{d}a}{\mathrm{d}t}\right)_y = \phi \frac{P_{i,f}}{P^2}\left(a_{i,f} + \frac{D_E}{B_E}\right)\left(\frac{\mathrm{d}P}{\mathrm{d}t}\right)_y \tag{5.11}$$

where ϕ is a crack velocity averaging factor derived by Pollet and Burns [106]. This is required since the crack velocity varies along the crack front's curved profile.

$$\phi(\alpha, d) = \left(\frac{1}{d}\int_0^d (sin\,[\alpha(d)]^{\frac{1}{n}}\right)^n \tag{5.12}$$

where n is the slow crack growth exponent and α is the function of the crack front angle to the specimen's surface. Other curved crack front corrections have been derived [91, 101, 108], however, Pollet and Burns' averaging process is more widely accepted in the literature. Fuller assumed that the ratio D_E/B_E, used in Equation 5.11, may be excluded if significantly less than $a_{i,f}$.

Another technique for slow crack growth determination using the DT technique includes the constant displacement rate technique. The crosshead is moved at a constant rate and the load is allowed to reach a plateau (with $\mathrm{d}P/\mathrm{d}t \approx 0$), where the expected increase in load from crosshead movement is balanced by the increase of the test specimen compliance due to crack growth. If the plateau load is given by P_c, Equation 5.9 reduces to

$$V_P(y,t) = \phi \frac{1}{P_c B_E}\left(\frac{\mathrm{d}y}{\mathrm{d}t}\right)_P = \phi \frac{y_P}{P_c B_E} \tag{5.13}$$

The subscript $_P$ denotes the constant load assumption.

Leevers correction

Leevers' proposed a correction for the errors caused by large deflections at the load points [18]. The Large Deflection Correction (LDC) corrects for the decrease in moment (w_m) due to the rotation of the loading contact points on the specimen's surface as shown in Figure 5.3. This is defined as w_m^{LDC} in this work. Earlier work done by Hine et al. [109] provided a different LDC, although this was since shown to generally underestimate the error [18].

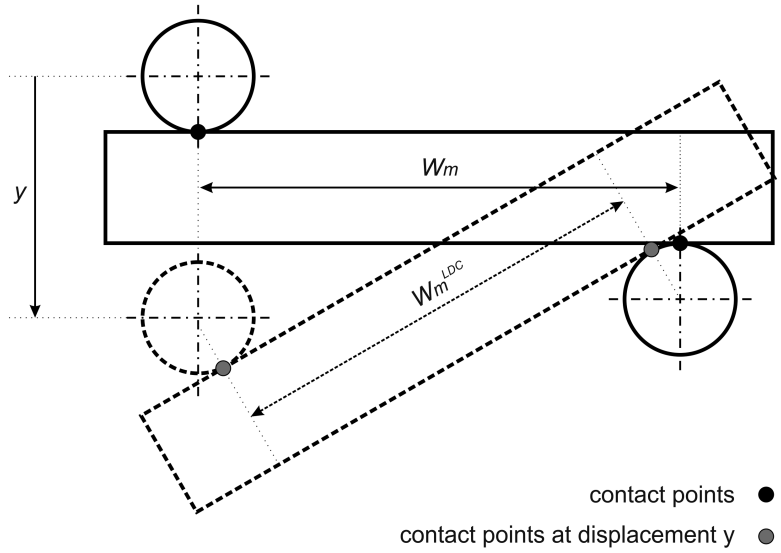

Figure 5.3 – Schematic of the load configuration and the large deflection error caused by the rotation of the loading points. A correction is provided by Leevers as w_m^{LDC} [18].

Chevaliers Correction

Chevalier and co-workers [95] reported a crack length dependence of the SIF in studies of zirconia and alumina. They attributed a minor crack length dependence to deflections of the unbroken ligament and then proposed a correction for load relaxation tests. The crack length independent SIF was then

$$K_I^{Ch}(P,a) = K_I^E(P)\left(\frac{a}{a_n}\right)^{\frac{m}{k}} \tag{5.14}$$

where, m and k are constants for the test specimen geometry and material considered. The crack length was estimated during load relaxation tests as

$$a^{ch}(P) = \frac{\left(\frac{P_{i,f}(B_E a_{i,f}+D_E)}{P}\right) - D_E}{B_E} \tag{5.15}$$

derived from the compliance relationship. Their correction results in a shift of the

VK curve and an increase of the stress corrosion index n [110]. Crack velocities are found using Equation 5.11 or Equation 5.13.

Ciccotti's correction

Ciccotti and co-workers [111, 102, 103] performed a three-dimensional FE elastic analysis on a symmetric DT geometry model, including contact between the crack faces. They concluded that appreciable deviations (as much as 40%) occurred from the conventional analytical solution (Evans' methodology) for strain energy release rate, and that these were due to non-linearity of the compliance relationship. They provided two correction factors φ and ξ for the calculation of K_I and V to account for experimental variables such as crack shape, groove width and depth, notch length and test specimen geometry.

$$C^{Ci}(a) = \varphi(a) B_A a \tag{5.16}$$

$$K_I^{Ci}(P,a) = \sqrt{\varphi(a)} K_I^E(P) \tag{5.17}$$

$$V^{Ci}(P,t,a)_y = -\vartheta \frac{\xi(a_{i,f})}{\varphi(a)} \frac{a_{i,f} P_{i,f}}{P^2} \left(\frac{dP}{dt}\right)_y \tag{5.18}$$

Both correction factors are a function of crack length, which may be estimated by

$$a^{Ci}(P) = C^{-1}\left(\frac{C(a_{i,f}) P_{i,f}}{P}\right) \tag{5.19}$$

The correction factors were derived from FE models with five different crack lengths for three different specimen geometries. Functions for the correction factors were then obtained by a 3rd order polynomial fitted to the five data points. It is important to note that the recorded values are conditioned by the sample geometry. In cases where the sample geometry differs, linear interpolation is used. Examples were published by the authors [103].

5.4.2 Evaluation Procedure

This evaluation aims to examine the aforementioned assumptions, on which the DT methodology is based, to achieve a crack length independent SIF. To do this, the evaluation consists of three parts:

Specimen Geometry Dimensions (mm)	Ratio	Notch a_n (mm)	Evaluation use Exp	FE	DIC	Recommended by
150:50:4	$3W : W : 0.08W$	20	x	x	x	Chevalier et al.
		40	x	x		[95]
150:50:5	$3W : W : 0.1W$	20	x			Tait et al.
		40	x			[36]
135:50:5.5	$3W : W : 0.11W$	20	x	x	x	Ciccotti et al.
		40	x	x		[102, 103]

Table 5.1 – Specimen dimensions and ratios considered for the experimental, FE and DIC evaluation.

- Experiments analysed using Evans' methodology and the corrections proposed by Leevers', Chevalier and Ciccotti using three specimen configurations.
- FE simulation of the full specimen geometry, which includes crack surface interactions, a realistic loading configuration and an assessment of misalignment.
- DIC observations to measure the out-of-plane deflections of the unbroken ligament.

Experimental Evaluation

Compliance tests, fracture toughness tests and VK investigations were undertaken using Polymethylmethacrylate (PMMA) specimens. PMMA is a clear, homogenous, isotropic brittle material that allows for easy observation of the crack tip and has similar reported fracture toughness to that of the nuclear graphite used in this work. The material properties of PMMA were taken as $\mu = 1.4$ GPa for the Shear modulus and $E = 3.7$ GPa for the Young's modulus [112].

Three different specimen geometry ratios were considered, normalised with respect to the width and notated by their length to width to thickness ratio ($L : W : d$). These are summarised in Table 5.1. These ratios were chosen from the dimensions previously used by Chevalier [95], Tait [36] and Ciccotti [102, 37, 103]. Starter notches were machined to lengths of $a_n = 20$ mm or 40 mm with a crack front inclination of $c = 4$ to closely resemble the curved front of a propagating crack and to ensure symmetrical crack initiation. Specimens were

pre-cracked to length a_p to achieve a sharp fully formed curved crack front unless the objective of the experiment dictated otherwise.

A DT fixture was constructed to reliably achieve near symmetrical crack growth. Details of the fixture design process can be found in Appendix B. This eliminated the need for side grooves to control crack growth. Any non-symmetrical crack propagation within the defined crack length independent SIF shown in Figure 5.2, (i.e. deviation of the crack path from the centreline of the specimen) was recorded as a_{off}. The crack length independent SIF region was regarded as $0.25 < a/L < 0.75$, according to Tait et al's recommendations [36].

The experiments were carried out in the Materials laboratory at the University of Cape Town at room temperature using a Zwick tensile/compressive servo controlled, screw driven testing machine with a 5 kN load cell. Crack length measurements, to an accuracy of 0.2 mm, used a Nikon SMZ10 microscope mounted on a sliding mechanism. Specimens were pre-cracked to length a_p at a low cross-head speed (> 0.1 mm/min, manually controlled), until a fully formed crack front was established. Load, displacement and time were recorded continuously. Compliance curves were thus determined according to Equation 5.2, Equation 5.3 and Equation 5.16 for the analytical, experimental and Ciccotti's compliance, respectively. SIF values were then calculated using Equation 5.5, Equation 5.14 and Equation 5.17 for Evans', Chevalier's and Ciccotti's methodologies respectively. Fracture toughness tests were conducted at a fast cross head speed of 4 mm/min sufficient to ensure unstable fracture [31] where the critical load P_c was used to calculate K_{Ic}. VK data was determined using load relaxation and constant displacement rate tests for comparative purposes using Equation 5.11 and Equation 5.13 for Evans', Leevers' and Chevalier's methodologies and Equation 5.18 for Ciccotti's method respectively.

Finite Element Model

A FE model of the DT geometry was constructed using ABAQUS/standard V. 6.7 [23]. The FE model represented the full DT geometry and loading configuration under constant displacement loading (Figure 5.4). Most of earlier FE models assumed a symmetrical DT geometry, in which the model only described half of the specimen, loaded in pure torsion [111, 33]. This was due to computational limitations that no longer apply. In these analyses the cracks were treated as discontinuities with smooth and frictionless surfaces where mode I loading was

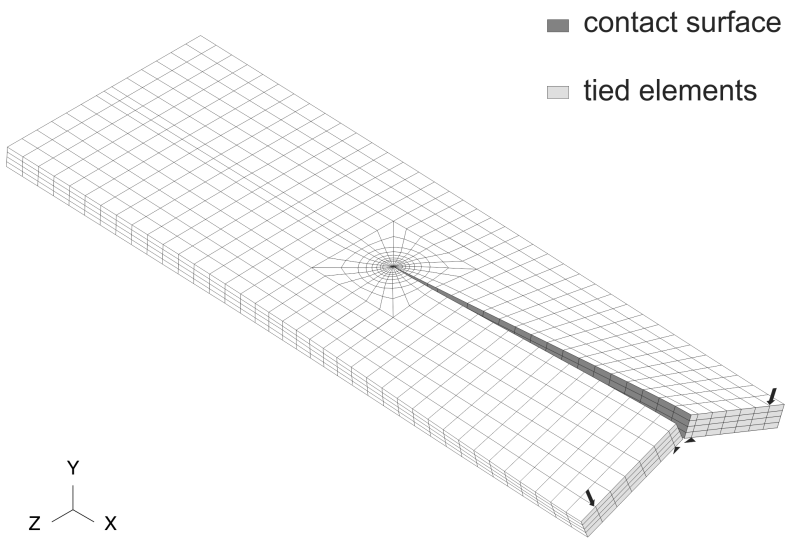

(a)

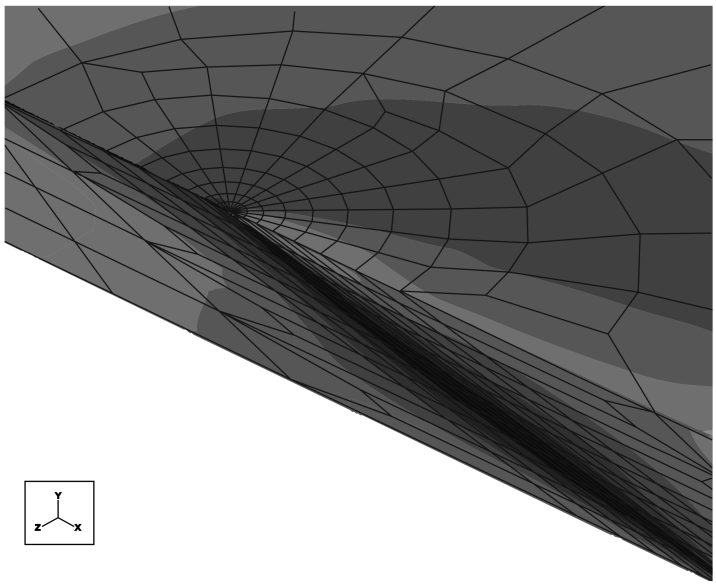

(b)

Figure 5.4 – a) Finite Element mesh for the $3W : W : 0.08W$ geometry with a crack front inclination of $c = 0$. Model represents the full DT geometry. b) Finite Element mesh for the $2.7W : W : 0.11W$ geometry with a crack front inclination of $c = 4$. Shown is half the DT geometry with maximum principle stress contours.

assumed. However, if the crack surfaces offer frictional resistance due to sliding in the DT configuration, the assumption of symmetry may lead to error. The modelling of the whole specimen provides a more realistic configuration that can analyse the effects of load misalignment and crack opening modes. Contact between the crack surfaces was defined by the Coulomb friction law for rough surfaces, with an assumed friction coefficient of 0.5 [113, 114, 115].

A concentrated mesh with collapsed elements at the crack tip was used (Figure 5.4a and b). This allows for a better description of the strain field near the crack tip and has been validated against analytical solutions [33]. Mode I and III stress intensity factors along the crack front were directly calculated by ABAQUS using the contour integral method [116]. In addition, the out-of-plane deflections of the ligament and the compliance relationship were extracted.

Rotational loading was applied as a displacement to an analytically rigid body, tied to the outer edge of the DT geometry (Figure 5.4a). This gave a four point bending loading configuration with a moment arm length of w_m. This way, the torsional load configuration incorporating the fixed support points (as a four point bend configuration) could be modelled excluding any point load effects. Twenty different specimen configurations were modelled. These consisted of two specimen geometry ratios, each with two different crack front inclinations, namely $c = 0$ and $c = 4$, at five crack lengths of 37.5, 56.25, 75, 93.75 and 112.5 mm respectively. The crack front inclinations were limited to a maximum inclination of $c = 4$ so as not to distort the elements internal angles below 10°.

Since non-grooved specimen geometries were considered, the effect of specimen misalignment was modelled as a percentage difference in the applied moment on each specimen halves torsion arm. This was considered to be an accurate representation of misalignment since misalignment of the specimen in the loading jig would result in a shift of the loading points and would thus cause an imbalance in the applied moment.

The models contained a total number of 7468 and 9465 quadratic brick elements for the geometries with crack front $c = 0$ and $c = 4$ respectively. PMMA was defined as a linear elastic material with the properties stated previously.

Digital Image Correlation

DIC allows full field displacement measurements to be obtained throughout the deformation of material in two or three dimensions, depending on the camera

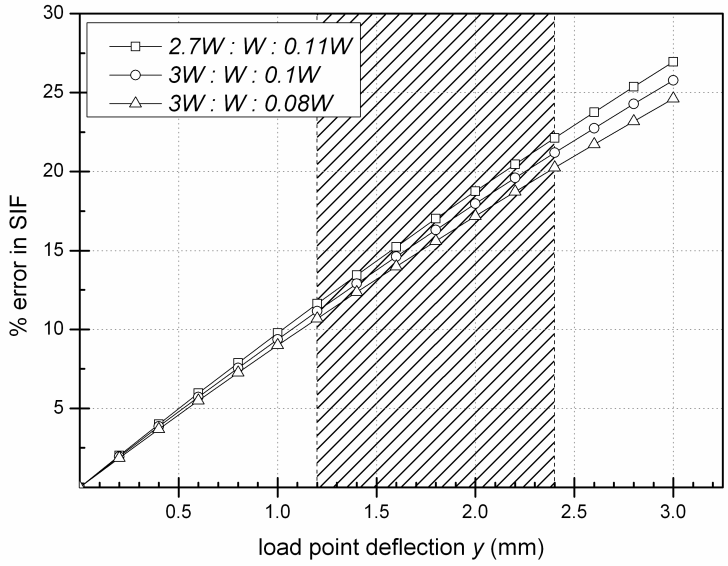

Figure 5.5 – Percentage error in the calculation of K_I for three specimen thicknesses when using Equation 5.2. All specimens have the same loading configuration shown in Figure 5.3.

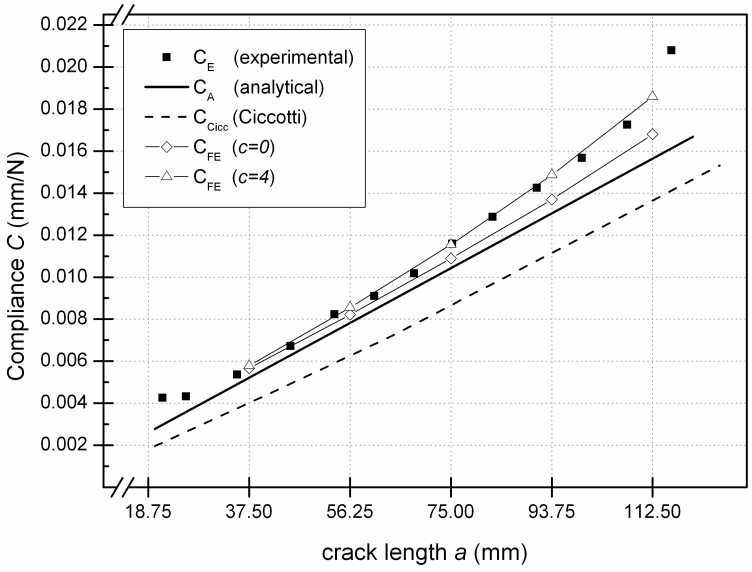

Figure 5.6 – Comparison between the various compliance relationships for the $2.7W : W : 0.11W$ geometry.

system [117]. DIC operates through the discretisation of an image into multiple interrogation windows, which are correlated with the same features in the following images. Displacement vectors are obtained for the change in position of each interrogation window, allowing strain distributions across the full image to be calculated [118]. Further details, regarding DIC technique, are discussed in the following sections under damage monitoring techniques.

The digital image correlation technique was employed at the University of Manchester to analyse the out-of-plane deformation during cracking of PMMA DT specimens. The system used two Davis ® Imager Pro X 4 Megapixel cameras and LA Vision DaVis software ver.7.2 [119]. The two-camera analysis was used as the DT specimen experiences some out-of-plane deflections. These can cause errors in single camera observations and it was necessary to measure the in-plane displacements accurately [120]. The displacement vector accuracy is dependent on the interrogation window size, and in this work the best results were obtained by an interrogation window size of 128 x 128 pixel window size with 75% overlap, which allowed for around 0.01 pixels accuracy [119]. The large overlap provided a sufficient number of displacement vectors. One pixel was approximately 50 µm, for an imaged area of 100 x 100 mm. The DT specimens were tested at 4 mm/min constant displacement rate with an image recording frequency of 1 Hz.

5.4.3 Results and Observations

52 specimens were tested in the experimental evaluation. This included 20 fracture toughness tests, 20 VK investigations (limited to a maximum of three relaxations per specimen), nine compliance tests and three DIC observations. Their respective dimensions are reported in Table 5.1.

Correction Factors

Table 5.2a shows all the calculated correction factors for the three specimen geometries considered, determined according their specified methodologies. The LDC correction was found to be essential, as large deflections at the load points result in a significant decrease of the moment arm w_m. One example is the decrease from 16 mm to 14.5 mm for the 4.0 mm thick specimen configuration. Failure to correct for these large deflections can result in an error in K_I of up to

Geometry configuration		Thickness correction	Crack-front correction	Chevaliers correction		Ciccotti's correction $\xi(a)\varphi(a) = x_1 + x_2 + x_3 + x_4$				$\varphi(a) = x_1 + x_2 + x_3 + x_4$			
$L : W : d$	a_n (mm)	$\psi(W, d)$	$\phi(\alpha, d)$	m	k	x_1 10^{-8}	x_2 10^{-6}	x_3 10^{-4}	x_4	x_1 10^{-6}	x_2 10^{-4}	x_3 10^{-2}	x_4
$3W : W : 0.08W$	20	0.861	0.143	3	47			-				-	
	40	0.861	0.143	3	47			-				-	
$3W : W : 0.1W$	20	0.874	0.143	2	47			-				-	
	40	0.874	0.143	2	47			-				-	
$2.7W : W : 0.11W$	20	0.882	0.143	1.2	48	-7.8	0.12	9.31	0.73	1.82	-.5.1	4.75	-0.47
	40	0.882	0.143	1.2	48	-2.5	-2.7	0.23	0.67	1.91	-5.4	5.04	-0.57

(a)

Geometry configuration $L : W : d$	Compliance constant (experimental)		(analytical)	(finite element) $c = 0$		$c = 4$	
	B_E 10^{-5}	D_E 10^{-2}	B_A 10^{-5}	B_E 10^{-5}	D_E 10^{-2}	B_E 10^{-5}	D_E 10^{-2}
$3W : W : 0.08W$	7.5	3.0	7.86	7.90	2.17	7.63	2.67
$3W : W : 0.1W$	9.7	1.8	10.12	-	-	-	-
$2.7W : W : 0.11W$	12.0	1.0	13.02	13.11	0.71	12.21	0.92

(b)

Table 5.2 – a) Correction factors for the considered specimen configurations. b) Compliance relationship data for all specimen configurations considered. Two starter notch length configurations of 20 and 40 mm were considered for the experimentally determined compliance.

25% (Figure 5.5). The crack front inclination was established at where the crack tip shape, once established, was found to remain constant with crack length.

Compliance Relationship

Table 5.2b summarises the linear compliance relationships found experimentally, analytically and through the FE model respectively. A good correlation was found between these relationships with less than 2% difference in their average values. It is worth mentioning that the assumption that D_E/B_E in Equation 5.11 is significantly less than $a_{i,f}$ (as commonly assumed) does not hold true here, as D_E/B_E has a magnitude of approximately 20 mm compared to $a_{i,f}$, which ranged from 37.5 to 112.5 mm. This becomes significant for the VK data plots and thus requires an experimentally determined compliance in order to reduce a significant shift in VK relationship data.

Since the crack length independence of the DT technique is dependent in the linearity of the compliance relationship, it provides a tool for assessing the aforementioned assumptions. This is shown in Figure 5.6, which compares the compliance relationships obtained from the experimental, analytical, the Ciccotti correction and the FE model for the $2.7W : W : 0.11W$ configuration. The experimentally and FE determined compliance show similar behaviour with a slight deviation from linearity at larger crack lengths. This observation was found in all specimen configurations (it is most exaggerated with the thicker $2.7W : W : 0.11W$ geometry) and thus suggests a crack length dependent geometry. Ciccotti's corrected compliance, which aims to provide a crack length independent geometry, did not agree with experimental data.

The non-linearity of the compliance has been attributed to the deformation of the unbroken ligament [95, 110], which introduces error in the prediction of torsional deformation of the broken ligaments. The direct measurement of surface displacements by two-camera DIC (Figure 5.7) confirms these out-of-plane deformations and shows, in good agreement with the FE model predictions, that these deformations increase with crack extension. This contributes to the overall non-linearity of the compliance data. This effect is again amplified by the thicker specimen configuration. This is discussed further later in more detail.

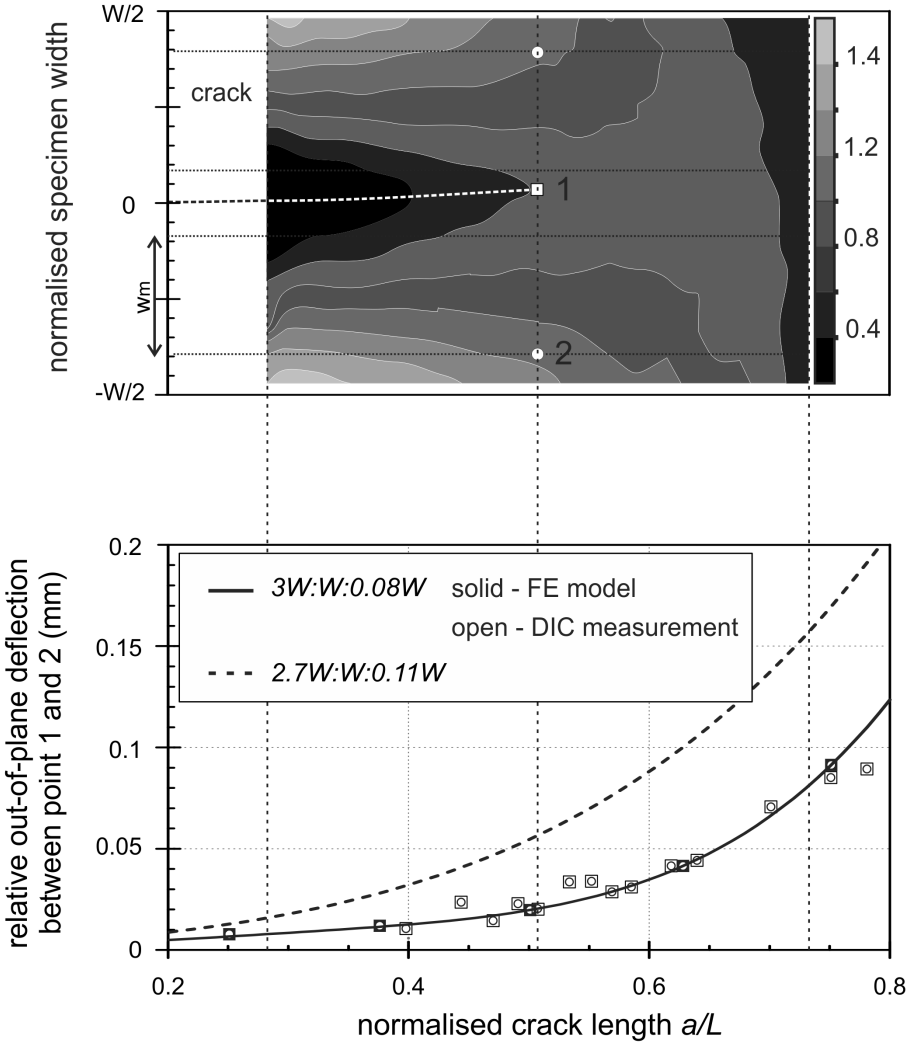

Figure 5.7 – Out-of-plane deformations of the specimen surface at crack length a = 76mm obtained through the DIC analysis and the relative load point deflections at the crack tip. Shown are the Abaqus and DIC obtained surface displacements.

Crack Length Independence

To further investigate the effect of the non-linear compliance, the various proposed corrections were compared by plotting the SIF (calculated according to each methodologies), against the crack length. This is shown in Figure 5.8a for

the $2.7W : W : 0.11W$ configuration. Both Chevalier's and Ciccotti's corrections achieved the crack length independent SIF (i.e. a constant SIF), however, a gradual decrease in the SIF with increasing crack length was observed when using Evan's "conventional" methodology, with or without the LDC. These findings are in agreement with the FE analysis (Figure 5.8b), where a clear crack length dependence on the SIF was found, especially for the thicker specimen configuration.

The testing procedures also contribute to the overall validity of a crack length independent geometry. Similarly to Figures 5.8, the variation of the SIF with crack length for specimens with various crack propagations for the $3W : W : 0.08W$ configuration is illustrated in Figure 5.9. The effects on a fully pre- and symmetrically cracked specimen were investigated and compared with either a non-pre-cracked or non-symmetrically cracked specimen, or both. The results clearly show the effect of misalignment on the pre-cracking procedure.

The main observations were:

- During the pre-cracking stage the curvilinear crack front develops. At this point the rate of crack extension area dA is not constant, but increases until a fully formed crack front has developed. This has been confirmed by Ricco et al. [121] who compared the load vs. time relationship for PMMA specimens with the corresponding crack speed vs. time recording obtained from video recordings. Hence, the assumption made in Equation 5.1 is not valid and it follows that during the pre-cracking phase artificially high SIF's are obtained that lead to erroneous fracture toughness readings or unreliable VK relationship data.

- During non-symmetrical or "skew" crack propagation the opposite can be observed. The calculated SIF decreases with increasing crack deviation (a_{off}). The argument follows that due to the non-symmetrical crack propagation the torsional stiffness changes in each half. The ability to support the same torsional load, in the case of the reduced specimen half, reduces and hence the ability to drive the crack propagation weakens. This argument is in agreement with Salem et al. [34] who tested non-symmetrical specimens and concluded that specimen symmetry should be within 1%.

There is an important observation to note; the common measurement of fracture toughness [91] is only dependent on the peak load and crack deviation is always

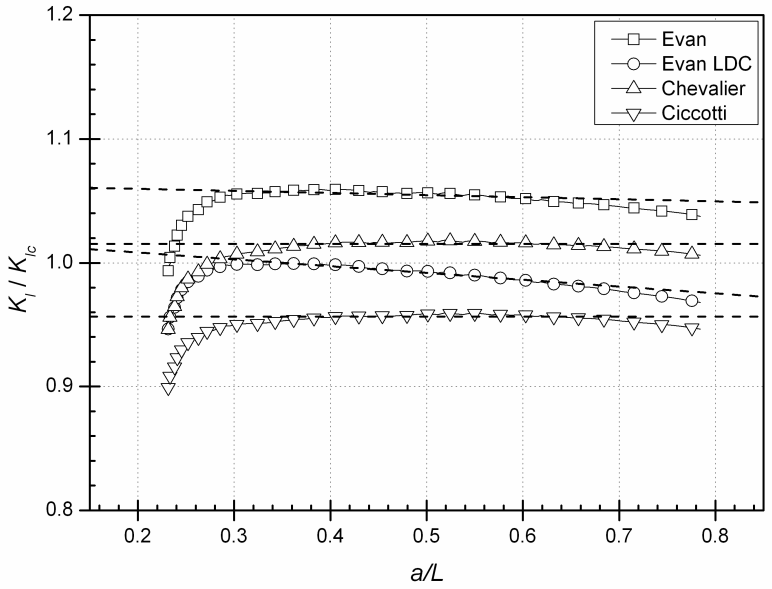

(a)

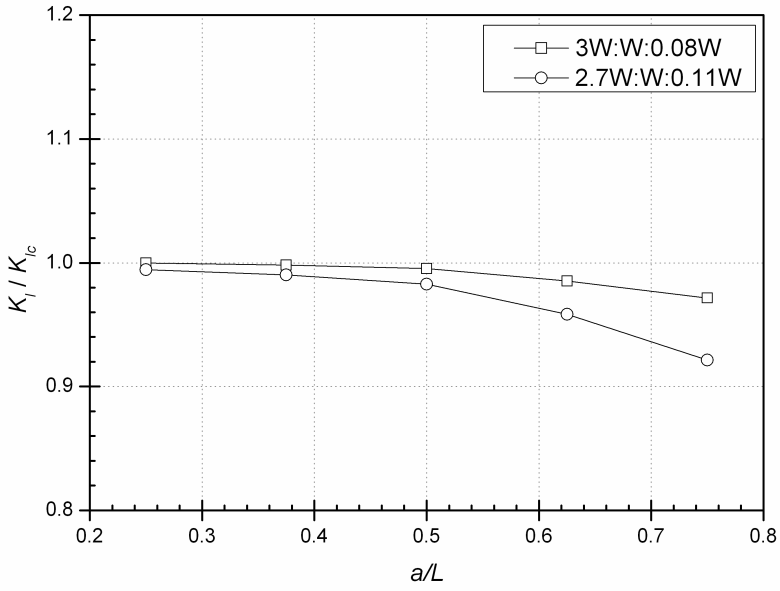

(b)

Figure 5.8 – a) Comparison of crack length independency. Plotted are Evans' model, Evans' model with LDC, Chevalier's model and Ciccotti's model for specimen dimensions $2.7W : W : 0.11W$. Crack length independence setup is identified by a horizontal fitted line. b) Comparison of crack length independency obtained from the FE analysis. Plotted are specimen dimensions $2.7W : W : 0.11W$ and $3W : W : 0.08W$.

small at short crack lengths (provided the starter notch is machined on the symmetry line), hence the consequence of misaligned specimen in fracture toughness testing is small. The effect of misalignment, however, becomes potentially adverse in VK investigations since a constant SIF is required over larger crack extensions.

The FE analysis provides additional insight into the SIF's independence of crack length. Visual inspections have shown that the crack front remains similar in shape over the middle section of the specimen. The SIF distributions along the specimen depth for two considered crack lengths, namely 37.5 mm and 112.5 mm are shown in Figure 5.10. Since an angled crack front was assumed ($c = 4$), the SIF profile is not representative of a real crack front, which is curved. However, it can provide insight into any variations of the profile with crack length. Figure 5.10 shows a small decrease between the two profile curves (with increasing crack length). This is in agreement with the experimental observations.

One of the more subtle difficulties associated with the double torsion technique is whether it is strictly appropriate to describe the failure as mode I. Fuller [31] believed that the fracture mode is indeed mode I since the loading configuration and specimen geometry are symmetrical about the crack plane. The contention that there is a mode III (shear) component appears to depend on the relative amount of axial to through thickness crack driving force [31]. The FE analysis conducted shows that indeed some mixed mode loading is shown in Figure 5.10. The analysis shows the ratio of mode III to mode I is less than 2% and no thickness dependence could be established between the two considered geometry configurations. The error induced by the assumption of pure mode I failure seems negligible considering experimental error. Comparative results with other techniques also show that the mode I assumption is applicable for materials which have much larger K_I/K_{III} ratio [31, 92].

Fracture Toughness

Table 5.3 shows the results of 20 fracture toughness tests, which were undertaken at a constant crosshead displacement of $\dot{y} = 4$ mm/min. Excellent agreement was found between the toughness values obtained from the Evans methodology and the FE model. Chevalier's and Ciccotti's corrections were derived for analysis of load relaxation tests, however, since the fracture toughness is obtained at a maximum load, their correction methodologies can be used. In agreement with Madjoubi [110], Chevalier's correction generally gives an overestimation in SIF

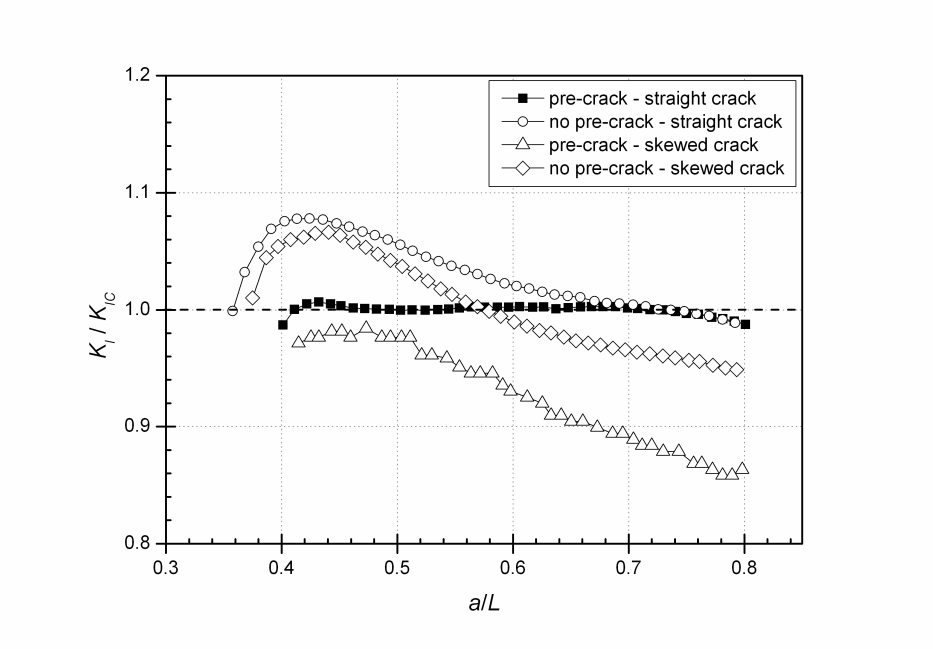

Figure 5.9 – Investigation of the crack length independency for four identical specimen configurations. Shown are: i) a pre-cracked specimen with "skew" crack propagation, ii) a pre-cracked specimen with symmetrical crack propagation, iii) no pre-crack with symmetrical crack propagation and iv) no pre-crack with "skew" crack propagation. Crack length independence setup is identified by a horizontal fitted line.

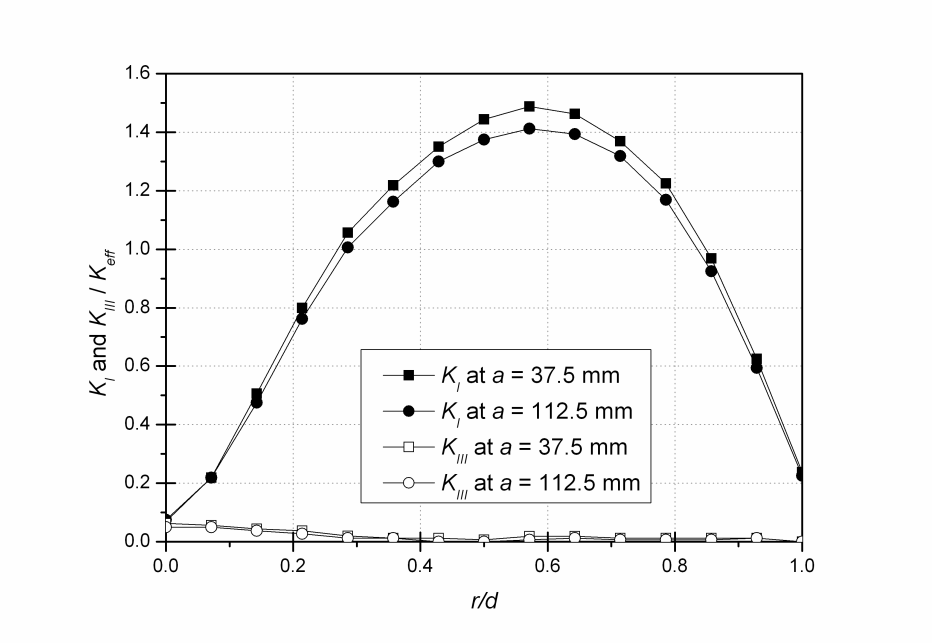

Figure 5.10 – SIF profile for mode I and mode II through thickness r/d at crack length a = 37.5 mm and 112.5 mm. $r/d = 1$ at upper tensile surface.

due to the exponent value. Ciccotti's correction on the other hand decreases the SIF. This may be attributed to the fact that Ciccotti's optimum specimen ratio of $2.7W : W : 0.117W$ was not entirely satisfied, although no dependence on specimen geometry ratio was observed within either analysis method.

Direct calculation of Fracture Toughness

To validate the calculated fracture toughness, an alternate approach was utilised, which directly calculates the fracture toughness using the Irwin relationship and specimen compliance. This method is similar to Albuquerque and Rodrigues' determination of R-curves using the DT geometry [39] and is based on the assumption of Linear Elastic Fracture Mechanics (LEFM).

This direct method makes use of consecutive loading and unloading curves, generated by loading and unloading the specimen with some crack propagation. The compliance C_1 at crack length a_1 was calculated as the slope of the loading curve. This procedure was repeated for a second cycle, C_2 and a_2. A schematic is shown in Figure 5.11. G_{Ic} and hence K_{Ic} were calculated using the following expression

$$G_I^P = \frac{P^2}{2}\left(\frac{\mathrm{d}C}{\mathrm{d}A}\right) \equiv \frac{1}{2d}P^2\left(\frac{C_2 - C_1}{a_2 - a_1}\right) \tag{5.20}$$

The advantage is that this methodology does not assume a linear compliance relationship, and hence the SIF is calculated directly from the energy required to propagate the crack. Since this methodology requires crack length measurement at each loading cycle, it cannot be used in load relaxation tests to investigate slow crack growth behaviour. However, it could be of use for constant rate of displacement tests, where the plateau load at a set displacement rate could be used to verify points on a VK curve obtained by the load relaxation technique. Excellent agreement was found between Evans, the alternate methodology and the FE model, which is summarised in Table 5.3.

Method	G_{Ic}			Equivalent K_{Ic}
	$3W : W : 0.08W$	$3W : W : 0.1W$	$2.7W : W : 0.11W$	$3W : W : 0.08W$
G_I^E	472±50	468 ±56	471 ±70	1.64 ±0.5
G_I^{E+LDC}	421 ±15	422 ±30	419 ±50	1.48 ±0.2
G_I^{Ch}	484 ±18	488 ±20	481 ±25	1.70 ±0.3
G_I^{Ch+LDC}	436 ±10	432 ±11	437 ±12	1.53 ±0.2
G_I^{Ci}	-	-	426 ±19	* 1.50 ±0.2
G_I^{Ci+LDC}	-	-	387 ± 8	* 1.36 ±0.2
G_I^P	419 ±9	421 ±10	420 ±10	1.48 ±0.2
G_I^{FE}	419	-	418	1.48

Table 5.3 – G_{Ic} and equivalent K for all specimen configurations. * has the $2.7W : W : 0.11W$ geometry configuration.

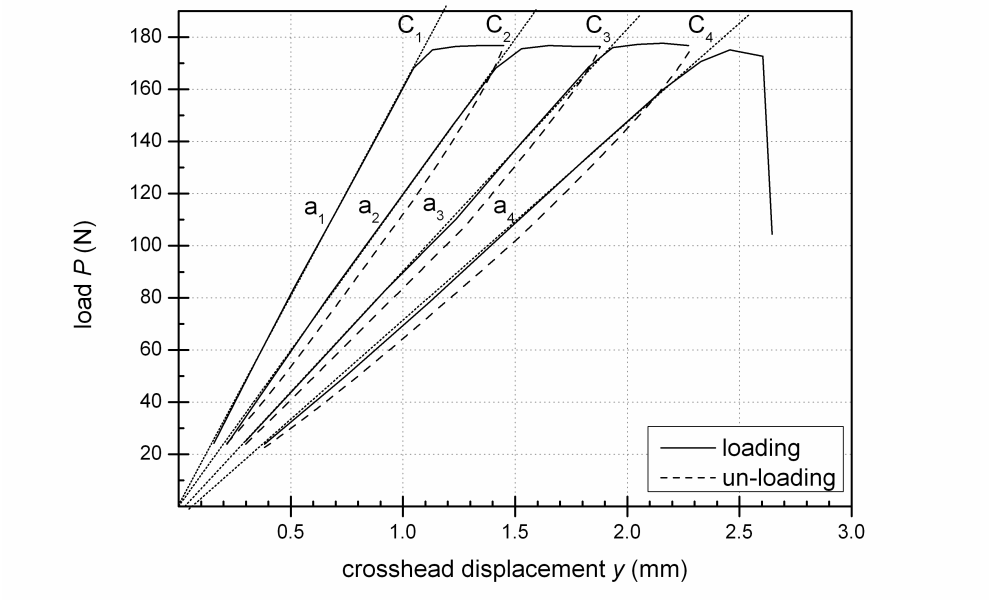

Figure 5.11 – Illustration of the direct method to determine G_{Ic} from the measured compliance at several loading and unloading curves.

Method	Geometry	n	$log(B)$
Evan's method	2.7W : W : 0.11W	32 ± 4	$2.2 \cdot 10^{-7}$
	3W : W : 0.08W	33 ± 3	$9.4 \cdot 10^{-7}$
Chevalier's correction	2.7W : W : 0.11W	35 ± 3	$5.8 \cdot 10^{-7}$
	3W : W : 0.08W	35 ± 2	$6.2 \cdot 10^{-7}$
Ciccotti's correction	2.7W : W : 0.11W	36 ± 3	$1.8 \cdot 10^{-7}$

Table 5.4 – Summary of experimental sub-critical crack growth data, where n represents the slope and $log(B)$ the y-axis intercept of the log-log linear relationship.

VK Relationship

Figure 5.12a shows the VK plots obtained using Evans' method, Chevalier's and Ciccotti's correction respectively. The results are summarised in Table 5.4. The reproducibility of VK relationship data using Evans "conventional" methodology, where several relaxation tests were conducted on a single specimen, shows a transverse shift. This effect has been discussed before [39, 95, 37, 36, 93] and is believed to be a consequence of a crack length dependent SIF. Figure 5.12b compares the relative scatter of VK relationship data as a function the y-axis intercept $log(B)$ deviation (which quantifies the shift in VK data lines) and specimen configuration. Chevalier's correction achieved the best reproducibility for all configurations, where Evans' method shows an increased error with the thicker specimen configuration. Ciccotti's correction could only be utilised for the $2.7W : W : 0.11W$ geometry with relatively good reproducibility.

Specimen Geometry

The DT specimen can be regarded as a thin plate that typically has the proportions of a microscope slide [36]. However, there do not appear to be standard specimen proportions. A review of DT specimen sizes presented by Tait et al. showed that the relative proportions are popularly a length of three times the width and a thickness between 1/6 and 1/15 of the width [36]. They recommended that specimen proportions should be of the order of $3W : W : 0.12$ to $0.08W$. The use of longer specimens ($L > 3W$) reduces the edge effects, however, it can be difficult to achieve symmetrical crack propagation if un-grooved specimens are used. This work has also shown that side grooves are not necessary and symmetrical cracking can be achieved by careful alignment.

It has been revealed in this analysis that the geometry configuration can influence

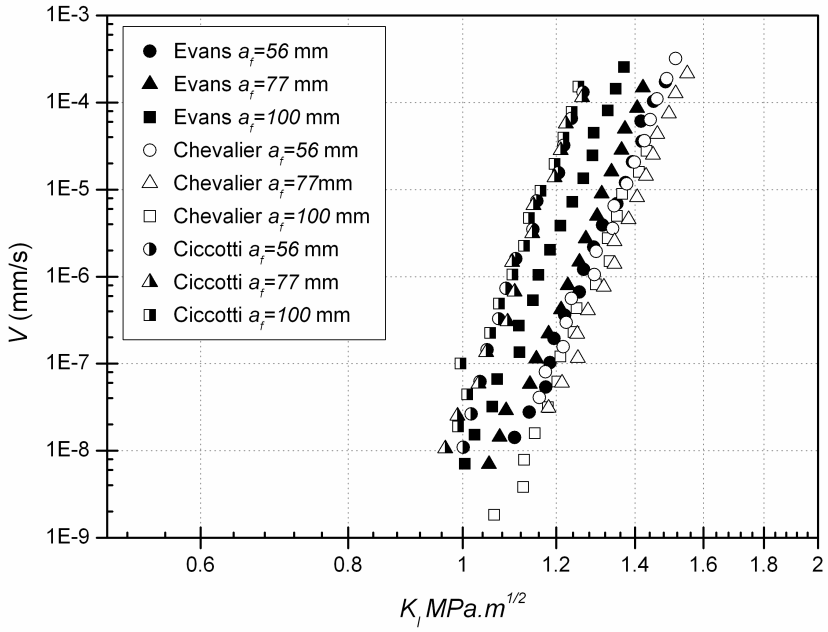

(a) VK curves obtained by successive relaxations using Evans' methodology with specimen ratio $3W : W : 0.08W$, Chevalier's methodology using $3W : W : 0.08W$ specimen geometry and Ciccotti's methodology using $2.7W : W : 0.11W$ specimen geometry.

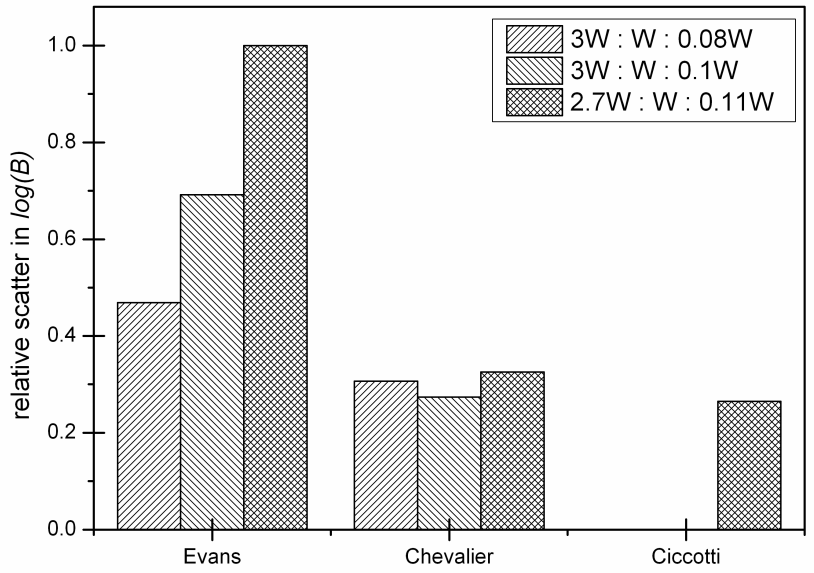

(b) Relative scatter in VK relationship data as a function of $log(B)$ (y-axis intercept).

Figure 5.12

the validity of the assumption of a crack length independent SIF. The general observed trend was a decrease in the SIF with increasing crack length, consistent with a smaller change of the out-of-plane deformations.

Repeatable data was achieved using the thinner $3W : W : 0.08W$ configuration, which showed the least SIF deviation with increasing crack length. The thicker and shorter configuration ($2.7W : W : 0.11W$) showed a less constant SIF, resulting in a reduced repeatability of VK relationship data.

Alignment

Poor crack plane alignment relative to the specimen symmetry line causes the crack to curve to one side rather than extending along the specimen centreline. The effect of this on the SIF's crack length independency was shown in Figure 5.9, where poor alignment resulted in lowered SIF readings.

Additionally, considerable variations in D_E (the compliance y-axis intercept) were attributed to the symmetry of crack growth. An experimentally determined relationship between D_E and a_{off} (Figure 5.13a) was established. From this a 95% confidence in D_E was established when a_{off} is less than $1/8W$. The shift of the compliance curve indicates a more compliant specimen configuration with increasing crack offset. This is due to the reduced stiffness of the broken specimen ligament, which has a reduced torsional load carrying capability.

There is, however, an additional consideration that contributes to the way fracture occurs in a misaligned specimen. Figure 5.13b represents the effect of misalignment on the DT geometry with respect to the SIF's calculated from the FE model. The mode III contribution to fracture with increasing misalignment is shown. A misaligned specimen causes significant mode III contributions of up to 20% in severely misaligned specimen configurations. With the aforementioned crack path offset threshold of $a_{off} = 1/8W$, it may be argued that an equivalent imbalanced load configuration has mixed mode fracture contribution of less than 6%.

5.4.4 Discussion

This evaluation of the DT technique used an experimental study, a full 3D FE model and digital image correlation to assess the underlying assumptions that

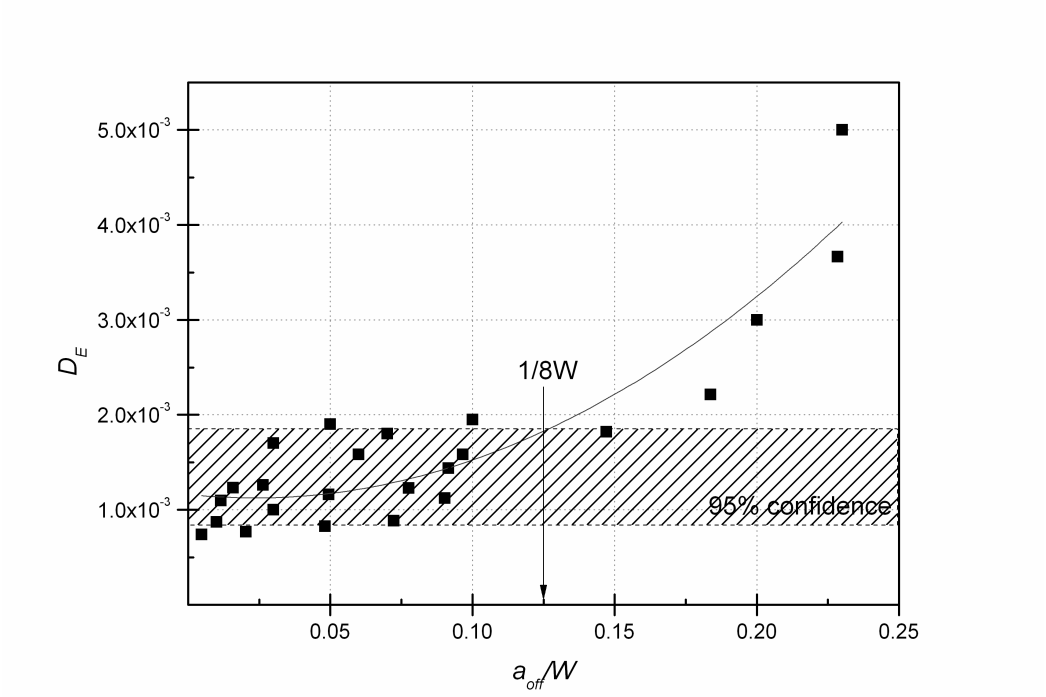

(a) Relationship of D_E and a_{off}. A $a_{off} < 1/8W$ limit was established.

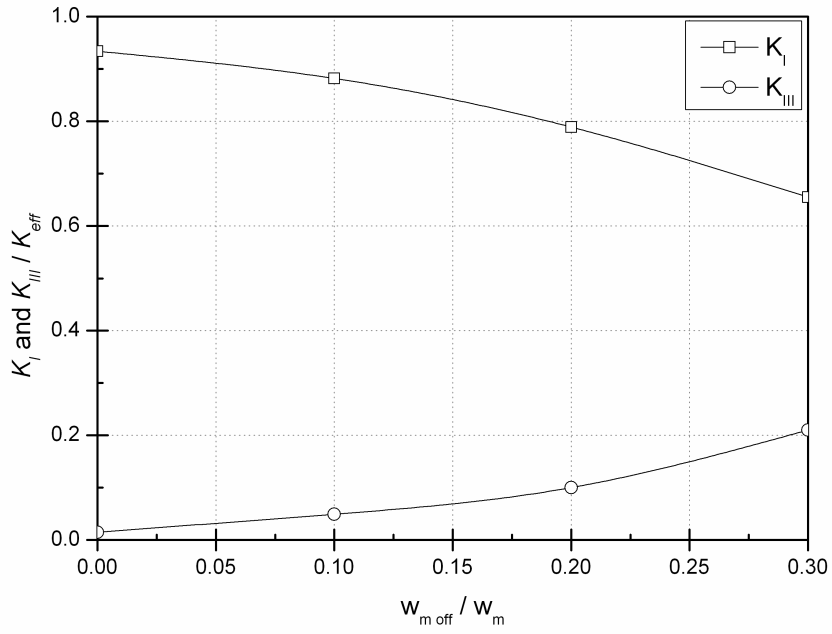

(b) Effect of misalignment on K_{eff} shown on left y-axis and the contributions of K_I and K_{III} on K_{eff} on right y-axis.

Figure 5.13

make the testing geometry crack length independent. A small but clear dependence of SIF on crack length was shown for all specimen configurations, especially for the thicker $2.7W : W : 0.11W$ geometry. It follows that the geometry is not entirely crack length independent, hence the need for a correction exists if a crack length independent test is required. The evaluation has shown that this can result in systematic error of fracture toughness data and will cause non-reproducibility of VK relationship data.

These discrepancies can be attributed to non-linearity of the compliance relationship, which is commonly assumed to be linear. The assumption that only the torsional deformations of the broken ligament halves contribute to the compliance does not hold. DIC verified the FE model prediction that the unbroken ligament does deform considerably, in contrast to the general assumption that it behaves rigidly. Further, it was shown that this deformation increases with increasing crack length, resulting in a crack length dependency of the SIF. Large deflections at the loading points result additionally in non-linearity as the lever arm length decreases with increasing deformation.

Another interesting point to consider: The deformation of the unbroken ligament has an opposite effect on the compliance relationship to the large deflections at the load points. The changes in the loading configuration due to large deflections at the load points result in a continuously *decreasing* compliance and the deformations of the un-cracked ligament result in a continuously *increasing* compliance. This makes the DT configuration complex and it may well be that in some cases these effects counter resulting in a nearly linear compliance and an effectively crack length independent system. Indeed, some investigators have obtained repeatable data with Evans' conventional method using a thin long specimen with a $3W : W : 0.08W$ configuration. This further suggests that the validity of the crack length independent DT technique thus depends on the loading configuration, the specimen geometry and material stiffness, which may combine to give an optimum specimen.

The various corrections established in the literature are intended to account for the crack length dependent effects of non-optimised specimens. Both Chevalier's and Ciccotti's corrections achieve a crack length independent specimen by correcting for the non-linear compliance. Chevalier's adjustment constants m and k are geometry specific, where a clear dependence on the specimen thickness was established. According to their method, thinner specimens require less correction, with almost negligible correction for the specimen with dimension ratio

$3W : W : 0.08W$. Ciccotti's work shows a great deal of attention to geometrical factors such as side grooves and starter notches, however, no variations in the thickness parameter were modelled.

At this stage it may be suggested that the FE model utilised, which was validated by DIC, may be used to develop an optimum specimen ratio for given loading configuration and material. This may provide a route to standardise the DT methodology and limit the need for the proposed corrections. However, for the time being an acceptable configuration and methodology has been formulated. The $3W : W : 0.08W$ configuration with the current load configuration is utilised in the graphite analysis. Evans "conventional" methodology is assumed.

5.4.5 Summary

An evaluation of the DT geometry was presented in this section, that provides a firm basis for the further testing on the nuclear graphite specimens. The evaluation, both experimental and a 3D FE model, has shown a measurable dependence of the SIF on crack length for all specimen configurations. It has been shown that the validity of the common assumption of crack length independence is dependent on the loading configuration, the specimen geometry and material.

The validity of the DT geometry depends on several factors. These include significant deflections at the loading points and the deformation of the unbroken ligament, which were measured using the 3D Digital Image Correlation system. This results in a non-linear compliance relationship that causes the SIF to become crack length dependent.

The corrections proposed to the DT technique by Chevalier and Ciccotti achieved a crack length independent configuration which enables reproducible fracture toughness and VK relationship data to be obtained for various specimen geometries. However, it was found that Chevaliers' correction overestimates and Ciccotti underestimates the calculated SIF by up to 10% in the geometries studied. Evans' conventional methodology, with a large deflection correction, can obtain valid fracture toughness and VK relationship data in some geometries; for example, un-grooved DT specimens with dimensions resembling $3W : W : 0.08W$. The middle half of the specimen achieves an almost crack length independent regime (within 2%), provided the crack tip remains within $a_{off} < 1/8W$ of the centreline for VK investigation.

The author believes that the DT methodology is a unique testing methodology, which best allows for the characterisation of the fracture characteristics of highly brittle materials and thus seems ideal for the investigation of the fracture characteristics of nuclear graphite.

5.5 Damage Monitoring Techniques

It has been recognised that damage development in nuclear graphite is associated with micro-cracking [16, 14, 13, 15, 4], which can significantly affect its fracture behaviour [15, 14, 4]. The functions of micro-cracking are not yet understood and hence, monitoring and measurement of this micro-cracking will provide useful understanding in the graphite fracture. To do this two techniques were used, namely ESPI and DIC.

It is worth mentioning that DIC provides accurate surface displacement mapping around a cracked section. This feature was further taken advantage of and a unique tool named JMAN was developed. JMAN allows the calculation of the J-integral (the measure of energy required for crack propagation) directly from DIC image sequences. This tool is described in detail in Chapter 6.

5.5.1 Electronic Speckle Pattern Interferometry (ESPI)

Strain laser analysis by means of ESPI is used for monitoring the development of surface strains during crack propagation in the DT specimen geometry. ESPI is a widely used technique to measure full-field deformation on surfaces of many kinds of objects and has previously been used to study crack nucleation and fracture propagation in nuclear graphite [82, 4] in which a fracture process zone was observed. The optical technique facilitates the detection of deformations with sensitivity smaller than the wavelength of light [122, 123]. In this work, the ESPI technique is applied to obtain quantitative measurements of the fracture process zone length.

A laser light is used to illuminate the specimen surface in a full-field manner using diverging optics. The reflected light is collected with a lens and imaged on a light sensitive chip of a video camera (CCD). In addition, a divergent reference beam, originating from the same laser light source, is superimposed via a beam splitter on the video camera. Both wave fronts, back scattered from the object and of

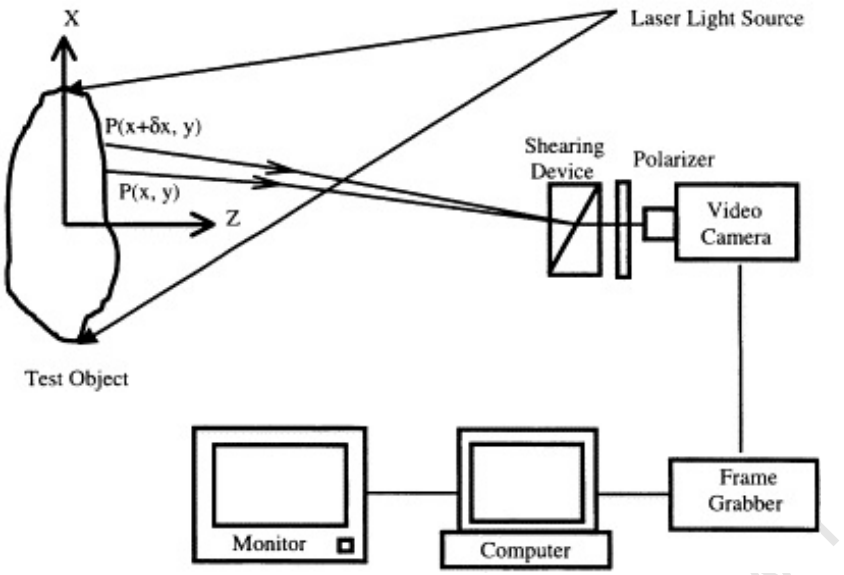

Figure 5.14 – Schematic diagram of ESPI

the reference beam interfere and form a speckle pattern. This is shown in Figure 5.14.

The intensity at each pixel on the CCD can be described by

$$I(x,y) = I_o(x,y)\,[1 + \gamma(x,y) \cdot cos\,(\phi(x,y))] \tag{5.21}$$

where x, y are the coordinates on the chip, I_o is the intensity of the laser light, γ describes the contrast function and ϕ the phase of the wave front [124]. After loading and deformation of the specimen surface the wave front emanating from the object is slightly deformed, whereas the wave front of the reference beam remains constant. Subtraction of the two images result in a fringe pattern, which reflects the deformation of the object surface between the original and deformed state.

The ESPI system used was developed by the University of Cape Town [125] and has a fast shutter system [126]. To perform the measurements, a laser light illuminated the DT specimen with a working distance of 100 mm. The region scanned by the strain laser analyser was about 30 x 30 mm. Speckle patterns from both were recorded by a high-resolution video camera and processed to produce a fringe pattern by subtracting the two different speckle patterns [125]. This was analysed, with in-house software, to determine the apparent in-plane displacements and hence the strain distribution on the specimen surface.

It is worth mentioning that the DT specimen experiences some out-of-plane deflections, and ESPI is affected by out-of-plane movements [127], which were not calibrated for in this work. Hence the ESPI analysis was semi-quantitative. Only the size of the FPZ was extracted from the ESPI analysis, identified by fringe discontinuities along the propagating crack. ESPI has been used previously as a full field strain mapping technique to obtain in situ, load resolved, strain fields from the surface of disc compression and tensile test specimens of IM1-24 by Joyce et al. [82]. Their analysis of these fields is used to show the development of the distribution of localised deformation, which can be linked to the micro-structure and damage processes. Similarly, Hodgkins et al [4] used ESPI to measure the crack length in IM1-24 CT specimens. Similarly, ESPI analysis has been undertaken on concrete to observe the development of micro-cracking and the fracture process.

5.5.2 Digital Image Correlation

DIC allows full field surface displacement measurements to be obtained throughout the deformation of material [117]. Although less sensitive to displacements than the ESPI technique, DIC is relatively easier to use and provides quantitative measurements of the surface deformations. The basis of DIC is the matching of one point from a digital image of an object's surface, in this case the DT specimen, before loading (the undeformed image) to a point in an image of the object's surface taken at a later time/loading (the deformed image). Assuming a one-to-one correspondence between the deformations in the image recorded by the digital camera and the deformations of the surface of the specimen, an accurate, point-to-point mapping from the undeformed image to the deformed image will allow the displacement of the object's surface to be measured.

The nature of DIC requires the surface of the specimen to have a pattern that produces varying intensities of diffusely reflected light from its surface. This pattern may be applied to the object or specimen or it may occur naturally. In graphite, fortunately, a sufficient random pattern exists and hence no additional patterns had to be applied.

The imaging process, to track displacements, works in such way that the camera converts the continuous intensity field reflected from the specimen surface into a discrete field of integer intensity levels or grey levels. In a CCD camera, this transformation occurs when the light incident on a sensor (commonly known as a

pixel) is integrated over a fixed time period. The displacement field for an object is obtained at a discrete number of locations by choosing subsets of pixels or interrogation windows from the initial image and searching throughout the second image to obtain the optimal match or fit of that pixel subset on that image. The pixel subset size of a subset can be between 8x8, 16x16 up to 1024x1024 pixels.

Usually, to provide a more useful representation of this intensity pattern, a surface fit method known as the bi-linear interpolation technique is used to represent the data in continuous form. Briefly, an expression of the form of

$$f_d + f_a x_1 + f_b x_2 + f_c x_1 x_2 \tag{5.22}$$

where f_a, f_b, f_c and f_d are constants, is used to estimate the intensity distribution for any square set of four sample points. A mathematical relationship between the actual object deformation and the 'deformation' or change in the stored intensity pattern is established by the following mathematical expression

$$(\mathbf{x}')_i = (\mathbf{x})_i + \mathbf{u}_i + \frac{\partial\{u_i(\mathbf{x})\}}{\partial x_j} dx_j \qquad i,\, j = 1,\, 2 \tag{5.23}$$

where $\mathbf{x}$' is the deformed position of an arbitrary point in the small subset, $\mathbf{u}$ is the vector displacement field and $\partial u_i/\partial x_j$ are components of the deformation gradient. To obtain the displacement and deformation gradient terms for a local subset, the difference between the initial subset and the deformed subset is minimised, defined by a correlation coefficient C

$$C\left(u_i, \frac{\partial u_i}{\partial x_j}\right) = \iint initial(\mathbf{x}) - deformed(\mathbf{x}) d\mathbf{x} \qquad i, j = 1, 2 \tag{5.24}$$

The deformations, which minimize the difference, as given in Equation 5.24, are defined as the local mapping of the actual object surface. It should be noted that a basic tenet of elasticity is that there exists a subset within the body such that the deformation in this small region may be expressed as a homogeneous deformation. Therefore, if the subsets are chosen sufficiently small and the various assumptions noted previously are generally valid, then the method described is useful for both large and small deformation processes.

The accuracy of DIC is dependent on several factors, including but not limited to camera resolution, lens optical quality, and pattern and contrast. Often the intensity pattern is oversampled using several overlapping interrogation windows

of features in the intensity pattern. Further, DIC allows sub-pixel displacement measurements by fitting a Gaussian function using non-linear least-squares algorithm to the gray levels [128]. This combination of oversampling, interpolation and quantization allows the original intensity pattern to be reconstructed with reasonable accuracy and the displacement field estimated with an accuracy of ± 0.02 pixels or better. The technique is independent of scale.

The DIC tests were undertaken at the University of Manchester and the setup used allowed for an accuracy of approximately ± 0.01pixel, which is equivalent to ± 25μm. DIC has been applied previously to study damage nucleation in nuclear graphite, revealing crack nuclei that were not possible to detect by normal optical methods [129, 47]. Further experimental details regarding the damage and crack monitoring are given in Chapter 7.

5.6 Summary

This chapter has described the experimental details of specimen preparation, the DT technique and damage monitoring techniques. The materials considered and their properties were also discussed accordingly. The aim was to present the experimental details required for the further investigation of nuclear grade graphite.

One of the major topics discussed was a detailed evaluation of the DT technique. The DT technique, to date, has not been standardised and many questions remain. Hence, an evaluation of the technique was formulated, which consisted of an experimental, finite element and DIC analysis. A optimum testing configuration was presented for the forthcoming graphite analysis. It is worth mentioning that a comprehensive literature review on the DT technique is provided in Appendix A.

Additionally, the damage monitoring techniques were discussed. It is believed that graphite undergoes micro-damage prior to and during cracking. ESPI and DIC techniques allow for the observation of such damage, where DIC allows for full field surface strain mapping during testing. These techniques are believed to provide useful tools for the monitoring and measuring of damage prior to and during fracture.

With this extensive experimental background it is now possible to examine damage initiation and crack propagation in nuclear graphite using the DT technique.

First however, a novel tool is presented, which enables the measurement of the J-integral directly from DIC images sequences.

Chapter 6

A Novel Approach to Calculate the J-Integral by Digital Image Correlation Technique

This chapter presents a novel methodology for extracting the J-integral measure from digital image sequences. This optical and non intrusive method enables to measure the energy required for crack propagation and hence provides a useful tool to characterise and measure fracture. The JMAN methodology is presented in this chapter and is separate to the main aim of this project. The JMAN methodology was used in the further fracture characterisation of nuclear grade graphite, yet is also believed to provide a tool in other applications. As a result this Chapter has been submitted for publication to the International Journal of Fracture.

6.1 Introduction

Assessing the integrity of cracked structures, in order to keep them in service as long as safely possible, has received considerable attention during the past five decades. Specifically, the aerospace, nuclear, oil and gas, and railway industries benefit from such techniques. Real-time monitoring of the condition of components, containing flaws such as cracks, in service and ensuring their safety is another aspect of structural integrity assessments. In order to standardise the assessment techniques a number of parameters have been introduced that essentially quantify the severity of the stress field around a crack. Crack mouth

opening displacement [130], energy release rate [57] and stress intensity factors [131] are among such parameters.

Standard procedures have been proposed to measure experimentally these parameters using defined designs such as compact tension or three point bend specimens in elastic [132] and elastic-plastic [133, 134] conditions. For a wide range of commonly occurring cracks (e.g. semi-elliptical cracks), there exist tables that relate the geometry, applied load and the stress intensity factor, or its equivalent parameter [135, 136]. However, the possible variety of loading conditions and geometries often require engineers to simplify the geometry and rely on over-conservative estimations. Therefore replacing a cracked component, which may be safe for continued service, is a common practice. If the functionality of the cracked component is important enough and replacing it causes significant financial or physical difficulties, then numerical techniques such as Finite Element (FE) are employed to more accurately calculate the stress intensity factors and to reduce the over-conservatism. For complex structures, due to the accuracy with which the boundary conditions can be defined and the possible refinement of the FE mesh, there may be significant errors between the calculated and real stress intensity factors. This led some specialists to regard numerical methods for calculation of the stress intensity factor as unreliable [137].

Full-field optical techniques such as the Digital Image Correlation (DIC) or electronic speckle pattern interferometry have proved to be powerful means to monitor cracks in a wide range of materials. Extracting the parameters to quantify the mechanical driving force for fracture (such as the Stress Intensity Factor (SIF)) from full-field optical techniques has received considerable attention during the past twenty years. These studies can be divided into two main categories:

- Numerically optimising the assumed SIF such that the theoretical displacement field matches the measured field.
- Calculating the energy associated with the changes in the displacement field and obtaining the strain energy release rate directly. The strain energy release rate then provides the SIF.

The majority of the investigations used the first optimisation method, with the displacement fields generally obtained by DIC. This method was used as early as 1981 by Chiang and Asundi [138] who simply plotted the vertical or horizontal displacements versus the square root of the distance from the crack tip, which

according to the Williams stress series should have a linear dependence [131], and hence estimated the SIF from the displacement-axis intercept of the fitted line. Huntley and Field [139] used least squares methods to minimise the difference between the theoretical and measured displacement fields to calculate the SIF. They also used a line integral method to extract the associated J-integral and concluded that the least squares approach had a smaller systematic error to the line integral. McNeill, Peters and Sutton [140] also used the least squares technique to measure the SIF in a three point bend test configuration. They pointed out that accurately defining the location of the crack tip is of paramount importance in this technique. Abanto-Buenbo and Lambors [141] subsequently postulated that as the calculated SIF should remain constant over the K-dominated region, this criterion could be used to select the area to calculate the SIF of a crack. They applied this to a functionally graded material.

Yau, Wang and Corten proposed a method [142], based on the so called interaction integral or M-integral that was first proposed by Chen and Shield [143]. Kim and Paulino [144] modified the method of Yau, Wang and Corten [142] and applied it to a functionally graded material to obtain the mode I and mode II SIFs as well as the T-stress. The interaction integral was also used by Rethroe et al. [145] to measure the SIF of a Compact Tension CT specimen in a homogeneous material. Rethore, Roux and Hild [146, 147] used the interaction integral as well to estimate both the 2D and 3D SIFs.

The SIFs in mixed mode loading first received attention by Yoneyama, Morimoto and Takashi [148, 149] who utilised a sophisticated least squares method to extract the surface displacement field of a single edge notch tension SEN(T) sample. A least squares technique was also employed by Roux and Hild [150, 151] to measure mode I and mode II SIFs of a four point bend sandwich test. Hamam, Hild and Roux [152] used two integrated and posterior methods, both based on least mean squares, to obtain the SIFs of a middle tension M(T) specimen. The sensitivity of the least squares technique for SIF calculation was studied by Rethore, Roux and Hild [146]. Recently Lopez-Crespo and co-workers [153] mapped the displacement field obtained by experiment to Muskhelishvili's complex potential in order to determine mode I and mode II SIFs. This method was also used by Yusef and Withers [154] in determination of SIF of a fatigue crack propagating within a residual stress field.

The above brief review shows that both integral and optimisation methods are used, and have been found to be robust. The optimisation methods require

consideration of the fundamentals of linear elastic fracture mechanics and they use mathematically complex techniques. The optimisation techniques are therefore limited to purely elastic fields and are highly sensitive to accurate location of the crack tip. When calculating the SIFs for cracks in quasi-brittle materials, such as nuclear graphite and concrete, using these methods may therefore be inaccurate due to difficulties in locating the crack tip, and the consequences of inelastic damage processes such as micro-cracking. In contrast to the optimisation methods, the alternative approach of calculating the SIFs by integral methods, in particular the M-integral, is both mathematically and theoretically complicated. However, such integral methods can be applied to both elastic and elastic-plastic fields. Therefore, it would be very useful if a method could be introduced that was both accurate and sufficiently simple, mathematically, to implement, and that could be applied to both elastic and elastic plastic fields. That is the aim of this work.

This chapter addresses the findings of a combined numerical-experimental study in which the displacement fields of different cracked components in a wide range of materials are measured through the DIC technique. The measured displacement field was taken directly to calculate the J-integral for elastic, elastic-plastic metallic materials and quasi-brittle materials. Based on the contour integral method, which was first introduced by Li et al and proven to be robust [116], the method has a solid theoretical foundation and is relatively simple. The methodology proposed does not require the crack tip to be located very accurately and can, in principle, be applied to both elastic and elastic plastic materials. This chapter proposes this methodology as an alternative to the existing SIF measurement techniques and shows the advantages of this method over the existing approaches.

6.2 Methodology

To obtain the J-integral an experimentally obtained displacement field through digital image correlation was used. Here, the technique of DIC is briefly described followed by the derivation of JMAN, the algorithm to extract the J-integral directly from the measured displacement field.

6.2.1 Digital Image Correlation

DIC allows full field displacement measurements to be obtained throughout the deformation of material [120]. DIC operates through the discretisation of an image into multiple interrogation windows, which are correlated with the same area in the following images. Displacement vectors can then be obtained for the change in position of each interrogation window, allowing strain distributions across the full image to be calculated [118]. DIC allows sub-pixel displacement measurements if sufficiently large interrogation windows are used [155]. The technique is independent of scale, with the quality of results depending on the image capture camera and in particular its bit depth and pixel resolution.

In this chapter, the digital image correlation technique was employed to explore the crack behaviour on the surface of the specimens using a DaVis ® Imager Pro X 4 Megapixel camera and LaVision DaVis software ver.7.2 [119]. The displacement field was calculated relative to the centre of the image, as rigid body motion of the specimen does not affect the J-integral calculations.

6.2.2 Extracting J-integral from a Displacement Field

The displacement vector field, obtained through DIC, is discretised into a FE domain (Figure 6.1). Four or nine points, of appropriate order, are considered as the nodes forming each element. Thus, each element node has a known, experimentally measured, displacement as the boundary condition. The elastic stresses and strains can be extrapolated at the integration points for each element following the conventional elastic finite element procedure [156]. The current methodology assumed two element types, a four node linear isoparametric quadrilateral element (Q4) and a nine node quadratic isoparametric quadrilateral element (Q9). Since the deformations calculated by DIC are representative of the specimen surface, plane stress conditions apply.

The classic FE boundary problem applies, where the displacement field u in conventional Cartesian coordinates (x_1, x_2) of a body is related to the applied force F by the body stiffness matrix S:

$$\{F\} = [S]\,\{u\} \tag{6.1}$$

To calculate the J-integral from the known displacement field, elastic strains

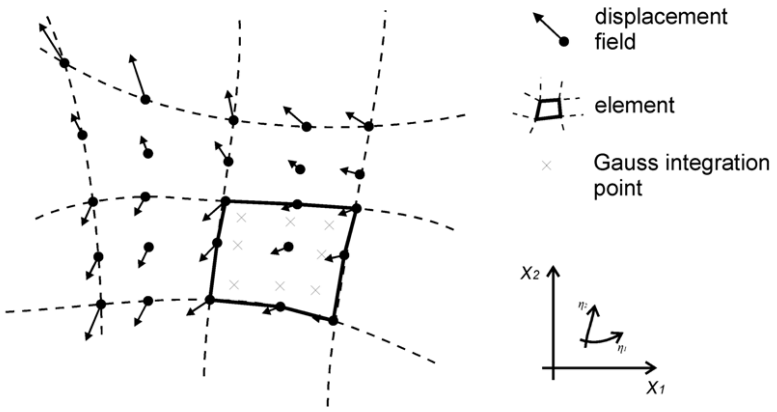

Figure 6.1 – Discretisation of DIC displacement field into FE domain. A nine node quadrilateral element with nodal displacements is shown.

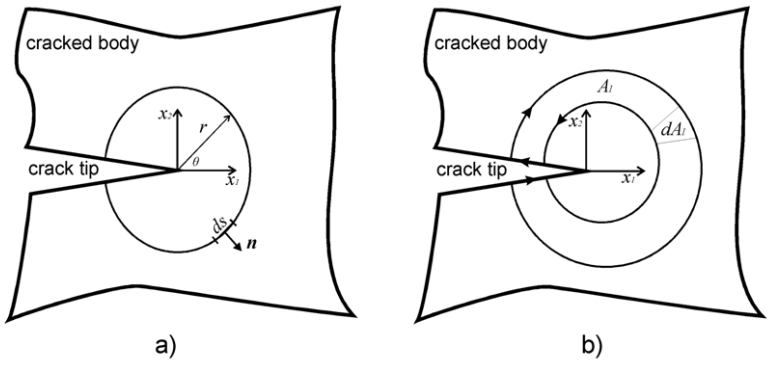

Figure 6.2 – Crack tip coordinates (a) arbitrary line contour (b) arbitrary area contour

and stresses at each integration point need to be calculated first. It is worth mentioning that the Equation (6.1) is not solved as the displacements at nodes are already known from the DIC data. It is used to find the strain field. The strain matrix ε at coordinate (x_1, x_2) is given by

$$\{\varepsilon\} = [B]\{u\} \tag{6.2}$$

where, B is the strain-displacement matrix formed by the differentiation of the interpolate shape functions and mapping from the local domain (η_1, η_2) to the global domain (x_1, x_2). Similarly, the stress matrix is evaluated by

$$\{\sigma\} = [D]\{\varepsilon\} = [D][B]\{u\} \tag{6.3}$$

where, D defines the stress-strain relations according to Hooke's law for linear elastic materials.

Rice introduced the J-integral as a path independent contour integral that quantified the rate of change in potential energy, with respect to crack length, within a region of material that contained a singularity [57]. The standard formulation of the J-integral, neglecting the kinetic energy and body forces, for a crack lying in the x_1 axis (Figure 6.2a) is

$$J = \int_{\Gamma} \left(\overline{W} n_1 - \sigma_{ij} n_i \frac{\partial u_i}{\partial x_1} \right) ds \tag{6.4}$$

where Γ is an arbitrary contour encompassing the crack tip, n is the unit normal vector to the contour at the small increment of arc length ds, u is the displacement field and W is the strain energy density

$$\overline{W} = \int_0^{\varepsilon_{ij}} \sigma_{ij} d\epsilon_{ij} \tag{6.5}$$

For an elastic field, the relation between the J-integral and the stress intensity factor, assuming pure mode I is

$$K_I = \sqrt{JE'} \tag{6.6}$$

where

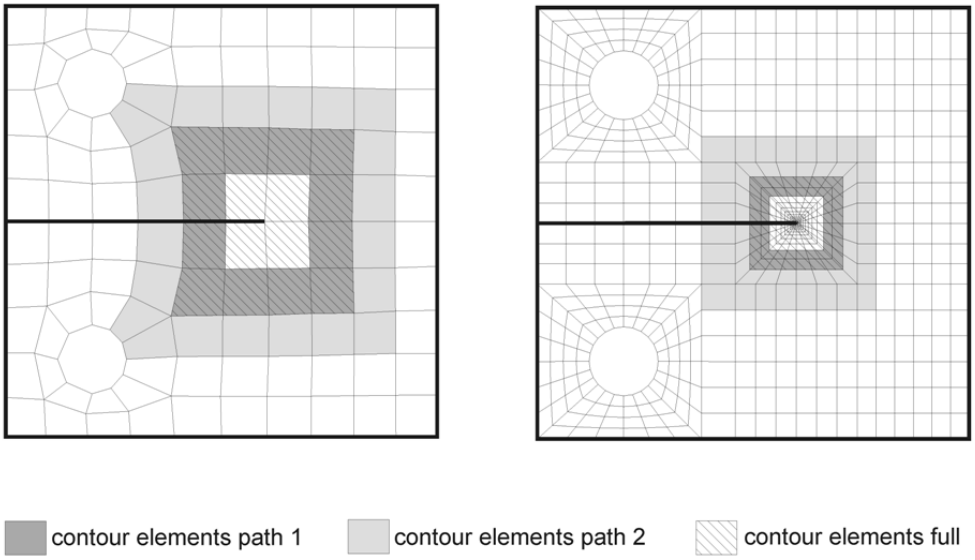

Figure 6.3 – Contours selected to calculate J-integral by JMAN from the ABAQUS mesh

$$E' = \begin{cases} E & \text{plane stress} \\ \frac{E}{1-\nu^2} & \text{plane strain} \end{cases} \tag{6.7}$$

There are a few methods to calculate the J-integral, the crudest of which is to directly evaluate the line integral of Equation 6.4. Calculation of the line integrals is not accurate and is mathematically complex. Li, Shih and Needleman [116] introduced an equivalent expression in terms of a volume integral using the divergence theorem. This volume integral can be converted to an area integral for 2D problems, with a crack lying on the x_1 axis (Figure 6.2b)

$$J = \int_{A_1} \left(\sigma_{ij} \frac{\partial u_i}{\partial x_1} - \overline{W} \delta_{1j} \right) \frac{\partial q_1}{\partial x_j} dA \tag{6.8}$$

where A_I is an area surrounded by two arbitrary contours encompassing the crack tip, q is a smooth function that ranges from 0 on the outer contour to 1 on the inner contour and is the Kronecker delta. Equation 6.8 can be evaluated in a

finite element model by dividing the area A_I into rings of elements

$$J = \sum_{\text{elements in } A_1} \sum_{p=1}^{GP} \left[\left(\sigma_{ij} \frac{\partial u_i}{\partial x_1} - \overline{W} \delta_{1j} \right) \frac{\partial q_1}{\partial x_j} det \left(\frac{\partial x_k}{\partial \eta_k} \right) \right]_p w_p \tag{6.9}$$

where p denotes the integration points (e.g. nine for a quadrilateral, isoparametric element), η is the local coordinate, w_p is the weight associated with each Gaussian integration point p for the total number of integration points per element (GP). If the displacements of a matrix of points around a crack are known along with the material properties, the J-integral can be calculated.

A routine called JMAN has been implemented using MATLAB® code. The input for JMAN is the location of points, their displacements as a function of load, and the material properties of Young's modulus and Poisson's ratio. The discretisation of the global displacement field into a linear elastic finite element problem allows for the computation of the respective stress and strain field at the element integration points, using Equations 6.2 and 6.3 respectively. From this, J can be calculated, using Equation 6.9, by selecting any contour around a region that contains the crack tip.

6.3 Verifying JMAN

6.3.1 Path Independency

Theoretically, the J-integral should be path independent for any contour surrounding a singularity in an elastic medium. This can be exploited to verify JMAN by calculating the J-integral, checking its path independency and comparing the values with an identical FE model. For this, a standard 2D compact tension (CT) specimen was modelled in ABAQUS/Standard Ver 6.9 [23], where the nodal displacements and the relevant J-integral were extracted. The unit thickness specimen had a crack length of $a/W = 0.5$, where a and W are the crack length and specimen width respectively. An arbitrary isotropic linear elastic material was chosen with Young's Modulus $E = 10.9$ GPa and Poisson's ratio $v = 0.21$ which does not affect the normalised stress intensity factor. Figure 6.3 shows two models with coarse and fine mesh respectively, which were used to evaluate the mesh sensitivity of the contour integral method. Numerical solution values of the associated SIF were calculated by the weight function method,

Method	Abaqus	Contour Integral Method JMAN				weight function method
		Element	Full	path 1	path 2	path 1&2	
fine	9.64	Q4	10.56	10.67	10.49	10.52	
mesh		Q9	9.67	9.72	9.50	9.66	9.66
coarse	8.90	Q4	9.83	10.24	10.08	10.13	
mesh		Q9	8.74	9.53	9.25	9.40	

Table 6.1 – Mode I geometry coefficient calculated by ABAQUS, JMAN and weight function method

taken from the Anderson Fracture Mechanics book [6]. The calculated SIFs were normalised using the following expression

$$f(a/W) = \frac{K_I t\sqrt{W}}{P} \tag{6.10}$$

where t is the thickness and P is the applied load. $f(a/W)$ is usually known as the mode I geometry coefficient.

Table 6.1 shows the mode I geometry coefficients obtained from ABAQUS, JMAN and the weight function methods. The fine mesh solution correlates well with the weight function method (less than 1% difference) however, considering that a larger interrogation window size in DIC provides more accurate displacement fields, the coarse mesh is assumed to be more representative of typical DIC results. The ABAQUS coarse mesh also performs well, within 4%, when compared to the weight function solution. It is worth noting that when calculating J by JMAN, only the displacement field was used whereas the weight function method requires the crack length. To check the path independency of the J calculated by JMAN, four different contour paths were considered (Figure 6.3). Two contour paths were comprised of only one ring of elements (contour path 1 and contour path 2), the third contour path was including the inner and outer nodes of contour path 1 contour and 2 respectively. Finally, the forth contour path included all nodes between the outer edge contour path 2 and the crack tip. The corresponding values are given in Table 6.1 and are in good agreement with the ABAQUS and weight function solutions (less than 2% deviation from the weight function value).

DIC window size	DIC accuracy (pixel)	element type	% overlap	JMAN % error	mesh size (no. of elements)	computational time (sec)
32 x 32 pixel	0.05	Q4	0	11.7	3969	34.4
		Q9	0	8.1	1089	15.5
128 x 128 pixel	0.01	Q4	0	2.5	225	2.0
			75	0.9	3969	34.4
		Q9	0	1.3	81	0.2
			75	0.5	1089	15.5

Table 6.2 – Monte-Carlo error analysis of extracting J from DIC obtained displacement fields. Shown are also the computational times taken for each analysis.

6.3.2 Error analysis

Since the J-integral in JMAN is calculated from the displacement field, the results rely on the accuracy of DIC. In this study the DIC algorithm used to obtain the surface displacement fields was developed by LaVision, and uses fast Fourier transform cross-correlation to compare sub-regions [155]. Multiple iterations are used during which the search sub-region is iteratively translated and deformed, using interpolation, until the highest correlation possible is achieved [155].

The accuracy of displacement field measured by DIC is dependent on the interrogation window size [119] and thus the sensitivity of the displacement field on J was evaluated for two different interrogation window sizes. This was done by a Monte-Carlo analysis where a percentage random error (according to the DIC accuracy) was introduced to the x_1 (crack propagation direction) components of the displacement vectors obtained from the coarse ABAQUS CT specimen. This way the error in displacement magnitude could be approximately simulated. In this analysis, changes in the x_1 direction are considered only since the crack propagation is considered in that direction. The rate of energy release in the x_1 direction is then calculated by differentiating the energy with respect to x_1 which makes the calculations highly susceptible to error in displacement in x_1. Table 6.2 reports the interrogation window size, corresponding displacement field accuracy and the error in calculated J. The accuracy of DIC is function of the image bit depth, and a 14 Mbit camera was assumed for the estimation of the DIC error.

It was found that a large interrogation window (128x128 pixels) with an accuracy of the displacement field of 0.01 pixels, results in a 98.7% percent confidence in J for Q9 elements using JMAN. The ABAQUS model showed that a coarse mesh

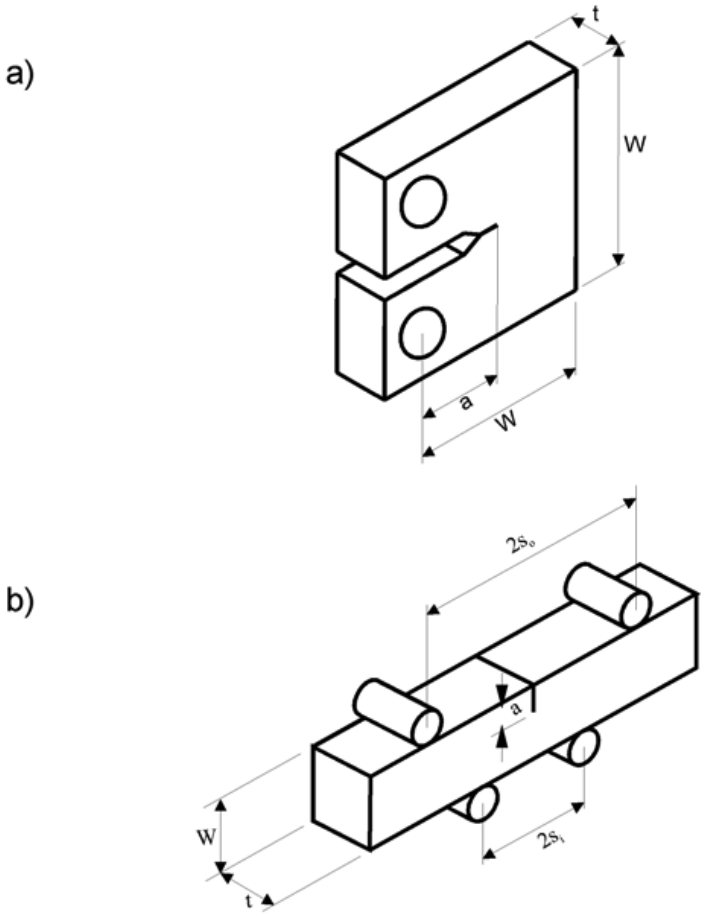

Figure 6.4 – Overview of the specimens (a) Compact tension CT (b) Four point bend 4PB

gives a less accurate J as the strain and stress fields are poorly approximated over the FE domain. This can be explained by the different methods of contour selection in ABAQUS and JMAN. In ABAQUS, a contour is automatically selected that includes the near tip elements. However, the stress and strain fields in the near tip elements are not accurate in this region unless a very fine mesh is utilised. That was not done in this analysis. In contrast, JMAN does not include the near tip elements since the DIC obtained displacement field is inaccurate at the crack tip. Instead a ring of elements is manually chosen, enabling the selection of valid contours that are beyond any crack tip plasticity (for metals) or micro-cracking (for quasi-brittle materials). A smaller interrogation window (32×32 pixels) produces a relatively finer mesh, at the cost of DIC accuracy (0.05 pixels), resulting

in a 91.9% confidence in J for Q9 elements for JMAN. Best results were obtained with an interrogation window size of 128x128 pixels with 75% overlap using Q9 elements. The overlap allowed for a sufficiently fine mesh and fast computational time with an uncertainty in J of less than 0.5%.

Currently used fitting methods for the extraction of SIF's from displacement fields, obtained through DIC for example, usually are computationally expensive and thus may require long computational times to run. JMAN on the other hand is simple and, as shown in Table 6.2, can solve for an equivalent SIF in 0.2 seconds if a large interrogation window is used with no overlap. The time shown is the time required for the algorithm to mesh the domain, calculate the equivalent stresses and strains from the displacement field and solve for J. A more accurate solution is found with the aforementioned 128x128 pixels with 75% overlap interrogation window, which has a computation time of 15.5 seconds on a regular PC.

Since only elastic conditions are considered in the current version of JMAN, the contour elements for the calculation of J must be located in an elastically deformed region. However, materials often exhibit non-linearity (e.g. plastic deformation or micro-cracking) close to the crack tip and elastic conditions do not apply in such areas. Since J is a measure of a global strain energy release rate a contour can be taken around the crack tip, sufficiently far from the nonlinear fracture process zone, and valid global J results are still obtained. The issue of valid contour selection, outside the non-linear zone or passing through it, has been the topic of many studies during the past 20 years (e.g. [157]). It is believed that the most reliable value is obtained when the selected contours are outside the fracture process zone, yet not touching the boundaries of the model [73]. This ensures a path independent integral and hence a global energy release rate.

6.4 Application of JMAN

Given that only the displacement field, obtained through DIC, is used for JMAN, it is proposed that JMAN is applicable at the surface of any specimen geometry and material. To verify this, JMAN was tested using data from four sets of experiments on different specimen geometries fabricated from different materials. A CT specimen made of stainless steel under low amplitude cyclic loading (primarily elastic), a CT specimen made of stainless steel under high static loading

(elastic-plastic), four point bend and Double Torsion (DT) specimens made of coarse grained, poly-granular graphite (quasi-brittle). The DT specimen results are presented in Chapter 8. The overview of the specimens is illustrated in Figure 6.4, while an overview of the DT geometry is given in Chapter 5. In the case where elastic conditions apply, an equivalent SIF was calculated and comparison with JMAN was made. In the case of the elastic plastic standard CT specimen, the comparison was made between JMAN and the standard method of experimental J-integral measurement [158]).

In all cases, the specimen surface deformation was recorded and the displacements were calculated relative to the centre of the image, with reference to an image recorded at a zero load. A 128x128 window with 75% overlap and 4 passes was chosen for all geometries considered. It should be noted when using large windows that since the DIC analysis solves for the average displacement field for an interrogation window [159], the features that are located on the one side of a crack contribute to displacement points located on the opposite side. This results in erroneous displacements that appear as large strains in the vicinity of the crack. This effect is exaggerated with large interrogation window sizes. However the problem is overcome by ensuring the contour is taken sufficiently far enough away from the crack.

6.4.1 J-Integral measurement in specimens with small scale plasticity

A standard CT specimen [158] was used by Yousef and Withers to monitor the SIF change under fatigue loading in real-time. Their data was re-analysed using JMAN to find the corresponding SIF. The material was AISI 316(L) stainless steel with stated properties of $E = 197$ GPa and $v = 0.3$ for the Young's modulus and Poisson's ratio respectively. The specimen dimensions were $W/t = 3.6$ with a specimen thickness of $t = 14$ mm. The specimen had a fatigue crack of length $a = 28.4$ mm which was initiated from tip of a notch. The test was load control with minimum and maximum load of 0.05 kN and 3 kN respectively ($R = 0.05$) At a load of $P = 2.67$ kN an equivalent SIF of 11.87 was calculated using the weight function method [6]. At this load the radius of plastic region, according to a simple Irwin approach [6], is calculated to be less than a millimetre (0.88 mm). Hence, only small scale yielding was present near the crack tip, allowing LEFM conditions are assumed. The respective DIC obtained displacements are shown in

Figure 6.5. Three contour integrals were taken around the crack tip to determine the J-integral using JMAN (Figure 6.5 shows one of the chosen contours). The SIFs obtained from these J-integrals were 11.6, 11.5 and 11.8 units. The JMAN results show excellent agreement (2% difference) with the weight function SIF. The displacement uncertainty due to the background noise, at a constant load, (if a large interrogation window is used of 128 x 128 pixels) was 0.005 mm, which resulted in an expected error of the calculated J of less than 0.05%.

Yousef and Withers used the method developed by Lopez-Crespo et al. [153], which calculates mode I and mode II SIFs based on fitting the measured displacement field with the theoretical elastic displacement field obtained from Muskhelishvili's complex function. The value they obtained was 13.1 . This is 10% higher than the values measured by JMAN or calculated from the weight function method. The authors believe this difference may be explained by the fact that Yousef and Withers require the whole displacement field in their fitting procedure. This includes the displacements close to the crack tip. Since DIC is not representative of actual displacements very close to the crack (dependent on interrogation window size) and some limited plasticity is present ahead of the crack tip, this may lead to an error in the fitting procedure. This problem does not arise with the JMAN analysis.

6.4.2 J-Integral measurement in specimens with significant plasticity

To verify the limits of applicability of JMAN for elastic-plastic conditions, data of a standard J-integral resistance curve (J_R-curve) test, performed by Wasylyk and Sherry [160] on a CT specimen were re-analysed. The material used was AISI 304(L) stainless steel with stated properties of $E = 206$ GPa and $v = 0.3$ for the Young's modulus and Poisson's ratio. The specimen dimensions were $W/t = 2$ and specimen thickness of $t = 25$ mm. Figure 6.6a shows the chosen contour for J_R-curve evaluation by JMAN. The results were compared to the J_R-curve behaviour determined by the compliance technique according to BS 7448 [158] by Wasylyk and co-workers [160] which is shown in Figure 6.6b.

Excellent agreement was obtained at low load, however with the onset of gross plasticity J values calculated through JMAN were clearly erroneous. This is because the current implementation of JMAN assumes linear elastic deformation and thus the stresses calculated at an element are only valid until the onset

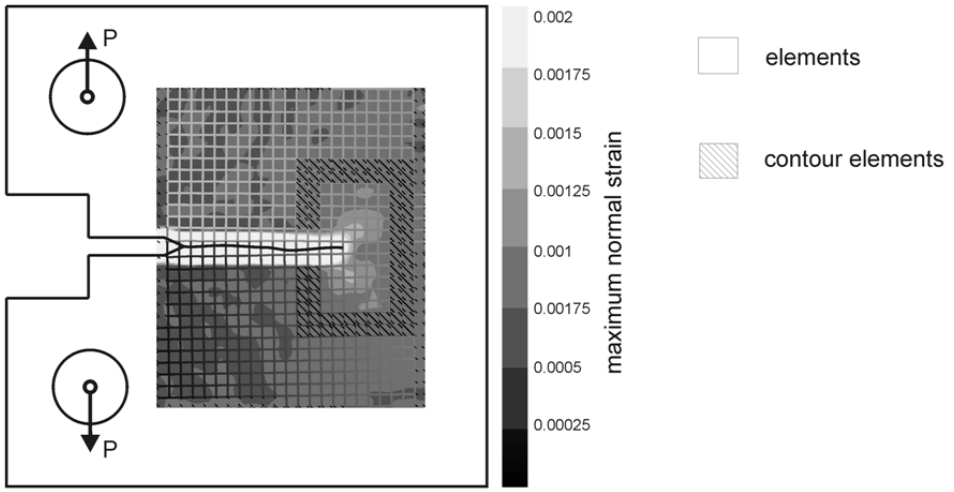

Figure 6.5 – Compact tension CT specimen with small scale yielding. Shown are the surface displacement field, JMAN's FE elements and area contour elements used to calculate J (specimen is not to scale).

of plasticity at that element. Wasylyk and co-workers showed that as the crack grew by 0.3 mm ($\Delta a = 0.3$ mm), extensive plasticity occurred across the ligament [160]. The contours used in the JMAN analysis contained plastically deforming elements once the crack extension was greater than 0.2 mm. The displacement uncertainty up to this point due to the background noise was 0.002 mm, which resulted in an expected error of the calculated J of less than 0.03%.

6.4.3 J-Integral measurement in quasi-brittle materials

Quasi-brittle materials undergo some non-linearity during loading due to the formation of the fracture process zone (FPZ) (i.e. micro-cracking) [19, 14, 16]. Since the main aim of this project is to characterise the fracture in graphite, which can be regarded as a quasi-brittle material [16, 4], the JMAN methodology provides a useful tool. Since graphite is known to undergo some non-linearity during fracture, the fitting methods for calculating SIFs prove unreliable. JMAN was

applied to measure the J-integral fracture energies associated with the formation and propagation of a crack in coarse grained poly-granular nuclear graphite. Two specimen geometries were considered for the JMAN methodology; a four point bend configuration and a DT configuration. The results obtained using the DT methodology are presented in Chapter 8, as this is the main aim of this project - to characterise fracture in nuclear graphite.

Four Point Bending Configuration

A four point bend fracture test was considered using single edge notched specimens of a Pile Grade A (PGA) orthotropic needle-coke nuclear graphite specimen [81]. The dimensions of the specimen ($L \times W \times d$) were $150 \times 30 \times 15$ mm with an inner span $s_i = 75$ mm and outer span $s_o = 125$ mm. The maximum applied force for a crack length of 21.5 mm was roughly 860 N. Unstable fracture occurred at this load. The displacements were calculated relative to the centre of the image, with reference to an image recorded at a zero load.

Using JMAN, the J-integral was calculated from the displacement field from three different contours around the crack tip (Figure 6.7 shows one of the chosen contours). Converting J to SIFs, using Equation 6.6 values of 1.93, 1.90 and 1.88 were obtained. The same test was simulated using ABAQUS, using a symmetrical 2D plane stress model (with a plane stress thickness of 15 mm) with linear elastic quadratic elements. Typical elastic material properties of $E = 11.9$ GPa and $v = 0.21$ were considered in the model [4]. The crack was simulated at a length of 21.5 mm ($a/W = 0.72$) using a concentrated mesh and collapsed elements at the tip. Hard contact between the stainless steel rollers and graphite was modelled. A load of 430 N was applied on the half model and mode I stress intensity factor was calculated by ABAQUS via the contour integral method to be 1.65 . From the weight function a SIF of 1.63 was calculated.

The JMAN value is close to the expected fracture toughness of PGA graphite [4]. The values from these contours compare well with less than 4% difference, showing no path dependency. The displacement uncertainty due to the background noise was 0.01 mm, which resulted in an expected error of the calculated J of less than 1.5%. Interestingly, J-integral values calculated by JMAN are about 15% higher than the values calculated from the elastic FE model using the same elastic constants. This difference may be explained by inelastic deformation, which is a characteristic of coarse poly-granular nuclear graphites [16, 15, 4]. This increases

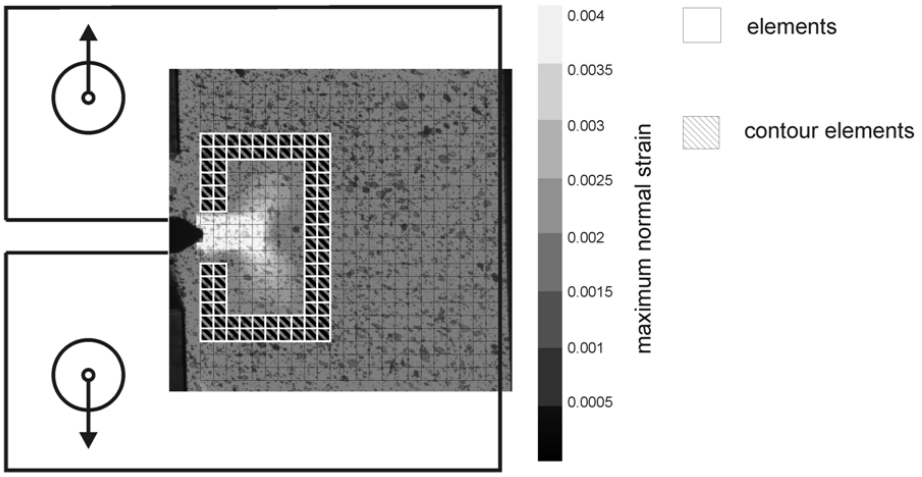

(a) Compact tension CT specimen with large scale yielding. Shown are the surface displacement field at crack length 0.2 mm, JMAN's FE elements and area contour elements used to calculate J (specimen is not to scale).

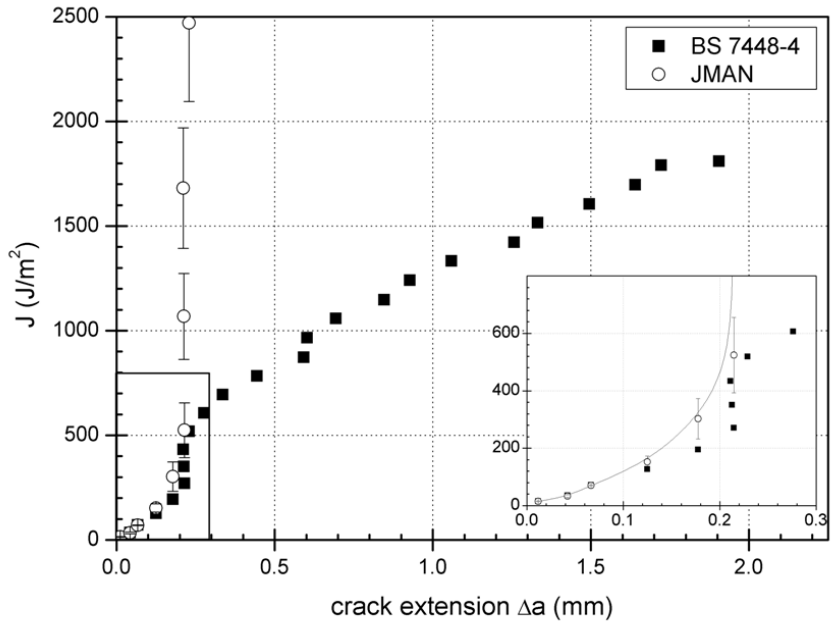

(b) J_R-curve behaviour of AISI 304(L) stainless steel obtained by BS 7448-4 and JMAN. JMAN obtains valid results until the onset of gross plasticity. (Data up to $\Delta a = 0.3$ mm are shown in the insert for clarity)

Figure 6.6

the effective crack length, in the same manner as the plastic zone correction to crack length in metallic materials [161], and hence increases the displacements in the elastically deforming region of the sample above that expected for a simple elastic analysis. The JMAN analysis therefore represents the crack driving force more accurately.

6.5 Discussion

Digital image correlation is a fast growing experimental observation technique, which allows measurement of surface displacements and hence surface strains with high accuracy. This was exploited to provide a novel methodology for evaluating the J-integral, directly from the surface displacement field. Based on a solid theoretical foundation and being mathematically simple, JMAN discretises the displacement field into a finite element problem enabling the determination of stresses and strains from the known material properties. Such fields are then used to categorise fracture parameters for various material types and testing configurations. The computation time is fast; it may be less than 0.2 seconds for a coarse mesh. This could allow in-situ assessment of cracks, provided that the digital image correlation analysis to provide the displacement fields is also implemented swiftly. This approach could provide a powerful NDT methodology for the assessment of cracked structures under dynamic loading, for example.

In the examples described in this chapter, a fatigue crack in a stainless steel sample was evaluated and the appropriate SIF was calculated using JMAN. The loading was such that only small scale yielding at the crack tip occurred, hence LEFM conditions applied. As a result, JMAN would allow continuous evaluation of the SIF throughout the load cycle. It can be concluded therefore, that the approach presented could provide a powerful tool for in-situ analysis of fatigue cracks. However, further investigations are required to calculate J-integral at different points of a cyclic load and compared with the theoretical values to verify the applicability of JMAN in a whole cycle. Caution should be taken when measuring the minimum where the crack closure is important ($R << 0.4$).

The characteristic R-curve behaviour of the elastic plastic ductile fracture of stainless steel was also analysed. Excellent agreement with the standard values was achieved prior to the formation of an extensive plastic zone throughout the ligament. JMAN is currently constrained to elastic fields and the associated

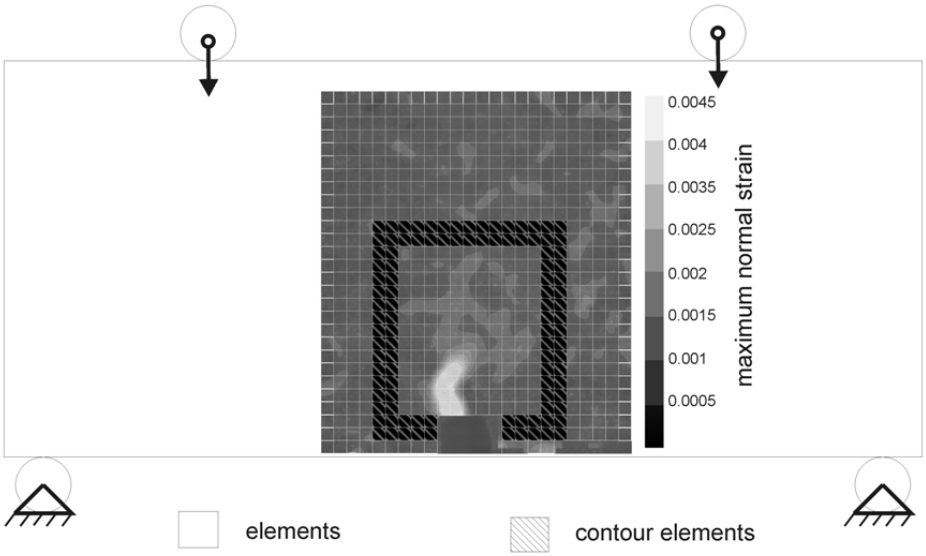

Figure 6.7 – Four point bend 4PB specimen. Shown are the surface displacement field, JMAN's FE elements and area contour elements used to calculate J (specimen is not to scale).

elastic energy at the integral contour. However, this analysis demonstrates that the JMAN analysis is not limited to linear-elastic or small-scale yielding problems, as long as plasticity is contained within the contour integral.

The fracture behaviour of a quasi-brittle material (nuclear grade graphite) was successfully analysed with JMAN and is presented in Chapter 8. Since graphite undergoes considerable micro-cracking and crack bridging as crack propagation occurs, standard fracture analysis proves difficult [4]. However, the JMAN analysis has the ability to categorise the fracture behaviour of such materials, provided the fracture process zone is contained within the chosen contour integral.

Currently, the FE discretisation in JMAN is based on a simple linear-elastic model, hence its application is limited to observations where the displacements can be measured in the elastic regime beyond the zone of inelastic deformation (i.e. the fracture process zone or crack tip plastic zone). It was demonstrated in the examples that for crack singularities that develop limited local nonlinear zones due to plasticity or micro-cracking, the linear elastic model categorises

the J-integral well. The JMAN analysis, however, could easily be extended to account for plastic strains, using the currently available FE formulation for plastic behaviour of metals, and could also be extended for quasi-brittle behaviour in other materials using appropriate and validated models. Furthermore, the JMAN analysis may be developed readily to allow J to be decomposed into mode I, mode II and T-stress components, and therefore to account for mode mixity or in-plane constraint effects.

6.6 Summary

A novel and simple methodology for extracting the J-integral from displacement fields obtained by digital image correlation at different loads has been presented. The displacement vectors are transformed into a finite element domain through a MATLAB implemented routine (JMAN) to obtain the J-integral as an area integral. The methodology was verified using an ABAQUS model, with excellent agreement between the standard ABAQUS and weight function calculated SIFs. JMAN was tested on three different specimen geometries for elastic, elastic-plastic and quasi-brittle materials. Excellent agreement with other fracture characterisation techniques was achieved.

One of the main advantages of the JMAN methodology presented here is that the analysis method has an advantage over standard methods in that precise location of the crack tip is not required. It is also insensitive to inelastic strains close to the crack tip that are contained within the chosen contour.

The JMAN methodology is intended to be utilised for the characterisation of fracture behaviour of nuclear graphite using the DT technique. This is presented in Chapter 8. Future development of JMAN is proposed, that would provide the contributions of mode I and mode II in the J-integral as well as the T-stress. JMAN may also be modified to account for plasticity and inelastic fracture processes in the FE domain, as well as residual stress effects.

Chapter 7

Observations of Mechanisms Associated with Crack Growth

There does not yet appear, in literature, to be a unified theory for explaining damage development in graphite prior to and during fracture . Effects such as micro-cracking, macro-crack initiation and crack bridging in the wake of the crack are known to exist, but are not fully understood. At this point, the question behind crack initiation is believed to be dependent on the formation and development of a fracture process zone (FPZ) [16, 4] where a non-linearity in load-displacement curves, due to micro-cracking, is said to occur at approximately 30% of the fracture load [17]. The previously reported observations of cracking in graphite have been highlighted in Chapter 3, however at this point, have failed to link the damage development, macro-cracking and crack bridging to the fracture characteristics of the material.

There has been, in addition, a need to understand the development of micro-cracking from the tip of a so-called "single crack", as the crack at this location is often somewhat diffuse or hidden in the process zone. An attempt of such a mechanistic understanding of damage development in graphite is formulated in this chapter, where damage development ahead and in the wake of the crack tip has been observed with the use of Electronic Speckle Pattern Interferometry (ESPI) and Digital Image Correlation (DIC). These are compared to the considered graphite grades and orientations, in an effort to identify the mechanism of fracture in graphite.

The sequence of the chapter is as follows; first, some previous studies on cracking in graphite are discussed to familiarise the reader with the subject, and crack-

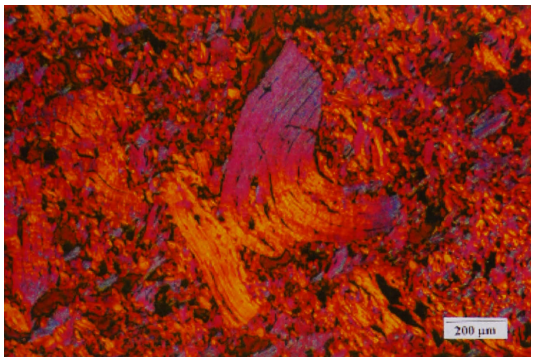

(a) PGA

(b) IM1-24

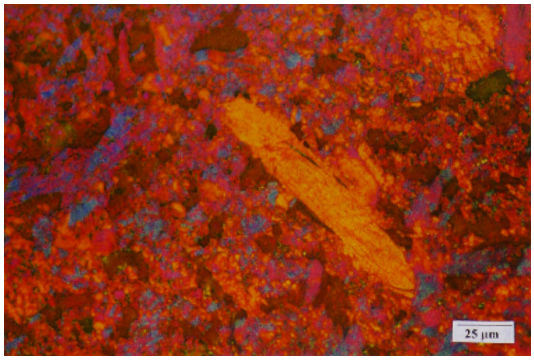

(c) IG110

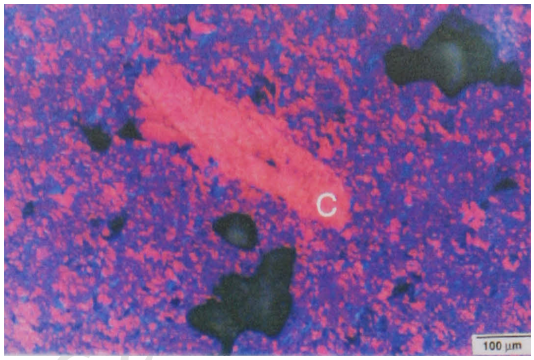

(d) UcarC

Figure 7.1 – Micro-graphs of polycrystalline graphite using polarised light to identify the filler grain orientation [16]. Figure (c) and (d) are at higher magnification due to the finer grain size.

ing on a micro-scale is specifically focused on. It is worth mentioning here that the investigation undertaken in this chapter is not on a microscopic scale and is intended to complement the existing understanding of micro-cracking and other mechanisms associated with cracking. This is followed by an experimental details section, observations and a short summary of the findings follow the previous studies. The materials considered are NBG10 and IM1-24. ESPI and DIC monitoring techniques are used for the observation of a FPZ, with efforts to link the FPZ mechanisms and size. Lastly, the observations of the crack tortuosity and crack bridging are given, comparing the considered graphite grades and orientations.

7.1 Previous Studies

Cracking in polycrystalline graphite such as Gilsocarbon (IM1-24) and nuclear block graphite 10 (NBG10) has been investigated by a number of researchers and the detection and monitoring of such cracking has utilised various techniques ranging from simple visual and microscope observations [14, 13, 24, 15], to more complex ESPI and Squid techniques and, more recently, x-ray methods [4, 82, 162]. It is well known that graphite is a porous material and that flaws exist even before any load is applied [4]. These defects exist due to the aforementioned folds in the hexagonal crystal structure in graphite. The degree of ordering of these hexagonal structures can vary significantly, which results in defects in the crystal structure [16]. For this reason, it is said that artificial graphite consists of three micro-structure phases; throughout which larger graphite grains are dispersed, termed the filler (the 2nd phase). Porosity forms the third phase. The size, distribution, shape and form (aspect ratio) of the particles and pores vary from grade to grade and are the principal factors that determine the bulk properties of every grade of graphite [3]. Thus, this seems suggestive that the fracture characteristics of artificial graphite vary for different graphite grades and are a function of its micro-structure and porosity.

Some, though limited, research has been conducted on the relationship between graphite failure/fracture, micro-structure and porosity. These are briefly discussed here to inform the reader of the complexity of the seemingly simple structure of artificial graphite.

7.1.1 Micro-structure of Polycrystalline Graphite

Fazluddin [16] studied the micro-structure of four nuclear graphite grades, namely; PGA (a coarse grained graphite with a grain size of approximately 1 mm and a distinct grain orientation due to its manufacturing process), Gilsocarbon (the same material considered in this work, a medium grained isotropic graphite of approximately half a mm grain size), IG110 (a fine grained isotropic graphite with an average grain size of 20 μm) and UcarC graphite (an extruded fuel-sleeve graphite which has an average grain size of 0.22 mm). The micro-structures of the four nuclear graphite materials considered by Fazluddin are represented by means of polarised light micro-graphs in Figure 7.1.

Figures 7.1a and 7.1b represent the micro-structure of nuclear graphite, where

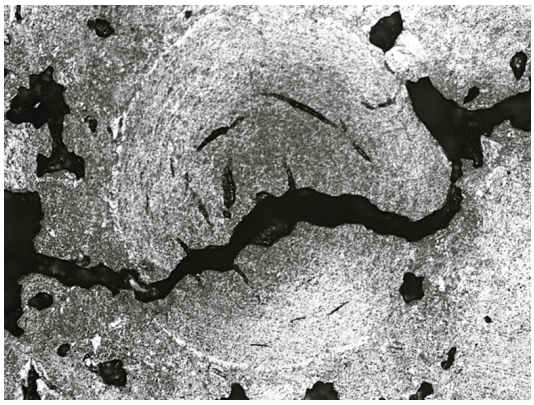

(a) Trans-granular crack propagation through an apparently complete filler grain in IM1-24 [4].

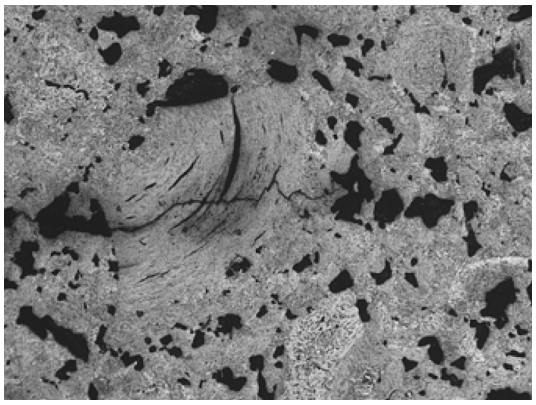

(b) Trans-granular cracking through fragments of filler grains in IM1-24 [4].

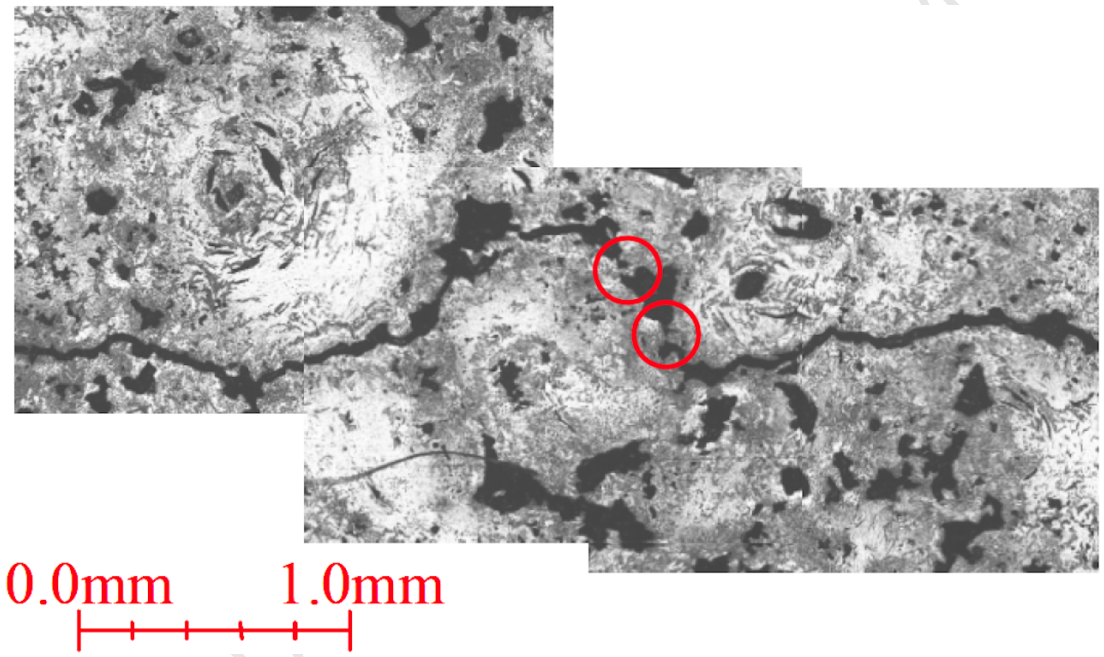

(c) The crack is forced to deflect around the boundary of the gains. Highlighted in the image are two points where crack bridging is occurring as a result of this deflection [4].

Figure 7.2 – Optical microscopy of the interaction of a crack with filler particles in IM1-24.

needle-coke filler particles can be clearly identified, which are surrounded by the binder phase. Because of the polarised light, the texture within the needle-coke grain is evident from the directional orientation of the interface colours within these grains. According to Fazluddin, grains which are orientated at 45º to the vertical line appear blue and grains orthogonal to the blue grains appear yellow in Figure 7.1a, while the distinct orientations are apparent in all the Figures. PGA

for example, which is an anisotropic material, shows a distinct orientation, where filler particles are predominantly orientated with the general extrusion direction (45^{o} towards the vertical line). IM1-24 on the other hand, with its characteristic large filler particles, has a random appearance as it has isotropic properties. The other two graphite grades considered by Fazluddin in Figure 7.1c and 7.1d show a similar trend, where IG110 shows a random texture compared to that of the UcarC grade. The distinguishing feature is the grain size, where the IG110 and UcarC have much smaller needle-coke particles.

Fazluddin's study of crack growth in CT and SENB specimen revealed a marked difference in the extent of crack deflection or crack tortuosity between his considered materials. He observed considerable crack path deflection in the course grained materials (PGA and IM1-24) compared to the IG110 graphite where crack deflection was not so marked. His work showed that crack deflection is a localised event along the crack path, occurring when the crack intersects pores and filler grains. There was also an indication, in the coarse grain materials, of an overall path deflection, which is consistent with the larger grain size in these materials. The cumulative effect of the multitude of crack tip deflections that occur along the crack front develops the complex crack path in graphite. Fazluddin observed that fracture was predominantly inter-granular, where cracks seldom penetrated the filler particles. In IM1-24 the larger spherical filler grains tend to have their basel orientation always aligned perpendicular to the crack, which makes it difficult for the crack to transverse the grain, except in those instances when the grain is orientated favourably. This can result in a higher energy requirement for initial crack growth. Ouagne [15] suggested that needle-coke graphites, such as PGA, tend to have a reduced crack initiation toughness as the inerlameller region within the macro-crack is more easily created. Examples of inter- and trans-granular cracking were shown by Hodgkins in IM1-24 [4] and are shown in Figure 7.2.

The preferred route of the crack is along the binder-filler interface for most artificial graphites [163, 4], where the crack passes easily around the poorly bonded grains. Walker et al. [86] has noted some important characteristics of the binder-filler interface, in relation to the probability that the crack is deflected by the filler grains. The less well bonded the interface, the easier it becomes for the crack to travel around the grain and the more pronounced the crack deflection. A strong interface forces the crack to traverse the grain.

(a) SEM images of IM1-24.

(b) magnified view of (a).

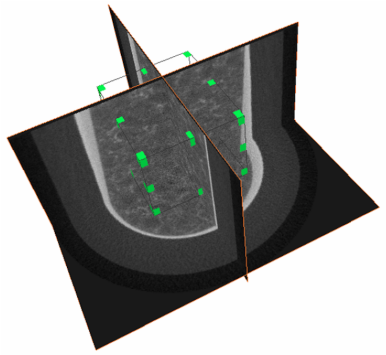

(c) Xray tomography map to quantify porosity in impregnated IM1-24.

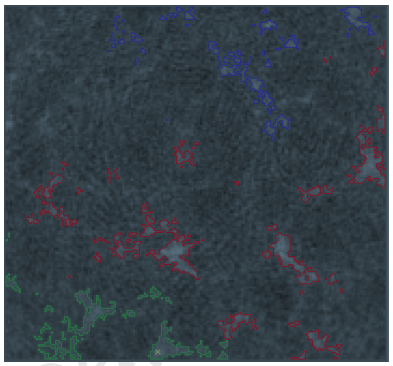

(d) Porosity identification in IM1-24. Various colours represent connected networks.

Figure 7.3 – Porosity identification undertaken by Hodgkins [19]

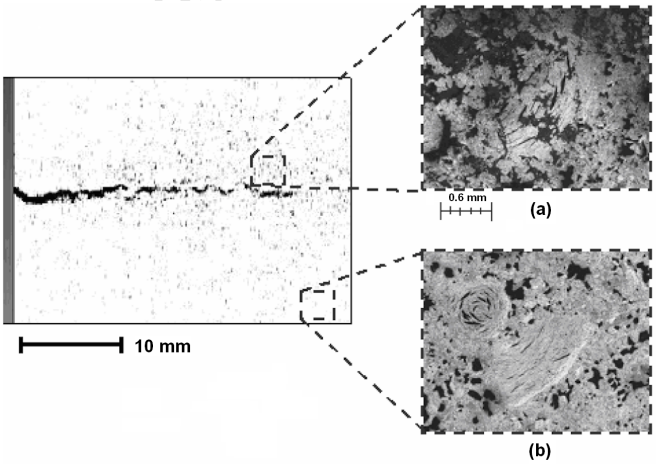

Figure 7.4 – Optical microscopy of surface cracking in a CT specimens [4]. (a) Material close to the crack contained a high proportion of cracks. (b) Material away from the crack, the micro-structure remained uncracked.

7.1.2 Flaws and Porosity in Polycrystalline Graphite

Pores are the third phase in graphite and form an important part to the structure, adding to graphite's defective nature. Pores form in defective sites between crystallites and can either be closed or open to the atmosphere. In polycrystalline graphite made from a mixture of coal-tar pitch and petroleum coke filler particles, pores originate from various sources [164] and are generally classed into three categories, i. e. macro-pores ($>$ 50 nm), meso-pores (2-50 nm), and, micro-pores ($<$ 2 nm) [164]. In polycrystalline nuclear graphites, macro-pores are usually of most concern, since they have the greatest influence on graphite properties [16]. Micro-pores can be located between crystallites, graphitised coke particles and disorganised carbon [3].

A typical SEM image of a filler particle is shown in Figure 7.3 showing the pores and lenticular cracks in IM1-24. McEnaney & Mays [165] emphasised the importance of pore shapes on the bulk properties, where for example, long crack-like pores promote internal stress-concentration in the graphite lattice. It is also necessary to determine the total porosity, in terms of open and closed porosity, to fully evaluate the effect of porosity on thermal, physical and mechanical properties [16]. The open porosity is especially relevant when oxidation takes place. Porosity networks can provide for CO_{-3} corrosion pathways, which form the basis for radiolytic oxidation, through the moderator bricks. Without these pathways the mechanism of radiolytic oxidation would only result in erosion of the material on the surface and would not weaken the graphite internally. For this reason macro-pores are considered to be part of the external surface area.

Hodgkins et al. [19] utilised X-ray tomography (XRμT) to measure and map connected pore networks. In their study porosity was categorised into three groups:

- Open Porosity (Por_O)
- Closed Porosity (Por_C)
- Total Porosity (Por_T)

The first of these terms describes the percentage of porosity that is connected to the surface, either directly or by pathways through other pores and void space. The second term identifies the percentage that is not connected to the surface, where the total porosity signifies the combined open and closed porosity.

Hodgkins showed that typical IM1-24 has around $Por_T = 20\%$ porosity for a cylindrical sample (diameter of 9 mm with a height of 6 mm). Further they found that pore voxels, traced from the edge of the analysis box, connected with around $Por_O = 12\%$ of the total volume. This results in a volume of the unimpregnated porosity of approximately $Por_c = 8\%$. In addition they showed that, in the volume of the analysis box, none of the networks grew sufficiently large to connect opposite faces of the analysis box. However, in some cases they observed that the total open porosity exceeded $Por_O = 28\%$. An illustration of their porosity mapping is shown in Figure 7.3. It is worth noting that the authors expressed their concerns regarding the sensitivity of their analysis. The resolution limit of the XRμT system was 26 μm.

The effects of porosity in any material are complex. Porosity can act as a stress concentrator and hence eases the initiation of fracture, or conversely, can result in the blunting of the crack tip upon entering the pore (an effect that is said to reduce the crack tip stress intensity). However, Fazluddin [16] pointed another noteworthy role which concerns the deflection of the crack at the pore. As a result the crack path can become indirect and tortuous which is said to result in a combination of crack path deflection, secondary crack formation, crack branching, and crack tip blunting. All these fracture processes may enhance the crack growth resistance.

7.1.3 Discussion

It becomes clear from this brief review given on the observations of the microstructure and porosity, that cracking in polycrystalline graphite is associated with complex mechanisms. Existing cracks in the filler particles and between interface bonds, or faults in the ordering of the hexagonal graphite structure, all contribute to the fracture mechanisms and hence characteristics. Various researchers have identified cracking mechanisms in graphite, however, no conclusive relation between macro-cracking and micro-cracking processes has been made. At this point in literature, a FPZ and crack wake bridging effects have been identified [16, 4, 19, 15] as micro-cracks in the region ahead of the crack tip and as friction bridges behind the crack tip. An illustration by Hodgkins [4] (Figure 7.4)shows this. An opening and propagating crack is currently regarded as having a process zone, limited to where the fracture surface sides of the crack no longer interfere and beyond which micro-cracking dominates. The form and size of the FPZ and

crack tip wake effects is, however, still open to debate.

It is well known that quasi-brittle materials undergo some non-linearity during fracture due to the formation and propagation of a FPZ and crack tip wake effects at larger crack lengths [166]. In concrete for example, which is a typical quasi-brittle material, the FPZ has been defined as the zone in which the material undergoes softening damage ahead of the crack tip and wake effects have been attributed to bridging of the intact ligament faces of a developing crack [166]. The fracture mechanisms in concrete are well understood and several failure and fracture models exist, which account for the aforementioned non-linearity. Since fracture in graphite is associated with a similar non-linearity, it seems vital to fully understand these mechanisms so that a failure model may be formulated. Hence, the aim of this chapter is to further contribute to the understanding of the fracture processes associated with cracking in graphite and the link between micro- and macro-cracking. It is known that micro-cracking occurs prior to and during fracture in graphite, and that due to the crack tortuosity friction planes exist in the crack wake. However, there currently appears, in literature, to be a lack of understanding of these mechanisms; the size of the process zone, the micro-macro crack interaction and the crack tip wake effects. It is this, that this chapter aims to concentrate on before commencing onto a determination of graphite's fracture characteristics and the link to other quasi-brittle materials, such as concrete. Observed in this chapter, using the DT geometry, will be damage development prior to fracture, the crack initiation process and crack propagation.

7.2 Experimental Investigation Details

The experimental procedures used to observe the damage development, crack initiation and propagation utilised the following techniques: the aforementioned DT technique, ESPI and DIC. The DT technique proves highly useful here, as the technique allows for stable crack propagation at constant crack driving force. As a result, the constant stress intensity factor ensures a critical load irrespective of crack length for large crack lengths (up to 75mm) [31, 36].

The damage and fracture observations made use of 45 specimens, which were of the aforementioned grades, namely NBG10 and IM1-24 grade graphite. Since NBG10 has two distinct grain orientations, 15 specimens were tested with the

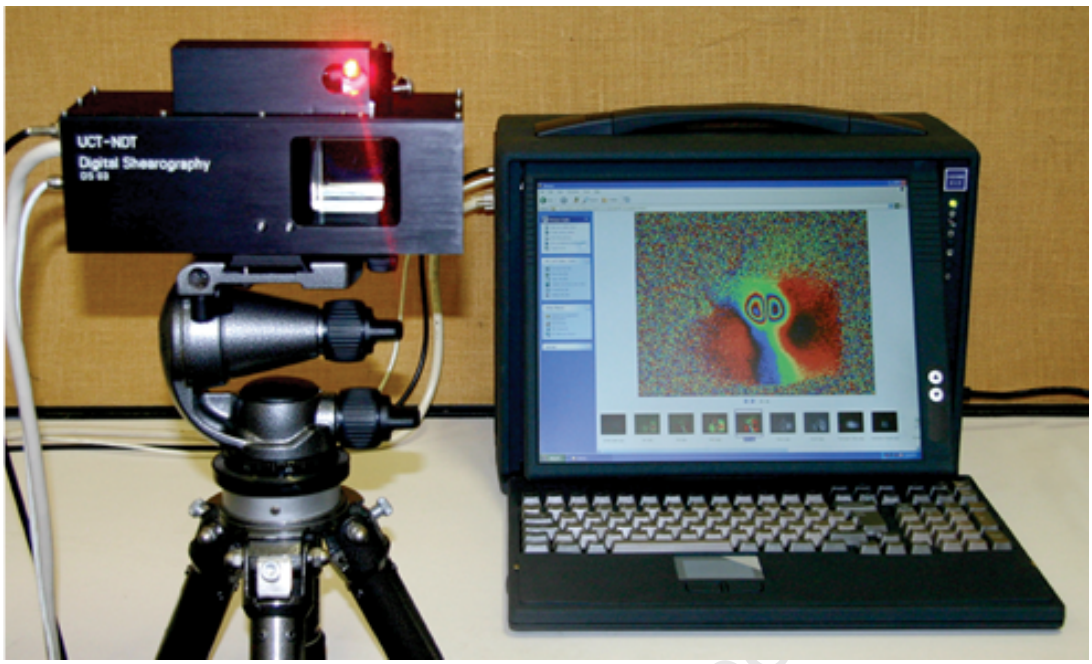

(a) ESPI setup used to monitor damage development prior to fracture at the University of Cape Town.

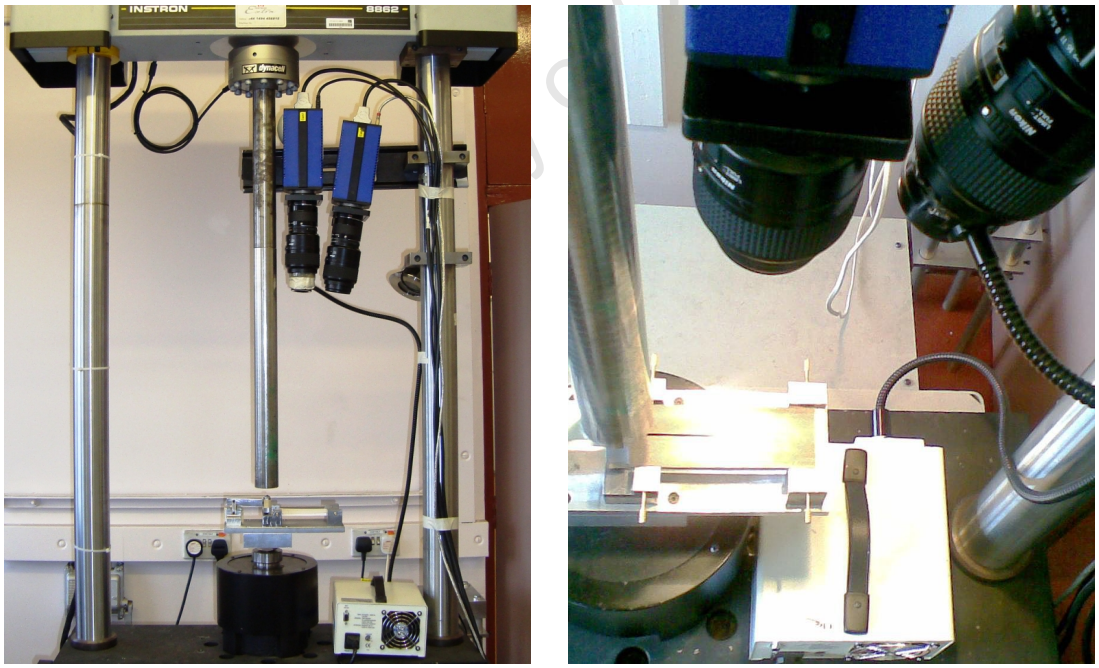

(b) Two camera DIC setup used at the University of Manchester. Shown also is the DT rig, loading configuration and light source. Shown is the complete setup and a bird's eye perspective of the test rig and loading configuration.

Figure 7.5

general extrusion direction (parallel) and 15 specimens were tested against the extrusion direction (perpendicular). The other 15 were specimens made from the IM1-24 grade graphite. For more specimen details the reader is referred to Chapter 5. ESPI tests were conducted in the Materials Department at the University of Cape Town (Figure 7.5a) and the DIC tests in the Materials Performance Centre in the School of Materials at the University of Manchester (Figure 7.5b). Tests were conducted according to the aforementioned methodologies described in Chapter 5.

7.2.1 DIC setup details

The DIC configuration for determining the displacement field included a two camera analysis, as the DT specimen experiences some out-of-plane deflections (as discussed in Chapter 5). A two camera setup enables the measurement of these out-of-plane displacements, and hence the in-plane displacements can be determined accurately [120]. In the camera system setup used (shown in Figure 7.5b), one pixel was approximately 25 µm, and the imaged area was approximately 50 x 50 mm. The displacement field was calculated relative to the centre of the image. The DT specimens were tested at 0.1 mm/min and 4 mm/min constant displacement rates, with various loading and unloading cycles applied. Details about the loading configurations are given in the next chapter, Chapter 8.

7.2.2 ESPI setup details

To perform ESPI measurements, a laser light illuminated the DT specimen with a working distance of approximately 100 mm, where the region scanned by the strain laser analyser was approximately 30 x 30 mm. The reflected light was combined with a reference light provided by the same laser source and speckle patterns from both were recorded by a high resolution video camera. These were processed to produce a fringe pattern by subtracting the two different speckle patterns [125]. This was analysed, with in-house software from the University of Cape Town, to determine the apparent in-plane displacements and hence the strain distribution on the specimen surface. It is worth mentioning that the DT specimen experiences some out-of-plane deflections. Since ESPI is affected by out-of-plane movements [127], the ESPI analysis was semi-quantitative. Only the size of the FPZ was extracted from the ESPI analysis, identified by fringe

discontinuities along the propagating crack.

7.3 Crack Initiation and Damage Development observations

To investigate the crack initiation and propagation in graphite, the observations have been split onto three main categories, namely damage development section and the propagation phase, which is divided into the fracture process zone and crack tip wake effects or crack tortuosity sections. During the damage development phase the formation of micro-cracks was observed ahead of the starter, where as during propagation the fracture process zone and crack tortuosity was studied.

7.3.1 Damage Development

The load displacement curve in Figure 7.6 shows the pre-peak nonlinear load response in NBG10 graphite (in the perpendicular orientation) and indicates the damage accumulation prior to any macro-crack propagation. It suggests that fracture does not occur at the peak load where the localisation of damage forms ahead of the notch (in the FPZ) prior to a single macro-crack [19]. ESPI observations below the load displacement curve show the development of such a FPZ at various points on the load displacement curve. These are typical holographic fringe patterns, showing the damage development from the notch tip prior to peak load. The damage development is visible as discontinuities in the fringe patterns. Kinks and distortions in the displacement fringes signify strain concentrations in those regions, while the fringe patterns elsewhere are continuous and smooth. The discontinuities form predominantly ahead of the notch tip indicating the development of a FPZ. A threshold of more than two fringe patterns per 2 x 2 mm square (in Figure 7.6) was arbitrarily adopted for the FPZ identification. It is worth mentioning that various other criteria were employed to quantify the FPZ with little consequence to the apparent FPZ size. It should also be noted that strain or displacement readings cannot be directly obtained from this experiment.

The fringe patterns shown at $^1/_3P_c$, $^2/_3P_c$, $^5/_6P_c$ and at the critical load point P_c in Figure 7.6a, (b), (c) and (d) illustrate the development of the FPZ prior to macro-crack propagation respectively. A sudden relaxation or pop-in can be observed in

the load-displacement curve at point (e) corresponding with the propagation of the FPZ (Figure 7.6e) indicating that a macro-crack has initiated. Once the FPZ has established, a macro-crack propagates from the notch (in the FPZ) and the extension of the macro-crack is accompanied by progression of the FPZ ahead of the macro-crack tip. During fracture several pop-in or load drops are observed in the load-displacement diagram (Figure 7.6f). These correspond to a sudden crack jump behaviour, which is further discussed in Chapter 8.

Some outliers of the strain localisation (i.e. localised strains significantly higher than the homogeneous strain expected at that location) were identified with increasing load. The majority of these strains increased linearly with applied load, where some contribute to the FPZ. These are indicative of local strain concentrations, probably owing to porosity. As the failure load was approached, more significant outliers developed at which point strain localisations within the FPZ appeared to coalesce before macro-crack propagation.

To gain further insight into damage development prior to fracture, DIC was utilised. DIC allows for accurate measurements of the in-plane surface displacement field and hence allows for the calculation of the maximum normal surface strain field at the surface [119]. It is worth mentioning that DIC calculates an average displacement over the chosen interrogation window and that the accuracy and precision of DIC are sensitive to the interrogation window size used to analyse the images [120]. Thus any strain localisations significantly smaller then the interrogation window are lost in the averaging process and cannot be identified. Images of the DIC obtained surface strain maps are shown in Figure 7.7, Figure 7.8 and Figure 7.9 for NBG10 in the parallel orientation, NBG10 in the perpendicular orientation and IM1-24 respectively.

Micro-cracking and the macro-crack have been described using the maximum normal surface strain field. Material which underwent more than a third of the maximum tensile strain (i.e. $\varepsilon < 0.06\%$, evaluated from the Young's modulus and tensile strength) may be said to have some damage, such as micro-cracking, where material which underwent more than 0.35% maximum normal strain is said to contain a macro-crack. This defines the approximate extent of micro-cracking and hence the FPZ. All strain measurements were undertaken relative to a zero load image.

These DIC analyses, at improved sensitivity of the strain mapping, show the same behaviour found from the ESPI observations. Figure 7.7, Figure 7.8 and

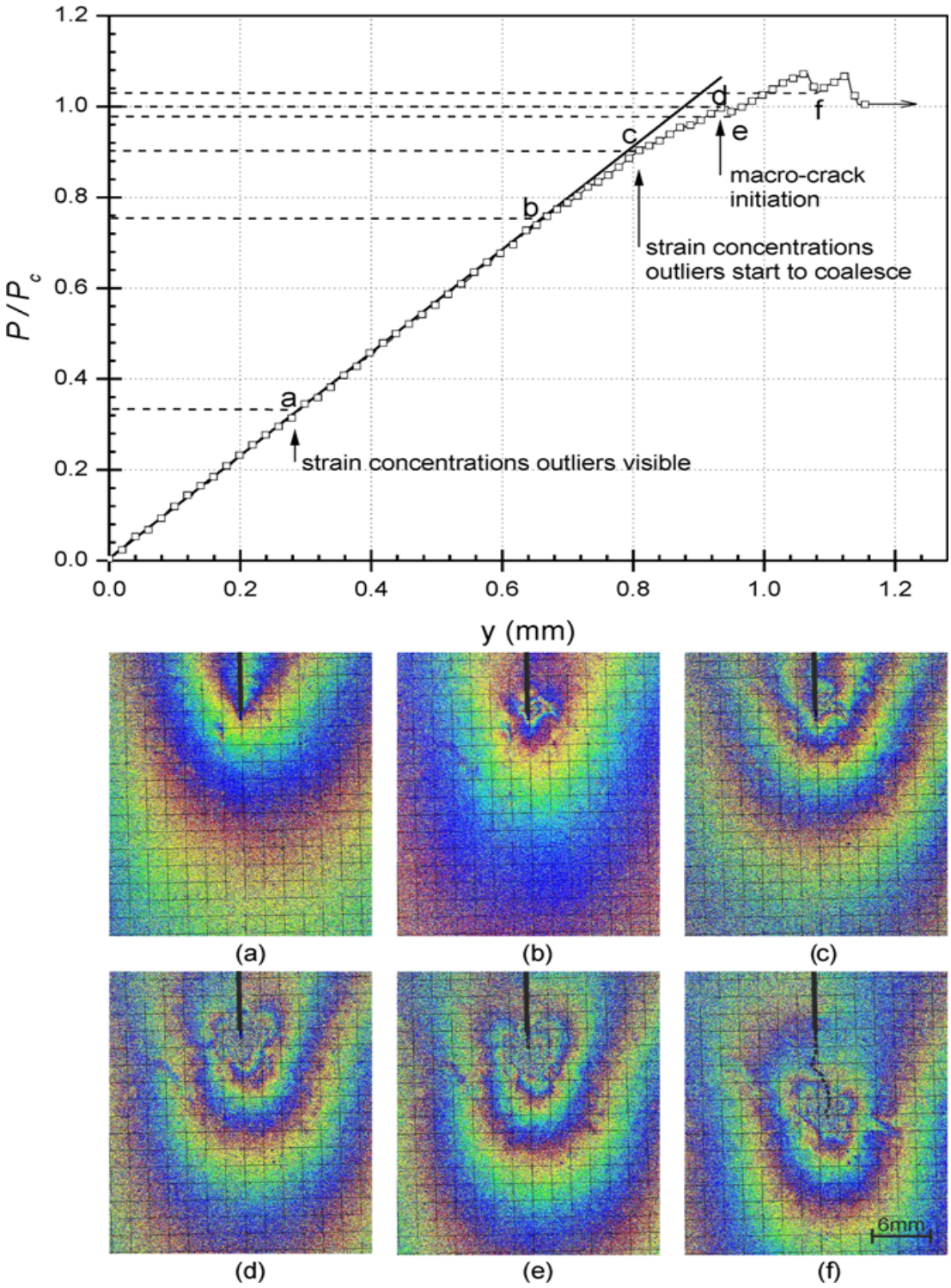

Figure 7.6 – ESPI observation of surface displacements ahead of the notch prior to a macro-crack initiation. The figure shows the load displacement curve and the corresponding images (a) to (f) taken during a constant displacement rate test of 0.1 mm/min for NBG10 graphite in the perpendicular orientation.

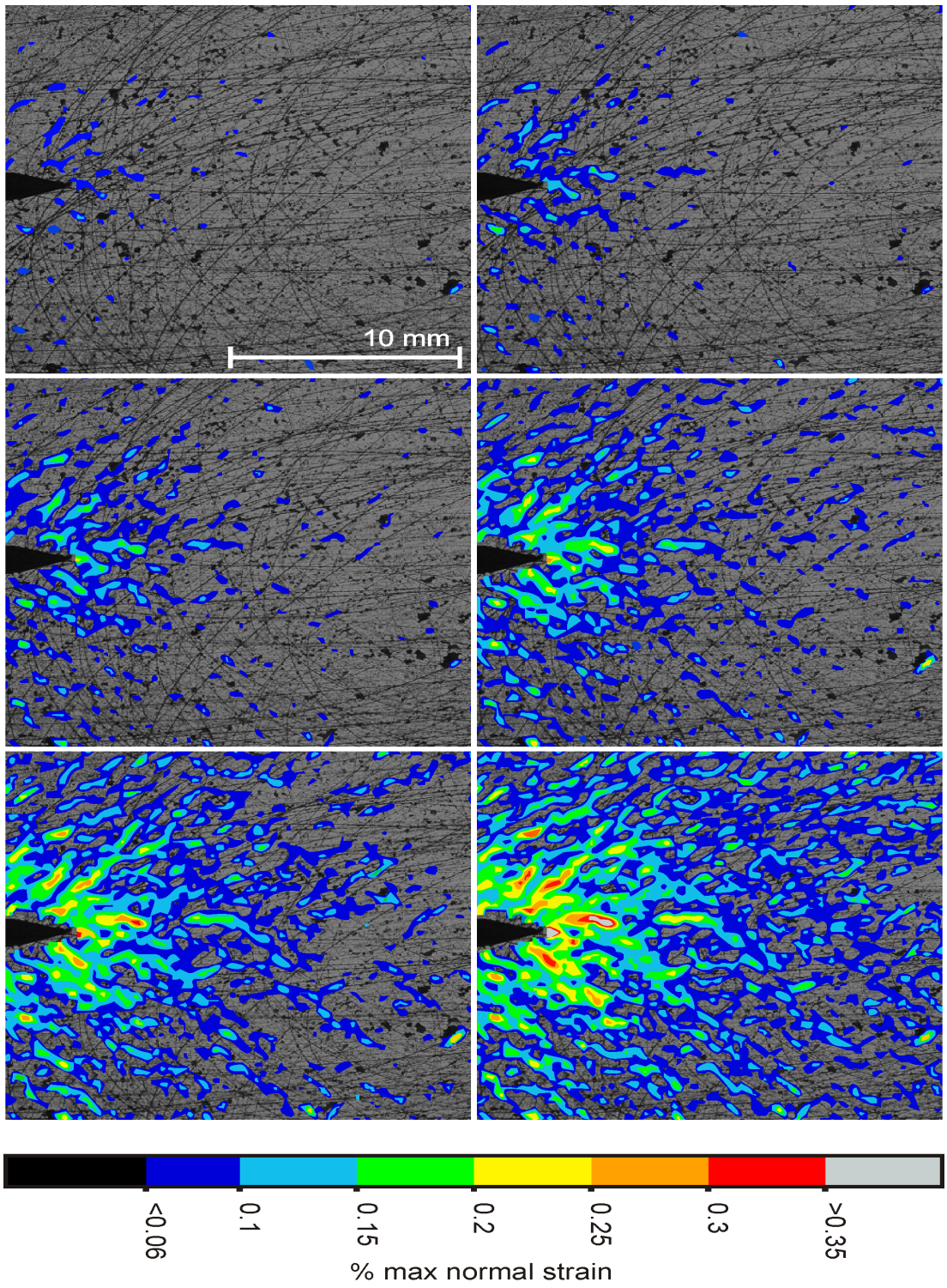

Figure 7.7 – Maximum normal strain mapping during damage initiation ahead of the starter notch. Material that has undergone more than 0.35% maximum normal strain is considered a macro-crack. The six figures show the damage development during a constant displacement rate (0.1 mm/min) tests in NBG10 in the parallel orientation. (DIC window size is 12x12 pixels with 25% overlap).

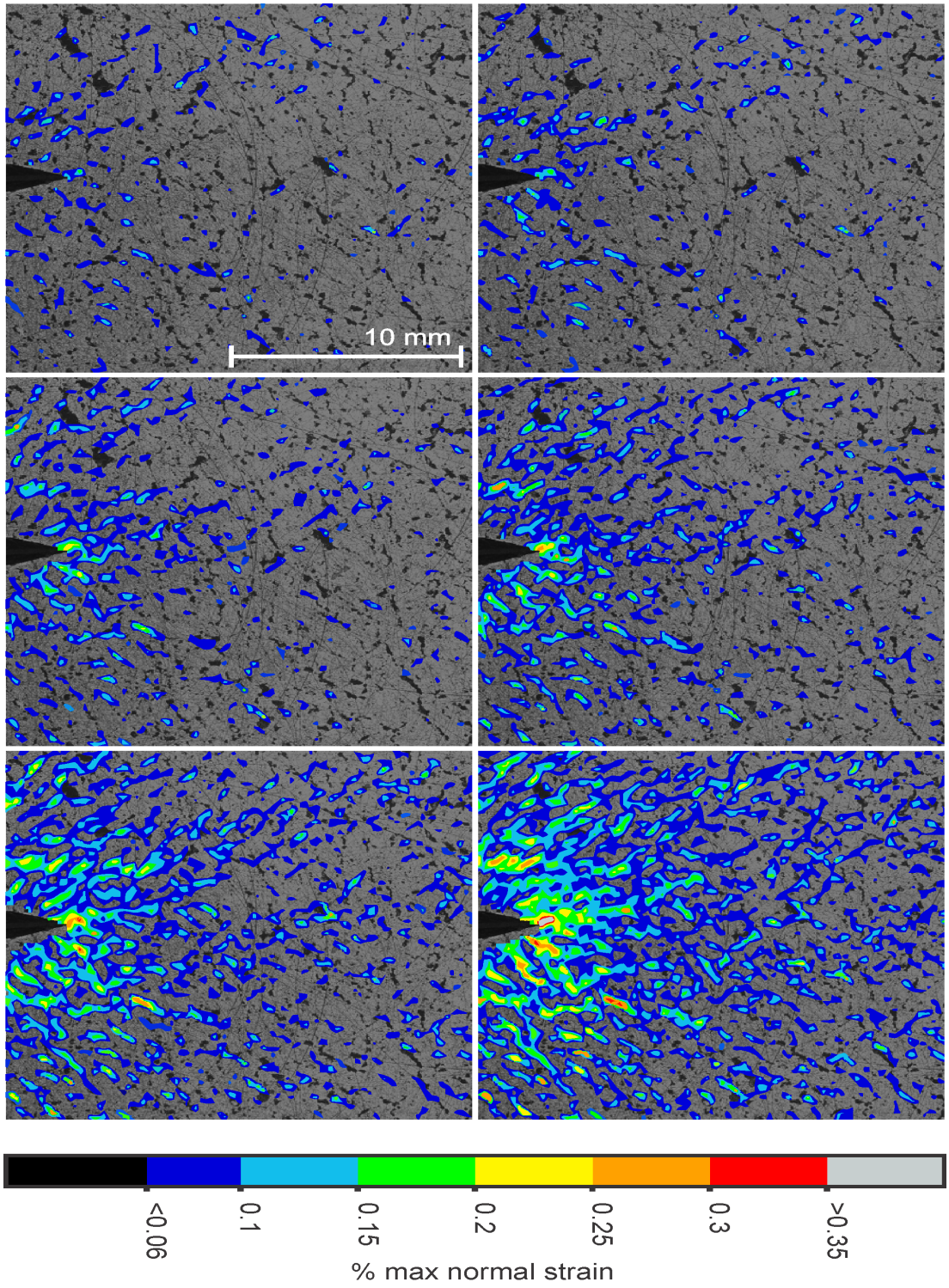

Figure 7.8 – Maximum normal strain mapping during damage initiation ahead of the starter notch. Material that has undergone more than 0.35% maximum normal strain is considered a macro-crack. The six figures show the damage development during a constant displacement rate (0.1 mm/min) tests in NBG10 in the perpendicular orientation. (DIC window size is 12x12 pixels with 25% overlap).

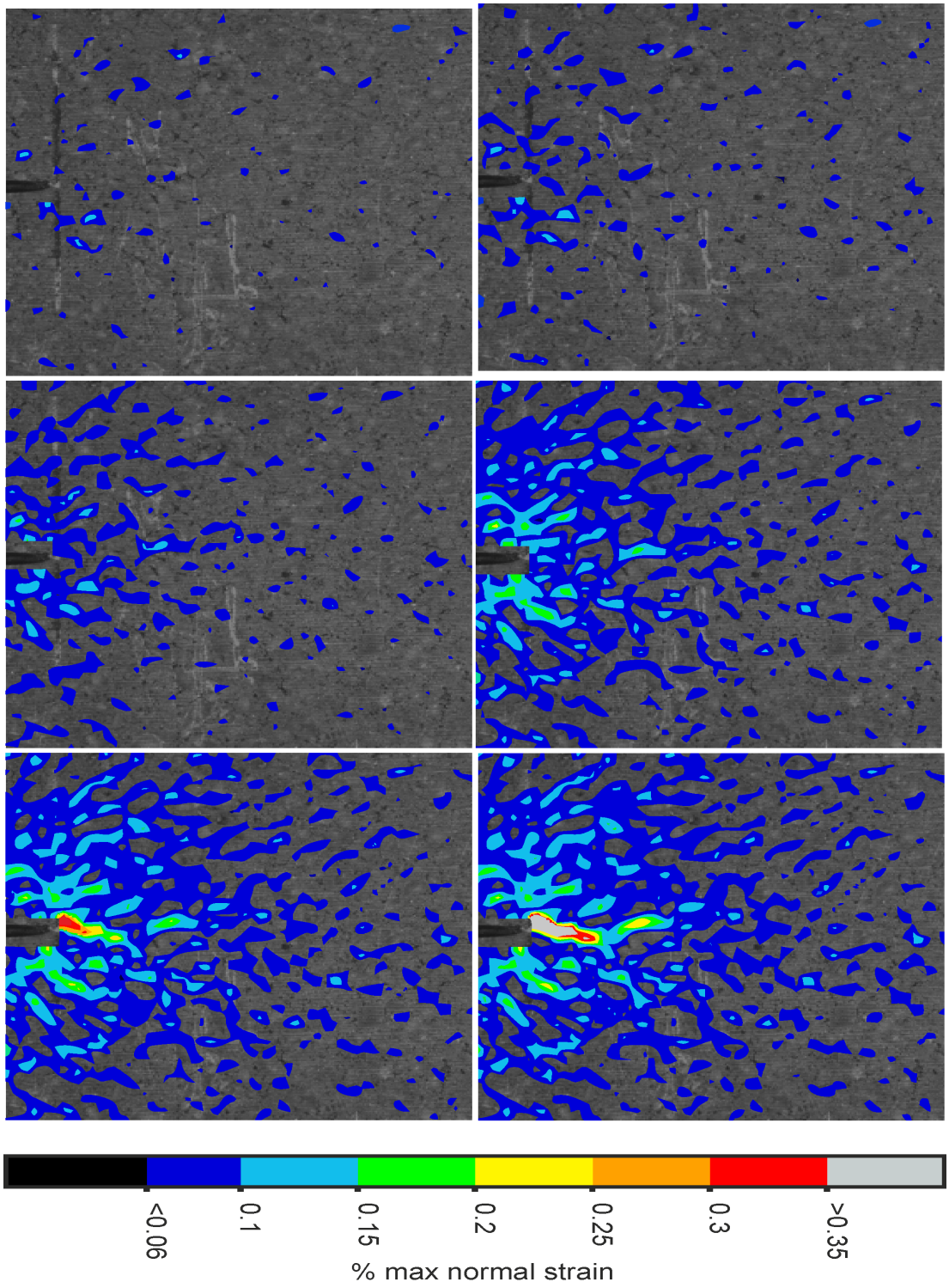

Figure 7.9 – Maximum normal strain mapping during damage initiation ahead of the starter notch. Material that has undergone more than 0.35% maximum normal strain is considered a macro-crack. The six figures show the damage development during a constant displacement rate (0.1 mm/min) tests in IM1-24. (DIC window size is 12x12 pixels with 25% overlap).

7.9 show micro-cracks that develop ahead of the notch tip which form the FPZ. Upon loading, cracks form along the crack direction plane and appear as localised strains and tend to be coincident with porosity. The visible behaviour of these cracks is such that micro-cracks grow in magnitude during loading. Larger micro-cracks form as micro-cracks coalesce. A critical point is reached when a macro-crack initiates from the notch. At this point several "macro-cracks" (defined as maximum normal strain $> 0.35\%$) may have formed head of the notch (this was especially found to be the case for NBG10 in the parallel orientation), which makes it difficult to define a crack tip.

The six images shown in Figure 7.7, Figure 7.8 and 7.9 correlate to load application of $0.3P_c$, $0.5P_c$, $0.7P_c$, $0.8P_c$, $0.9P_c$ and P_c respectively, at which point a macro-crack has initiated. The images show that strain concentrations are visible at $0.3P_c$, which may be classified as micro-cracking[17]. These grow in concentration and at around $0.7P_c$ to $0.8P_c$the strain concentrations start to coalesce to form bigger and more prominent cracks. It is at this point where most non-linearity occurs in the load displacement curve signifying the onset of fracture.

A significant difference in NBG10 between the two crack propagation orientations, i.e. with or against the grain, was observed in the way micro-cracks form. In both directions micro-cracking predominantly coincides with porosity. Since the porosity is predominantly orientated with the notch direction in the parallel orientation, a high density of relatively long micro-cracks form along the porosity and grain boundaries. However, in the perpendicular orientation these micro-cracks tent to be shorter and less prominent as the porosity is less favourably orientated. In IM1-24, the amount of high strain concentrations ($< 0.2\%$) compared to NBG10 is limited. There is less visible coalescence with micro-cracking in the identified FPZ prior to macro-crack initiation.

7.3.2 Fracture Process Zone

In contrast to the damage development investigations, the load displacement curve of a crack with existing FPZ (achieved through the loading of a pre-cracked specimen) shows no pre-peak nonlinear load response (Figure 7.10). This suggests brittle behaviour and can be explained due to the presence of the existent FPZ. Unlike the damage accumulation (by micro-cracking) prior to macro-crack propagation, a pre-cracked specimen does not require this energy to form the FPZ as the FPZ propagates with the crack. Instead, the behaviour is linear until

a critical point is reached and macro-crack propagation continues. ESPI observations below the load displacement curve show the propagation of the FPZ at various points on the load displacement curve. The fringe patterns are shown at approximately $1/3P_c$, P_c and at some point during fracture in Figure 7.10a, (b) and (c). Sudden relaxations can be observed throughout the load-displacement curve.

Figure 7.11, Figure 7.12 and Figure 7.13 show examples of the FPZs during crack propagation. These DIC images were obtained in a similar manner to the damage development observation images, where a threshold of $> 0.35\%$ normal strain signifies a macro-crack. Shown in each image is the propagating crack at three crack lengths (at the initiation stage, and during crack propagation at crack lengths of approximately 15 mm and 25 mm). A larger interrogation window (128 x 128 pixels with 75% overlap) was utilized for the strain mapping of the FPZ. This helps identify more clearly the gradients of strain associated with the FPZ as an average. The results are shown in Figure7.14 and show the subtle difference in the shape and size of the FPZ.

Figure 7.11, Figure 7.12 and Figure 7.13 clearly show the FPZ ahead of the crack tip in the two materials considered. Material discontinuities such as voids or grain boundaries contribute to apparent high strain localisations which can be observed at some considerable distance ahead of the apparent crack tip (of the order of 20 to 30 mm), as well as in the defined FPZ. Crack nucleation at discontinuities such as pores was also found by Joyce [82], who used high resolution ESPI mapping of surface deformations to observe damage development in the IM1-24 grade, under diametral compression loading. Hodgkins et al [4, 19] similarly observed diffuse micro-cracking using X-ray micro-tomography in the same material. Such micro-cracks would be expected to be aligned perpendicular to the maximum tensile stress [167], and examination of the FPZ in NGB10 in the parallel and perpendicular orientation (7.11 and Figure 7.12) shows that the general direction of the strain localisations caused to micro-cracks is predominantly parallel with the extrusion direction. The most significant difference is noticeable in 7.14 for NBG10 between the crack propagation with or against the general grain orientation. The "with grain" (parallel) orientation shows a longer and more narrow FPZ. This coheres with the observation that damage occurs along grain boundaries and porosity, where these are predominantly orientated with the crack propagation direction.

Additionally, the ESPI images can be utilised to estimate the FPZ size. Fig-

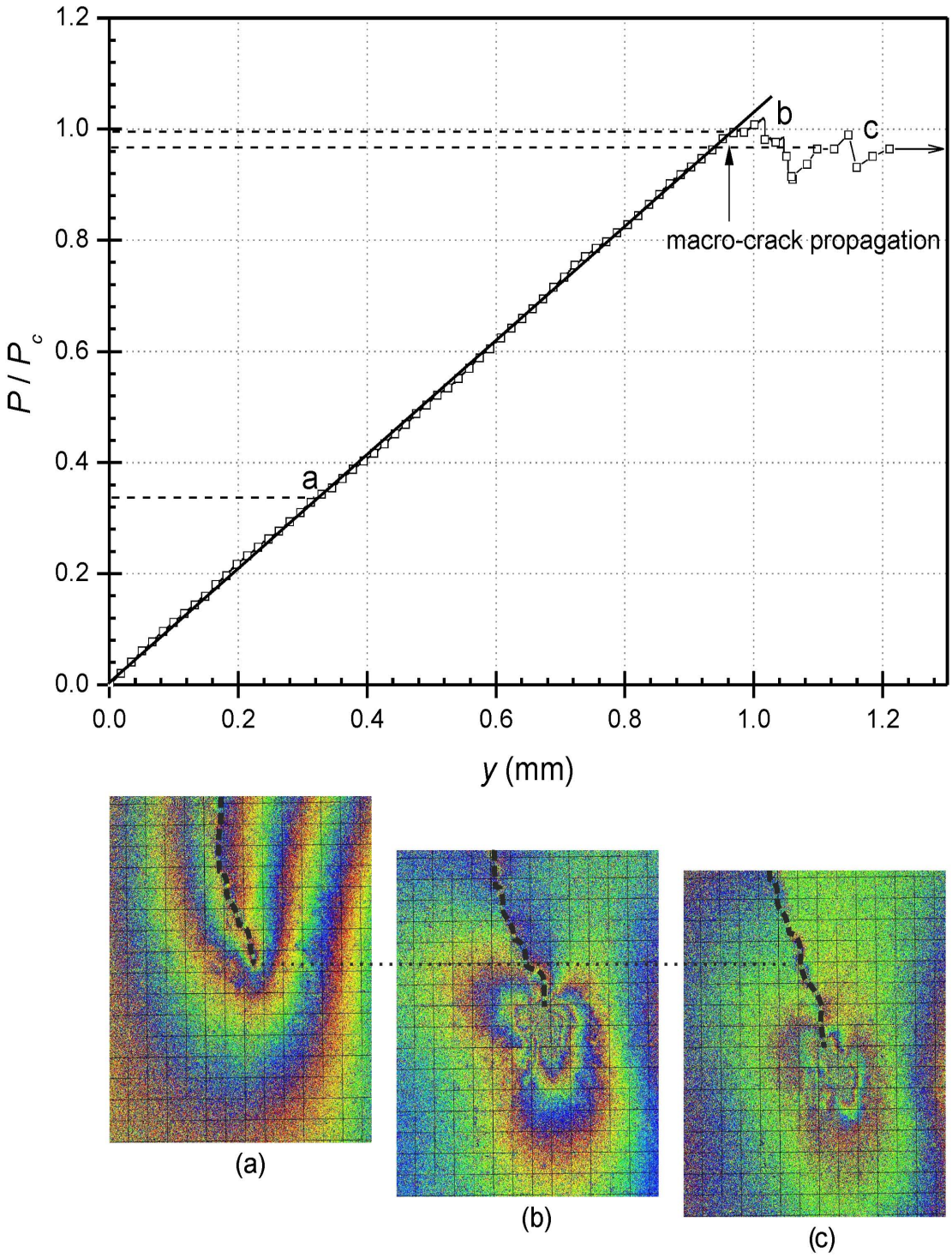

Figure 7.10 – Comparison of cracking paths and interactions with micro-structure: a) crack arrest at pores (NBG10), b) crack branching (NBG10) and c) crack bridging (IM1-24). In addition, the crack path and porosity interaction is visible.

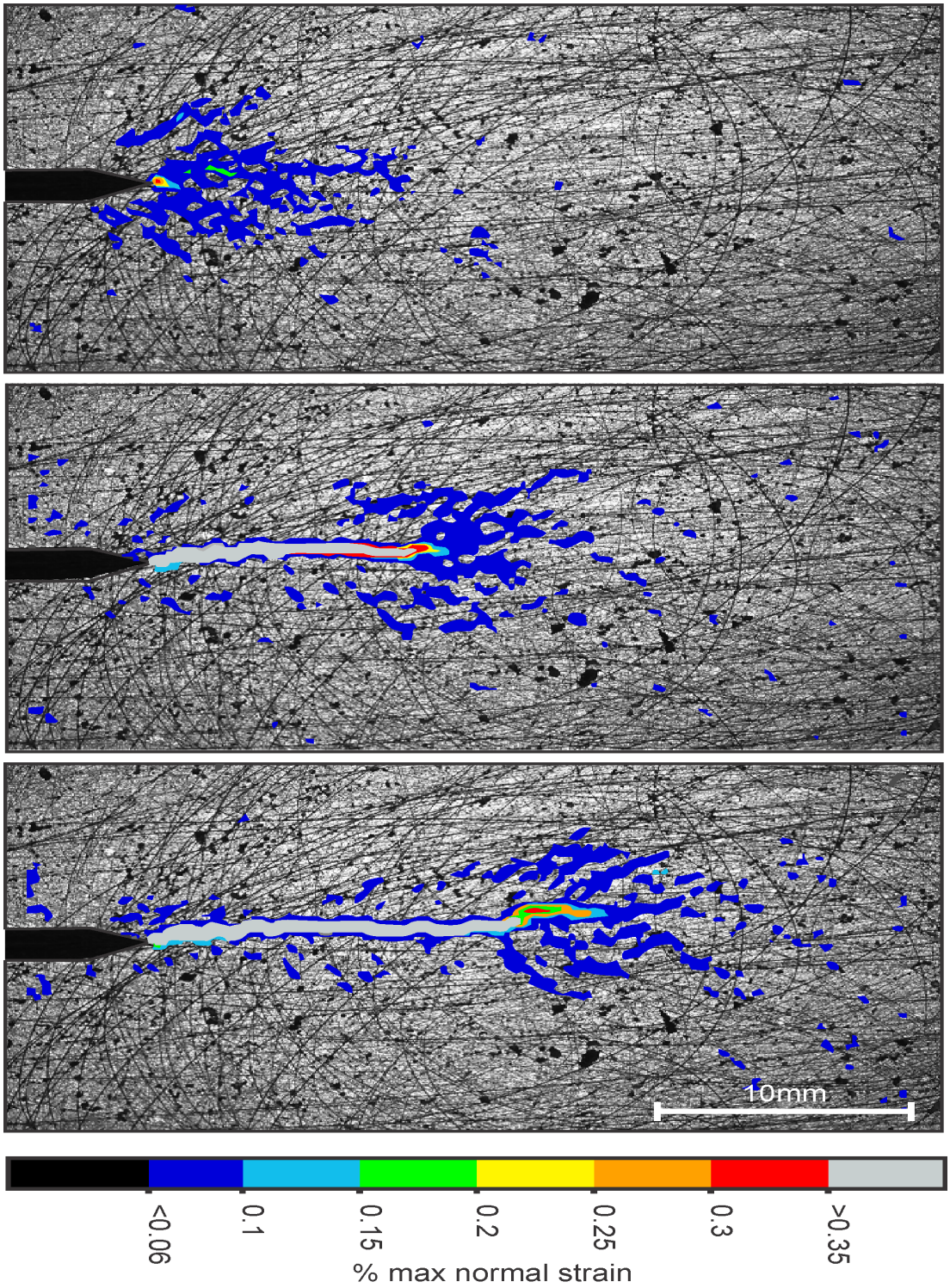

Figure 7.11 – Maximum normal strain mapping during crack propagation. Material that has undergone more than 0.35% maximum normal strain is considered a macro-crack. The three figures show the damage development during a constant displacement rate (0.1 mm/min) tests in NBG10 in the parallel orientation (DIC window size is 12x12 pixels with 25% overlap).

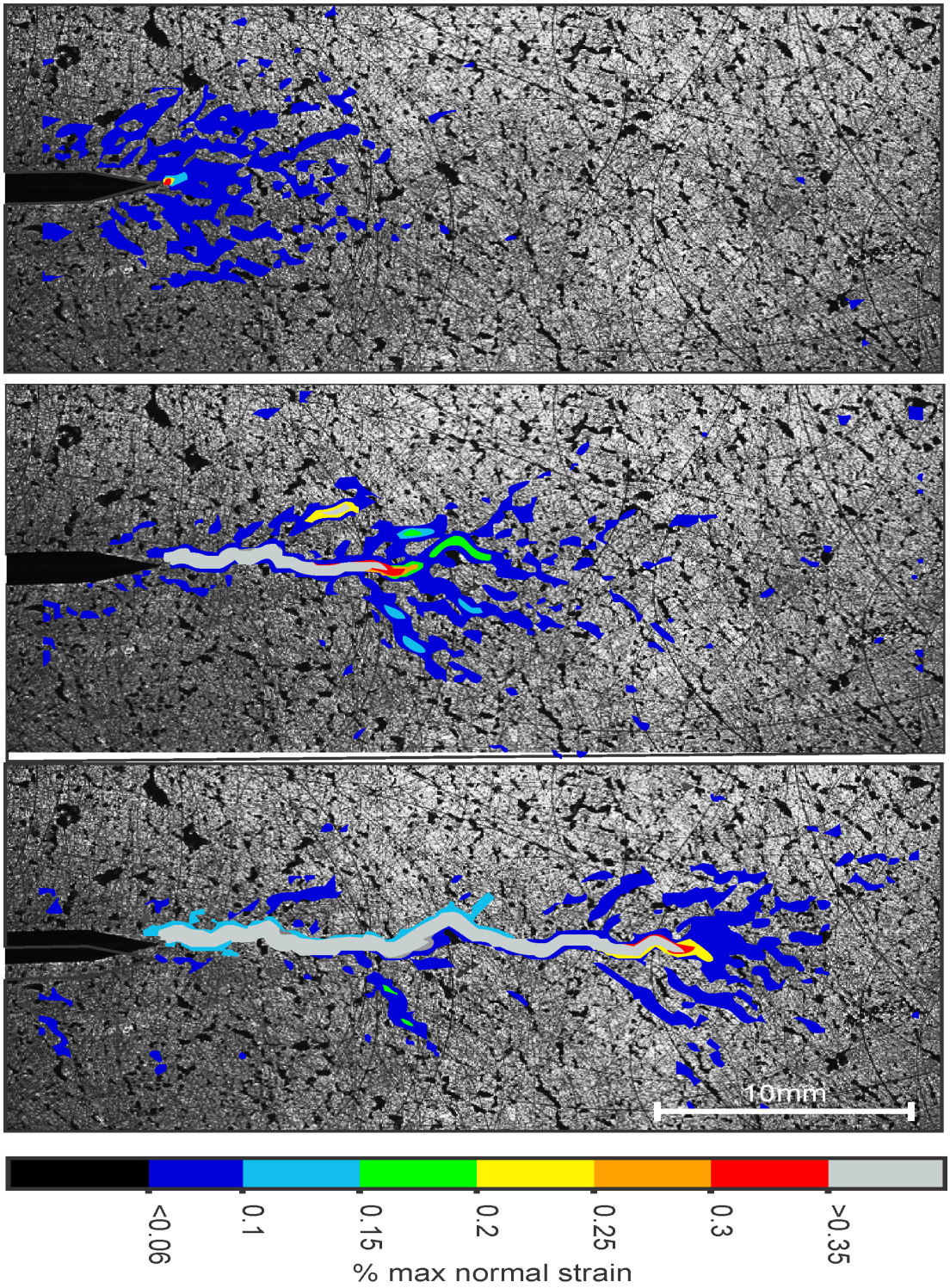

Figure 7.12 – Maximum normal strain mapping during crack propagation. Material that has undergone more than 0.35% maximum normal strain is considered a macro-crack. The three figures show the damage development during a constant displacement rate (0.1 mm/min) tests in NBG10 in the perpendicular orientation (DIC window size is 12x12 pixels with 25% overlap).

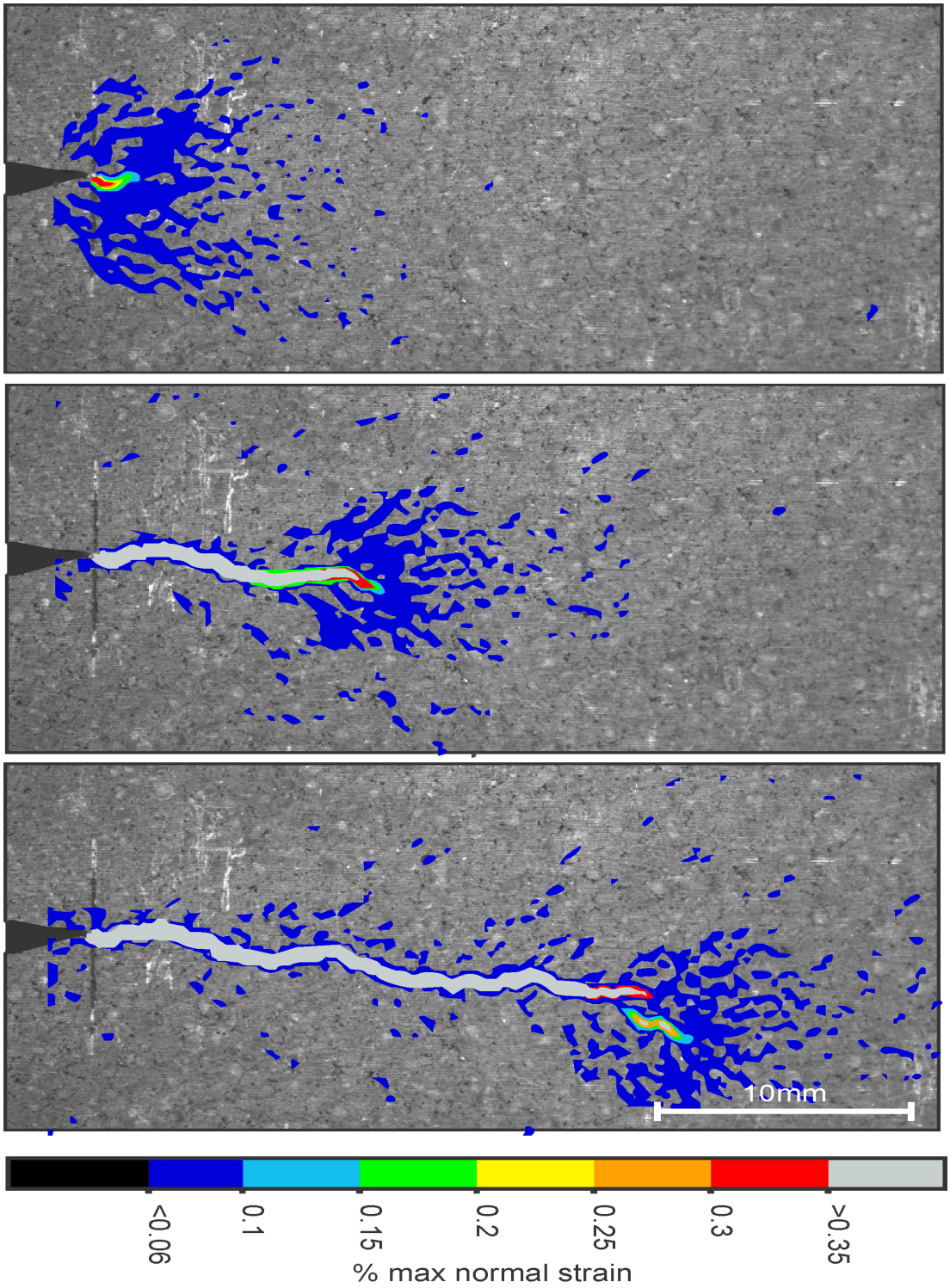

Figure 7.13 – Maximum normal strain mapping during crack propagation. Material that has undergone more than 0.35% maximum normal strain is considered a macro-crack. The three figures show the damage development during a constant displacement rate (0.1 mm/min) tests in IM1-24 (DIC window size is 12x12 pixels with 25% overlap).

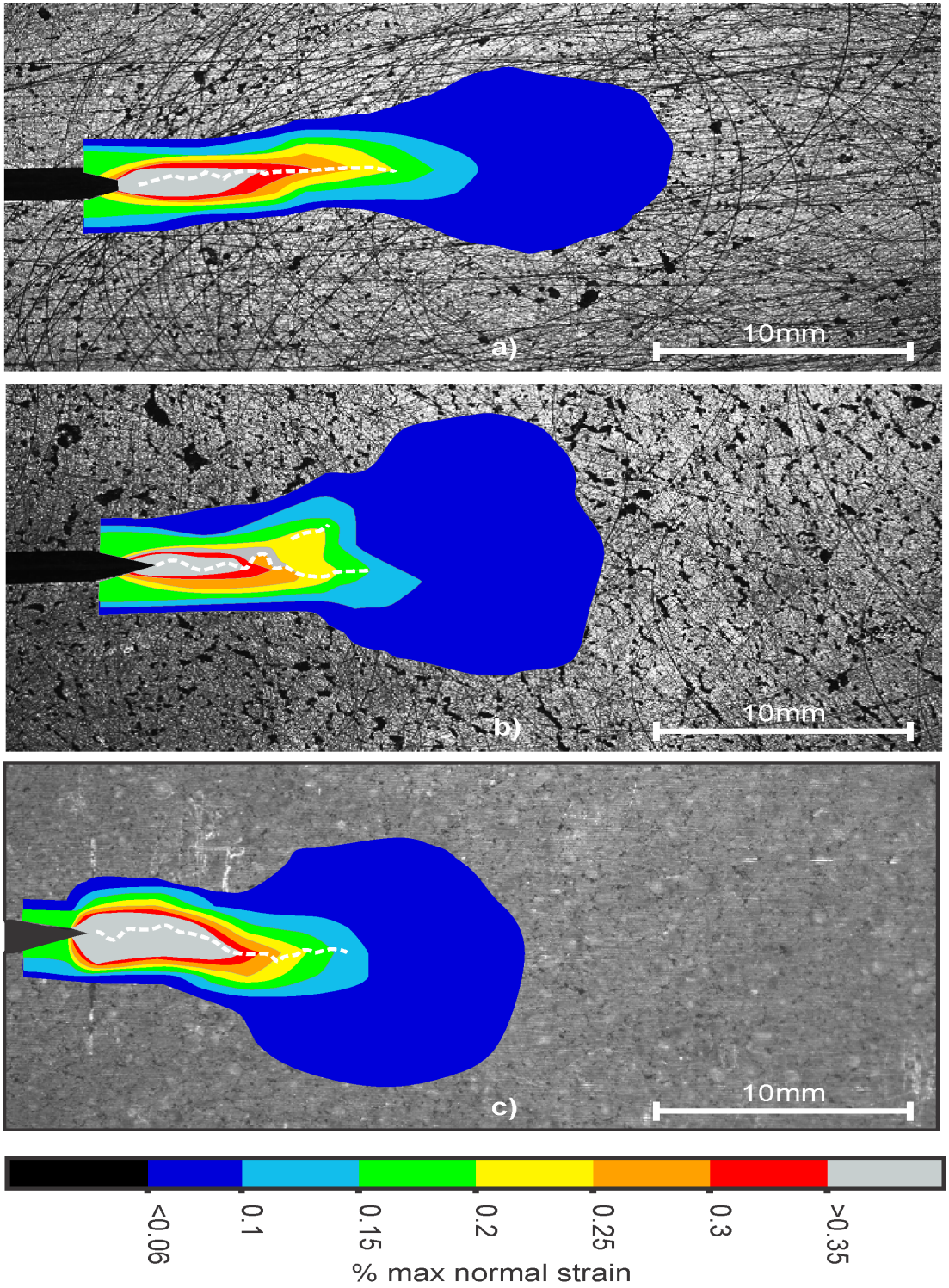

Figure 7.14 – Maximum normal strain mapping during crack propagation. Material that has undergone more than 0.35% maximum normal strain is considered a macro-crack. The three figures show the damage development during a constant displacement rate (0.1 mm/min) tests in IM1-24 (DIC window size is 12x12 pixels with 25% overlap).

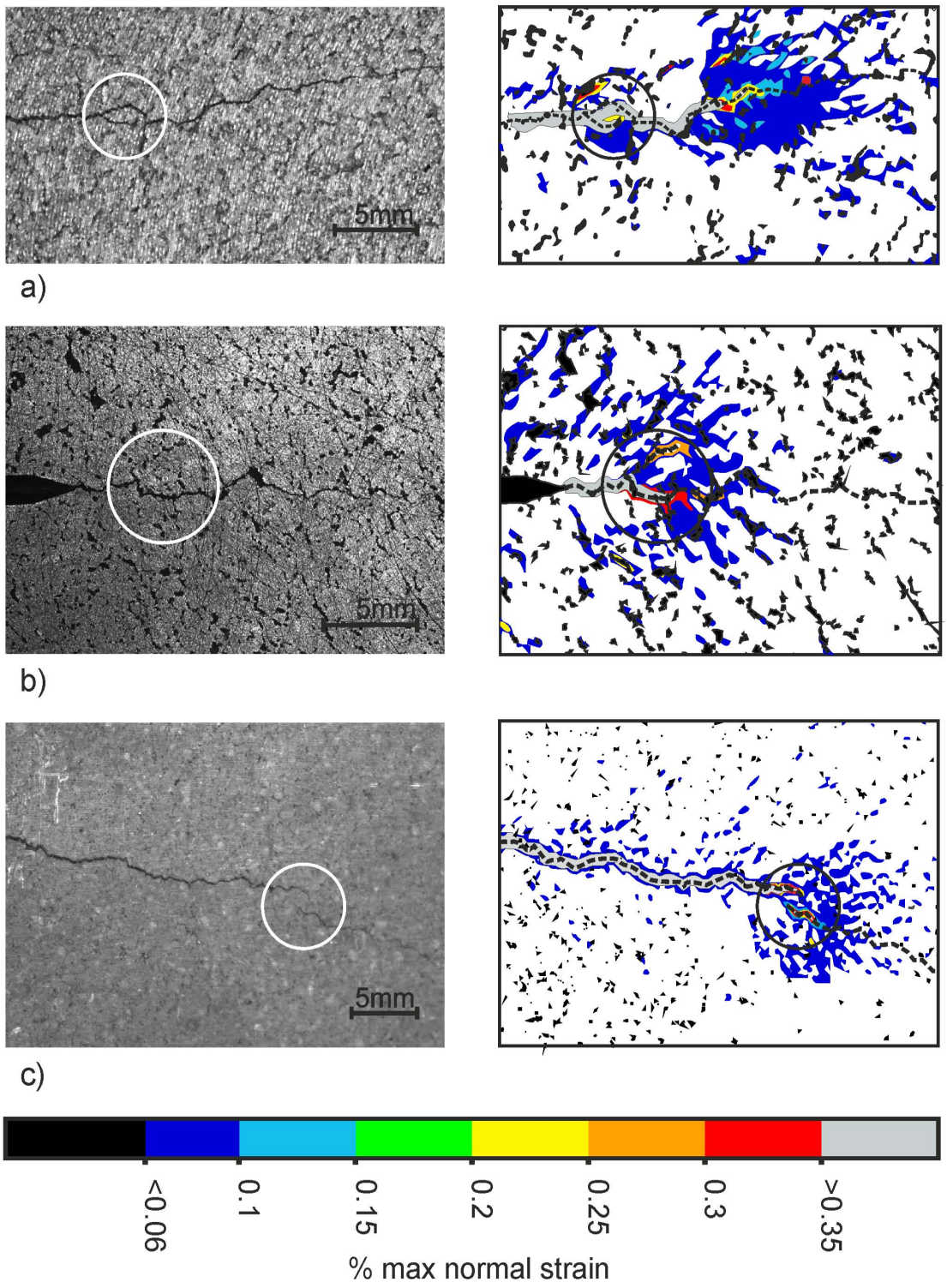

Figure 7.15 – Comparison of cracking paths and interactions with micro-structure: a) crack arrest at pores (NBG10), b) crack branching (NBG10) and c) crack bridging (IM1-24). The crack path and surface porosity are shown.

ure 7.16 illustrates this. The FPZ length ahead of the crack tip is estimated as a function of the crack opening displacement, during the first loading cycle of a typical DT test. The crack opening displacement was measured across the notch tip. The FPZ was found to be approximately 8 - 10 mm in size for both crack propagation directions in NBG 10 and also in IM1-24. However, comparison of the FPZ formation energy, approximated by the shaded region in Figure 7.16 (normalised by the sample thickness and the FPZ length), between NBG10 specimens of different orientation indicates that 10% more energy is required to form the FPZ prior to macro-crack initiation parallel to the extrusion direction (approximately 37 J/m^2), compared to crack propagation perpendicular to the extrusion direction (approximately 32 J/m^2). The recorded fracture initiation energy in IM1-24 was approximately 47 J/m^2. It is worth mentioning that this energy measurement is prior to any macro-crack extension and thus cannot be expressed as a J_R term. This measurement is mainly indicative of the damage softening prior to fracture. The size of this process zone of the ESPI and DIC observation are in agreement.

7.3.3 Crack Tortuosity

The crack path tortuosity shown in Figure 7.11 to Figure 7.13 indicates that the crack is likely to deflect along porosity that constitutes a crack path of least resistance. Crack deflection is considered to be a toughening mechanism. Non-planar cracks may create frictional surfaces that contribute to the overall fracture resistance during cracking. It has previously been observed in IM1-24 by X-ray tomography [19], that tortuosity of the crack path can give rise to crack bridging.

The most tortuous paths are observed for NBG10 with a crack propagating perpendicular to the extrusion direction (Figure 7.12), where crack propagation was observed to follow voids that were visible on the material surface. Cracks propagating parallel to the extrusion direction in NBG10 were found to coalesce with larger micro-cracks, although it is likely that such micro-cracks also initiated from porosity (Figure 7.11).

Three mechanisms of cracking may contribute to the crack tortuosity, namely; the formation of a secondary macro-crack, i.e. an arrested macro-crack due to a large pore which results in the formation of a secondary crack, bypassing the primary crack (Figure 7.15a), crack branching (Figure 7.15b) or crack bridging, where the crack has advanced beyond a grain boundary (Figure 7.15c). All these

mechanisms may affect the fracture resistance.

It follows that the fracture properties of nuclear graphite are strongly influenced by the heterogeneous structure, particularly the population and orientation of pores or flaws and grain orientation. These appear to significantly affect the FPZ and crack path/tortuosity. Micro-cracks that develop ahead of the crack tip lower the effective elastic modulus of the damaged material, and produce an inelastic or plastic strain. Crack tortuosity is an additional toughening mechanism.

7.4 Understanding the Mechanisms associated with Cracking in Nuclear Graphite

Nuclear or artificial graphite is a heterogeneous material consisting of filler particles, and a binder phase. Some graphite grades are anisotropic; where a preferred grain orientation is introduced through the manufacturing process. Internal voids ranging up to several millimetres in size may be regarded as another major component of the graphite fracture characteristsics. These voids may include pores, cracks or flaws [3].

These defects have been shown to play an important role in the mechanical behaviour of graphite [16, 19, 13]. The properties of graphite are influenced by its micro-, mezo- and macro-structures, which are characterised by the number and distribution of internal pores and cracks. The fracture process was shown to be influenced by the porosity and grain orientation of the material, where a macro-crack is primarily involved with the initiation and propagation of internal micro-cracks. It is worth mentioning that the size of these micro-cracks was not investigated. However, since the approximate size of existing flaws (prior to any load) ranges from the micro to the macro scale it follows logically that fracture processes are influenced by particles and voids in the same scale.

Heard et al. [17] showed that micro-cracking, can occur at loads of 30% of peak load and it was shown in this investigation that gross cracking between visible pores in the graphite material occurs around 70% of the peak load. The DIC observations, in agreement with Sakai, Fazluddin and Hodgkins, amongst others, have indicated that during the pre-peak, non-linear phase internal flaws initiate and propagate at existing discontinuities. These cracks are isolated and randomly distributed predominantly ahead of the notch tip and orthogonal to the tensile

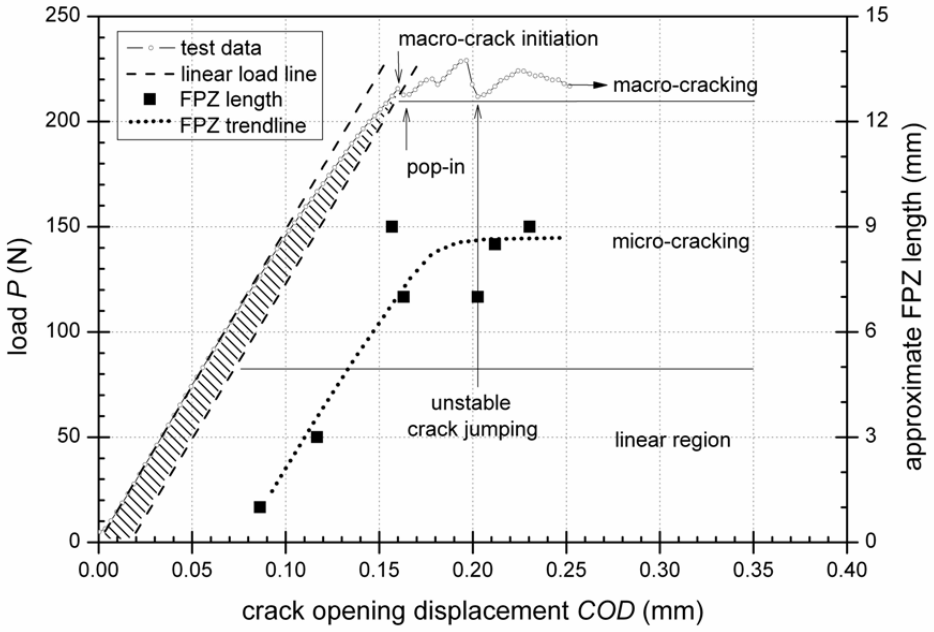

Figure 7.16 – Load and FPZ size as a function of crack opening displacement for the first loading cycle of a DT test in the NBG10 parallel orientation. The shaded region represents the energy required for the formation of the FPZ prior to macro-crack propagation. The size of the FPZ is approximated as the distance from the notch or macro-crack tip to the edge of the high strain concentration of fringe patterns.

strain in the loading direction. It is during this phase that most damage accumulates and ultimately the internal cracks start to localize into a macro-crack, which propagates with increasing load. These are visible as strain localisations when observed using ESPI or DIC and may be referred to as the FPZ.

When strain localization occurs, i.e. the FPZ forms, the distribution of tensile strain in the loading direction is no longer uniform. A critical point is reached when a macro-crack forms and propagation of this macro-crack is primarily associated with bridging or branching through the maze of micro-flaws. It is imperative to state that for the macro-crack to propagate a FPZ needs to be presents ahead of the crack tip. The reader is at this point referred back to Figures 7.7 to 7.13 which show the interaction and coalescence of strain localisations during fracture.

By the same rationality of the above argument, it follows that the interaction of micro-cracks in the micro-scale also influences the flaws in the mezo-scale and in turn on the macro-scale. Therefore, fracture processes in graphite may primarily

depend on the stability of these interfacial cracks.

Another factor to consider is the tortuosity of the macro-crack path. It was shown in this work and by previous researchers that crack deflection occurs when the path of least resistance is around a relatively stronger particle or along a weak interface like a void. Other cracking mechanisms, which were identified, include crack arresting, crack branching and crack bridging (Figure 7.15). These mechanisms are important toughening processes in graphite and these cause energy dissipation through friction planes.

This process is also present in quasi-brittle materials and investigations have focused on this zone, especially its size and its constituents [168]. The effects of these processes in the crack wake are such that one frequent question is whether the non-linearity's should be considered by the fracture process zone or crack wake. In concrete, Thouless [169] has shown that both approaches are equivalent as far as structural analysis is concerned; i.e. bridging and damage zones may be considered equivalent, but can give different physical insights. Based on their observations using laser holographic interferometry, Castro-Montero et al. [170] reported that the fracture process zone consisted of a wake zone behind the observed crack-tip and a zone in front of the tip. The wake process zone increased with crack extension, whereas the front zone remained primarily constant in size. Since size of the wake zone was much larger than that of the front zone, they concluded that most of the toughening in concrete occurs in the wake zone. This fact suggests that the increasing size of the wake process zone rather than the constant size of the crack-tip process zone should be primarily responsible for the growing R-curve behavior in concrete. Similar observations have been reported for silicon carbide [171] and in artificial graphite [13]. In this work, bridging effects in the wake were identified, some up to 20 to 30 mm behind the crack tip where, according to Hodgkins [4], crack bridging occurred at up to 55 mm behind the crack tip in CT specimens.

The experimental techniques utilised in this chapter have shown the brittle nature of graphite. From the observed non-linearity, which exists before the peak load (shown in Figure 7.16) and the micro-cracking prior and during macro-crack propagation, it can be deduced that the behaviour described is very comparable to that of other quasi-brittle materials.

7.5 Summary

This chapter presented the observations of mechanisms associated with crack growth. Presented were the observations of two distinct phases of cracking in graphite, namely the initiation phase or damage development prior to fracture and the propagation phase, split into two categories, the FPZ and crack tip wake effects or tortuosity. The full field surface displacement measurement techniques of ESPI and DIC were used to observe and measure crack initiation and propagation.

The observations show extensive micro-cracking ahead of the crack tip and crack tip wake effects such as crack bridging, crack branching and crack arresting. These mechanisms indicate the aforementioned quasi-brittle behaviour and strongly suggests that graphite is a quasi-brittle material. It was shown that grain structure and porosity play an important role in the way graphite fractures. Cracks tend to follow a path of least resistance and crack propagation was observed to follow voids that were visible on the material surface. Micro-cracks form in the crack direction plane and appear as localised strains which tend to be coincident with porosity and grain boundaries.

Prior to the initiation of the macro-crack the application of load produces a non-linear load displacement curve in test specimens. ESPI suggest that residual strains occur at isolated locations throughout the material with an increasing number of strain localisations ahead of the starter notch. DIC confirms that severe micro-structural damage occurs prior to macro-crack initiation ahead of the notch tip. Following the initiation and growth of the primary crack, a FPZ exists ahead of the crack tip which contains a high density of micro cracks. Some micro-cracking remains visible in the wake, yet most close after the macro-crack propagated past. The propagation in the FPZ is predominantly associated with crack bridging between micro-cracking and porosity.

The boundary of the micro crack zone observed, using ESPI, suggests that the size of this FPZ is approximately 10 mm in length and matches the surface strain field observed by DIC. Crack wake effects were observed in the first 20 mm of the crack and are predominantly comprised of crack bridging and branching. Following this evidence from DIC suggests that the crack is continuous.

Chapter 8

The Mechanisms of Crack Propagation and Failure

Chapter 7 has shown that the fracture of polycrystalline graphite is associated with extensive micro-cracking and slip deformations in the crack wake. These inelastic micro-cracking and plastic-slippage mechanisms have been shown to cause marked non-linearity in graphite behaviour and there have been attempts to classify these experimentally observed facts of mechanical non-linearity as Elastic Plastic Fracture Mechanics (EPFM) behaviour (similar to those experienced by some metals). The fracture mechanics route provides a powerful tool to assess the integrity of components and Chapter 2 introduced parameters to characterise and predict crack growth in materials using fracture mechanics. These parameters have specific definitions and are limited to those materials characterised by, in this case, non-linear (EPFM) fracture.

It is worth mentioning at this point that many previous studies have attempted to categorise fracture by either Linear Elastic Fracture Mechanics (LEFM) or EPFM. These have been discussed extensively in Chapter 3, however, many uncertainties concerning fracture and failure of nuclear graphite remain. It's currently understood that the fracture toughness of nuclear graphite seems to be around 1 to 2 $MPa\sqrt{m}$. There seems to be a dependency of crack length or rather the wake region of the crack tip and the FPZ on the fracture behaviour. Standard methods for fracture toughness measurements do not agree with each other and often a wide range for fracture toughness values have been reported. For IM1-24, for example, various specimen configurations ranging from Compact Tension (CT), Single Edge Notched Beam (SENB) to Chevron Notched

Short Rod (CNSR) specimens have reported a range of fracture toughness from $1.8MPa\sqrt{m}$ [4], $1.2MPa\sqrt{m}$ [45] to $0.9MPa\sqrt{m}$ [14]. Additionally, due to the non-linear behaviour many efforts have been made to characterise fracture by R-curve behaviour. This has lead to the generation of different R-curves and at present there is no universal agreement as to which, if any, of the techniques employed in these studies is a true material property and appropriate for characterising graphite's fracture behaviour. At this point in time, the fracture mechanics based methodologies have not managed to adequately describe and predict the crack propagation behaviour in graphite for a variety of geometries using fracture mechanics.

One of the main problems with assessing fracture characteristics of graphite is its brittle tendency. With standard test geometries, such a SENB, it can prove difficult to achieve stable controlled cracking to do the necessary measurements. The problem of propagating cracks controllably in nuclear graphite was addressed by Shi et al[45], who used "sandwiched" three-point bending specimens for the determination of fracture toughness parameters and R-curve behaviour. The sandwiched specimens allowed them to pre-crack brittle specimens to a certain length in a controlled manner as the outer steel beams would maintain the overall rigidity of the setup, or compliance. Their stable crack length range was reported at 1 mm to 2 mm, however, they had to account for frictional losses between the steel beams and the graphite, which were established by means of a finite element analysis. It is for this reason that the Double Torsion (DT) technique came to mind. The DT configuration is well suited for studies of fracture and slow crack growth characteristics of highly brittle materials. The technique allows for stable controlled crack growth, irrespective of how brittle the material is, for relatively large stable crack extensions (e.g. up to 75 mm for a specimen of 150 mm length) and also allows for easy crack tip observations, due to the way the specimen is loaded. It is worth mentioning that the DT technique is yet to be standardised and there has been limited application to elastic-plastic fracture mechanics conditions (EPFM).

The choice of the DT specimen is thus fairly evident; a specimen geometry that facilitates slow crack growth studies in brittle materials and allows for controlled crack propagation at critical load. Since graphite cracking can be unstable due to the non-linearity associated with micro-cracking, this constant Stress Intensity Factor (SIF) type specimen is essential. In addition, the geometry is fairly simple to prepare and analyse.

The principal purpose of the experiments described in this chapter is to address the key issues surrounding the current state of fracture property determination in nuclear graphite using the DT technique.

1. The first is to establish the LEFM fracture criterion of graphite using the DT technique. This includes fracture toughness and crack velocity versus stress intensity (VK) relationship data. Although it had been established that an LEFM fracture criterion may not be valid for graphite fracture, it is believed that some insight may be gained in the understanding of fracture in graphite nevertheless. VK relationship data can provide insight into the stability of fracture.

2. What are the EPFM fracture parameters and how do these compare to the trends obtained by the LEFM methodology. Is EPFM the most appropriate fracture parameter for characterising fracture in graphite? More specifically, is R-curve behaviour an intrinsic material property that captures the characteristics associated with fracture?

3. Do the observed mechanisms associated with cracking correlate with the fracture behaviour determined in this chapter? Are the observed mechanisms responsible for rising crack growth resistance and over what range of crack lengths are the mechanisms observed?

4. Can fracture mechanics provide a tool for characterising fracture/failure of virgin nuclear graphite.

An attempt to answer these questions is made through the following experimental investigation (in conjunction with the observation made in the previous chapter). The DT method is applied to study the two medium grained graphites in order to establish the criteria for crack nucleation and propagation in such materials. Since the DT technique is not currently capable of measuring EPFM parameters, a modification is proposed to the technique using Sakai's energy principle [14]. This is presented in the next section. A novel methodology for directly calculating the R-curve behaviour from the surface displacement field, introduced in Chapter 6, is employed.

8.1 Experimental Investigation Details

The experimental procedures used to determine the fracture characteristics utilised the following techniques: the aforementioned DT technique (introduced, reviewed and evaluated in Chapter 5), adapted here to account for elastic fracture mechanics and Digital Image Correlation (DIC) in conjunction with the JMAN methodology (described in Chapter 6). The crack propagation characteristics investigation was undertaken in parallel with the observation of mechanisms associated with crack growth in the previous chapter. This made use of 45 specimens, which were of the aforementioned grades, namely NBG10 and IM1-24 grade graphite. Since NBG10 has two distinct grain orientations, 15 specimens were tested with the general extrusion direction (parallel) and 15 specimens were tested against the extrusion direction (perpendicular). The other 15 were specimens made from the IM1-24 grade graphite. For more specimen details the reader is referred to Chapter 5. A figure of the laboratory setup is shown in Chapter 7 in Figure 7.5b.

8.1.1 Double Torsion Technique Testing

The DT technique has been introduced and critically reviewed in Chapter 5. The testing configuration was utilised for static tests under constant position control for VK relationship investigations and steady ramping tests to initiate and propagate cracks in a controlled manner. A modified approach for the DT methodology is proposed to account for graphite's non-linearity. This EPFM adaption is based on Sakai's energy principle and is described below, following the details of the experimental procedure.

8.1.2 Adaptation of the DT Geometry for Elastic Plastic Fracture Mechanics

Since graphite deformations are associated with non-linear mechanisms, the DT technique is adapted to account for this. At this juncture it bares mention that it is not assumed that graphite undergoes plastic deformations in the sense of ductile metallic materials. The FPZ and wake region have shown to result in irreversible energy dissipation during fracture and this energy, in its totality, can be measured accordingly. Sakai et al [14] used an approach for the determination of EPFM fracture parameters (i.e. the energy lost due to the irreversible energy

dissipation) under the assumption that these "plastic" deformations contribute to Griffiths modified energy balance. Again, the term "plastic" energy is used very loosely here and in a sense refers to the irreversible energy dissipation due to the FPZ and wake region.

The net rate of change of work input ΔW, relates to the rate of change of internal elastic energy ΔU_{el}, the rate of change of internal "plastic" energy ΔU_{pl} and the rate of change in surface energy ΔU_{γ} with the extension of the crack.

$$\Delta W = \Delta U_{el} + \Delta U_{pl} + \Delta U_{\gamma} \tag{8.1}$$

This empirical/graphical approach, allows one to calculate the energies associated with crack propagation. Adapted for the DT geometry, this technique makes use of cyclic loading and unloading where J_{el}, J_{pl} and J_R are obtained experimentally from the areas between the loading and unloading curves for crack extension area ΔA. In other words the work done by the mechanical testing machine is measured. If ΔA is small, this energy divided by ΔA is equivalent to the crack growth resistance J_R. In Figure 8.1 $\Delta\pi_J$ and $\Delta\pi_p$ are the linear elastic and non-linear plastic contributions to π_R respectively and W_{wof} is the work of fracture as a function of advancing crack length according to

$$J_R \equiv area(BAED) = \frac{\Delta\pi_R}{\Delta A} = \frac{\Delta}{\Delta A}(W - U_{el})_c \tag{8.2}$$

$$J_{el} \equiv area(BAE') = \frac{\Delta\pi_J}{\Delta A} = \frac{\Delta}{\Delta A}(W - U_{el} - U_{pl})_c \tag{8.3}$$

$$J_{pl} \equiv area(BE'ED) = \frac{\Delta\pi_p}{\Delta A} = \frac{\Delta U_p}{\Delta A} \tag{8.4}$$

$$2W_{wof} = \frac{\int_0^S J_R(A)dA}{A} \tag{8.5}$$

ΔA is approximated by $\Delta A = \Delta a \cdot d$, as the crack front shape has been previously shown to remain constant for the DT specimen geometry in a range of materials [91, 105, 31, 35, 172, 95].

The J-integral represents the strain energy release rate or energy per unit fracture surface area in a material and may be measured here as the fracture resistance J_R. J_R represents the energy required to propagate the crack complete with FPZ and wake region. The above methodology establishes the difference between the linear and non-linear contributions to J_R. J_{el} represents the energy associated

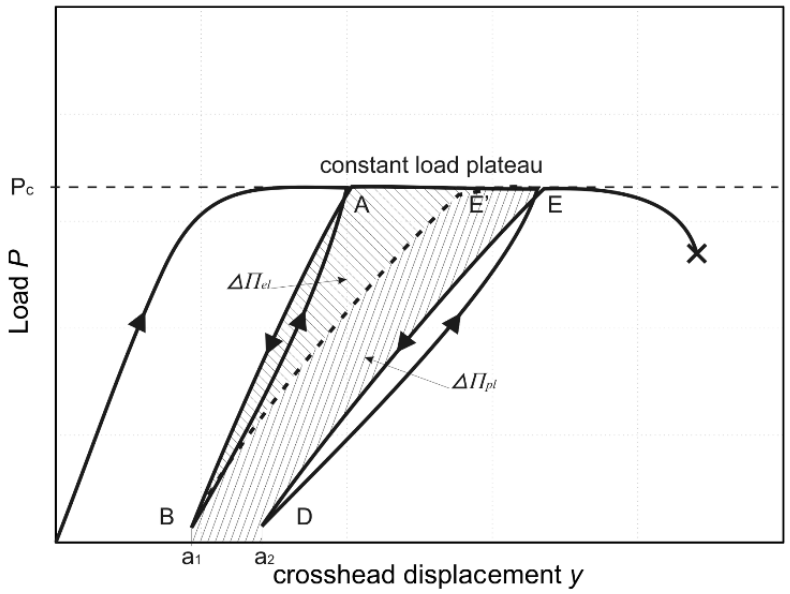

Figure 8.1 – Illustration of idealised load vs. cross head displacement for an elastic plastic body (EPFM) for the evaluation of J_{el}, J_{pl}, J_R and w_{wof} using the DT technique. Loading and unloading paths are shown as ↑ and ↓ respectively.

with the formation of the macro-crack. The slope of the loading and unloading curves is solely dependent on the specimen compliance, which is only dependent on the crack length on the DT geometry. Hence, the hysteresis is a measure of the energy lost due to "plasticity", or more correctly the irreversible energy dissipation.

Given that Sakai reported up to 40% irreversible, so called "plastic", energy dissipation during fracture in Chevron Notched specimens [14] and the scatter of reported fracture toughness, a measure of the elastic linear contribution can provide a more reliable measure of the fracture toughness as the "plastic" contribution may not necessarily be a material constant. In some cases the non-linear plastic contributions in J_R, for example in metallic materials, are said to be geometry dependent [6, 173]. This is discussed later. The adapted methodology outlined above for determining fracture resistance values J_R will be referred to as the DT methodology in this text.

8.1.3 R-curve

One way to more realistically characterise the crack propagation behaviour of quasi-brittle materials is by determining the R-curve of the given material [166]. The R-curve behaviour of several artificial graphite grades, including IM1-24, have been previously investigated [14, 4, 15, 16]. The R-curve is a measure of crack propagation resistance with respect to crack extension and to obtain this curve experimentally, stable crack growth is required. Albuquerque et al. [39] were the first to discuss the R-curve behaviour using the DT technique. The material tests made use of a ceramic tile material. They refer to their methodology as the energetic method and, similar to Sakai's methodology, they calculate the area underneath the load displacement curve. However, they do not use the loading and unloading methodology and simply assume perfect linear elasticity and hence take their zero load-displacement point as the unloading point, i.e. the lower reversal point. The EPFM adapted DT methodology, however includes the lower reversal points and thus incorporates non linearity.

The evaluation of the R-curve behaviour was attempted at three different starter notch lengths of 20 mm, 40 mm and 60 mm respectively at slow cross head speeds of 0.1 mm/min. The adapted DT methodology in conjunction with JMAN was employed to categorise the R-curve behaviour accordingly.

8.1.4 Detecting and Measuring Crack Propagation

Three crack tip monitoring techniques were employed. The first method utilised a microscope mounted on a sliding mechanism, which enabled the measurement of crack lengths to 0.2 mm accuracy. This rather crude method was useful for observing the crack tip for compliance calibration tests. Further monitoring methods were the Electronic Speckle Pattern Interferometry (ESPI) and DIC techniques. These were primarily used for damage and crack propagation observations (Chapter 7), however they also provided the ability to undertake accurate crack length measurements. It is worth mentioning that the maximum crack extension in the DT geometry occurs on the tensile surface due to the way the specimen is loaded. Thus, measuring the crack length on the surface provided sufficient information for compliance, VK relationship data and R-curve investigations. Crack propagation could also be monitored, in experiments of this type, by a fall in the applied load according to ASTM E1820. This is discussed further at a later stage in this

chapter.

8.2 Crack Propagation Characteristics

The investigation of the crack propagation characteristic is split into three sections; the first section discusses general observed crack propagation aspects and the compliance calibration. This is followed by LEFM results, where the determined fracture toughness and VK relationship properties are given. The EPFM results are given followed by discussion.

8.2.1 Controlled Crack Propagation

An example of a load-displacement curve at a ramp rate of 4 mm/min obtained through application of the DT technique is shown in Figure 8.2a. A cyclic load displacement curve is shown in Figure 8.2b. Note the hysteresis of this curve indicates the aforementioned irreversible energy dissipation, believed to be a result of the FPZ and the wake region. Figure 8.2b was used to calculate the compliance relationship and the adapted DT methodology.

One of the distinguishing observations in the two figures, besides the constant load plateau, is so called "crack-jumping" behaviour. Crack-jumping behaviour has been defined in ASTM E1820 as unstable crack growth spurts, represented as a sudden load drop of more than 5% on the load displacement curve. These load drops were found to be in the order of 9% here. In concrete crack-jumping behaviour has been said to occur due to the linking of micro-cracks, which results in sudden unstable propagation. Since the DT technique enjoys a crack length independent SIF, this sudden propagation remains somewhat controlled.

The significance of this observation is the statistical scatter of the peak load point prior to the crack-jump or sudden load drop. These will result in large variations

Material	Compliance (mm/N)
NBG10 (Parallel)	$C = 3.59 \cdot 10^{-3}a + 1.35 \cdot 10^{-3}$
NBG10 (Perpendicular)	$C = 3.45 \cdot 10^{-3}a + 1.32 \cdot 10^{-3}$
IM1-24	$C = 4.19 \cdot 10^{-3}a + 1.58 \cdot 10^{-3}$

Table 8.1 – Experimental compliance relationship obtained for the two considered graphite grades

in fracture toughness, since these are a function of the peak load. More so, the crack propagation for each loading and unloading cycle varied significantly and, as such, the experimentally determined J_R, J_{el} and J_{pl} values will be effected similarly.

8.2.2 Compliance Relationship

The compliance relationship for the DT specimen was determined according to Chapter 5 and is listed in Table 8.1. The values compare well to the DT's analytical compliance relationship for the elastic constants stated in Chapter 5 (within 2%).

The obtained compliance data fits the DT linear compliance well. The compliance relationship was used for LEFM SIF calculations and VK relationship data.

8.2.3 LEFM Assumption

The linear elastic parameters, K_{Ic} and G_{Ic}, and VK relationship data were determined and stated accordingly below. The methodology and procedure was according to the DT evaluation undertaken in Chapter 5.

Fracture Toughness

The critical strain release rate energy G_{Ic}, assuming LEFM, was calculated and the equivalent fracture toughness K_{Ic} was found. It is worth mentioning that in Chapter 5 a critical review of the DT technique was undertaken, which concluded that Evans' model with large deflection correction (LDC) yielded the most accurate values for the strain energy release rate and hence fracture toughness. As such this procedure was used here.

The results are tabulated in Table 8.2. K_{Ic} values are between 2.1 and 2.6 MPa$\sqrt{}$m for the different graphite grades and orientations as an 63% average. Since large scatter is experienced due to the aforementioned crack jumping behaviour a statistical Weibull approach (a normal distribution of scattered data approach) was utilised to represent the LEFM data in Figure 8.3. The typical Weibull curve was evaluated according to Stienstra and Anderson's three parameter Weibull distribution model [6]. The Weibull parameter is a weakest link mechanism where

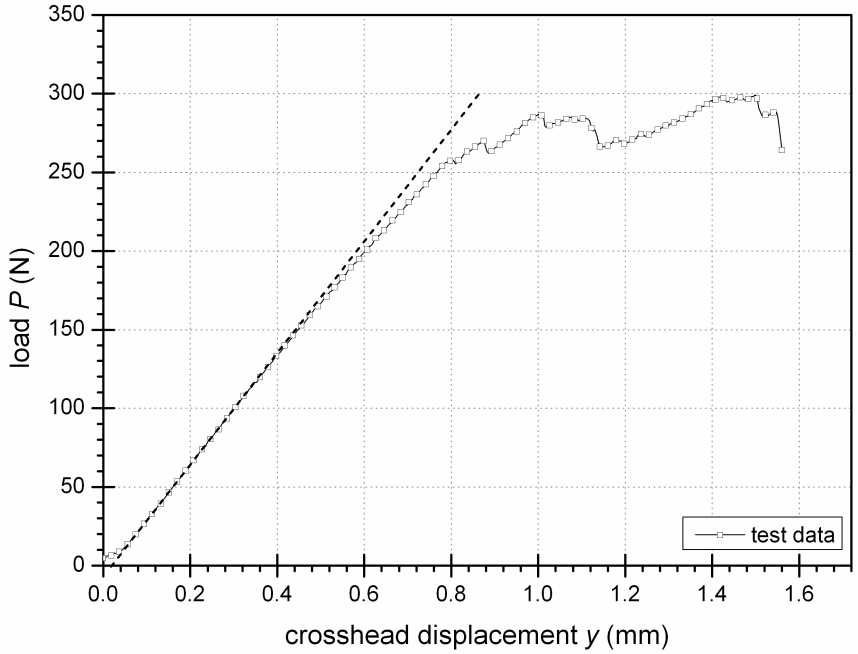

(a)

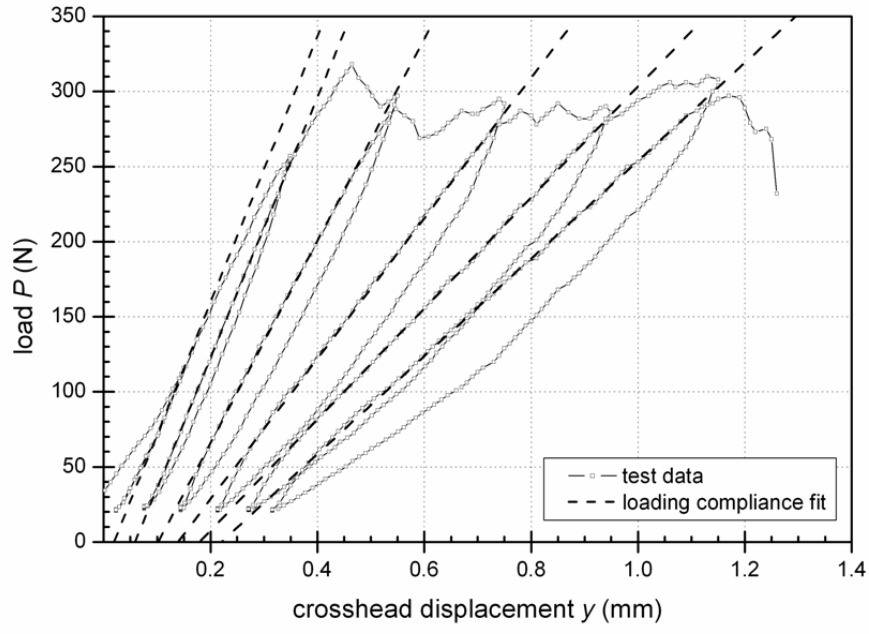

(b)

Figure 8.2 – Load displacement curves in (a) constant displacement rate of 0.1 mm/min and (b) cyclic displacement rate at 0.1 mm/min for NBG10 graphite (perpendicular orientation). The dashed lines repesent a linear load-displacment fir.

Material	G_{Ic} (J/m^2)	K_{Ic} (MPa$\sqrt{}$m)	Weibull slope	Weibull K_{min} (MPa$\sqrt{}$m)
NBG10 (Parallel)	450±40	2.1	4	1.75
NBG10 (Perpendicular)	480±30	2.3	4	2.1
IM1-24	480±50	2.6	4	2.2

Table 8.2 – LEFM fracture toughness data and Weibull parameters. The Weibull slope has been defined as 4 for K_{Ic} data [6].

failure, controlled by K_{Ic} in this case, is a statistical distribution of the experimentally obtained fracture toughness data.

It was found that NBG10 in the parallel orientation has a lower fracture toughness to that of the perpendicular orientation. This is explained by the lower fracture load. The statistical distribution in Figure 8.3 shows larger scatter for NBG10 in the parallel orientation. The basis of the Weibull approach is probability for initiation and propagation, so that, when a flawed structure is subjected to an applied SIF, the micro-cracks may or may not initiate in a favourable orientation and location. In graphite this was shown to be the case. Initiation of the macro-crack was shown to be governed by the weakest link mechanism (Chapter 7). It may be concluded that the probability for a weakest link mechanism is relatively more likely in the parallel orientation and IM1-24. These findings are in agreement with the crack propagation observations where cracking in the parallel orientation was predominantly associated with the linking of larger micro-cracks.

IM1-24 has the highest LEFM fracture toughness of 2.6 MPa$\sqrt{}$m. These LEFM determined fracture toughness values are significantly higher than those reported in literature, which were determined through other testing techniques (Chapter 3).

Crack Velocity vs. Stress Intensity

The load relaxation technique and constant displacement technique were both used to determine the VK characteristics of the graphites. The critical review of the DT technique in Chapter 5 has found reliable VK data for homogeneous materials (PMMA). However, the aforementioned crack jumping behaviour of graphite resulted in very short relaxation periods (Figure 8.4a). This resulted in limited VK data. However, despite this material shortcoming, an attempt was made to solve for the VK data within the short relaxation period.

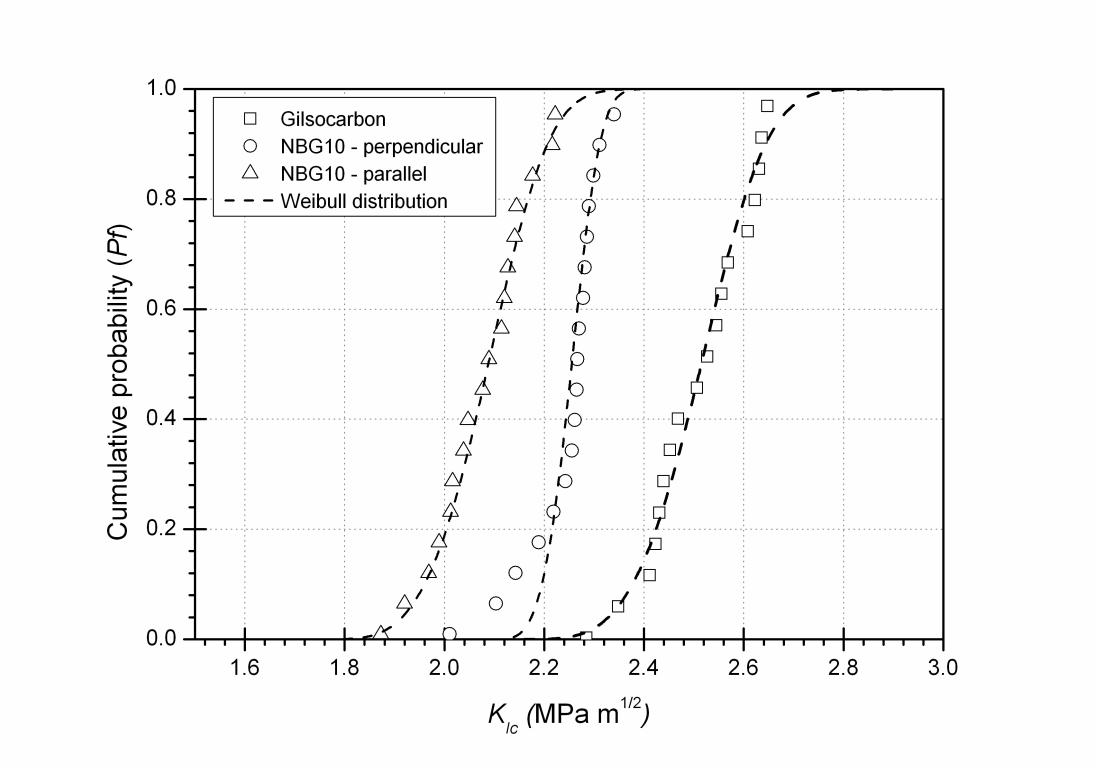

Figure 8.3 – Fracture toughness data for NBG10 (perpendicular and parallel orientation) and IM1-24. The data have been fit to Stienstra and Anderson's [6] three parameter Weibull distribution. These parameters are given in Table 8.2.

Material	VK slope n
NBG10 (Parallel)	315±40
NBG10 (Perpendicular)	210±30
IM1-24	340±40

Table 8.3 – Summary of recorded VK parameters.

The results are shown in Figure 8.4b for crack propagation perpendicular and parallel to the preferred grain direction in NBG10 and for IM1-24. The linear log-log relationship quantifies the sub-critical crack growth index. The load relaxation data shows decreasing gradients of the VK relationship, with most stable cracking in IM1-24, followed by the perpendicular and parallel orientations of NBG10. This trend is also seen in the constant displacement tests, although the data is more scattered. These VK relationships reflect the coarse nature of the material through short relaxation periods and limited crack propagation. It is

worth mentioning that Figure 8.4b may be utilised as a performance comparison tool, where IM1-24 characteristics are perhaps most desirable as cracking is most stable at a higher SIF.

8.2.4 EPFM Assumption

The EPFM values for J_R, J_{el} and J_{pl} were determined using the adapted methodology and the JMAN methodology. The values of J_R, J_{el} and J_{pl} reach a plateau following the onset of crack propagation (Figure 8.5a). This was expected as the DT technique was designed to provide a plateau of constant crack driving force. The energy enclosed by the loading and unloading cycles per crack extension area was used to calculate J_R, J_{el} and J_{pl}, according to the modified DT method. The aforementioned crack-jumping behaviour caused sudden load drops and irregular crack extensions, which resulted in significant variability in macro-crack extensions. In some cases small macro-crack extensions are associated with large non-linearity, attributed to micro-cracking. As a consequence, large scatter was observed in the calculated J_{pl} and hence J_R values. However, consistent values for J_{el} were achieved for both materials. This is shown in Figure 8.5b where, like with the LEFM results, the Weibull distributions are shown for J_{el} and J_{pl}.

There was no significant difference for J_{el} in the NBG10 parallel and perpendicular directions. IM1-24, which has an entirely different micro-structure, also exhibited a very similar elastic fracture contribution. This suggests that J_{el} is a measure of the fracture resistance of the graphite itself, and excludes the non-linear effects. Plotting data for J_R and J_{el} vs. J_{pl} (Figure 8.6) shows the convergence to a fracture resistance of 240 J/m^2 and 250 J/m^2 for NBG10 and IM1-24 respectively (i.e. at zero plasticity). This is equivalent to a SIF of around 1.2 - 1.3 MPa$\sqrt{\text{m}}$ for both materials.

The convergence in Figure 8.6 shows that crack propagation in graphite is accompanied by significant non-linear effects. This is in agreement with the ESPI and DIC observations of the FPZ and the wake region, and the irreversible energy dissipation shows that a plateau region with crack growth exists, indicating that the FPZ remains somewhat constant once established.

At this point, fracture in graphite may be understood as a primary or macro-crack with the irreversible energy dissipation due to the FPZ and wake region, which can contribute up to 50% in energy dissipation in the considered graphite grades.

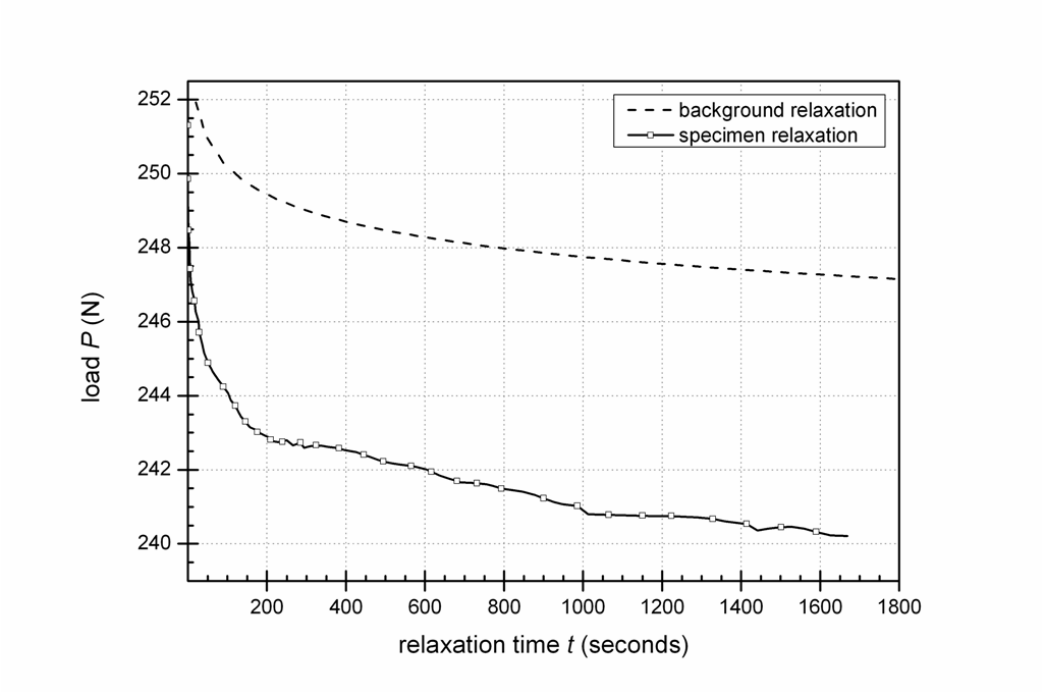

(a)

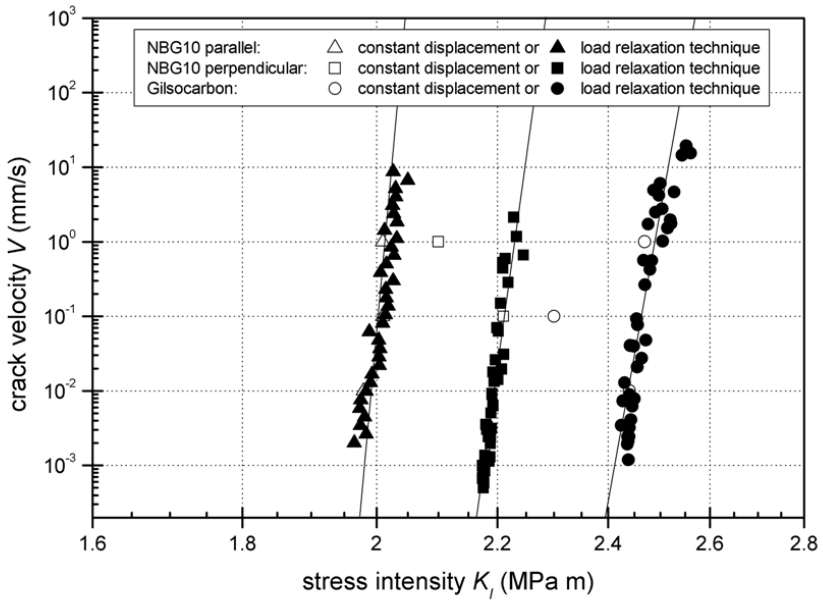

(b)

Figure 8.4 – (a) Relaxation curve used to determining VK data in NBG10 graphite (perpendicular orientation), showing the specimen and the background relaxation. (b) VK data (log-log scale) of NBG10 in the parallel and perpendicular direction and IM1-24. Data are shown for both the constant displacement and load relaxation methods.

There is an additional observation that needs consideration though. The scatter in J_{pl} shows a large variation in the "plastic" effects during the propagation of the macro-crack, which strengthens the aforementioned weakest link argument. The large statistical variation of J_{pl} and relatively insignificant variation in J_{el} demonstrate the fundamental cracking behaviour of graphite. When a graphite structure is subjected to an applied load, micro-cracks may or may not initiate near pores or grain boundaries. What the criterion is (for the initiation of such flaws) is not known at this stage, however the orientation and location plays an important role. A macro-crack develops and propagates only when sufficient micro-cracking is present. The macro-crack can be seen as a weakest link mechanism that is dependent on the availability of micro-cracking and wake region effects. Hence, cracking in graphite is a function of the energy lost due to the micro-cracking ahead of the crack tip, and crack-bridging, branching and arresting in the wake region, rather than primary crack associated with micro-cracking and the wake region. In other words, the amount of "plastic" energy dissipated during fracture is dependent on the micro-structure and orientation, and possibly other conditions such as load configuration, test geometry, etc. where the so-called elastic contributions are a material property in itself.

This hypothesis can be demonstrated comparing the plateau region of NBG10 specimens that were cracked in the parallel and perpendicular directions. It has been shown that the specimens in the parallel direction experience larger plasticity effects. The values of J_{pl} differ by approximately 8% with orientation, making the fracture resistance higher in the parallel orientation. The J_{el} values, however, are similar. The grain orientation in the parallel orientation is *with* the crack propagation direction, making it more favourable for micro-cracking. The DIC observations have shown this, where micro-cracking and crack bridging effects are more prominent in the parallel direction (Chapter 7). Hence, the FPZ may be seen as more pronounced and less stable, where macro-crack propagation is predominantly governed by crack bridging of larger micro-cracks. The slow crack growth analysis supports the above argument in demonstrating that crack growth in the parallel direction is relatively less stable. As such, the difference in fracture behaviour between the two orientations is only dependent on the irreversible energy loss due to micro-cracking and wake effects. IM1-24 shows the largest "plastic" energy dissipation during propagation, with its J_{pl} being 16% greater than the mean NBG10 value.

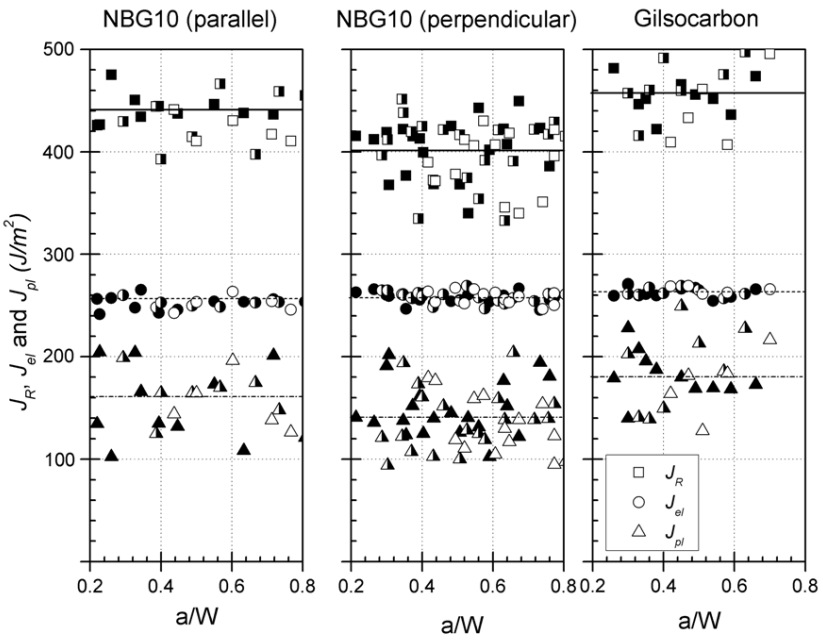

(a)

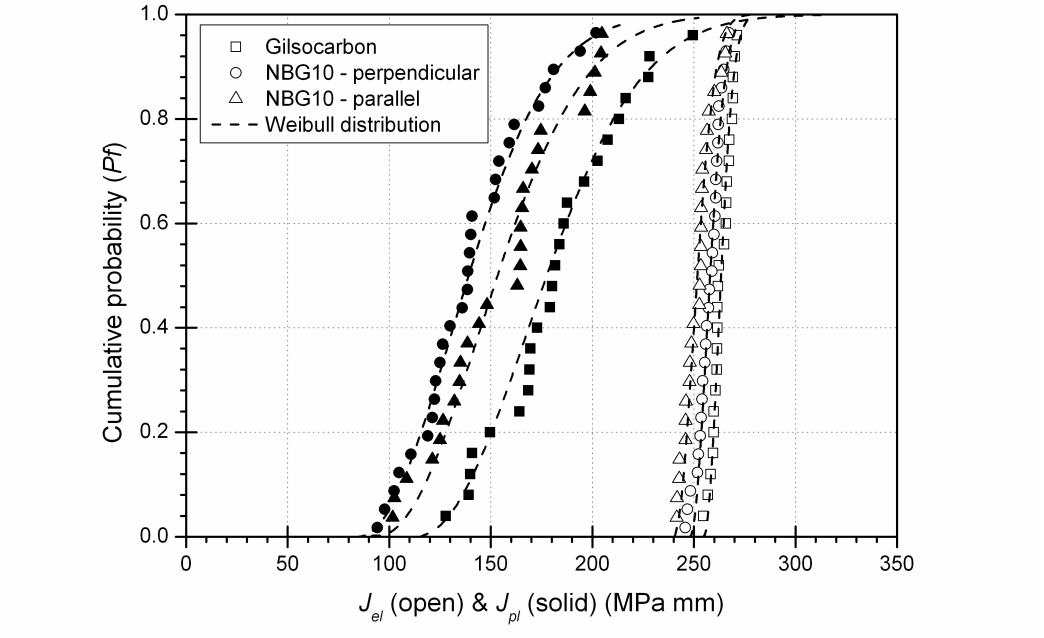

(b)

Figure 8.5 – Data for J_R, J_{el} and J_{pl} vs. crack length in IM1-24, NBG10 in the parallel orientation and NBG10 in the perpendicular orientation. (a) Data from the 20, 40 and 60 mm notched specimens is represented by solid, half and open symbols respectively. (b) Data fitted to Stienstra and Anderson's [6] three parameter Weibull distribution. These parameters are given in Table 8.4.

Material	J_R (J/m^2)	J_{el} (J/m^2)	J_{el-min} (J/m^2)	J_{pl} (J/m^2)	J_{pl-min} (J/m^2)
NBG10 (Parallel)	480±50	265	250	185	95
NBG10 (Perpendicular)	480±30	260	250	140	85
IM1-24	450±40	260	255	170	115

Table 8.4 – EPFM J_R, J_{el} and J_{pl} data and Weibull parameters. The Weibull slope has been defined as 2 for J parameters [6].

R-curve behaviour

The R-curve behaviour in the form of J versus the relative crack extension is shown in Figure 8.7. These data for the fracture resistance, J_R, were obtained by application of JMAN (Chapter 6) to the displacement fields from DIC and also using the DT methodology described above. Various initial notch lengths of 20, 40 and 60 mm were used. In the JMAN analysis, the contour was taken in the elastic region, outside the observed FPZ. Examination of several contours showed the values to be path independent in this region. The uncertainty in the DIC calculated displacement field (for the large interrogation window used of 128x128 pixels) was 0.005 mm, which resulted in an error of the calculated J of less than 0.05%. The data are compared in Figure 8.5a, which shows no effect of the initial notch length.

Both methods for determining the R-curve behaviour are in agreement, and the two methods are shown to be equivalent. The advantage of the JMAN methodology is the ability to continuously measure J_R at very short crack extensions, which proves difficult for the DT methodology. However, the reliability of JMAN depends on the accuracy of the DIC calibration (Chapter 6), and the DT methodology can be easier to apply.

The common characteristics of R-curves are observed, i.e. rapidly rising initial behaviour (Stage I to II in Figure 8.7) followed by a plateau or slowly rising region (Stage II to III in Figure 8.7). The value of J-integral at initiation, at which crack propagation begins from the notch, is around 65 J/m^2 (±6) and 72 J/m^2 (±8) for NBG10 in the perpendicular and parallel orientations respectively and 105 J/m^2 (±12) for IM1-24. A J initiation value has previously been reported as 108 J/m^2 for IM1-24 [15]. No significant effect of cross head displacement rate on the R-curve was observed. These observations, when combined with the DIC and ESPI observations of the FPZ (Chapter 7), show that the formation of the FPZ

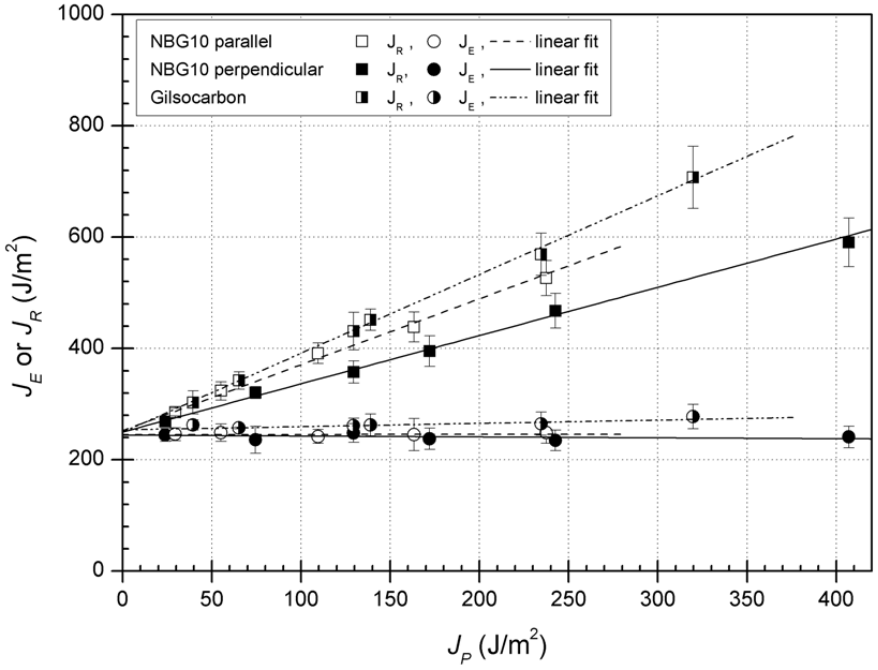

Figure 8.6 – Relations between non-linear fracture toughness parameter J_R, J_{el} and the plastic energy dissipation J_{pl}.

is coincident with the initial rise in the R-curve, and hence controls J initiation.

Figure 8.7 also shows a more slowly rising initial R-curve for the parallel orientation compared to the perpendicular crack system in NBG10. This may be explained by less extensive micro-cracking perpendicular to the macro-crack extension direction in comparison to the parallel orientation, and hence a lower work of fracture in the FPZ. The slow crack growth analysis supports the above argument in demonstrating that crack growth in the parallel direction is less stable.

As the propagating FPZ is observed to be constant in size, the continuously rising R-curve (Stage II to III in Figure 8.7) may be due to frictional contact, caused by the crack tortuosity that forms a bridging zone in the wake of the crack [40]. This is in agreement with Sakai [14], who also concluded that the formation of a plateau suggested the length of the bridging zone had stabilised. Inspection of Figure 8.7 suggests that this length is approximately 35 - 40 mm (after III) in the DT specimens tested. In IM1-24 this zone was previously estimated by Fazluddin [16] to have a length of 2 - 2.5 mm in bend specimens and 6 to 7 mm

in CT specimens, 55 mm in CT specimens by Hodgkins [4] and 9 – 11 mm by Ouagne [15]. It has been shown by Fuller [31] that contact stresses develop in the DT geometry, which would affect frictional contact. Thus, crack bridging and its contribution to the R-curve may differ from other specimen geometries, such as compact tension and bend.

8.3 Re-analysis of Hodgkins, Ouagne and Fazluddin's Gilsocarbon Data

It has been established that the application of LEFM to characterise graphite fracture has limitations due to non-linearity. As a result the focus to characterise fracture in graphite has been shifted to EPFM. As previously discussed, the damage in the FPZ was shown to contribute up to 50% to the fracture resistance, and the rising R-curve behaviour is strongly influenced by the formation and propagation of the FPZ and crack tip wake region. Given that the FPZ is not small compared to the specimen dimensions (the reader is referred to Chapter 7) the FPZ plays an important role in graphite fracture.

Currently in literature, most fracture characteristic data is available for IM1-24 graphite. Such examples are Hodgkins [4], Ouagne [15] and Fazluddin [16]. Both Hodgkins and Ouagne assumed non-linear fracture mechanics to characterise IM1-24 and utilised Sakai's graphical approach to empirically find J_R, J_{el} and J_{pl} parameters. Similar to the DT geometry, a plateau region was observed in these CT specimens, during which the crack growth resistance was constant. This plateau region, though relatively shorter than the plateau region obtained with DT, is indicative that a constant FPZ and wake region exists. Their results are tabulated in Table 8.5. It is worth mentioning that Hodgkins results were re-analysed (from the provided load-displacement plots) as only a J_R parameter was provided.

Table 8.5 indicates that the elastic contribution to fracture, i.e. the energy lost due to the macro-crack propagation, is within reasonable agreement, indicating a energy requirement of approximately 230 $\mathrm{J/m^2}$. The overall fracture resistance J_R and non-linear "plastic" contributions J_{pl} show large variations in experimentally obtained results. It follows that, if indeed the elastic contribution to fracture remains constant for various geometries and sizes, the plastic contribution depends on the specimen configuration and size. Previously, size effects have been

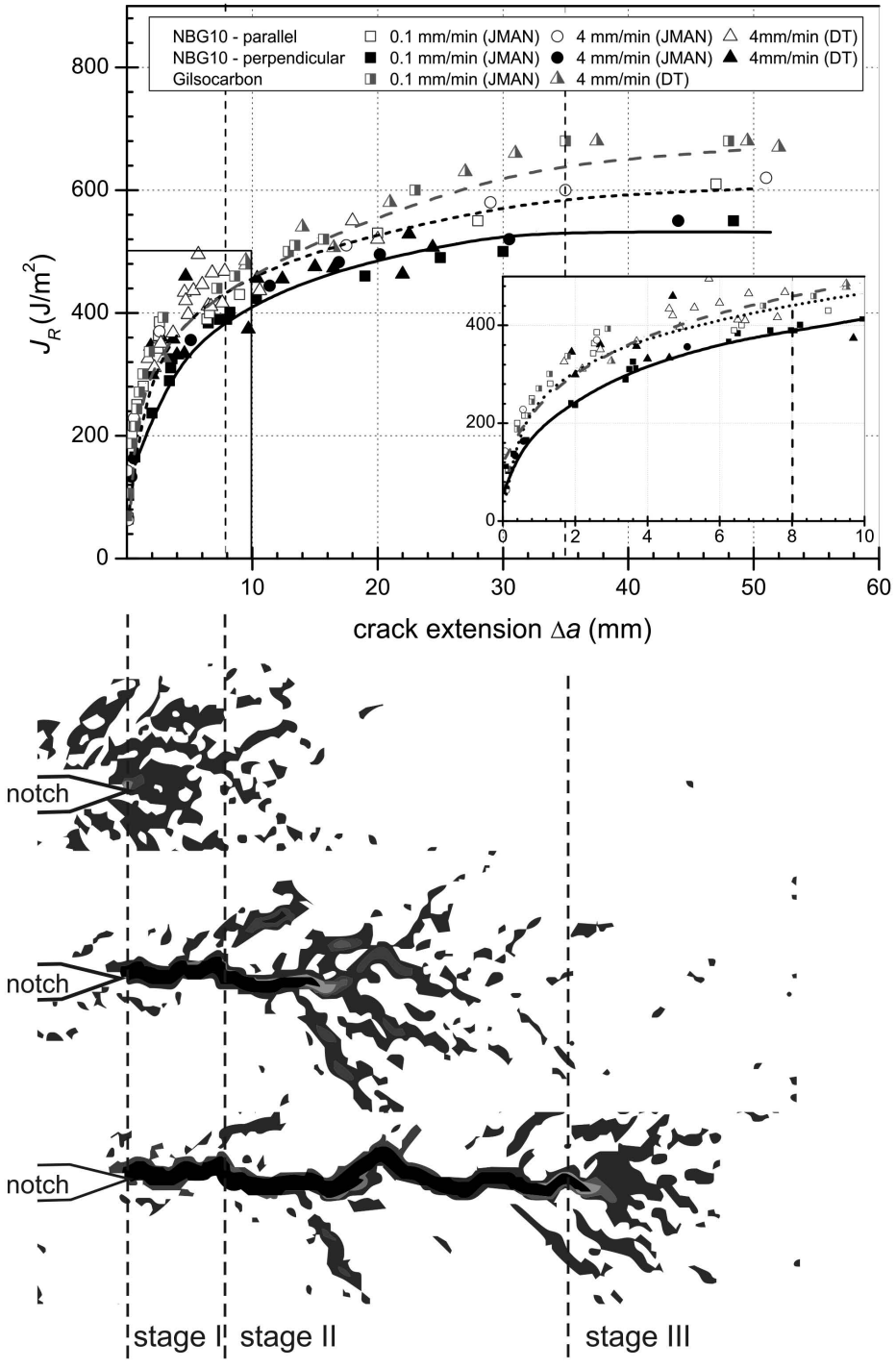

Figure 8.7 – Typical R-curve behaviour determined in NGB10 (parallel and perpendicular) and IM1-24. The data obtained independently by the JMAN and the adapted DT methodologies are compared.

	Geometry	W	B	J_R	J_{el}	J_{pl}
Ouagne [15]	CT	50	15	268	208	60
Hodgkins [4]	CT	100	50	310	230	80
	CT	50	20	300	245	55
	CT	45	30	280	230	50
Fazluddin [16]	CT	48	10	≈ 410	-	-
	SENB	12	10	≈ 280	-	-
Becker (this work)	DT	50	4	440	250	190

Table 8.5 – Comparison of EPFM data from literaturevfor Gilsocarbon.

discussed in quasi-brittle materials such as concrete [21, 166], where it was concluded that in smaller test geometries, such as the DT geometry, non linear effects are dominant due to the relatively large FPZ [166].

The differences in reported FPZ and wake region cause some concern when using conventional EPFM. The R-curve is said to be crack tip wake and FPZ dependent, and since a range of wake region lengths have been reported, it suggests that the R-curve behaviour is geometry dependent in graphite. Again, this has shown to be the case for quasi-brittle materials [174] and it is clearly shown to be the case for graphite in Figure 8.8. The figure compares the IM1-24 R-curve behaviour of several specimen geometries, namely the DT geometry (evaluated in this work), Compact Tension (CT) geometry and Single Edge Notched Beam (SENB) evaluated by Fazluddin [16] using a potential drop system, optical method and elastic compliance, and Hodgkins using Xray tomography [19]. The R-curves curves show a similar trend; a rapidly rising initial behaviour followed by a plateau or slowly rising region, however, the magnitude and steepness varies significantly. The DT obtained R-curve, which is found to have a FPZ of approximately 8 - 10 mm and a wake of 35 – 40 mm, shows a more rapidly and continuously rising R-curve behaviour compared to that of the CT geometry, which is found to have a FPZ of approximately 6 mm [4, 16] and the SENB, which is found to have a FPZ of approximately 2 - 3 mm [16].

There is however an additional consideration which needs to be mentioned which concerns the assumption of plane stress vs. plane strain. The critical SIF (the fracture toughness) is only a material constant when certain conditions are met. For LEFM conditions, the plastic zone must be small compared to the specimen thickness in order to achieve plane strain conditions at the elastic-plastic interface [6]. Only then is the fracture toughness a true material property. Similarly, there

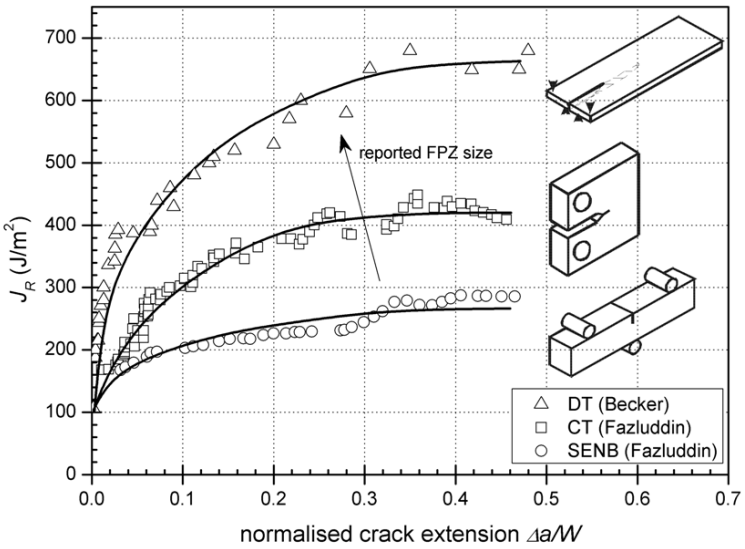

Figure 8.8 – Typical R-curve behaviour determined for IM1-24. The data obtained independently by the JMAN and the adapted DT methodologies are compared.

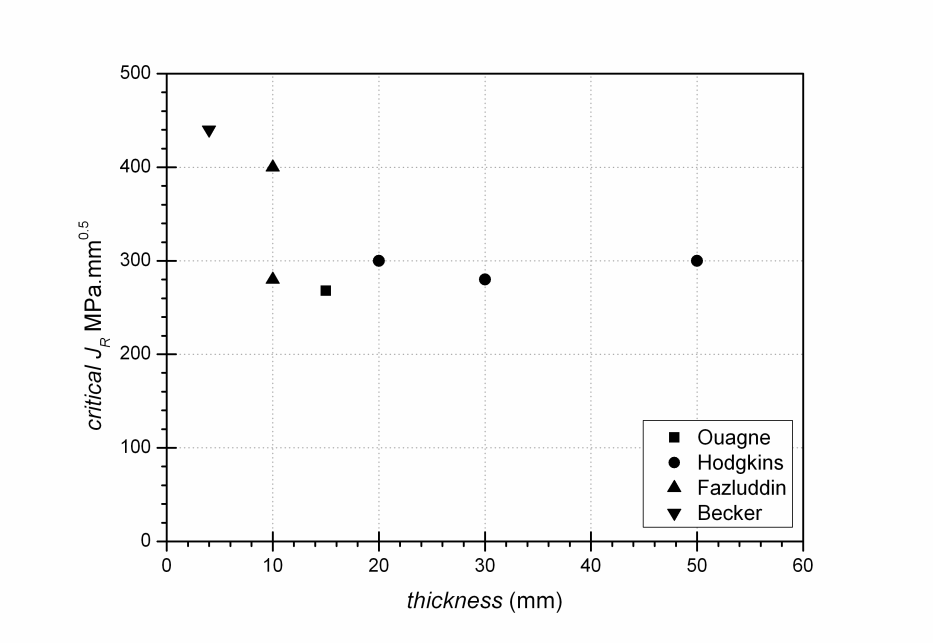

Figure 8.9 – Suggested effect of specimen thickness on recorded fracture resistance in IM1-24.

is no reason why this requirement should not be met in plastic fracture (i.e. ductile behaviour) [6]. The following conditions have been proposed for materials that undergo significant plastic yielding during fracture [175]

$$d = 25 \cdot \left(\frac{J}{\sigma_{ty}} \right) \tag{8.6}$$

According to this thickness criterion; when the plastic zone reaches a significant fraction of the plate thickness, the stress state at the edge of the plastic zone is plane stress, however, plane strain conditions may persist at the crack lip, deep inside the plastic zone. With further plastic deformation, however, the level of stress triaxiality at the crack lip relaxes. A lower degree of stress triaxiality usually results in a higher toughness, hence a small specimen thickness (relative to the plastic zone size) corresponds to a nominally plane stress fracture. The through-thickness constraint can, in addition, influence the shape of the R-curve, particularly for ductile materials. The R-curve for a material in plane stress is often much steeper than the plane strain R-curve for the same material. Some materials have a relatively flat plane strain R-curve, resulting in toughness that is single valued, while the plane stress R-curve rises with crack growth [6].

This trend may have been observed for the reported IM1-24 results, as shown in Figure 8.9. The DT geometry, being the thinnest of the geometries considered, achieved the highest fracture resistance (compared to that of a ten times thicker specimen).

However, to satisfy the thickness criterion, assuming Equation 8.6 is valid, a specimen thickness of approximately 0.5 mm is required for plane strain conditions for IM1-24 (as shown in 8.6). In addition, the thickness criterion fails to account for the difference in results obtained for "same-thickness" specimens with a different geometry (for example the difference in J_R between the CT and 3PB configuration in Table 8.5). Thus, there are complex phenomena occurring during fracture which need further consideration.

8.4 Understanding Fracture in Graphite

It was demonstrated that the fracture behaviour of graphite deviates significantly from the predictions of the LEFM. The reported LEFM fracture toughness data for graphite show large differences, from 0.83MPa$\sqrt{}$m (disk compact tension [78])

1.2 MPa$\sqrt{m}$ (SENB) [45] to 2.3 MPa$\sqrt{m}$ (DT geometry). The primary reason for the observed deviation of the behaviour of artificial graphite from the LEFM prediction is the formation of an extensive FPZ ahead of a pre-existing notch or crack. It was shown in Chapter 7 that the material in this zone progressively softens due to micro-cracking. It was seen in the previous sections that the pre-peak and post-peak non-linearity are primarily a result of micro-cracking. This process has a major influence as it reduces the flux of energy that can be released into the macro-crack-tip while simultaneously increasing the overall fracture surface area and thereby the energy dissipation. Another feature, which contributes to the overall fracture behaviour, is frictional sliding in the crack wake region. These have been discussed in Chapter 7.

It follows that the fracture criterion must be capable of describing such behaviour and include in it a description of the irreversible energy dissipation processes. Thus, fracture characterisation necessitates non-linear criterion. Such non-linear parameters can be characterised under the assumption of EPFM, which make it possible to distinguish plasticity from crack growth. These parameters, such as the J-integral, have shown the ability to account for these processes and R-curve behaviour can successfully describe the entire crack initiation and formation process in metallic materials. Here, the flow of energy to the fracture process is restricted by the growth of the plastic zone, which effectively acts as a toughening mechanism [176]. However, it is worth distinguishing non-linear fracture applicable to ductile materials from that applicable to quasi-brittle materials, such as graphite. This is because in ductile materials the FPZ, though small, is surrounded by a large nonlinear plastic zone, whereas in graphite the FPZ practically occupies the entire zone of non-linear deformation and a so called "plastic" zone is practically absent. The non-linear zone is the FPZ and the crack wake region. Its size is essentially, though not exclusively, a property of the material and is governed by the dimensions of the inhomogeneities in the micro-structure [177]. As a consequence its size has often been viewed as a constant, however, it was shown that this is not the case.

The reported FPZ size varies significantly between SENB, CT and DT geometry from around 2 - 3 mm to 6 - 7 mm to 8 - 10 mm respectively. Further, the wake region varies considerably between these geometries and it follows logically that these processes are dependent on the specimen geometry and not a material constant. It is however worth mentioning that the methodologies, which have been used to obtain these approximations, are different. Fazluddin approx-

imated his FPZ and wake region through a potential drop system and Hodgkins approximated his FPZ and wake region from X-ray tomography observations.

This is not the first time that a size effect was discussed in graphite fracture. A paper by Romanoski and Burchell [78] observed a substantial scatter in standard K_{Ic} values from various geometries including the CT, Disk Compact Tension (DCT), short rod and CNSR specimens amongst others. Additionally they tested various sizes of CNSR specimen and concluded a strong dependency on size. The material tested was IG-110, H-451 and S-2020. Size effects in R-curve behaviour were also noticed by Fazluddin, but were not discussed further [16].

The behaviour of graphite appears to be very similar to that of other quasi-brittle materials such as concrete. Fracture, for example in concrete, is associated with a FPZ in which extensive micro-cracking results in irreversible energy dissipation. Cracking is predominantly associated with a weakest link process of coalescence of micro-cracks in the FPZ and bridging, branching and crack arresting mechanisms in the wake region. These mechanisms have been identified as part of quasi-brittle fracture and at this point it seems almost trivial to suggest the use of quasi-brittle fracture methodologies for graphite fracture characterisation.

In quasi-brittle materials size effects have been discussed extensively. Size effect is a term used to describe the apparent fall in nominal strength observed in many quasi-brittle materials when nominally identical specimens of larger size are tested [177]. To date it is understood that if the size of the zone is sufficiently small, relative to the dimensions of the specimen, then LEFM provides suitable characterising parameters (G_c & K_c); if the zone encompasses a considerable amount of the effective length of the specimen, then other non-linear assessment techniques are required. It is reported that under these circumstances, the fracture behaviour cannot be characterised by a single parameter with the conventional elastic or elastic-plastic fracture mechanics approach [177]. An account must be taken of the effects of the FPZ and wake region [178]. It is for this reason that the non-linear parameter J_R or R-curve is an erroneous fracture parameter in quasi-brittle materials, and hence nuclear graphite.

The work undertaken in this chapter cannot be completely dismissed. The experimental program has facilitated for the understanding and realisation of the shortcomings when analysing graphite fracture using EPFM. The parameters, which have been obtained, can provide useful fracture parameters which are utilised in the next chapter.

8.5 Summary

This chapter presented the fracture characteristics of graphite obtained through the use of the DT technique. The DT technique was successfully applied in the study of crack propagation, which included slow crack growth characterisation of NBG10 and IM1-24. As with the observations of mechanisms associated with crack growth, NBG10 was investigated in the parallel and perpendicular extrusion direction. Through the use of the DT technique, stable crack growth at a constant driving force were attained over relatively large crack length (up to 75 mm). These made it suitable for the measurement of fracture characteristics of quasi-brittle materials, which experience non-linearity due to micro-cracking in the fracture process zone and crack bridging in the wake.

A modified approach to the DT methodology was proposed. The use of a graphical analysis, of loading/unloading force-deflection curves, enabled the ability to measure the non-linear fracture characteristics as a J-integral parameter (as shown in Figure 8.1). Evaluated were the elastic and so called "plastic" or non-linear contributions to fracture. In addition, an analysis of the displacement fields ahead of the crack tip, using the JMAN method (introduced in Chapter 6), was used to calculate the J-integral during crack initiation and propagation. The independent analysis of the modified DT methodology and the JMAN method gave the same results.

The values of J_R (the fracture resistance), J_{el} (the elastic contribution) and J_{pl} (the plastic contribution) reach a plateau during crack propagation (as shown in Figure 8.5a). This was expected as the DT technique enjoys a constant load plateau of constant crack driving force. No significant difference was found for the elastic contribution in NBG10, in the parallel and the perpendicular orientation, and IM1-24, suggesting that this is a measure of the fracture resistance of the graphite material itself, and excludes the non-linear, so called "plasticity" effects. Similarly, these "plastic" energies show the same plateau region indicating that the FPZ remains constant once established. This behaviour is in agreement with the ESPI and DIC observations of the FPZ. However, significant large scatter in the J_{pl} values is noticeable (as shown in Figure 8.5b); plotting charts of J_R and J_{el} vs. J_{pl} shows convergence to a fracture resistance of $J_{el} = 240$ J/m^2 for both crack orientations (refer to Figure 8.6). This is similar to the obtained plateau value. The convergence confirms that crack propagation in graphite is accompanied by significant non-linear effects. Comparing the plateau region of

the specimens that were cracked in the parallel and the perpendicular direction, we may conclude that the specimens in the perpendicular direction experience larger plasticity effects (by 8%).

The R-curve analysis of the two materials has shown the typical quasi-brittle R-curve behaviour. This is consistent to the development of the FPZ and crack wake effects. The application of JMAN on NBG10 graphite in the parallel and perpendicular orientations show these to have the similar initiation toughness of around 65 J/m^2 and 72 J/m^2 for the perpendicular and parallel orientations respectively. IM1-24 was found to have an initiation toughness of 105 J/m^2 (Figure 8.7).

Comparison between of the obtained R-curves shows a more sharply rising R-curve for NBG10 in the parallel oriented crack system and IM1-24. This suggests that micro-cracking and crack bridging effects are more prominent and further suggests differences in the way the FPZ fractures.

Comparison of the R-curve data with other data available in literature, suggests a geometry dependent fracture behaviour, where the non-linearity due to the FPZ and the wake effects result in variations of the apparent fracture toughness (as shown in Figure 8.8). It was found that the reported FPZ size varies significantly between various geometries showing a relationship between the non-linear fracture behaviour and the FPZ and wake region size. It was identified that the observed and measured behaviour is very similar to that of other quasi-brittle materials, for example concrete. In these a clear size effect on geometry has been established and fracture cannot be categorised by conventional elastic plastic fracture mechanics.

Chapter 9

Further Discussions and Modeling Graphite Fracture

Throughout this thesis each chapter has been written with the intent to be self contained; providing an introduction, the main subject matter and relevant discussions. This chapter maintains a similar format, yet aims to provide further discussions on the previous chapters, highlighting important issues and conclusions. It intends to link the four main aspects of this thesis; the Double Torsion (DT) technique, the proposed JMAN methodology, the failure observations and the measured fracture parameters. In addition, this chapter intends to develop on the experimental graphite fracture programme by comparing the observed and measured characteristics to that of other quasi-brittle materials and their appropriate fracture models. From these existing quasi-brittle fracture models a model for nuclear graphite is formulated and presented. A discussion on the understanding of the failure of nuclear graphite components is formulated.

It is worth mentioning that the formulation of a graphite fracture model is in itself a broad topic and beyond the scope of this PhD. The formulation presented in this chapter is a proposal of a methodology to model and predict graphite fracture. The intention is to show that graphite behaves like a quasi-brittle material and quasi-brittle failure models exist that can adequately describe graphite fracture. The model presented shows a good correlation to available experimental data from Hodgkins [4] and Fazluddin [16].

9.1 Introduction

As it has been stated in the introduction, polycrystalline graphite has in recent years attracted considerable attention regarding the structural assessment of its material behaviour. Earlier failure models included a Weibull analysis approach, whereby failure is governed by a weakest link process [179] and linear elastic fracture mechanics (LEFM) models [42]. Subsequent attempts have included some Finite Element (FE) models, which included Burchell's micro-structural based fracture model [41], and Zou et al's. numerical simulation of moderator bricks [180]. With the understanding that the fracture of polycrystalline graphite is associated with extensive micro-cracking and irreversible slip formations along the basal planes, most recent attempts to model fracture in graphite (including Chapter 8 in this work) have associated fracture with non-linear, elastic plastic fracture mechanics (EPFM).

With the aim of this thesis being the contribution to the understanding of graphite fracture, it utilised the Double Torsion (DT) geometry together with optical observation techniques (Digital Image Correlation, DIC, and Electronic Speckle Pattern Interferometry, ESPI) and optical analysis techniques (JMAN) to observe and measure the fracture behaviour of graphite. The successful application of the DT geometry and the JMAN methodology enabled the characterisation of graphite fracture mechanisms. These are discussed below, in the order of the thesis aims described in Chapter 4.

9.2 The Validity of the DT Geometry

The DT technique was shown to be a valid test geometry, however, the common assumption of crack length independence is limited by the loading configuration, the specimen geometry and material. The discrepancies of a crack length independent Stress Intensity Factor (SIF) can be attributed to non-linearity of the compliance relationship, which is commonly assumed to be linear. The linear compliance relationship arises due to the assumption that only the torsional deformations of the broken ligament halves contribute to the specimen's compliance. This, however, does not hold true. DIC verified the FE model prediction that the unbroken ligament deforms considerably together with large deflections at the loading points, resulting in the non-linearity of the compliance relationship. What makes the the DT configuration complex is that the changes in the loading

configuration due to large deflections at the load points result in a continuously decreasing compliance and the deformations of the un-cracked ligament result in a continuously increasing compliance. It may well be that in some cases these effects cancel each other out, resulting in a nearly linear compliance and an effectively crack length independent system. Indeed, some investigators have obtained repeatable data with Evans' conventional method using a long thin specimen with a $3W : W : 0.8W$ configuration. Despite this, the applicability of the DT geometry for graphite analyses was believed to be excellent, due to its ability to facilitate for test conditions that allowed for stable crack initiation and propagation, whilst enabling for easy crack tip observations, due to the way the specimen is loaded.

9.3 Digital Image Correlation and the Development of JMAN

To compliment the DT technique, optical observation and measurement techniques were utilised. This utilised the DIC technique and the development of a novel approach to calculate the J-integral by DIC displacement field measurement, called JMAN. What makes JMAN novel is its ability to calculate the energy associated with crack growth (i.e. J integral) directly from the DIC obtained images without requiring the measure of crack length. Based on a solid theoretical foundation and being mathematically simple, JMAN discretises the displacement field into a finite element problem enabling the determination of stresses and strains from the known material properties. Such fields are then used to categorise fracture parameters for various material types and testing configurations. The computation time is fast; it may be less than 0.2 seconds for a coarse mesh. This could allow for in-situ assessment of cracks, provided that the digital image correlation analysis to provide the displacement fields is also implemented swiftly. This approach could, for example, provide a powerful NDT methodology for the assessment of cracked structures under dynamic loading.

Currently, the FE discretisation in JMAN is based on a simple linear-elastic model, hence its application is limited to observations where the displacements can be measured in the elastic regime beyond the zone of inelastic deformation (i.e. the fracture process zone or crack tip plastic zone). It was demonstrated, by three examples, that for crack singularities that develop limited local nonlinear

zones due to plasticity or micro-cracking, the linear elastic model categorises the J-integral well. The JMAN analysis, however, could be extended to account for plastic strains, using the currently available FE formulation for plastic behaviour of metals, and could also be extended for quasi-brittle behaviour in other materials using appropriate and validated models. Furthermore, the JMAN analysis may readily be developed to allow J to be decomposed into mode I, mode II and T-stress components, and therefore to account for mode mixity or in-plane constraint effects.

The influence of residual stress fields could also be included. The original form of the J-integral is defined for stress and strain fields in isotropic homogenous medium, which guarantees the path independency. As many researches have recently shown, the J-integral loses its path independency in the presence of a residual stress field (e.g. [181]). The residual stress field can arise from manufacturing processes such as welding [182], heat treatment such as quenching [183] or pre-loading the specimen such as warm pre-stressing [184]. In addition, residual stresses have been observed in HTTR's graphite blocks due to radiolytic oxidation[185]. These are amongst the main causes of cracking in engineering components. Crack closure in fatigue is another example of a residual stress field interaction with cracks [186], where calculating the J-integral can properly define the stress field . Methods of calculating the J-integral in the presence of residual stress have therefore received much attention over the past ten years. For example, modifications to the J-integral formulation have been introduced to ensure the path independency of the J-integral even in the presence of residual stress field (such as Jmod [187] or JEDI [188]. Such modified formulations can also be exploited in JMAN.

9.4 The Mechanisms of Fracture in Graphite

Defects, such as micro-cracks and porosity, in the graphite matrix play an important role in the mechanical behaviour of graphite. The properties of graphite are influenced by its micro-, mezo- and macro-structures, which are characterised by the number and distribution of internal pores and cracks.

The fracture process was shown by ESPI to be influenced by the porosity and grain orientation of the material, where a macro-crack is primarily involved with the initiation and propagation of internal micro-cracks. The DIC observations

have indicated that during the pre-peak, non-linear phase internal flaws initiate and propagate at existing discontinuities. These cracks are isolated and randomly distributed, predominantly ahead of the notch tip and are orthogonal to the tensile strain in the loading direction. It is during this phase that most damage accumulates and ultimately the internal cracks start to localize into a macro-crack. The propagation of the macro-crack is primarily associated with bridging or branching through the maze of micro-flaws. Hence, for the macro-crack to propagate a FPZ needs to be present ahead of the crack tip. It follows that the interaction of micro-cracks also influences the macro-crack. Therefore, fracture processes in graphite may depend primarily on the stability of these interfacial cracks which is a function of the material structure.

These processes result in tortuosity of the macro-crack. It was shown that crack deflection occurs when the path of least resistance is around a relatively stronger particle or along a weak interface like a void. Other cracking mechanisms, which were identified, include crack arresting, crack branching and crack bridging. These mechanisms are important toughening processes in graphite and cause energy dissipation through friction planes.

The fracture process can thus be seen as a function of micro-cracking damage and not conversely, as previously believed. It is this that makes graphite fracture comparable to those mechanisms in other quasi-brittle materials.

9.5 Modeling Graphite Fracture Using Fracture Mechanics

The experimentally observed facts of inelastic micro-cracking mechanisms have been shown to result in marked mechanical non-linearity in graphite behaviour. It was recognised that the fundamental understanding of graphite failure emerges from the recognition of the fact that graphite contains defects, such as micro-cracks and voids, even without the application of an external load. These defects grow, and new defects are formed, under load, until they reach proportions that are likely to compromise the integrity of the structure and a macro-crack forms/propagates. These mechanisms of fracture, predominantly observed in the Fracture Process Zone (FPZ), are lumped together into a single term J_R using EPFM. Hence, fracture is associated with the formation, growth, and coalescence of micro-defects on the one hand, and for the localization of macro-fractures on

the other. The inelastic fracture mechanisms are associated with the so called "plastic" contribution (as with plasticity in metallic materials) and the macro-crack with the elastic contribution to J_R.

There is however, another fracture mechanism that needs to be addressed. The initiation of micro-cracks in the FPZ occurs at loads of approximately a third of the peak load [17]. During loading of undamaged material the material in the FPZ progressively degrades due to the microcracking until a macro-crack initiates. Similarly, the wake region of an established macro-crack softens due to crack bridging and other frictional effects. These mechanisms continuously reduce the flux of energy that can be released into the macro-crack during the crack initiation phase, while simultaneously increasing the overall fracture surface area and thereby the energy dissipation or fracture resistance. These toughening mechanisms can be characterised by the R-curve, whereby both the formation of the FPZ and the macro-crack propagation contribute to the fracture resistance. The R-curve can be seen as a material property and should, in essence, be applicable for any geometry configuration and size (as long as the crack mouth opening is in its designated mode).

Assuming that the toughening and crack propagating mechanisms are truly a material property, the EPFM route may be applied in conjunction with the R-curve behaviour to characterise graphite fracture. However, the analysis undertaken in Chapter 8, strongly suggests this not to be the case. The R-curve behaviour observed by the various geometry and specimen configurations show that the R-curve is predominantly dependent on the size of the FPZ and the wake region. These have found not to be constant, with the following observations:

- G_{Ic} and hence K_{Ic} seem dependent on specimen geometry and size (literature)
- J_{pl} and hence J_R seem dependent on specimen geometry and size
- R-curve behaviour seems dependent on specimen geometry and size

however,

- J_{el} appears to be_*independent* on specimen geometry and size

An additional fundamental question needs to be addressed; is a single crack or discrete approach for measuring crack growth resistance a reasonable assumption

with the knowledge that gross damage occurs at higher stress locations prior to fracture (i.e. at a third of the failure load) and that macro-fracture is dependent on micro-damage. The evidence found through the ESPI and DIC observations suggests not. The resistance to pure tensile loading appears to be dominated by de-cohesion in the FPZ. The FPZ forms a large area, in which larger micro-cracks continuously form and close. These localised stress concentrations lead to a progressive and localised reduction in the Young's modulus.

Since the EFPM determined values were shown not to be a material constant and fracture may require a non discrete approach, another approach is required. Modern analysis techniques exist for quasi-brittle materials that allow for a size and geometry independent formulation of the formation, growth, and coalescence of micro-defects on the one hand and for the localization of macro-cracks on the other. It may therefore be possible to predict, with a high degree of confidence, the integrity of cracked graphite components and to evaluate their residual life and safety margins using such existing quasi-brittle failure models. These models are discussed below. A non-local damage plasticity model for concrete and other quasi-brittle materials is proposed, which has been adapted for graphite. The model shows good agreement with experimental data.

9.6 Modeling Failure of Quasi-Brittle Materials

The mechanisms of failure, which have been observed and measured for graphite, are not unique. Concrete, rock and many other materials including various fiber composites and particulate composites, coarse-grained or toughened ceramics, ice, cemented sands, grouted soils, bone, paper, wood, wood-particle board, etc experience similar mechanism of fracture [21]. Such materials are said to require a different kind of fracture mechanics than ductile-brittle metals [21]. In both metal and quasi-brittle structures of normal sizes, fracture mechanics is non-linear due to the development of a sizable non-linear zone that develops at the fracture process zone (FPZ). In metals most of this zone involves hardening plasticity, and the FPZ, defined as the zone in which the material undergoes softening damage (tearing), is quite small. In quasi-brittle fracture the plastic flow is non existent and the non-linear zone is almost entirely filled by the FPZ (Figure 9.1, from Ref. [20]). Further, the FPZ in quasi-brittle materials may occupy a much larger portion of the cross-section of the structure and is often believed to be geometry and size dependent [21].

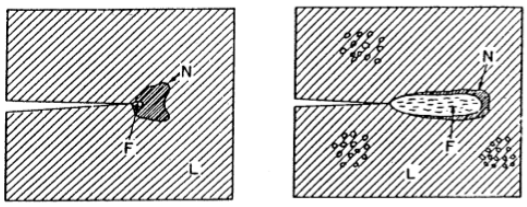

Figure 9.1 – FPZ in metals (left) and in quasi-brittle materials (right) (from Ref. [20]).

Size effects in quasi-brittle fracture have been addressed by Bazant [189]. Depending on structure size D (understood as the dimension of the with crack cross-section [189]) and the typical FPZ length ℓ_{ch}, different theories are appropriate for analyzing failure. These may be approximately delineated as follows [21]

For	$D/\ell_{ch} \geq 100$	Linear elastic fracture mechanics (LEFM)
For	$5 \leq D/\ell_{ch} < 100$	Non-linear quasi-brittle fracture mechanics
For	$D/\ell_{ch} < 5$	Non-local damage; plasticity models

In the last case, to be more precise, the strength-based plastic limit analysis gives only crude engineering estimates of the small-size behavior, while accurate analysis, at least in theory, calls for non-local damage models [190, 191].

The above categorisation for quasi-brittle materials raises an interesting point. Chapter 8 established that polycrystalline graphite behaves like a quasi-brittle material. It follows that the assessment of polycrystalline graphite components in the nuclear environment, i.e. Gilsocarbon blocks in AGR reactors, would thus require non-linear or non-local damage analysis models. Further, the DT and Compact Tension (CT) test specimen configuration would prove hugely erroneous when using EPFM, which explains the difference in R-curve behaviour observed in Chapter 8. It is worth noting that fracture mechanics is not currently used for the assessment of graphite components in reactors. At this point in time, the failure criteria consists of a critical tensile stress, calibrated using component specific test data.

In concrete, it was found that R-curves depend on specimen size, geometry and initial crack length [174]. Some material of different sized Three Point Bend (3PB) specimens have shown that infinite size and finite specimens follow the same R-curve behaviour, but with different plateau values [174]. The same was

observed in Chapter 8 when comparing the R-curve obtained through various geometries and size in graphite.

It is worth mentioning that several approaches to model quasi-brittle fracture, more specifically concrete fracture, exist. Currently, there are two main trends to study fracture of quasi-brittle materials. These predominantly rely on the FE method. The first are discrete models, that represent the fracture process by cohesive elements that are inserted in a FE mesh only when the opening condition is met. Such elements can also implement contact and friction algorithms. The second are continuum models, based on the strong discontinuity approach. Fracture is simulated with the degradation of the bulk material.

Three models are discussed below. It is worth mentioning that the aim is not to discuss all the models in literature available on quasi-brittle fracture. For further reading, the reader is referred to Karihaloo [22]. The review will lead to the formulation of the proposed graphite fracture model.

9.6.1 Cohesive Crack Models

Conceptually the simplest and one of the earlier models used to characterise the behavior of a quasi-brittle fracture with a finite-size FPZ is the cohesive crack model. This model is also referred to in concrete applications as the "fictitious crack model" and has been derived by Hillerborg [192]. The basic hypothesis of the cohesive crack model is that, for mode I fracture, the FPZ of a finite width can be described by a fictitious line crack that transmits normal stress $\sigma(x)$ and that this stress is a function (monotonically decreasing) of the separation u (called also the opening displacement, or opening width) shown in Figures 9.2b and (d).

$$\sigma = f(u) \tag{9.1}$$

By definition, $f(0) = f_{tu}$ = direct local tensile strength of the quasi-brittle material. A terminal point of the softening curve $f(u)$ is denoted as u_f; $f(u_f) = 0$. The crack wake region, in which the cohesive stresses represent the forces transmitted across an almost formed crack, is distinguished from the FPZ, in which no distinct crack can yet be discerned.

Typically the function $f(u)$ (Figure 9.2d), which describes the stresses as a function of crack opening u, initially descends very quickly followed by a more gradual

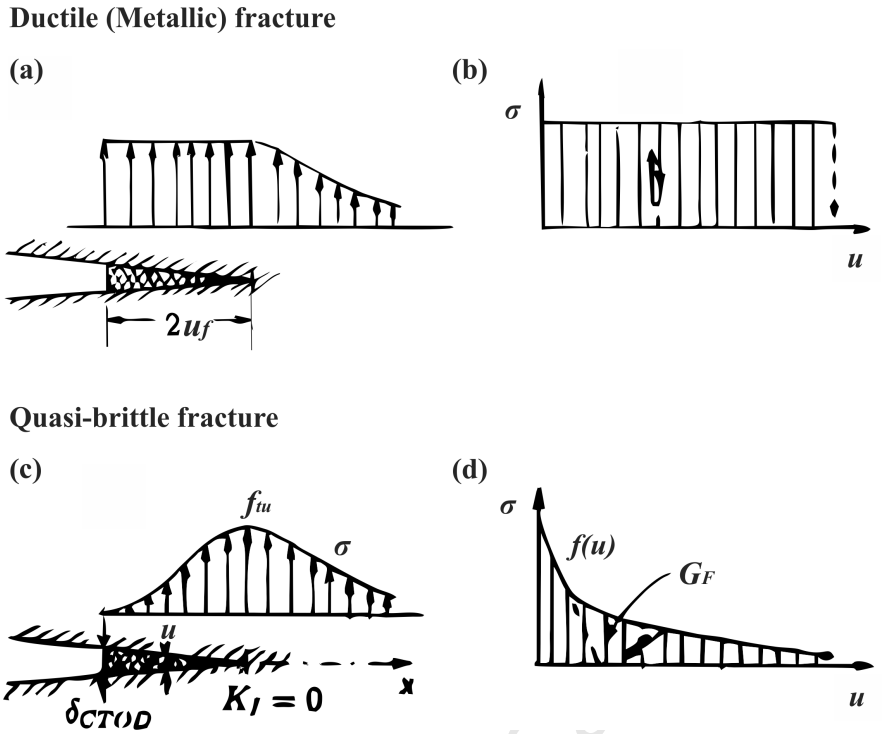

Figure 9.2 – Stress distributions and softening curves: (a, b) cohesive crack model for ductile (metallic) materials; (c, d) cohesive crack model for quasi-brittle materials (from Ref [21]).

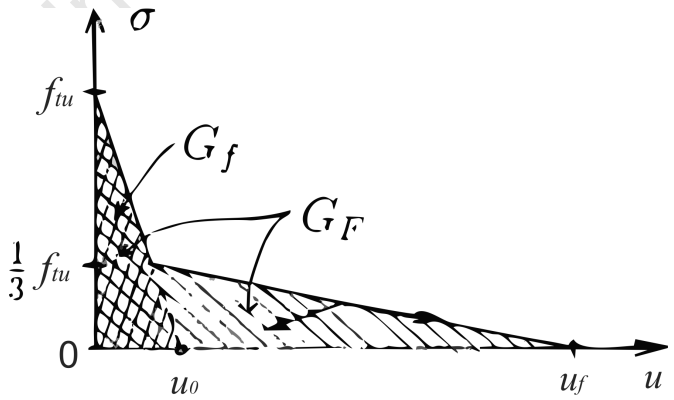

Figure 9.3 – Bi-linear softening stress-separation law (from Ref [21]).

decent. The importance of the shape of $f(u)$ is believed to be less significant [22] although much work has been dedicated to its effects on the fracture model. In the initial work of Hillerborg et al. [192], the softening curve $f(u)$ is described as a decaying exponential with a horizontal asymptote below u axis . Later Petersson [193] described the curve using a simple bi-linear form (Figure 9.3).

According to Hillerborg [192], the area under the entire softening stress-separation curve $f(u)$ represents the total energy dissipated by fracture per unit area of the crack plane G_F in J/m^2 (Figure 9.3). It is often deduced that the area under $f(u)$ also represents the energy dissipated per unit area of crack plane as the FPZ and wake region moves forward by da, i.e. the J-integral [57]. This is theoretically important as this is the energy that must be equal to the energy release rate of the structure/specimen, i.e. J_R.

Assuming the generally accepted bi-linear approximation of the softening curve shown in Figure 9.3 [21], the cohesive crack model can be characterized by two fracture energies

$$G_F = \int_0^\infty f(u)\mathrm{d}u \tag{9.2}$$

$$G_f = \frac{{f_{tu}}^2}{2\sigma_0'} \tag{9.3}$$

G_F corresponds to the area under the entire curve $f(u)$, i.e. the total energy dissipated during fracture, while G_f to the area under the initial tangent of slope σ_0', i.e. the area under the initial steep segment extended down to the u axis. In essence, G_f represents the the initial fracture energy [166] .

The fracture energy G_F, measured as the area under the complete load-deflection curve of the specimen, was shown to be significantly size dependent [166]. This appears to be a weakness of the cohesive crack model. The sources of this size dependence have been carefully analyzed by Guinea, Planas, and Elices [194, 195], who suggested how the size dependence of G_F could be mitigated. As for G_f, it may be expected to be essentially size independent because it is approximately equal to J_{el} (the energy associated with the formation of two new crack surfaces), which is size independent [166]. Thus, the size dependence of G_F appears to be

caused by the tail of the stress- displacement curve. The size dependence implies that the stress-displacement curve $f(u)$ cannot be unique, contrary to the basic hypothesis of the cohesive crack model [166]. The importance of G_f is that it solely controls the maximum load at the onset of fracture and is size independent [196].

According to Bazant [21], for the scaling and size effects, it is important to realise that the fracture energy and the material strength imply the existence of a fracture characteristic length. In view of the bi-linear approximation, $f(u)$ possesses two fracture characteristic lengths [21]

$$\ell_1 = \frac{E' G_f}{{f_{tu}}^2} \tag{9.4}$$

$$\ell_{ch} = \frac{E' G_F}{{f_{tu}}^2} \tag{9.5}$$

In theory, the complete fracture process can be described, once the three parameters to model fracture using a cohesive crack model; G_F, G_f, f_{t0} or ℓ_{ch}, ℓ_1, f_{tu} are known (not forgetting that these may be geometry dependent). For practical use the fictitious crack model is used widely in the FE analysis of concrete structures.

9.6.2 Crack Band Models

One concern of the cohesive crack model is that the micro-cracking and crack bridging is not continuous and that it does not necessarily develop in a narrow discrete region in line with the continuous crack. As such, it has been proposed, by Bazant et al. [189], that the tension-softening relation $f(u)$ can be equally well approximated by a strain-softening relation $f(\varepsilon)$, i.e. a decreasing stress with increasing inelastic strain. The tension-softening behaviour is considered in a "smeared" manner, where the strain is related to u and G_F, so that the ultimate strain at rupture, ε_c, is related to u_c. In other words, ε_c is a fracture criterion. To relate the inelastic strain ε to u and G_F, a band of width h is introduced, in which the micro-cracks are distributed.

Typically, in a FE analysis, the micro-cracks are assumed to be smeared over an element, where the whole element fractures when the uniaxial tensile strength

limit is reached. The softening response relationship is according to the $f(\varepsilon)$ function, where the element loses its ability to carry any load when ε_c is reached.

9.6.3 Brittleness and Size Effect

In the non-linear quasi-brittle fracture models that were described above, the brittleness of the material is not characterised by the material fracture toughness, but by a parameter that is a function of the maximum normal tensile strength f_{tu} and the fracture energy G_F. This is an important observation. The aforementioned size effect of quasi-brittle fracture, which was observed by Bazant [21], is said to be dependent on the ratio D/ℓ_{ch}. To recap, D is the dimension of the with crack cross-section [189] and ℓ_{ch} the characteristic length, dependent on the intrinsic brittleness of the *material* (the brittle response of a structure should not be confused with the intrinsic brittleness of the material). Since the characteristic length is said to be a function of G_F and f_{tu} (Equation 9.5), the brittleness of a quasi-brittle *structure* increases with an increase in the intrinsic brittleness, which is characterised respectively by a decrease in ℓ_{ch} and u_c, and the increase in dimension D.

It is further understood that the elastic–perfectly plastic constitutive law (Figure 9.4a) is not appropriate for describing the localisation of damage into a crack, nor the brittleness, in the sense that no "metallic plasticity" exists. Even the strain-softening constitutive laws (Figure 9.4b) do not suitably simulate the localisation phenomena, especially for reproducing dimensional effects. Only a double constitutive law which uses stress and strain up to the maximum load, and stress and crack opening in the softening stage (Figure 9.4c) can be useful for this purpose [21].

To explain this size effect, Karihaloo [22] took an analogy of three bars of the same material but of different lengths under tension (Figure 9.5a). The structure stiffness of each bar decreases with the increase in length, however, the peak-stress f_{tu} and dissipated energy W (of each bar structure) must remain constant, since the net work $W = G_F A$ (A is the cross-sectional area). If a linear softening response is assumed, then the triangle formed by the elastic branch, the softening branch, and the axis Δy, where Δy is the total elongation of the bar, must always contain the same area, i.e. energy. The maximum elongation Δy_c must also be the same, since failure is governed by the u_f, the terminal point of the softening curve. As a result, as soon as the stiffness of the bar falls below f_{tu}/u_f so that

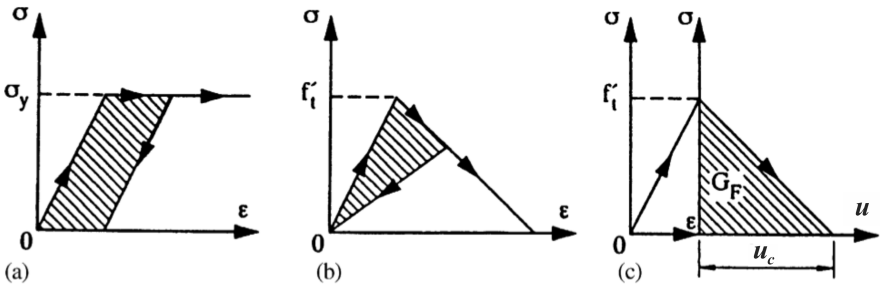

Figure 9.4 – Material constitutive laws: (a) elastic–perfectly plastic; (b) strain softening; and (c) cohesive with linear softening (from Ref. [22]).

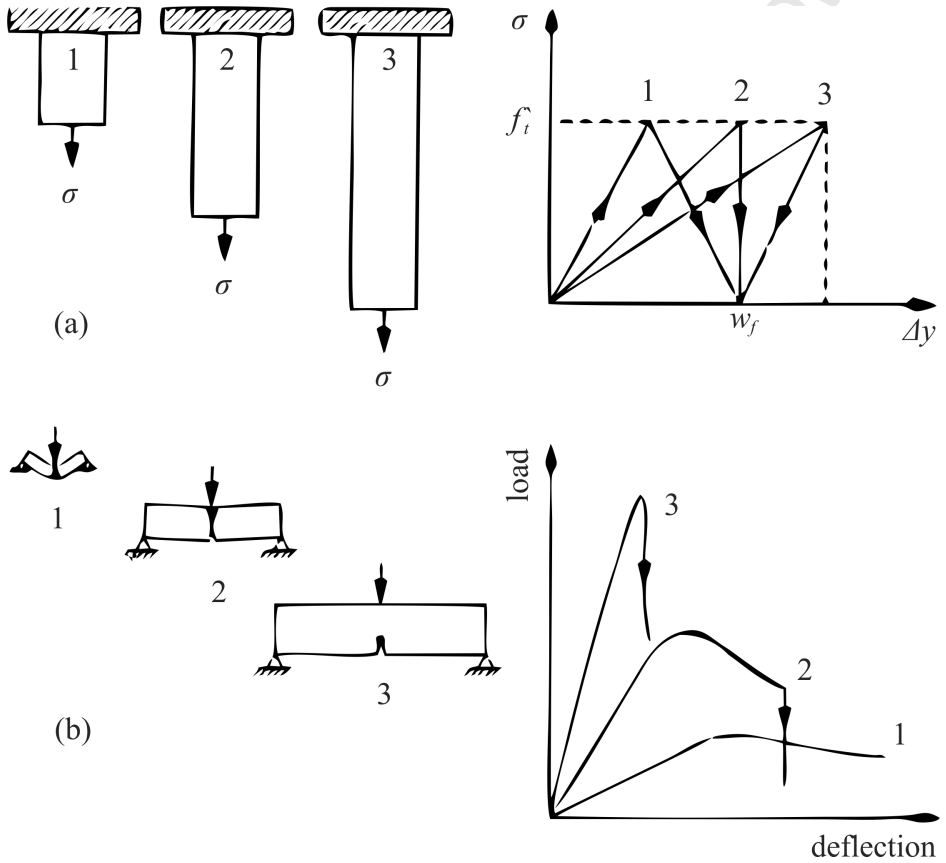

Figure 9.5 – (a) The response to uniaxial tension may be unstable or catastrophic depending on length of bar and (b) ductile–brittle dimensional transition in three-point bend tests. 1, 2 and 3 represent ductile, ductile-brittle and brittle structural behaviour respectively. In (b) these correlate to stable, stable-unstable and unstable crack propagation respectively (from Ref [22]).

its length exceeds $\ell_1 = Eu_f/f_{tu}$; the softening branch takes on a positive slope and represents a particularly unstable failure phenomenon, called "snap-back" (Figure 9.5a, bar #3). The term "snap back" used by Karihaloo [22] is somewhat ambiguous, however, it does facilitate for catastrophic failure. The ratio of stored elastic energy prior to failure versus the dissipated energy due to failure governs whether fracture is more ductile or brittle in nature. Since the failure stress and the critical displacement remain constant, failure occurs when either is reached, provided the net energy dissipation remains during failure (i.e. area under the load displacement curve in (Figure 9.4a).

The same transition from ductile to brittle response can also be noticed in structures of complex form as the dimensions increase but the geometric ratios remain unchanged. The load-deflection curve of three-point bend specimens is shown in Figure 9.5b. Similarly to the above analogy, brittle fractures can be interpreted through a virtual "snap-back" branch. It is not the individual values of G_F and f_{tu} that determine the degree of brittleness or ductility of a structure, but their non-dimensional function—the brittleness ratio ℓ_{ch}/D [21].

9.6.4 Continuum-based Approaches

Continuum damage models have the ability to represent the progressive evolution of micro-cracks and nucleation and growth of voids with the use of a set of material state variables. These alter the elastic and/or plastic behaviour of the quasi-brittle material in their entirety at a macroscopic level and thus allow for a size independent formulation. Continuum-based approaches prove useful in the application of finite sized structures such as specimens [21]. It is worth mentioning that continuum-based approaches are not discrete methods and, as such, not a fracture mechanics methodology. However, the continuum-based approach can rely on the same fundamental material behaviour characterised by fracture mechanics. The practical implementation of continuum damage models is very similar to the plasticity theory used for metals, where yield or failure surfaces, in conjunction with a flow/hardening rule, need to be defined. Their implementation is through the FE method.

There are two types of continuum damage models. These may be distinguished by their ability to account for "plastic" deformations. Earlier models allow for no residual damage, irrespective of the degree of damage suffered, whereas more recent models recognise the need for "plastic" deformations. The first, the standard

damage model, is rather an unrealistic representation of quasi-brittle fracture (as discussed in the previous section) and thus this work predominantly focuses on the later, coupled plasticity and damage models. Again, the section below only provides the reader with an introduction into continuum-based approaches. The damaged plasticity (DP) model for concrete and other quasi-brittle materials is presented. The reader who is not familiar with the theory of plasticity is referred to Chapter 2.

Plasticity Theory

Plasticity is a tool for describing elastic-plastic material behaviour. Commonly utilised in metallic materials, many problems involving quasi-brittle materials have been quite successfully treated by means of plasticity theory [197]. The procedure is to apply the plasticity theory in the compression zone and treat the zones in which at least one principal stress is tensile by one of several versions of fracture mechanics [197].

Like most plasticity models, the DP model defines a yield criterion. The yield criterion is defined by a surface (if a three dimensional problem is assumed) which defines the boundary of elastic behaviour. The evolution of the yield function, with plastic deformations, depends on the flow/hardening rule. The yield functions in biaxial tests (i.e. plane stress) on concrete are illustrated in Figure 9.6. The size of these yield functions are based on the material properties defined for the uniaxial behaviour. In uniaxial tension, the material is normally defined to be elastic up to the tensile strength and is also equal to the failure surface. In concrete, the biaxial compressive meridian yield surface hardens according to a prescribed flow rule [198]. This is discussed later (Figure 9.6).

Several different yield criteria have been defined for quasi-brittle failure. In Figure 9.7 (from Ref [21]) some common failure surfaces are presented together with experimental concrete data from Kupfer and Gerstle [199]]. For steel, the Von Mises failure criterion is most commonly utilised (Figure 9.7a), whereas the yield criteria most often utilised for quasi-brittle materials is the Drucker-Prager or Mohr-Coulomb criteria (Figure 9.7b and Figure 9.7c, respectively).

Since the DP model allows for plasticity, the strain tensor is decomposed into an elastic part and a plastic part. Thus, under uniaxial tension, the stress-strain response follows a linear-elastic relationship to the point of the failure stress f_{tu}. The failure stress corresponds to the onset of micro-cracking. Beyond this,

the formation of micro-cracks is represented macroscopically with a softening stress-strain or stress/displacement response (as discussed in the previous section). Under uniaxial compression the response is similar, however is typically characterised by stress hardening, after yielding f_{c0}, followed by strain softening beyond the ultimate stress f_{cu}. Since quasi-brittle failure is said to be rate dependent, a rate-dependent model is assumed. The stress is a function of the strain and strain rate.

$$\sigma_t = f(\tilde{\varepsilon}_t^{pl}, \dot{\varepsilon}_t^{pl}, f_i) \tag{9.6}$$

$$\sigma_c = f(\tilde{\varepsilon}_c^{pl}, \dot{\varepsilon}_c^{pl}, f_i) \tag{9.7}$$

where the subscripts t and c refer to tension and compression, $\tilde{\varepsilon}^{pl}$ the equivalent plastic strains, $\dot{\varepsilon}^{pl}$ the equivalent plastic strains rates, and f_i are other predefined field variables, like temperature, etc.

The connection between the yield surface and the stress-strain relationship is determined by a flow rule. In a simple case, the plastic potential function coincides with the yield surface and plastic flow develops normal to the yield surface (associated flow). However, quasi-brittle failure experiences non-associated flow (the plastic potential does not coincide with the yield criterion) and two separate functions are required [200]. An example of a plastic potential function is illustrated in Figure 9.8. This function is the Drucker-Prager hyperbolic plastic potential function and is typically used for the quasi-brittle damaged plasticity model [23]. It is worth pointing out for the later sections of this chapter, that in plasticity theory, if a three dimensional problem is assumed, the principle stresses are generally visualised in the p - q plane (p being the hydrostatic pressure and q the Von Mises criterion).

Damage Theory

The progressive evolution of micro-cracks, nucleation and growth of voids are represented in quasi-brittle damage models by a set of variables that alter the elastic and/or plastic behaviour at the macroscopic level. When the material is

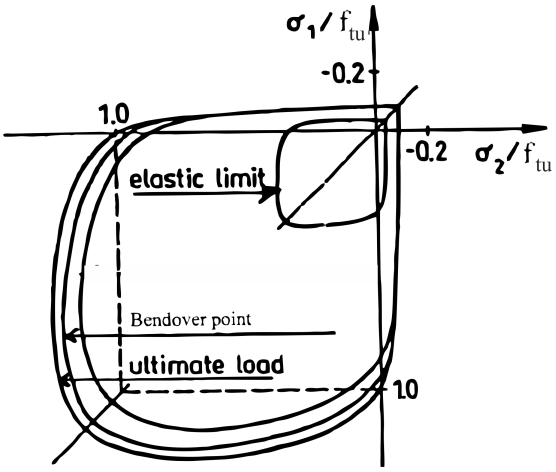

Figure 9.6 – Typical loading curves under biaxial stresses of concrete (from Ref [22])

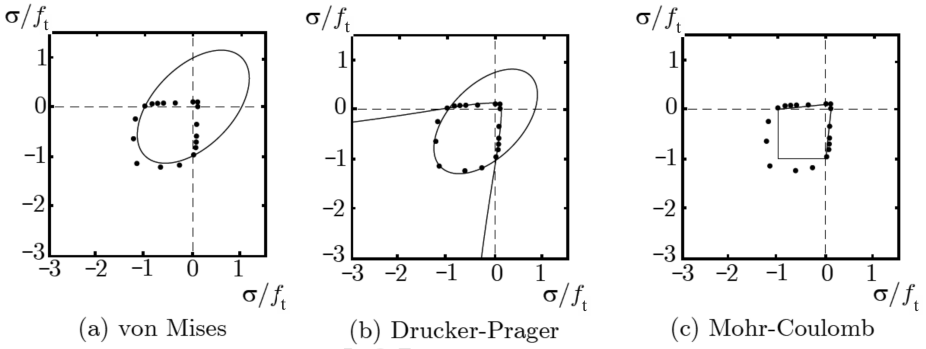

Figure 9.7 – Yield criteria for biaxial stress state illustrated for plane stress state (from Ref [21])

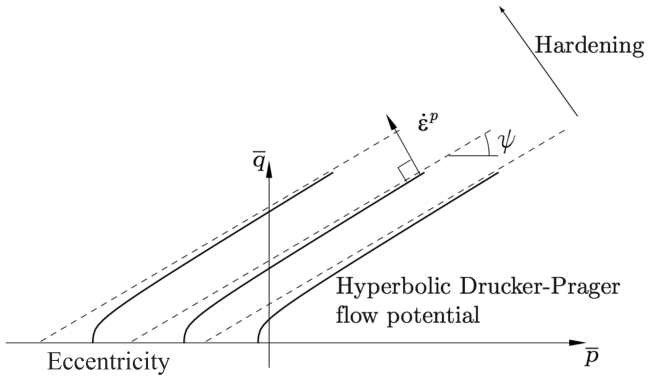

Figure 9.8 – The Drucker-Prager hyperbolic plastic potential function in the meridional plane (from Ref [23]).

loaded beyond the yield criterion, the elastic stiffness of the material degrades. i.e. micro-cracking occurs.

In damage models the total stress-strain relation has the following form

$$\sigma = \mathbf{E}^s : \varepsilon \tag{9.8}$$

where σ is the stress tensor, ε is the strain tensor. The stiffness tensor $\mathbf{E}^s$ of the damaged material depends on a number of internal variables which can be tensorial, vectorial or scalar. If scalar, isotropic damage is assumed, damage may be characterised by scalar damage variables, d_t and d_c, for the tensile and compressive meridian respectively. These are also assumed to be functions of the plastic strains and the additional field variables. The damage variables take values from zero, representing the undamaged material, to one, which represents total loss of strength, i.e. a macro-crack.

$$d_t = f(\tilde{\varepsilon}_t^{pl}, \dot{\varepsilon}_t^{pl}, f_i); \quad 0 \leq d_t \leq 1 \tag{9.9}$$

$$d_c = f(\tilde{\varepsilon}_c^{pl}, \dot{\varepsilon}_c^{pl}, f_i); \quad 0 \leq d_c \leq 1 \tag{9.10}$$

If E_0 is the initial (undamaged) elastic stiffness of the material, the stress-strain relations under uniaxial tension and compression loading are, respectively (as shown in Figure 9.9)

$$\sigma_t = (1 - d_t)E_0(\varepsilon_t - \tilde{\varepsilon}_t^{pl}) \tag{9.11}$$

$$\sigma_c = (1 - d_c)E_0(\varepsilon_c - \tilde{\varepsilon}_c^{pl}) \tag{9.12}$$

The model requires the specification of the tension softening and compression stiffening degradation by means of a post failure stress-strain relation or by applying a fracture energy cracking criterion (similar to the cohesive crack model). The implementation of the continuum-based approach is through the FE method.

Like the cohesive crack model and the crack band model the approach requires the definition of a characteristic length [23]. For this, the characteristic crack length is based on the element geometry and formulation. A typical length is taken as a line across an element for a first-order element and half of the same typical length for a second-order element.

9.6.5 Discussion

The quasi-brittle fracture models that have been discussed are some of the more common methodologies utilised to model quasi-brittle fracture. Adaptions to the cohesive crack models and crack band models exist to account for size effects experienced in quasi-brittle fracture. Through these corrections the generation of R-curve behaviour that is a true material behaviour is enabled [21]. To this day though, in literature, not one universal model exists that, in every aspect, can perfectly describe quasi-brittle fracture [201]. This being said, these models describe quasi-brittle fracture well in most applications. These models have recognised that a softening behaviour due to micro-cracking exists, which contributes significantly to the way quasi-brittle materials fracture.

These failure mechanisms have also been observed in polycrystalline graphite. In fact, the previous two chapters (Chapter 7 and 8) have established that graphite fracture is associated with the typical aforementioned quasi-brittle failure mechanisms. It thus follows that the existing fracture models may be utilised to model the fracture of graphite. It is worth mentioning that each of the methodologies presented that have been used to model the fracture of quasi-brittle materials have their own advantages and disadvantages. The aim of this work was not to assess each methodology, but to choose, what is believed to be, the most appropriate methodology to model graphite fracture. For further reading on quasi-brittle fracture models the reader is referred to Yu et al. [202].

The continuum-based approach and more specifically a damaged plasticity model for concrete and other quasi-brittle materials is believed to represent graphite fracture best. The argument for this is summarised below:

- According to Bazant [21] small structures (relative to their FPZ length) are best modelled using continuum-based approaches.
- The fracture mechanisms of graphite in tension (as well as in compression [203]) are associated with stiffness degradation as well as with inelastic de-

formations. Unlike discrete models, the damage plasticity model allows for the degradation of the bulk material and not only at a predefined flaw/crack.

- Damage plasticity models allow for the capture of the effects of irreversible damage associated with the failure mechanisms that occur.
- Since the predictions in crack patterns and deflections and especially the FPZ length can differ considerably (and hence rely on the mesh), discrete models often give too stiff behaviour after cracks have initiated [201]. Continuum-based models simulate crack propagation as the degradation of the bulk material, irrespective of location and orientation, and hence do not experience stiffening behaviour.
- The damage plasticity model allows for a loading-unloading scenario, where the accumulation of damage is associated with irreversible deformations in the load-displacement curve.
- Material degradation is said to occur at approximately 1/3 of the peak load in medium grained polycrystalline graphite [17]. The damage plasticity model allows for this.
- ABAQUS ® version 6.9, a commercially available FE software, provides the ability to model damaged plasticity for concrete and other quasi-brittle materials [23]. Thus, no additional coding of computation algorithms (such as the JMAN methodology presented in Chapter 6) was required for the graphite fracture model.

In light of the above argument, a continuum-based model for quasi-brittle materials was chosen in the attempt to build a model for graphite fracture. It is worth mentioning that this model was first proposed to model concrete fracture by Lubliner [197], but has since gained popularity in other quasi-brittle applications [22].

9.7 Damaged Plasticity Model for Gilsocarbon

The above section established that a failure model exists that can, to a certain degree of accuracy, model fracture in quasi-brittle materials. It was established that the fracture behaviour that these quasi-brittle fracture models are based on,

are very similar to the fracture behaviour observed and analysed in polycrystalline graphite in this work. The non-local continuum-based model provides a tool for modeling quasi-brittle fracture and is shown to provide a tool for modeling medium grained polycrystalline graphite fracture consistently.

9.7.1 Introduction

The non-local DP model utilised here to model graphite failure is based on the model proposed by Lubliner et al. [197], modified by Lee and Fenves [204] and is available in the Abaqus ® version 6.9 environment (defined as "Damaged plasticity model for concrete and other quasi-brittle materials"[23]). The full analytical derivation can be found in Lee and Fenves [204]. It is worth mentioning that the DP model, at this point in time, assumes an isotropic material. Therefore, only the behaviour of Gilsocarbon (IM1-24) can be modeled (as Gilsocarbon is a near isotropic material with an anisotropy factor of 1.03 [88]). Anisotropy modification to the DP model exist [205, 206], however these are currently not available in Abaqus ® version 6.9.

In this section an overview of the main ingredients of the model are given. This is followed by identification of parameters, the modeling procedure and the results. Two dimensional CT and 3PB specimen simulations are presented. The material properties utilised for the DP model, unless specified otherwise, are according to the properties specified in Chapter 5 for IM1-24 (Gilsocarbon). It is worth noting that the DP model that is available in Abaqus ® version 6.9 [23] is capable of three dimensional analysis. This being said, the problems presented in this work are two dimensional. With the current available computational capabilities (at the University of Manchester) a three dimensional analysis, with a refined mesh, would typically require around 3 weeks to complete (on a server cluster of 4 CPU's each running at a 2.8 GHz processing capability). Since the graphite fracture model presented here is intended to investigate the possibility of using existing quasi-brittle fracture models for graphite failure (and due to the time constraints) a two dimensional plane stress analysis was undertaken.

9.7.2 Model Definition

The model is based upon the continuum-based approach described in the previous section. It uses concepts of isotropic damaged elasticity in combination with

isotropic tensile and compressive plasticity to represent the inelastic behaviour of quasi-brittle materials [23]. The model has been designed for applications in which the material is subjected to monotonic, cyclic, and/or dynamic loading under low confining pressures [23].

In this method the failure is modeled implicitly in the FE environment and consists of a combination of non-associated multi-hardening plasticity and scalar (isotropic) damaged elasticity to describe the irreversible damage that occurs during the fracturing process. This requires the definition of a yield surface and a flow rule that allows the yield surface to expand and change shape as the material is "plastically" loaded. The term "plastically" is used very loosely here, as the material strictly speaking does not undergo plastic deformations. However, failure is associated with irreversible energy dissipation similar to that of metallic plasticity, which can be modelled in a similar fashion. The two main failure mechanisms are tensile cracking and compressive crushing. The tensile softening behaviour is defined as G_f in tensile cracking and as a stress-strain hardening relationship in compressive crushing. The degradation of the elastic stiffness in tension and compression is defined as a scalar variable, which is a function of the cracking strain or displacement.

In the Abaqus environment the user is allowed control of stiffness recovery effects during cyclic load reversals [23]. This option has not been considered in the presented graphite failure model. Additionally, graphite failure can be defined as being sensitive to the strain rate., however, a static, strain rate independent, model is assumed.

Yield Criterion and Non-Associate Flow Rule

The group of the constitutive parameters to characterise the yield surface identify the shape of the yield surface and flow potential function. The yield function takes the form of the Drucker and Prager yield criterion, first utilised by Lubliner et. al. [197], then modified by Lee and Fenves [204] to account for different evolution of strength under tension and compression. The evolution of the yield surface is controlled by the two hardening variables $\tilde{\varepsilon}_t^{pl}$ and $\tilde{\varepsilon}_c^{pl}$. In terms of effective stresses, the yield function takes the form [23]

$$F = \frac{1}{1-\alpha}\left(\bar{p} - 3\alpha\bar{p} + \beta(\tilde{\varepsilon}^{pl})\left\langle\hat{\bar{\sigma}}_{max}\right\rangle - \gamma\left\langle-\hat{\bar{\sigma}}_{max}\right\rangle\right) - \bar{\sigma}_c\left(\tilde{\varepsilon}_c^{pl}\right) \leq 0 \qquad (9.13)$$

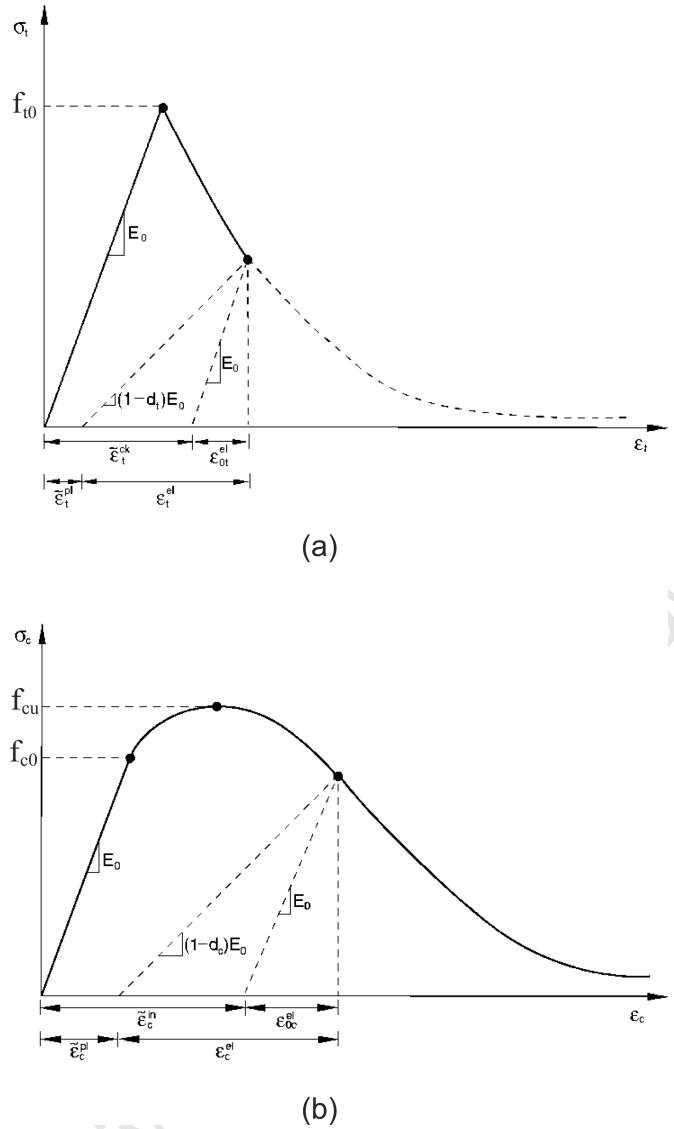

Figure 9.9 – Softening response to uniaxial loading in (a) tension and (b) compression (from Ref [23]).

where, α, β and γ are dimensionless constants, $\langle \hat{\sigma}_{max} \rangle$ is the algebraic maximum principal stress, $\bar{p}$ the hydrostatic pressure, which is a function of the first stress invariant I_1 (defined as $\bar{p} = I_1/3$), and $\bar{q}$ the Von Mises equivalent stress, described as $\bar{q} = \sqrt{2J_2}$ (where J_2 is the second deviatoric stress invariant). α, β and γ are given as [23]

$$\alpha = \frac{(f_{b0}/f_{c0}) - 1}{2\,(f_{b0}/f_{c0}) - 1} \tag{9.14}$$

$$\beta = \frac{f_{c0}}{f_{t0}}(\alpha - 1) - (1 + \alpha) \tag{9.15}$$

$$\gamma = \frac{3(1 - \kappa_c)}{2\kappa_c - 1} \tag{9.16}$$

κ_c is the ratio of the second stress invariant on the tensile meridian to that on the compressive meridian at initial yield for any given value of the pressure invariant such that the maximum principal stress is negative (the default value is 2/3 [23]). Since a two dimensional problem is assumed here (plane stress), the parameter γ, which is based on the full triaxial tests, is of little significance [204].

To compute the non elastic stress-strain behaviour, the plastic-damage model assumes non-associated potential flow as [23]

$$\dot{\varepsilon}^{pl} = \lambda \frac{\partial G(\bar{\sigma})}{\partial \bar{\sigma}} \tag{9.17}$$

where, the flow rule G is the Drucker-Prager hyperbolic function (which was illustrated in Figure 9.8) [23]

$$G = \sqrt{(\epsilon_{cc} f_{t0} tan\psi)^2 + \bar{q}^2} - \bar{p} tan\psi \tag{9.18}$$

where ϵ_{cc} is the eccentricity which defines the rate at which the plastic potential function approaches the asymptote (Increasing the eccentricity provides more curvature to the low potential). ψ is the dilation angle (measured in the $\bar{p}$ - $\bar{q}$ plane at high confining pressure). The reader is referred to Figure 9.8 for a visual representation of eccentricity and dilation angle.

Loading Behaviour

The post-yield behaviour is defined by a strain-hardening/softening behaviour. This is done by means of a stress-strain relation or by applying a fracture energy cracking criterion (introduced in the cohesive crack model). For a stress strain relation, a cracking strain $\tilde{\varepsilon}_t^{ck}$ is defined as the total strain minus the elastic strain corresponding to the undamaged material (Figure 9.9). Tension softening data needs to be provided in terms of the cracking strain [23].

$$\tilde{\varepsilon}_t^{pl} = \tilde{\varepsilon}_t^{ck} - \frac{d_t}{1 - d_t} \frac{\sigma_t}{E_0} \tag{9.19}$$

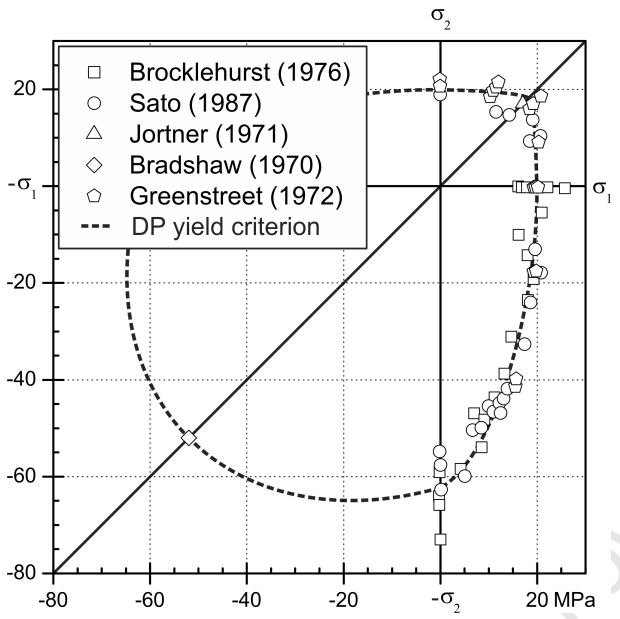

(a)

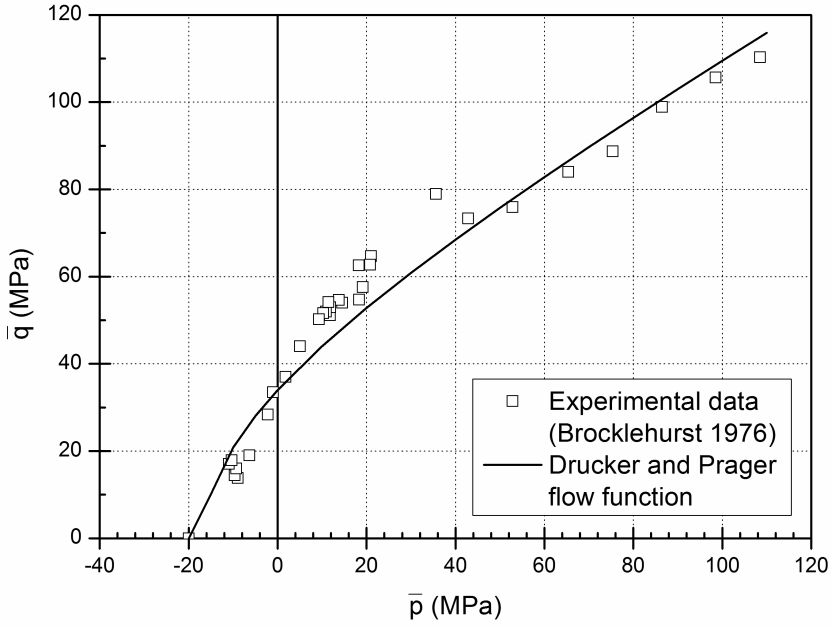

(b)

Figure 9.10 – (a) Biaxial failure data for IM1-24. The data was extrapolated from Brocklehurst [24], Sato et al. [25], Jortner [26], Bradshaw [27] and Greenstreet [28]. (b) Drucker-Prager hyperbolic plastic potential function in the meridional plane. Experimental data was extrapolated from Brocklehurst [24].

Alternatively the post-yield behaviour may be defined according to the energy criterion described earlier (the energy required to open a unit area of crack) [23]. According to the aforementioned methodology, quasi-brittle behaviour is characterised by a stress-displacement response. This fracture energy can be invoked by specifying the post-yield stress as a function of cracking displacement, or alternatively, the fracture energy G_f. The tensile damage is converted to a cracking displacement value using a relationship where the specimen length l is assumed to be one unit length in FE implementation [23].

$$u_t^{pl} = u_t^{ck} - \frac{d_t}{1 - d_t}\frac{\sigma_t l}{E_0} \tag{9.20}$$

The DP model requires the specification of the tension softening and compression stiffening degradation by means of a post failure stress-strain relation or stress-displacement relation.

9.7.3 Identification of Parameters for the DP Model

The numerical strategy for solving the non-local DP problem requires knowledge of the aforementioned constitutive material parameters. These parameters describe the material properties and govern the behaviour of the model. These include the definition of the yield surface, the flow rule, the load response and the material degradation (the DP model assumes a scalar damage variable in both compression and tension).

Yield Surface and Flow Rule

Three independent material strength data are required to determine the biaxial yield criterion using Equation 9.13: (1) the tensile yield stress f_{t0}, (2) the compressive yield stress f_{c0} and (3) the uniaxial compressive yield stress to biaxial yield compressive stress ratio f_{b0}/f_{c0}. Since a plane stress problem is assumed, the parameter κ_c (in Equation 9.16) was assumed as the default value of $2/3$ [23].

The plane stress cross section for the failure surface in the principal stress space is shown in Figure 9.10a for IM1-24. The data in Figure 9.10a was extrapolated from literature of various sources on the biaxial behaviour of IM1-24. These are listed in the caption which predominantly include data from Brocklehurst [24]. The typical uniaxial compressive yield stress to biaxial yield compressive stress

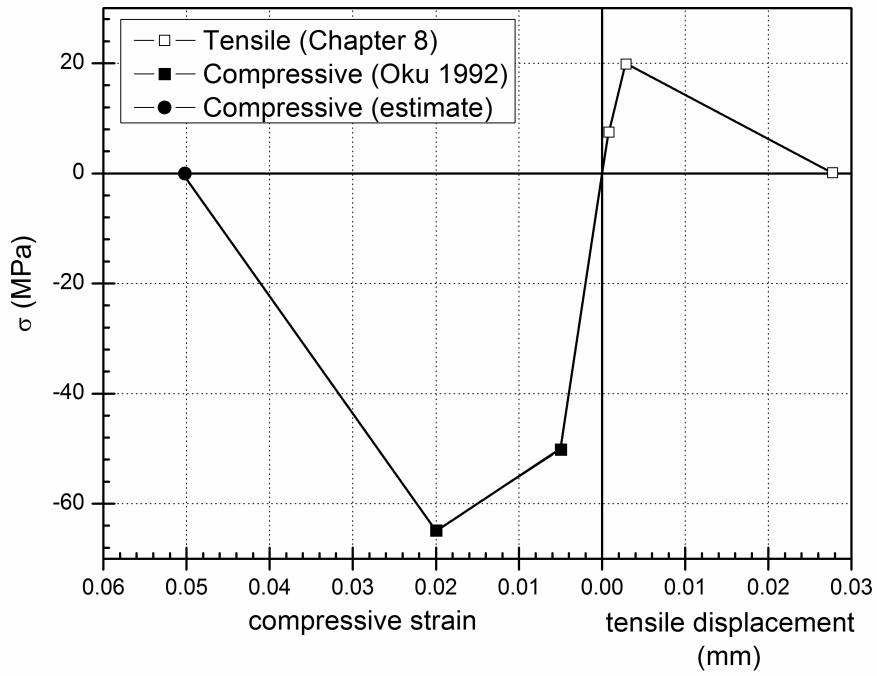

Figure 9.11 – Softening behaviour of IM1-24. Tensile softening as a stress-displacement relationship (from Chapter 8) and compression in stress-strain relationship (from Oku [29]).

ratio was shown to be of the order of 0.81 [27]. The figure shows that the Ducker-Prager criterion is an excellent fit of the failure data. The constitutive parameters are summarised in Table 9.1.

It is worth mentioning that the DP model requires the yield criterion and not the failure surface as shown in Figure 9.10a. Since the yield surface expands with plastic deformation to form the failure surface, a yield surface may be extrapolated according to uniaxial yield criteria [22].

Quasi-brittle materials are known to undergo a significant volume change (dilatancy), which is caused by the large amount of the inelastic strain. The dilatancy can be modeled by the numerical model. It is noted that the dilatancy is controlled by the ψ parameter in the flow function according to Equation 9.18. The values ψ and the eccentricity ϵ_{cc} are accepted to fulfil the best fitting of the curve (in the meridian plane) to the experimental data (see Figure 9.10b). The experimental data was extrapolated from Brocklehurst [24, 76]. The dilation angle, measured in the p - q plane at high confining pressure, was found at approxi-

mately 30^{o}. Similar values were determined for concrete, where ψ is between 30^{o} to 40^{o} [201]. The parameters are summarised in Table 9.1.

Stiffness Degradation and Calibration with Experimental Data

The tension softening behaviour or post-yield behaviour is defined according to the fracture energy criterion G_f, which is thought to be a material constant (Chapter 8). To recap, G_f can be seen as the energy lost due to the formation of the macro-crack surfaces, i.e. J_{el} [21, 166]. The total fracture energy lost due to fracture G_F includes G_f and the energy which is lost due to the stiffness degradation from micro-cracking [202]. G_F is believed to be size and geometry dependent [166]. G_f for IM1-24 was determined as 250 J/m^2 (in Chapter 8). Additionally, it was also found that approximately 47 J/m^2 of the fracture energy is lost prior to the peak load or macro-crack (in Chapter 7). This energy, is a result of micro-cracking and as such does not contribute to G_f. However, the pre-peak softening behaviour can contribute to the way graphite fractures (Chapter 7) and thus has been incorporated into G_f in such way that the total energy lost remains 250 J/m^2. This is illustrated in Figure 9.11.

Similarly, from the experimental observations of IM1-24 in Chapter 7, it was clear that the degradation of stiffness from micro-cracking occurs and becomes more severe as the strain increases. The degradation damage variable defined in Equation 9.9 assumes the value of $0 \leq d_t \leq 1$. To determine the stiffness degradation behaviour for IM1-24 requires a complex testing apparatus such as the tests done by Gopalaratnam and Shah [207] for concrete. At this point in time this data was not available for polycrystalline graphite and thus a linear evolution of the damage variable with effective plastic displacement. This ensures that when the effective plastic displacement reaches a critical value, the material stiffness will be fully degraded. The parameters are summarised in Table 9.1.

Since the DP model is intended to calculate the load displacement response of CT and 3PB specimens, the compressive load response is not of importance. However, for completeness the data was defined according to Oku [29] for IM1-24. The stiffness degradation behaviour was also defined as a linear evolution of the damage variable with effective plastic displacement. This is shown in Figure 9.11 and the parameters are summarised in Table 9.1.

Elastic Properties:

Young's modulus	E_0	11900 GPa
Poisson's ratio	v	0.21

Yield Surface and Flow Rule:

Dilation angle	ψ	30°
Eccentricity	ϵ_{cc}	4.8
Biaxiality ratio		0.81
Triaxiality ratio	κ_c	0.667

Tension softening:

Stress (MPa)	Cracking Disp. (mm)
6.7	0
20	0.0008
1	0.025

Tension damage:

Scalar damage	Cracking Disp. (mm)
0	0
1	0.025

Compression hardening:

Stress (MPa)	Cracking strain
20	0
65	0.015
1	0.045

Compression damage:

Scalar damage	Cracking strain
0	0
1	0.045

Table 9.1 – The material parameters of DP model for Gilsocarbon (IM1-24)

9.7.4 Model Behaviour

The behaviour of the DP model, using the IM1-24 data, is presented. Simulated is a monotonic uni-axial loading, full cyclic monotonic uni-axial loading and mesh-sensitivity behaviour simulations. It is worth noting that only limited experimental data for IM1-24 is available in current literature and thus, the presented simulations could not be compared to experimental data. However, structural examples of CT and 3PB specimens are presented in the next section, which are compared to experimental data.

The verifications assume linear elastic quadratic full integration elements. The

material properties used for each model are presented in Table 9.1 and represent the non-local DP properties of IM1-24 graphite. The element mesh size of 7.4 x 7.4 mm was used (unless specified otherwise), as it presents the characteristic length of IM1-24 (according to Equation 9.5). The model was implemented in the environment of ABAQUS/Standard.

Monotonic Uni-axial Loading

The DP model monotonic uni-axial loading response is shown in Figure 9.12. No experimental data for monotonic testing is currently available for IM1-24 for comparative purposes (to experimentally determine the stiffness degradation behaviour for IM1-24 requires a complex testing apparatus and was not the scope of this work). The monotonic loading behaviour shows the softening response (plasticity) of IM1-24 and the stiffness degradation (damage). The typical experimentally observed load response of IM1-24 has a very steep post-peak curve. The numerical model cannot yield such a steep post-peak curve because the assumed softening response is constructed from a linear function (see Table 9.1).

Full Cyclic Monotonic Uni-axial Loading

The full cyclic (tension and compression) monotonic uni-axial loading response is shown in Figure 9.13. The load path resembles the hysteresis curve of the simulation results in Figure 9.12, because energy is dissipated during the tensile reloading (path B-C-D). Similar to Lee and Fenves examples [204], this example shows that the present model can simulate quasi-brittle material behavior subjected to cyclic loading for which the hysteresis curve in the tensile region is negligible compared with the compressive counterpart. For both cases (tensile and compression) the degradation of stiffness is simulated at each unloading/reloading cycle as well as the softening behaviour.

Mesh Sensitivity

The sensitivity of the numerical solution to element size is examined, similarly to Lee and Fenves [204], to check the ability of the characteristic length [208] to provide mesh objectivity. Three meshes (mesh A, B, and C) with the same specimen dimensions (14.8 x 7.4 mm) but different element sizes are tested to examine the sensitivity to mesh size, as illustrated in Figure 9.14. The characteristic length,

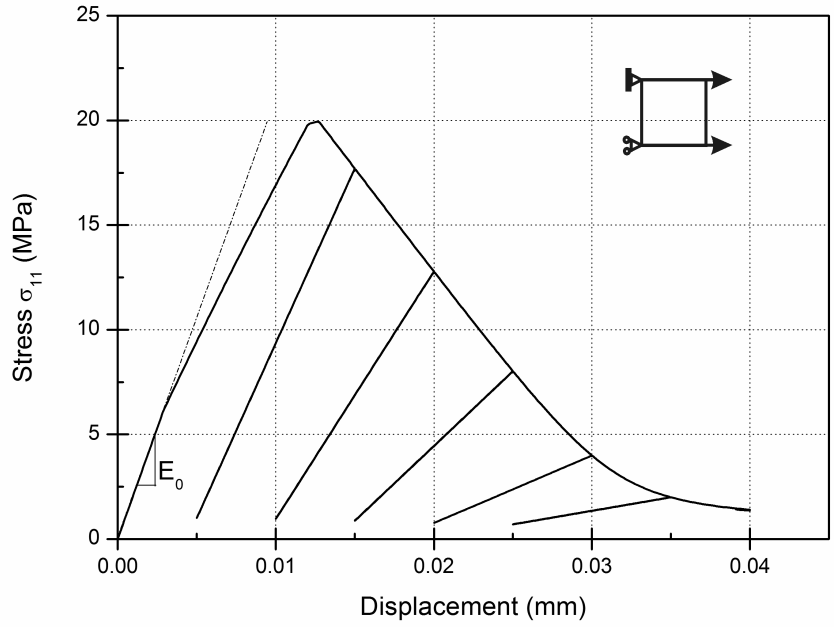

Figure 9.12 – Numerical solution of cyclic uniaxial loading in tension.

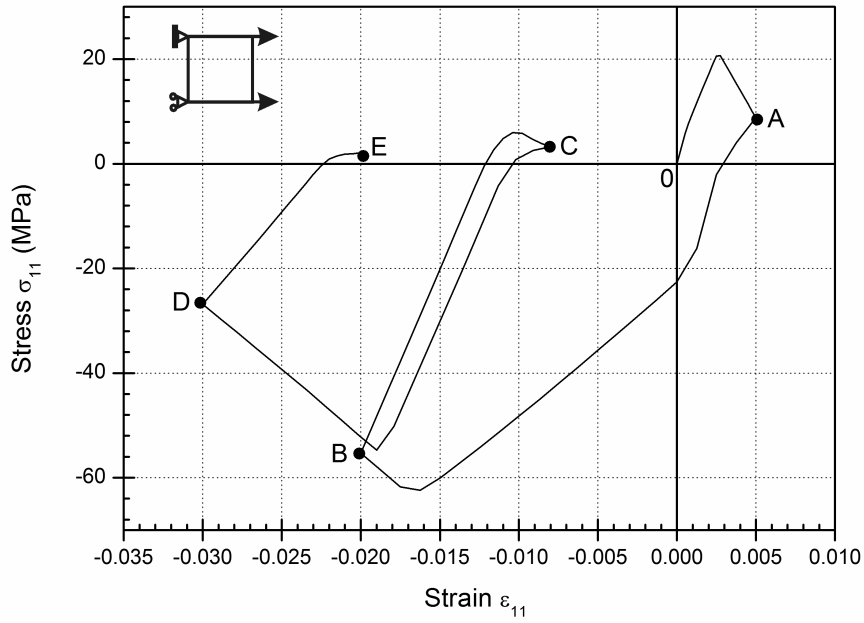

Figure 9.13 – Numerical Solution for Full Cyclic Loading (Path: O-A-B-C-D-E)

which is defined as the element size for each case, was defined accordingly in Figure 9.14; mesh A, 7.4 mm; mesh B, 3.7 mm; and mesh C, 1.65 mm). Figure 9.14 shows the load-displacement curves measured at the right end of each mesh. The softening response of the finer mesh is indicative of a more brittle material. This is because the ratio of the softening compared to the length of elastic unloading zone is different in each mesh case. As a result, the global load-displacement responses cannot be identical, even though the dissipated energy for all three cases is equal [204].

9.8 Structural Examples

The non-local DP model, which has been adapted for IM1-24 graphite, was implemented using three specimen geometries. Although the majority of experimental work undertaken in this project used the DT geometry (see Chapters 7 and 8), the computational examples presented here are 3PB and two CT specimens. An attempt of modelling the DT geometry showed convergence difficulty as the DT geometry is complex and requires a full three dimensional analysis with defined contact (see Chapter 5). As such, the geometries presented here are two dimensional and do not require complex loading configurations, i.e. boundary conditions.

The computations of the standard test geometries were implemented in the environment of ABAQUS/Standard. The models and the computations lead to the estimation of the nucleation and evolution of fracture. The numerical results are in agreement with the experiments provided by Hodgkins [4] and Fazluddin [16]. Of special interest are the regions of localized strains, in which the damage part is active. The scalar damage variable in tension is used to compare crack patterns for the numerical and experimental models. The examples assume linear elastic quadratic full integration elements. The material properties used for each model are presented in Table 9.1, which represent the DP properties of IM1-24.

9.8.1 CT Specimen

The first examples are two CT specimens tested by Fazluddin [16] and Hodgkins [4] respectively. The two considered specimens, which were sized according to ASTM E1820 and BS7448, have slightly different geometry configurations (shown

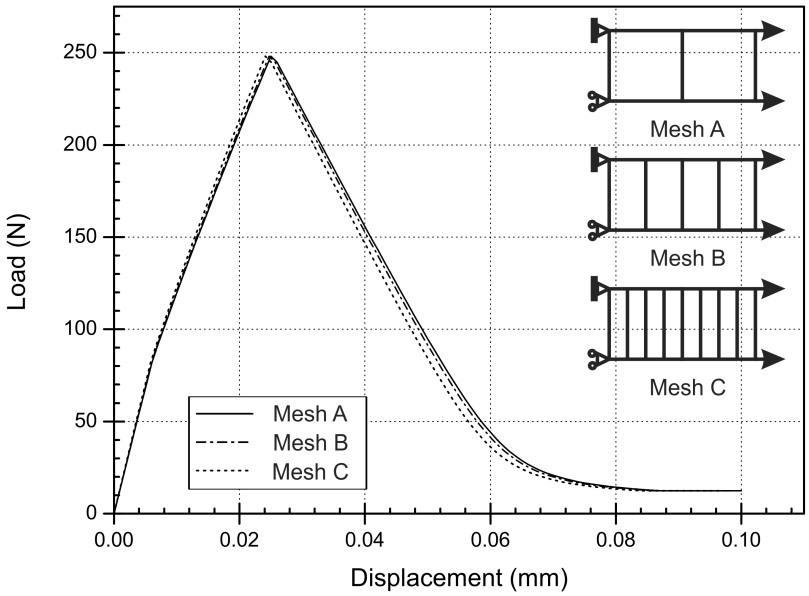

Figure 9.14 – Load-displacement curves for different meshes

in Figure 9.15). For Hodgkins' specimen configuration the width of the rear of the specimen was reduced in order to allow the progression of crack growth to be monitored in three dimensions using X- Ray tomography [4]. The material was IM1-24 graphite for both specimens and the properties are tabulated in Table 9.1. The numerical models consist of 1480 and 1320 four noded linear plane strain elements for Fazluddin's and Hodgkins specimen geometries respectively and only represent the symmetrical half of the CT specimen. To avoid convergence issues, DP elements are utilised in the region in which fracture is expected to occur, the rest is considered as a linear elastic model (see Figure 9.15). Some mesh refinement was performed in the vicinity of the notch-tip. Boundary conditions are applied with an analytically rigid pin with defined hard frictionless contact in displacement control. The load-displacement response of the analyses are compared to the experimental bounds in Figure 9.16. The corresponding active (damaged) regions are shown in Figure 9.17 for Fazluddin's specimen configuration.

The general behaviour is well captured by the simulation for both considered CT specimens (Figure 9.16). The tensile damage localisation at peak load, which is manifested by a reduction of the load accompanied by fracture (single dominant crack), shows similarities to the observations shown in Chapter 7. A FPZ forms in

which the degradation of the material occurs (Figure 9.17). The size of the FPZ was found to be dependent on the pre-peak softening behaviour, which is defined by the tensile softening curve (Figure 9.11). Thus, the size may not correspond to experimental observation, but can provide a comparison tool between different specimen configuration simulations. This will be discussed in the next section.

The experimental data from Hodgkins provided a load-unloading response, which was simulated in Figure 9.16b. The non-local DP model is capable, to a certain degree, of simulating this behaviour. The load-displacement response is, however, not identical. This is because the model does not allow for element removal after an element has failed (i.e. $d_t = 1$, shown in a gray shade in Figure 9.17). Since the stress-displacement behaviour has been defined with a failure stress of 1 MPa due to numerical stability [23], some load carrying capability remains resulting in an inaccurate load-unloading response when fracture has occurred.

9.8.2 3PB Specimen

Similarly to the CT specimen, Fazluddin [16] provided experimental data for 3PB specimens. The FE mesh utilised for the comparison is shown in Figure 9.18. The numerical model consists of 896 four noded linear plane strain elements and, like the CT specimen, only represent the symmetrical half of the specimen. Some mesh refinement was performed in the vicinity of the notch-tip to account for stress concentrations. Boundary conditions are applied with analytically rigid pins with defined hard frictionless contact in displacement control as a three point bend configuration. To avoid convergence issues, DP elements are utilised in the region in which fracture is expected to occur, the rest is considered as a linear elastic model (see Figure 9.18). The load-displacement response of the analyses are compared to the experimental bounds in Figure 9.20. The corresponding active (damaged) regions are shown in Figure 9.19 for Fazluddin's specimen configuration.

As with the CT specimen, the general behaviour is well captured by the analyses. A notable difference is that the tensile damage localisation size exists between the CT and 3PB simulation. The 3PB clearly shows relatively smaller tensile damage localisation ahead of the notch at peak load, which is in agreement with Chapter 8. It was reported that the FPZ is geometry and size dependent.

An additional point worth mentioning concerns the load-displacement response. The 3PB geometry indicates a more brittle response compared to the CT geome-

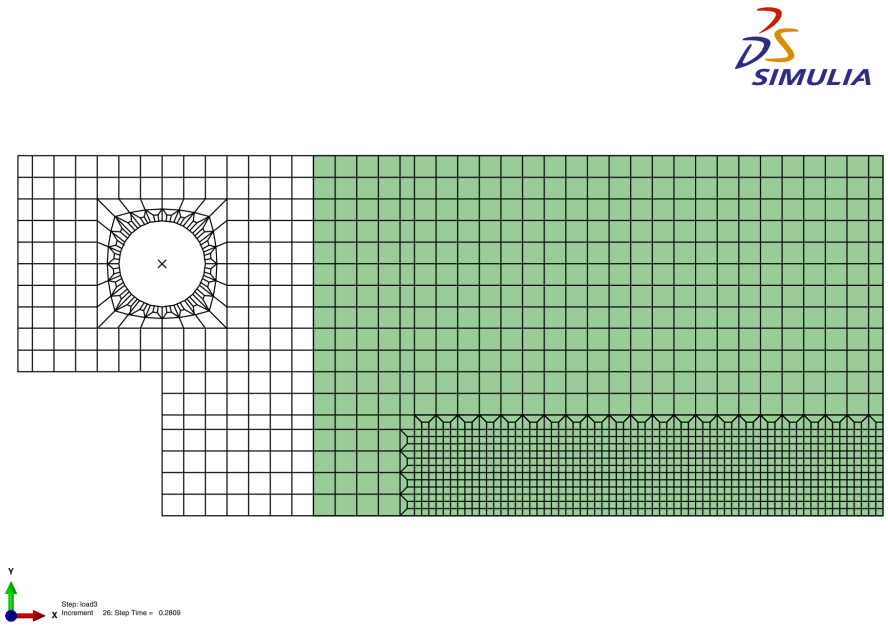

(a)

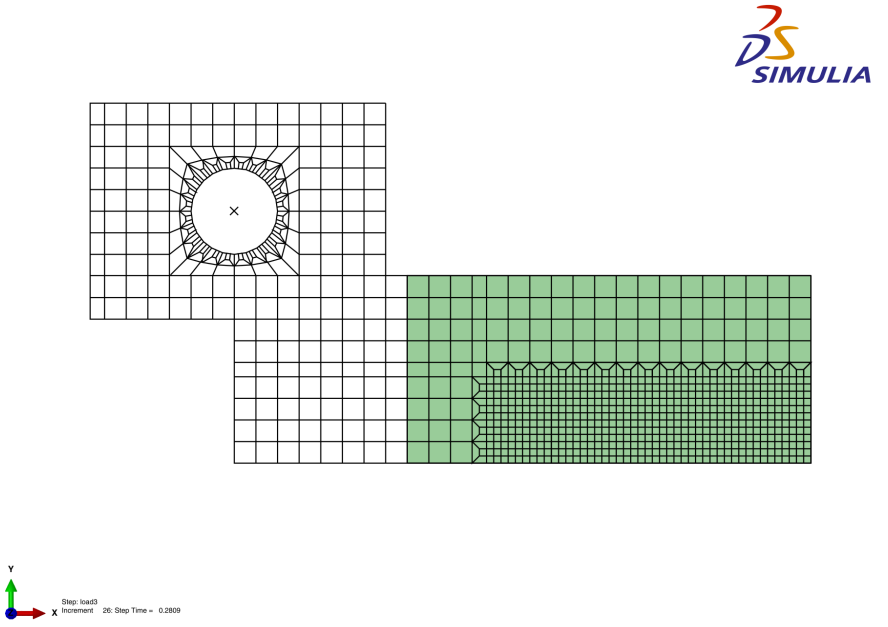

(b)

Figure 9.15 – FE mesh of the two DP simulated CT specimens. (a) according Fazluddin's CT specimen [16] with $W = 50$ mm , and (b) according Hodgkins' CT specimen [4]with $W = 87$ mm. Green elements indicate DP elements and white indicates linear elastic elements.

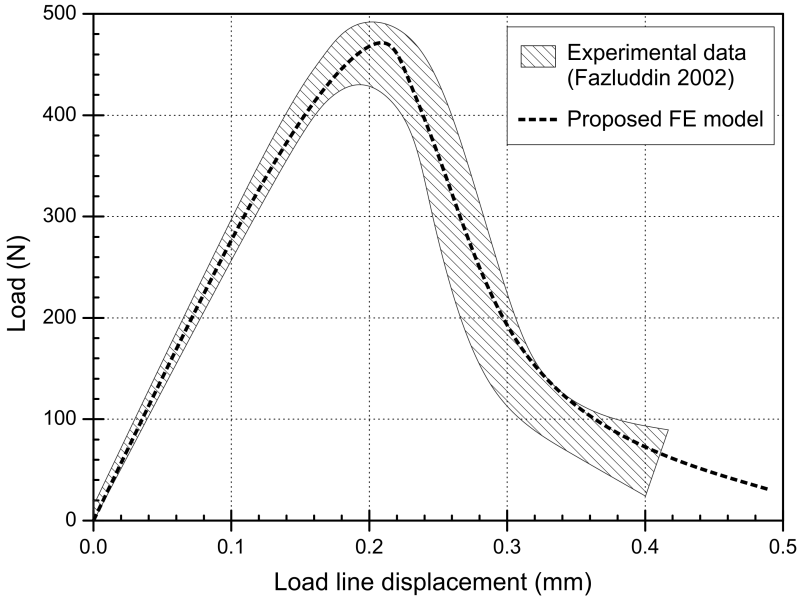

(a)

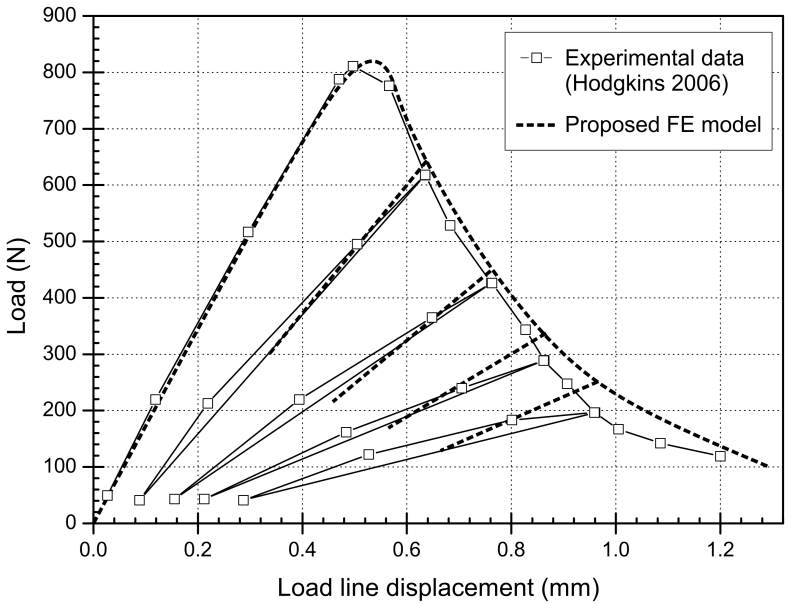

(b)

Figure 9.16 – CT Specimen load displacement curves. Comparison with experimental data of (a) Fazluddin [16] and (b) Hodgkins [4].

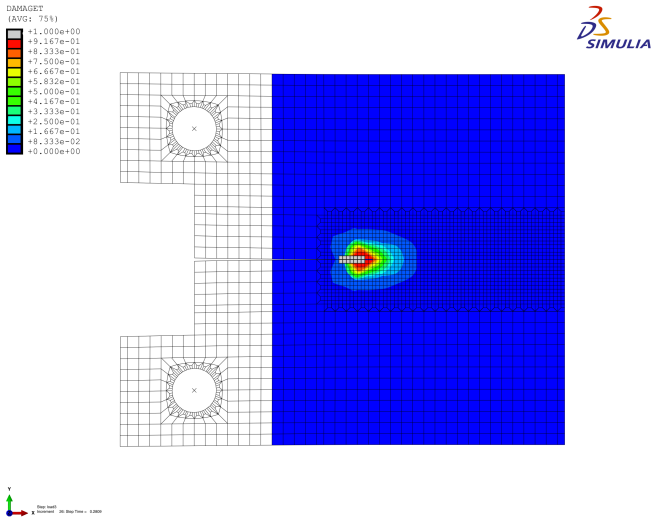

Figure 9.17 – The active (damaged) regions of Fazluddin's CT specimen [16] for the non-local model. Tensile damage variable range $0 \leq d_t \leq 1$. White squared represent linear elastic elements.

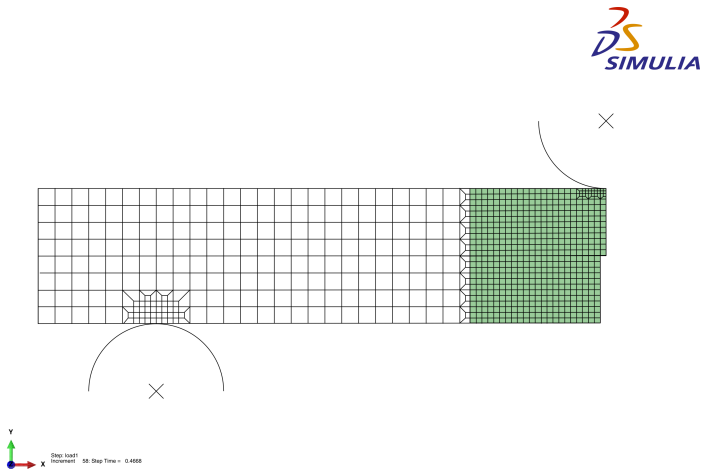

Figure 9.18 – Fazluddin's geometry and loading setup of the three point bending simulation [16]. Green elements indicate DP elements and white indicates linear elastic elements.

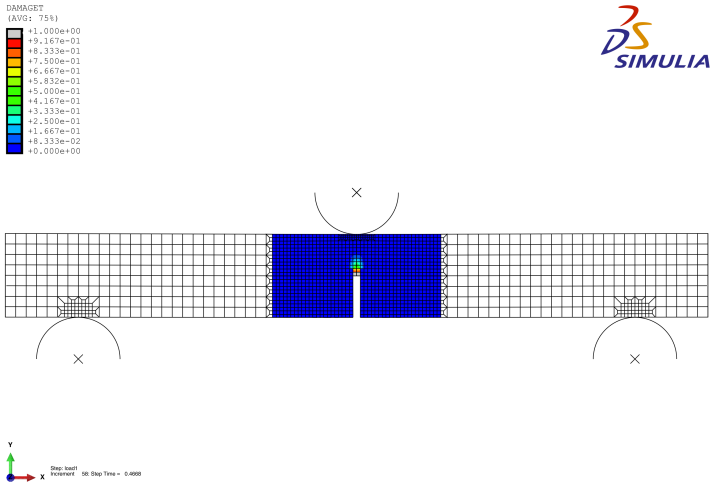

Figure 9.19 – The active (damaged) regions of the Fazluddin's 3PB specimen [16] for the non-local model. Tensile damage variable range $0 \leq d_t \leq 1$. White represent linear elastic elements.

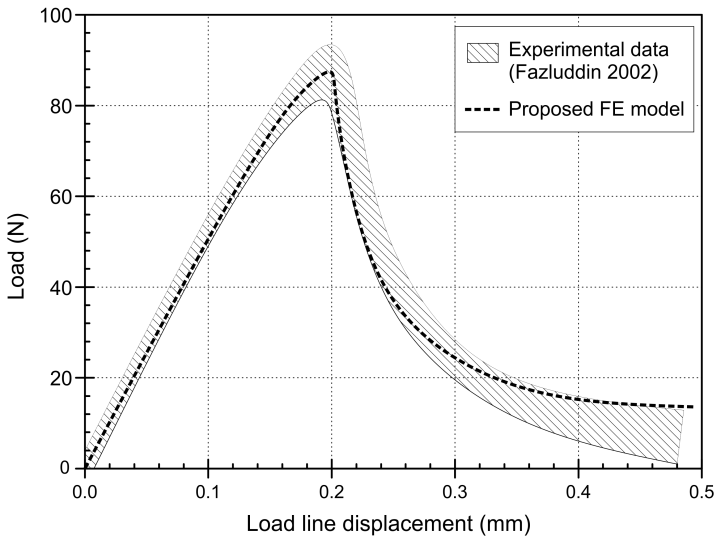

Figure 9.20 – 3PB specimen load-displacement curves. Comparison with experimental data of Fazluddin [16].

try, which is noticeable by the more severe post peak load drop (when comparing Figure 9.16 and Figure 9.20). This observation agrees well with experimental data. In Chapter 8 it was shown that the R-curve behaviour of 3PB specimens shows a more brittle behaviour to that of CT specimens. It was argued that the less brittle response of CT specimens is due to more energy being lost in the FPZ. It was reported that the CT specimen has more pronounced "plastic" deformations and as such a relatively larger FPZ. The computational less brittle response of 3PB specimens shows a similar trend and hence can be attributed to the softening (irreversible energy dissipation) response, i.e. the size of the tensile damage localisation zone.

9.8.3 Discussion

The non-local DP model was shown to estimate fracture more accurately than the commonly assumed EPFM method. The examples have shown that using the DP model enables a proper definition of the failure mechanisms of IM1-24 graphite, including the softening and degradation of the material, and most importantly, since the DP model is a non-local approach, it is size and geometry independent. From a practical point of view, based on the criteria defined in this work and found in literature, it was possible to identify the constitutive parameters of the DP model for graphite. This allowed the numerical modelling to analyse two specimen geometries (CT and 3PB), where the cause for cracking was evaluated and verified against observations and experimental data. The study also served as a link between the real behaviour of polycrystalline graphite and its numerical modelling. On this note, one could argue that the success of the DP model for graphite lies in that both specimen geometries are highly constrained. Thus, further modeling is necessitated to claim the success of the model.

The DP model presented was not the first attempt to model graphite fracture in the context of continuum damage mechanics. Zou et al's [87] presented a phenomenological failure model, based on an interfacial delamination in composite laminates problem, where a damage parameter is employed and the interfacial constitutive law is expressed to take account of the effects of damage. Like with the presented DP model, both the conventional stress based and fracture mechanics based failure criteria are included in the failure model to construct a damage surface. Damage initiates when the stress-based criterion is first satisfied. Zou et al's model however, is a cohesive crack model and as such is confined to a prede-

fined crack path. A linear stress analysis is required to find out the location and direction of the maximum principal stresses, which then allows the likely cracking site and crack growth path be introduced into the FE mesh. The DP model presented in this work is a non-local approach. The bulk material softens; the degradation and fracture initiation occurs at the most damaged location. Hence, the DP model does not rely on a predefined crack path. This is believed to be a more realistic approach as damage, i.e. micro-cracking, can occur at a 1/3 of the fracture load [17].

The DP model parameters, which define the model behaviour, describe the average experimentally obtained graphite behaviour. Based on a plasticity model, the degradation and hence softening of the material is confined to the defined yield criteria and flow rule. If non-exclusively monotonic loading is to be studied, the numerical methods should be able to describe both the stiffness degradation and the plastic deformations that graphite exhibit in experiments. As damage develops, the yield surface shrinks in the stress space, leading to a softening interfacial constitutive law. Fracture has occurred when the work done by the tractions meets the fracture mechanics based criterion. The DP failure model can be viewed as an extension or generalisation of the cohesive zone model proposed by Zou et al. [87], in that it couples together the effects of stress/displacement curves to derive a combined non-local stress and fracture mechanics based failure criterion.

This being said, the experimental observations in Chapter 7 have shown that micro-cracking appears to be in the direction of the maximum principal stress and it is believed that failure occurs as a function of mode I failure [87]. The difference between equi-biaxial and uniaxial behaviour is believed to be dependent on the size and shape of the fracture process zone [209]. This can contribute to the effect of stress state on fracture strength, which should be considered in terms of strain energy release [209]. The biaxial failure behaviour defined by the model, does not rely on the fundamental behaviour but rather on an average observed criteria. Size effects have not been considered in the biaxial failure, which cloud results in erroneous biaxial load simulations. At this point in time the biaxial behaviour of graphite is not fully understood.

A drawback of the presented model was the risk of convergence difficulties which might interrupt a simulation. Some sources of instability can include local yielding, snap-through and localised material failure. Avoiding convergence difficulties was achieved by defining the mesh, boundary conditions and loads so as to min-

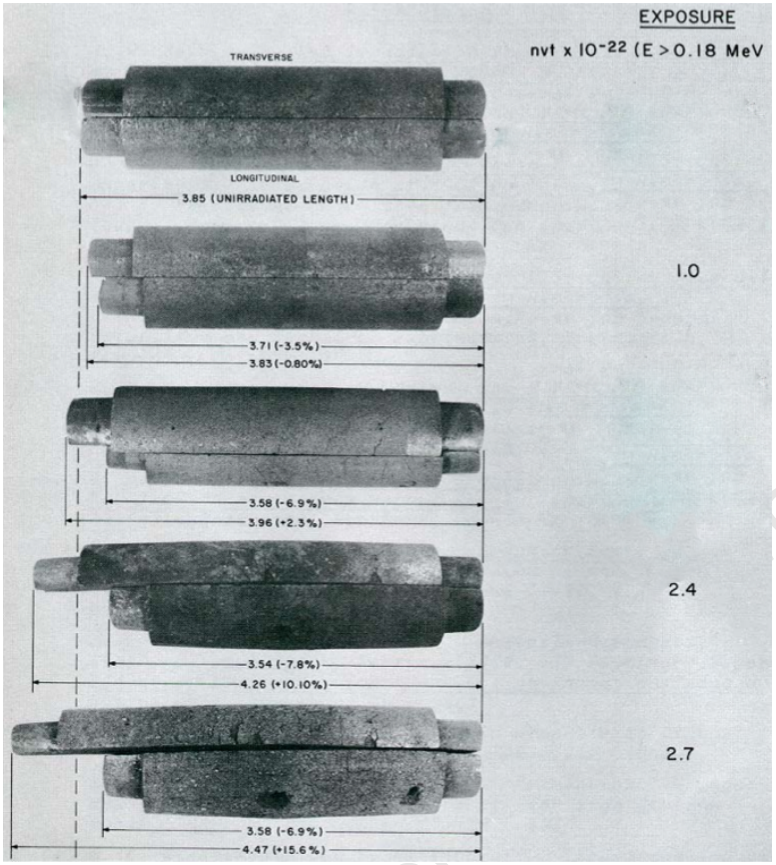

Figure 9.21 – Shrinkage of CSF graphite irradiated at 800oC to various irradiation doses (from Ref [30])

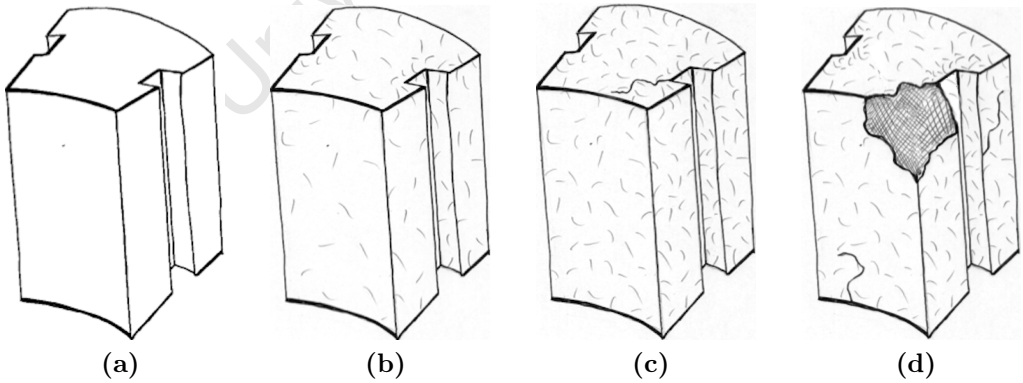

Figure 9.22 – Damage and fracture development in nuclear graphite components. (a) undamaged virgin material, (b) intergranular and transgranular micro-cracks form at high stress locations (damage), (c) macro-cracks start forming at weakened (damaged) locations and (d) failure.

imise potential numerical singularities. Additionally the convergence criteria was changed, allowing for more computational steps between each iteration. The analyses showed little mesh dependency, however elements with large aspect ratios can have different behaviour (depending on the direction in which they crack) [204].

It is worth mentioning that the adapted non-local DP model for quasi-brittle materials was not compared to all loading conditions for graphite fracture. This was not the scope of this project. The non-local DP model presented here is intended to investigate the possibility of using existing quasi-brittle fracture models for graphite failure. The two specimen configurations analysed showed excellent agreement with experimental results. The author believes that the numerical simulation of the failure of graphite moderator bricks can be carried out using the presented non-local DP failure model. The failure model can characterise crack propagation and can simulate the damage zone ahead of the fracture tip.

9.9 Understanding the Failure of Graphite Components

Assessment of the risks of component failure is an important part of the safety cases for nuclear power reactors. In the case of graphite moderated reactors this assessment includes the risk of fracture of the graphite components in the moderator, which must withstand externally applied stresses and internal stresses resulting from dimensional changes caused by neutron damage and thermal stresses, especially on shutdown [15]. In the case of Magnox and Advanced Gas-cooled Reactors (AGRs) operating in the United Kingdom, the effects of oxidation by the carbon dioxide based coolant upon the properties of the graphite must also be considered [15]. Examples have been published by Marsden [210] where the deformations, as a result of radiation, of CSF graphite were shown (illustrated in Figure 9.21). To understand the failure of graphite components in the nuclear environment, the failure processes need to be recognised. To date, none of the failure criteria have been able to satisfactorily describe a range of experimental fracture results [86, 15].

Previous research, though limited in number, on fast neutron irradiation and radiolytic oxidation has been undertaken [3, 211, 212, 16]. Radiation and oxidation results in the overall degradation of the bulk material. This includes the reduction

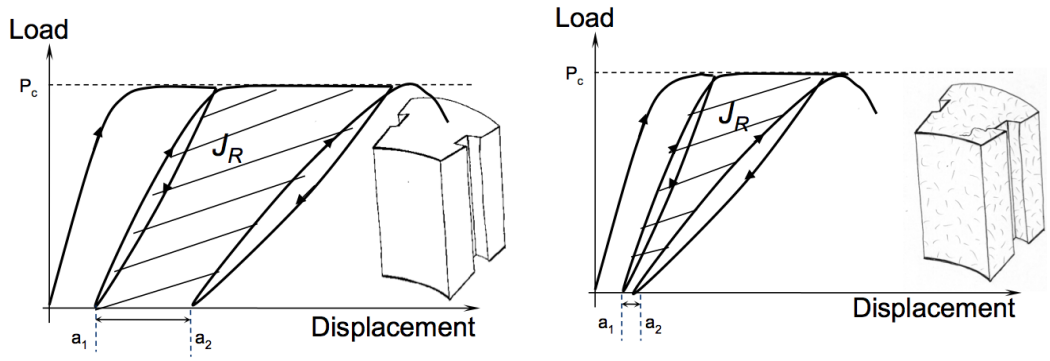

(a) Virgin material **(b)** Irradiated

Figure 9.23 – Illustration of the effect of global material degradation on the fracture resistance. (a) virgin materials fracture resistance versus (b) the diminished fracture resistance due to global damage accumulation. Both exhibit an identical crack propagation, but the energy in-balance is accountable to the non-linear energy dissipation which is a function of the micro-cracking required for macro-crack propagation.

in strength, Young's modulus, dimensional change and porosity amongst others [210]. It thus follows that irradiated graphite should have considerably different properties, including fracture properties, compared to the virgin, un-irradiated material. This being said, Fazluddin [16] showed that the K_R-curve behaviour of oxidised graphite has similar crack growth mechanisms, however, at a diminished toughness. It thus seems coherent to suggest that the mechanisms of fracture remain similar in irradiated material, i.e. the non-linear energy dissipation and degradation during fracture have similar mechanisms. Since the testing of irradiated material is very costly, due to the safety precautions that have to be met, testing was only performed on virgin material. It was believed that a valid failure understanding could be formulated from the virgin material results.

Since the structural integrity of graphite components in the nuclear environment is generally compromised due to cracking, fracture mechanics (which deals with the study of the propagation of cracks in materials) has been used in an attempt to asses the structural integrity of such components. This assumes that cracking the graphite components can be treated as a singularity where the mechanisms associated with cracking are a function thereof. In such a case, the fracture mechanics approach would dictate that the component's integrity is assessed using the flaw size (the crack), the remote stress (and possible stress raisers such as key ways or multiple large cracks) and the materials fracture parameters.

The conventional fracture mechanics methodology assumes that the fracture characteristic or parameter is an inherent material property. This, however, was shown to be an erroneous assumption as the damage or degradation of the material in the FPZ and crack wake is geometry and size dependent. As such, a 3PB configuration can behave significantly differently to that of a CT or DT configuration. There is, however, an additional failure mechanism which needs to be considered. For this, let us assume that a virgin graphite brick (undamaged) is just subjected to a stress (i.e. loading stress): The brick, which is illustrated in Figure 9.22a, can initially be assumed to be micro-crack free (but not free of material flaws). With the increase of that stress, micro-cracks initiate from the internal flaws (such as pores or filler particles) at high stress zones (Figure 9.22b). These stresses don't have to be significant as it has been reported that micro-cracking occurs at approximately a third of the peak load. In addition, it was established that the interaction of micro-cracks in the micro-scale influences the flaw in the mezo-scale and in turn on the macro-scale. Therefore, fracture processes in graphite are primarily dependent on the stability of these interfacial cracks. Hence, at some critical point the micro-cracks coalesce to form one or several macro-cracks (Figure 9.22c). Only at this point can the fracture mechanics methodology be utilised. Upon further loading, the macro-crack propagates or becomes unstable and the brick fails (Figure 9.22d).

With the understanding that the propagation of a macro-crack is a function of the population of micro-cracking, it follows that a somewhat damaged component (i.e. a global population of micro-cracks exist due to a global stress or possibly irradiation damage) should fracture differently to a undamaged component. The energy to drive a crack through damaged material would be considerably different to that of virgin material, since the non-linear energy dissipation that is associated with crack propagation, i.e. the formation of micro-cracks in the FPZ, is less. Thus, a damaged or irradiated material would be expected to behave in a more brittle and linear fashion (as illustrated in the load-displacement diagram in Figure 9.23). This is exactly what Fazluddin observed [16]. He showed that the the loss of binder phase and the resultant increase in porosity due to oxidation lowers the fracture energy as well as the bridging stress that is generated within the bridging zone. The observed R-curve behaviour has more similarities with that of a typical brittle material, categorised by a much steeper initial rise followed by a constant toughness.

It follows that the history of the component plays an important role. Material

that has been damaged will fracture differently to that of a virgin material. The likelihood of macro-crack propagation, which propagates through the linking of micro-cracks, is dependent on the statistical distribution and population density of micro-flaws in the vicinity of the macro-crack tip, which in turn is dependent on the "amount" of damage of the material. As such, the observed cracking behaviour in the same material components may differ considerably.

There is an additional factor which needs to be considered. The size effect, which is commonly observed in quasi-brittle materials, also plays an important role in graphite fracture. According to Bazant [21], the brittleness of the component is dependent on its size where a larger component behaves in a more brittle fashion. The reason for this, as explained by Karihaloo [22], is that the ratio of the stored elastic energy of the component versus the energy released by fracture governs whether ductile or brittle fracture occurs (the reader is referred to Figure 9.5). Hence, a large component would behave differently to a smaller specimen.

Fracture mechanics does not allow for the assessment of these intricate mechanisms of failure, since it assumes a constant material property and a discrete approach to evaluate crack growth resistance. Thus, to solve the problem of simulating and predicting failure of graphite components would require a continuum-based approach that accounts for the overall material degradation. Marsden [210] has predicted the degradation and deformations of graphite bricks in AGRs using FE analyses (however, these analysis have not been experimentally validated), but has had limited success with predicting crack initiation and propagation. It is believed by the author that a combined approach of the presented damaged plasticity model and Marsden's degradation prediction model could successfully simulate the fracture and failure of medium grained polycrystalline graphite.

9.10 Summary

In summary, the analysis showed that graphite fracture is associated with significant micro-cracking in the fracture process zone (FPZ) prior to and during macro-cracking as well as crack bridging in the wake of the crack tip, which contributes up to 50% of the irreversible energy dissipation. Micro-cracks tended to nucleate at pores, causing deflection of the crack path. Rising R-curve behaviour was observed, which is attributed to the formation of the FPZ, while crack bridging and distributed micro-cracks are responsible for the increase in

fracture resistance. The R-curve analysis of the two materials has shown the typical quasi-brittle R-curve behaviour. Comparison of the R-curve data with other data available in literature suggests a geometry dependent fracture behaviour, where the non-linearity due to the FPZ and the wake effects result in variations of the apparent fracture toughness. It was found that the reported FPZ size varies significantly between various geometries showing a relationship between the non-linear fracture behaviour and the FPZ and wake region size.

The experimental programme has thus shown that conventional fracture mechanics is not an appropriate measure of the crack growth mechanisms in nuclear graphite. The facts concerning the size and geometry dependency of conventional fracture mechanics and the question regarding the validity of a single crack approach have resulted in the introduction of a damage mechanics based failure model. The model is the adaption of an existing non-local damage plasticity model for concrete and other brittle materials which allows for the degradation of the material and for so called "plasticity" and was shown to correlate well with experimental data. The model is based upon the continuum-based approach. It uses concepts of isotropic damaged elasticity in combination with isotropic tensile and compressive plasticity to represent the inelastic behaviour. In this method the failure is modeled in the FE model and consists of a combination of non-associated multi-hardening plasticity and scalar (isotropic) damaged elasticity to describe the irreversible damage that occurs during the fracturing process. This requires the definition of a yield surface and a flow rule that allows the yield function to soften/harden as the material is "plastically" loaded. The model is available in the ABAQUS/Standard environment [23]. A static, strain rate independent model was assumed.

Three specimen geometries were considered and modeled using IM1-24 graphite. These included two CT specimen geometries, by Hodgkins et al. [4] and Fazluddin [16] and a 3PB geometry by Fazluddin [16]. The examples have shown that using the DP model enables the proper definition of the failure mechanisms associated with IM1-24 graphite fracture. The model is able to simulate the softening and degradation of the material and, most importantly, since the DP model is a non-local approach, is size and geometry independent.

Chapter 10

Conclusions and Recommendations

This project set out to contribute to the understanding of the mechanisms associated with the crack initiation and propagation of two medium grain nuclear graphites, namely Nuclear Block Graphite 10 (NGB10) and Gilsocarbon (IM1-24). The thesis developed on the results of earlier work undertaken by Hodgkins [4], Fazluddin [16] and Ouagne [15] among others and is believed to have provided an explanation of the mechanisms associated with damage development and the modeling of graphite failure.

The work was split into four sections in which; the Double Torsion (DT) testing methodology was critically evaluated and adapted to account for non-linearity, a novel approach to calculate the J-Integral by Digital Image Correlation (DIC) displacement field measurements was proposed, the observations and mechanisms associated with graphite fracture and last, a non-local continuum-based damaged plasticity model for graphite fracture was proposed. The project successfully employed these techniques to fulfill the thesis objectives. The key conclusion with some recommendations is summarised below:

- The evaluation of the DT technique, using an experimental, DIC and a 3D Finite Element (FE) analysis, has shown that the validity of the common assumption of crack length independence is dependent on the loading configuration, the specimen geometry and material. Significant deflections at the loading points and the deformation of the unbroken ligament were measured using a 3D DIC system. The unaccounted deformations result in a non-linear compliance relationship that causes the Stress Intensity Factor (SIF) to become crack length dependent. The corrections proposed by

Chevalier and Ciccotti achieved a crack length independent configuration, which enables reproducible fracture toughness and VK relationship data to be obtained for various specimen geometries. However, it was found that Chevaliers' correction overestimates and Ciccotti underestimates the calculated SIF by up to 10% in the geometries studied. Evans' conventional methodology, with a large deflection correction can obtain valid fracture toughness and VK relationship data in some geometries. For example; ungrooved DT specimens with dimensions resembling $3W : W : 0.08W$. The middle half of the specimen achieves an almost crack length independent regime (within 2%), provided the crack tip remains within $a_{off} < 1/8W$ of the centreline for VK investigation.

The author believes that future developments should include efforts on the standardisation of this test method. It would prove useful to establish relationships between approximate material properties and specimen dimensions.

- In addition to the DT geometry, a novel and simple methodology for extracting the J-integral from displacement fields obtained by DIC at different loads was presented. The displacement vectors are transformed into a finite element domain through a MATLAB implemented routine (JMAN) to obtain the J-integral as an area integral. The JMAN methodology was verified using an ABAQUS model, with excellent agreement between the standard ABAQUS and weight function calculated SIFs. JMAN was tested on three different specimen geometries for elastic, elastic-plastic and quasi-brittle materials. Excellent agreement with other fracture characterisation techniques was achieved. The JMAN analysis has the advantage over standard methods in that precise location of the crack tip is not required. It is also insensitive to inelastic strains close to the crack tip that are contained within the chosen contour.

  Future developments of JMAN are proposed which would provide the contributions of mode I and mode II in the J-integral as well as the T-stress. JMAN may also be modified to account for plasticity and inelastic fracture processes in the FE domain, as well as residual stress effects for characterisation of other materials.

- The DT technique and the JMAN methodology provided an excellent tool and were successfully applied to nuclear graphite for the study of crack

initiation and propagation, including slow crack growth characterisation. Because of the way the DT is loaded, it allowed for the observation and measurement of the Fracture Process Zone (FPZ) prior and during fracture for the first time in graphite.

The observations show that prior to the initiation of the macro-crack the application of load produces a non-linear load displacement curve in test specimens. Electronic Speckle Pattern Interferometry (ESPI) suggest that residual strains occur at isolated locations throughout the material with an increasing number of strain localisations ahead of the starter notch. DIC confirms that severe micro-structural damage occurs prior to macro-crack initiation ahead of the notch tip. Following the initiation and growth of the primary crack a FPZ exists ahead of the crack tip which contains a high density of micro cracks. Some micro-cracking remains visible in the wake, yet most close after the macro-crack propagates past. The propagation in the FPZ is predominantly associated with crack bridging between micro-cracking and porosity.

Extensive micro-cracking ahead of the macro-crack tip and wake effects (such as crack bridging, crack branching and crack arresting) indicate the aforementioned quasi-brittle behaviour. It was shown that grain structure and porosity play an important role in the way graphite fractures. Cracks tend to follow a path of least resistance and crack propagation was observed to follow voids that were visible on the material surface. Micro-cracks form in the crack direction plane and appear as localised strains which tend to be coincident with porosity and grain boundaries.

The values of J_R (the fracture resistance), J_{el} (the elastic contribution) and J_{pl} (the plastic contribution) reach a plateau during crack propagation. No significant difference was found for the elastic contribution in NBG10 (in the parallel and the perpendicular orientation) and IM1-24, suggesting that this is a measure of the fracture resistance of the graphite material itself and excludes the non-linear, so called "plasticity" effects. Similarly, these "plastic" energies show the same plateau region indicating that the FPZ remains constant once established. However, significant large scatter in the J_{pl} values is noticeable. This behaviour is in agreement with the ESPI and DIC observations of the FPZ, and plotting charts of J_R and J_{el} vs. J_{pl} shows convergence to a fracture resistance similar to the obtained plateau value. The convergence confirms that crack propagation in graphite

is accompanied by significant non-linear effects.

The initial R-curve rises with the formation of the FPZ and then with continuing crack extension rises slowly. This is consistent to the development of the FPZ and crack wake effects. Comparison of R-curve data shows a geometry dependent fracture behaviour, where the non-linearity due to the FPZ and the wake effects results in variations of the apparent fracture toughness. It was found that the reported FPZ size varies significantly between various geometries showing a relationship between the non-linear fracture behaviour and the FPZ and wake region size. It was identified that the observed and measured behaviour is very similar to that of other quasi-brittle materials. In these a clear size effect on geometry has been established and fracture cannot be categorised by conventional elastic plastic fracture mechanics.

- Based on the fact that graphite fracture is size dependent, an alternate failure model was proposed. The model is based upon a continuum-based approach and uses concepts of isotropic damaged elasticity in combination with isotropic tensile and compressive plasticity to represent the inelastic behaviour of graphite. Failure is modeled in the FE model and consists of a combination of non-associated multi-hardening plasticity and scalar (isotropic) damaged elasticity to describe the irreversible damage that occurs during the fracturing process. This requires the definition of a yield surface and a flow rule that allows the yield function to soften/harden as the material is "plastically" loaded. The model is available in the ABAQUS/Standard environment [23]. A static, strain rate independent model was assumed.

  Three specimen geometries were considered and modeled using IM1-24 graphite. These included two CT specimen geometries, by Hodgkins et al. [4] and Fazluddin [16] and a 3PB geometry by Fazluddin [16]. The examples have shown that using the DP model enables the proper definition of the failure mechanisms associated with IM1-24 graphite fracture. The model is able to simulate the softening and degradation of the material and most importantly, since the DP model is a non-local approach, is size and geometry independent.

  Future work would include further consideration of available quasi-brittle failure models for graphite failure. These could include more complex anisotropic models.

Bibliography

[1] PBMR, "Pebble Bed Modular Reactor (Pty) Ltd, http://www.pbmr.com." 1999.

[2] J. Lord, N. McCormick, and M. Joyce, "The Use of Digital Image Correlation Techniques to Measure the Elastic Modulus of Irradiated Graphite," in *Graphite Research Meeting*, (University of Manchester), 2010.

[3] R. Nightingale, *Nuclear graphite*. Battelle-Northwest, Richland, Wash. Pacific Northwest Lab.: London: Academic press, 1962.

[4] A. Hodgkins, *Crack propagation in nuclear graphite*. PhD thesis, University of Manchester, 2006.

[5] D. Pollard and R. Fletcher, *Fundamentals of Structural Geology*. Cambridge University Press, 2005.

[6] T. Anderson, *Fracture mechanics : fundamentals and applications*. London: CRC press, 2nd ed. ed., 1995.

[7] S. Wiederhorn and L. Bolz, "Stress Corrosion and Static Fatigue of Glass," *Journal of the American Ceramic Society*, vol. 53, pp. 543–548, Oct. 1970.

[8] B. Atkinson and P. Meredith, "The theory of subcritical crack growth with applications to minerals and rocks," *Fracture mechanics of rock*, vol. 2, pp. 111–166, 1987.

[9] M. Ciccotti, *An Exhaustive Analysis Of The Double Torsion Method For Supercritical Crack Propagation In Lava Rocks And Its Implications For The Understanding Of Earthquake Physics*. PhD thesis, Universita' di Bologna, 1998.

[10] M. Meyers and K. Chawla, *Mechanical Behavior of Materials*. Cambridge University Press, 2009.

[11] J. Chaboche, *Comprehensive Structural Integrity*, ch. 2.04 - Damage Mechanics, pp. 214–281. Elsevier, 2006.

[12] A. Fossum and R. Brannon, "The Sandia Geomodel - Theory and Users Guide," *SAND2004-3226, Sandia National Laboratories, Albuquerque, New Mexico*, vol. 155, no. August, 2004.

[13] M. Sakai, J. Yoshimura, Y. Goto, and M. Inagaki, "R-curve Behavior of a Polycrystalline Graphite: Micro cracking and Grain Bridging in the Wake Region," *Journal of the American Ceramic Society*, vol. 71, pp. 609–616, Aug. 1988.

[14] M. Sakai, K. Urashima, and M. Inagaki, "Energy Principle of Elastic-Plastic Fracture and Its Application to the Fracture Mechanics of a Polycrystalline Graphite," *Journal of the American Ceramic Society*, vol. 66, pp. 868–874, Dec. 1983.

[15] P. Ouagne, G. Neighbour, and B. McEnaney, "Crack growth resistance in nuclear graphites," *Journal of Physics D: Applied Physics*, vol. 35, pp. 927–934, May 2002.

[16] S. Fazluddin, *Crack growth resistance in nuclear graphites*. PhD thesis, University of Sheffield, Apr. 2002.

[17] P. Heard, M. Wootton, R. Moskovic, and P. Flewitt, "Crack initiation and propagation in pile grade a (pga) reactor core graphite under a range of loading conditions," *Journal of Nuclear Materials*, vol. 401, no. 1-3, pp. 71 – 77, 2010.

[18] P. Leevers, "Large deflection analysis of the double torsion test," *Journal of materials science letters*, vol. 5, no. 2, pp. 191–192, 1986.

[19] A. Hodgkins, T. Marrow, P. Mummery, B. Marsden, and A. Fok, "X-ray tomography observation of crack propagation in nuclear graphite," *Materials Science and Technology*, vol. 22, no. 9, pp. 1045–1051, 2006.

[20] Z. Bazant, "Mechanics of fracture and progressive cracking in concrete structures," *Fracture mechanics of concrete: Structural application and numerical calculation*, vol. 1, pp. 1–94, 1985.

[21] Z. Bazant, "Concrete fracture models: testing and practice," *Engineering Fracture Mechanics*, vol. 69, pp. 165–205, Jan. 2002.

[22] B. Karihaloo, *Comprehensive Structural Integrity*, ch. 2.10 - Failure of Concrete, pp. 214–281. Elsevier, 2006.

[23] ABAQUS, *User's Manual, Version 6.9*. ABAQUS Inc., Prvidence, Rhode Island, 2010.

[24] J. Brocklehurst, "Fracture of Polycrystalline Graphite," tech. rep., TRG Report 2302(s), 1973.

[25] S. Sato, "Fracture criterion of reactor graphite under multiaxial stresses," *Nuclear Engineering and Design*, vol. 23, pp. 49–62, Oct. 1987.

[26] J. Jortner, "Multiasdal Response of ATJ-S Graphite, Technical Report AFML-TR-71-253," tech. rep., McDonnell Douglas Astronautics Company, Santa Monica, 1971.

[27] W. Bradshaw, "Mechanical and Thermal Properties of Glass-like Carbons," tech. rep., Lockheed Missiles and Space Co., Palo Alto, Calif. Lockheed Palo Alto Research Lab., Jan. 1972.

[28] W. Greenstreet, G. Yahr, and R. Valachovic, "The behaviour of graphite under biaxial tension," *Carbon*, vol. 11, pp. 43–57, Feb. 1973.

[29] T. Oku and M. Eto, "Relation between static and dynamic Young's modulus of nuclear graphites and carbon," *Nuclear Engineering and Design*, vol. 143, pp. 239–243, Sept. 1993.

[30] B. Marsden, "Irradiation Property Changes in Polycrystalline Graphite," in *Graphite Symposium*, (Pretoria), 2009.

[31] E. Fuller Jr, "An evaluation of double-torsion testing-analysis," *Fracture Mechanics Applied to Brittle Materials*, vol. 678, p. 3, 1979.

[32] A. Shyam and E. Lara-Curzio, "The double-torsion testing technique for determination of fracture toughness and slow crack growth behaviour of materials: A review," *Journal of Material Science*, vol. 41, pp. 4093–4104, 2006.

[33] G. Trantina, "Stress Analysis of the Double-Torsion Specimen," *Journal of the American Ceramic Society*, vol. 60, no. 7-8, pp. 338–341, 1977.

[34] J. Salem, "Fracture Toughness of thin plates by the Double Torsion Test Method," in *Mechanical Properties and Performance of Engineering Ceramics II: Ceramic Engineering and Science Proceedings, Volume 27, Issue 2*, 2006.

[35] B. J. Pletka, E. R. Fuller, and B. G. Koepke, "Fracture Mechanics Applied to Brittle Materials ASTM STP 678," 1979.

[36] R. Tait, P. Fry, and G. Garrett, "Review and evaluation of the double-torsion technique for fracture toughness and fatigue testing of brittle materials," *Experimental Mechanics*, vol. 27, pp. 14–22, Mar. 1987.

[37] M. Ciccotti, N. Negri, L. Sassi, and G. Gonzato, "Elastic and fracture parameters of Etna, Stromboli, and Volcano lava rocks," *Journal of Volcanology*, vol. 98, pp. 209–217, May 2000.

[38] P. Zhu, "The predictions and applications of fatigue lifetime in alumina and zirconia ceramics," *International Journal of Fatigue*, vol. 26, pp. 1109–1114, Oct. 2004.

[39] M. Albuquerque and J. Rodriguez, "Characteristics of the double-torsion test to determine the R-curve of ceramic materials," *Materials Research*, vol. 9, pp. 361–368, Dec. 2006.

[40] W. Reynolds, *Physical properties of graphite*. Elsevier, 1968.

[41] T. Burchell, "A micro structurally based fracture model for polygranular graphites," *Carbon*, vol. 34, no. 3, pp. 297–316, 1996.

[42] A. Rose and M. Tucker, "A Fracture Criterion for Nuclear Graphite," *Journal of Nuclear Materials*, vol. 110, no. 2-3, pp. 186–195, 1982.

[43] A. Carpinteri, B. Chiaia, and P. Cornetti, "A scale invariant cohesive crack model for quasi-brittle materials," *Engineering fracture mechanics*, vol. 69, pp. 207 – 217, 2002.

[44] J. Wang and K. Liu, "An innovative technique for evaluating fracture toughness of graphite materials," *Journal of Nuclear Materials*, vol. 381, pp. 177–184, Oct. 2008.

[45] L. Shi, H. Li, Z. Zou, S. Fok, B. Marsden, A. Hodgkins, P. Mummery, and T. Marrow, "Analysis of crack propagation in nuclear graphite using three-point bending of sandwiched specimens," *Journal of Nuclear Materials*, vol. 372, pp. 141–151, Jan. 2008.

[46] B. Mitchell, "The mechanical testing of nuclear graphite," *Journal of Nuclear Materials*, vol. 322, pp. 126–137, Nov. 2003.

[47] M. Mostafavi, D. Smith, and M. Pavier, "Combined In and Out of Plane Constraint Effect on the Fracture Behaviour of Aluminium 2024, A Micromechanical Study," vol. In Preparation, 2010.

[48] R. Cahn, *The physics of graphite*. Applied Science Publishers, London, 1981.

[49] F. Feata, "Radiolytic oxidation of single crystals of graphite by oxygen, carbon dioxide, and methane+ carbon dioxide mixtures," *Chemistry Division, U.K.A.E.A., Research Group, Atomic Energy Research Establishment, Harwell, Didcot, Berks.*, vol. 64, pp. 3093–3099, 1968.

[50] T. Burchell and L. Snead, "The effect of neutron irradiation damage on the properties of grade NBG-10 graphite," *Journal of Nuclear Materials*, vol. 371, pp. 18–27, Sept. 2007.

[51] W. Callister, *Fundamentals of materials science & engineering*. New York: Wiley & Sons, 2001.

[52] S. Zumdahl, *Chemistry. 1st edition*. DC Heath & Co, 1986.

[53] J. Knott, *Fundamentals of Fracture Mechanics*. Butterworth & Co. Publishers, London, 1973.

[54] D. Broek, *Elementary engineering fracture mechanics*. Kluwer Academic Publishers, 1999.

[55] A. Griffith, "The phenomena of rupture and flow in solids," *Philosophical Transactions of the Royal Society of London, Series A, Containing Papers of a Mathematical or Physical Character*, vol. 221, pp. 163–198, 1921.

[56] B. Lawn and T. Wilshaw, *Fracture of Brittle Solids*. Cambridge University Press, 1975.

[57] J. Rice, "A Path Independent Integral and the Approximate Analysis of Strain Concentration," *Journal of applied mechanics*, vol. 35, no. 2, pp. 379–386, 1968.

[58] L. Grenet, "Mechanical strength of glass," *Bull. Soc. Enc. Industr. Nat. Paris (Ser. 5)*, vol. 4, pp. 838–843, 1899.

[59] B. Atkinson, "Subcritical crack growth in geological materials," *Journal of Geophysics*, vol. 89, no. B6, pp. 4077–4114, 1984.

[60] B. Lawn, "Physics of fracture," *Journal of the American Ceramic Society*, vol. 66, no. 2, pp. 83–91, 1983.

[61] J. Jaeger and N. Cook, *Fundamentals of Rock Mechanics*. Chapman and Hall, London, 1976.

[62] T. Nose and T. Fuji, "Evaluation of fracture toughness for ceramic materials by a single-edge-precracked-beam method," *Journal of the American Ceramic Society*, vol. 71, no. 5, pp. 328–333, 1988.

[63] A. E1304, "ASTM E1304-97 Standard Test Method for Plane-Strain (Chevron-Notched) Fracture Toughness of Metallic Materials."

[64] L. Iannucci and J. Ankersen, "An energy based damage model for thin laminated composites," *Composites Science and Technology*, vol. 66, pp. 934–951, June 2006.

[65] A. Corigliano, *Comprehensive Structural Integrity*, ch. 3.09 - Damage and Fracture Mechanics Techniques for Composite Structures, pp. 462–534. Elsevier, 2006.

[66] S. Murakami and N. Ohno, "A continuum theory of creep and creep damage," in *3rd IUTAM Symposium on Creep in Structures* (A. Ponter and D. Hayhurst, eds.), (Springer-Verlag, Leicester), pp. 422–443, 1980.

[67] S. Murakami, "Notion of Continuum Damage Mechanics and its application to anisotropic creep damage theory," *Journal of Engineering Materials Techniques*, vol. 105, p. 99, 1983.

[68] A. Plumtree and J. Nilsson, "Fatigue at High Temperature," in *Societe Francaise de Metallurgie*, pp. 396–405, 1986.

[69] P. Germain, Q. Nguyen, and P. Suquet, "Continuum thermodynamics," *Journal of applied mechanics*, vol. 50, pp. 1010–1020, 1983.

[70] J. Lemaitre, *Engineering Damage Mechanics*. Berlin Heidelberg: Springer-Verlag, 2005.

[71] K. Saanouni, *Numerical Modelling in Damage Mechanics*. British Library Cataloguing-in-Publication Data, 2003.

[72] J. Lubliner, *Plasticity Theory: Revised Edition*. Pearson Education, Inc., 2006.

[73] W. Brocks, I. Scheider, and G. Geesthacht, "Numerical Aspects of the Path-Dependence of the J-Integral in Incremental Plasticity," *Technical Note GKSS/WMS/01*, vol. 8, no. October, pp. 1–33, 2001.

[74] J. Corum, "A determination of the fracture toughness of EGCR-type AGOT graphite," *J NUCL MATER*, vol. 22, no. 1, pp. 41–54, 1967.

[75] M. Ayatollahi and A. Torabi, "Tensile fracture in notched polycrystalline graphite specimens," *Carbon*, vol. 48, pp. 2255–2265, July 2010.

[76] C. Berre, P. Mummery, B. Marsden, T. Mori, and P. Withers, "Application of a micromechanics model to the overall properties of heterogeneous graphite," *Journal of Nuclear Materials*, vol. 381, pp. 124–128, Oct. 2008.

[77] T. Marrow, A. Hodgkins, M. Joyce, and B. Marsden, "Damage nucleation in nuclear graphite," *Energy Materials: Materials Science and Engineering for Energy Systems*, vol. 1, pp. 167–170, Sept. 2006.

[78] G. Romanoski and T. Burchell, "The effects of specimen geometry and size on the fracture toughness of nuclear graphites," in *Proceeding of the IAEA Specialists meeting on the Status of Graphite Development for Gas Cooled Reactors*, 1991.

[79] R. Tait and K. Rosie, "Microstructural Crack Behaviour Studies of Nuclear Graphite Using an in situ Double Torsion Rig Inside a Scanning Electron Microscope," in *IYNC2010*, no. 271, pp. 12 – 18, 2010.

[80] K. Wen, T. Marrow, and B. Marsden, "Micro cracks in nuclear graphite and highly oriented pyrolytic graphite (HOPG)," *Journal of Nuclear Materials*, vol. 381, pp. 199–203, Oct. 2008.

[81] J. Bowmer and T. Marrow, "Low cycle fatigue of nuclear graphite," Master's thesis, University of Manchester, Manchester, 2009.

[82] M. Joyce, T. Marrow, P. Mummery, and B. Marsden, "Observation of microstructure deformation and damage in nuclear graphite," *Engineering Fracture Mechanics*, vol. 75, pp. 3633–3645, Aug. 2008.

[83] H. Hubner and W. Jillek, "Sub-critical crack extension and crack growth resistance in polycrystalline Alumina," *Journal of Materials Science*, vol. 12, pp. 112 – 125, 1977.

[84] R. Knehans and R. Steinbrech, "Memory effect of crack resistance during slow crack growth in notched Al2O3 bend specimens," *Journal of Materials Science Letters*, vol. 1, pp. 327–329, Aug. 1982.

[85] R. Pabst, J. Steeb, and N. Claussen, "Micro cracking in a process zone and its relation to continuum fracture mechanics," in *Fracture mechanics of ceramics; Proceedings of the International Symposium*, pp. 821–833, 1978.

[86] M. Tucker, A. Rose, and T. Burchell, "The fracture of polygranular graphites," *Carbon*, vol. 24, no. 5, pp. 581–602, 1986.

[87] Z. Zou, "Failure predictions for nuclear graphite using a continuum damage mechanics model," *Journal of Nuclear Materials*, vol. 324, pp. 116–124, Jan. 2004.

[88] S. Preston and B. Marsden, "Changes in the coefficient of thermal expansion in stressed Gilsocarbon graphite," *Carbon*, vol. 44, pp. 1250–1257, June 2006.

[89] R. Tait, *PhD Thesis*. PhD thesis, University of Cape Town, 1975.

[90] J. Outwater and D. Gerry, "On the Fracture Energy, Rehealing Velocity and Refracture Energy of Cast Epoxy Resin," *The Journal of Adhesion*, vol. 1, pp. 290–298, Oct. 1969.

[91] A. Evans, "A method for evaluating the time depended failure characteristics of brittle materials - and its applications to polycrystalline alumina," *Journal of Material Science*, vol. 7, pp. 1137–1146, 1972.

[92] D. Williams and A. Evans, "A simple method for studying slow crack growth," *Journal of Testing and Evaluation*, vol. 1, p. 264, 1973.

[93] M. Ebrahimi, J. Chevalier, and G. Fantozzi, "Slow crack-growth behaviour of alumina ceramics," *Journal of Materials Research Society*, vol. 15, no. 1, pp. 142–147, 2000.

[94] S. Baskaran, S. Bhaduri, and D. Hasselman, "Effect of crystallites on subcritical crack growth and strain-rate sensitivity of strength of cordierite glass-ceramics," *Journal of the American Ceramic Society*, vol. 68, no. 3, pp. 112–119, 1985.

[95] J. Chevalier, M. Saadaoui, C. Olagnon, and G. Fantozzi, "Double Torsion testing a 3Y-TZP Ceramic," *Ceramics International*, vol. 22, pp. 171–177, 1996.

[96] M. Ferber and S. Brown, "Subcritical crack growth in dense alumina exposed to physiological media," *Journal of the American Ceramic Society*, vol. 63, no. 7-8, pp. 424–429, 1980.

[97] B. Pletka and S. Wiederhorn, "A comparison of failure predictions by strength and fracture mechanics techniques," *Journal of Materials Science*, vol. 17, no. 5, pp. 1247–1268, 1982.

[98] O. Sano, "A revision of the double-torsion technique for brittle materials," *Journal of Materials Science*, vol. 23, no. 7, pp. 2505–2511, 1988.

[99] G. Vekinis, M. Ashby, and P. Beaumont, "R-Curve behaviour of Al2O3 ceramics," *Acta metallurgica et Materialia*, vol. 38, p. 1151, 1990.

[100] J. Chevalier, A. De Aza, L. Gremillard, R. Zenati, and G. Fantozzi, "Slow Crack Growth in Zirconia Ceramics: From the Single Crystal to the Composites," *Materials Engineering*, vol. 12, no. 2, pp. 159–178, 2001.

[101] P. Leevers, "Crack front shape effects in the double torsion testing," *Journal of Material science*, vol. 17, pp. 2468–2480, 1982.

[102] M. Ciccotti, G. Gonzato, and F. Mulargia, "The double torsion loading configuration for fracture propagation: an improved methodology for the load-relaxation at constant displacement," *International Journal of Rock Mechanics and Mining Science*, vol. 37, pp. 1103–1113, 2000.

[103] M. Ciccotti, N. Negri, G. Gonzato, and F. Mulargia, "Practical application of an improved methodology for the double torsion load relaxation

method," *International Journal of Rock Mechanics and Mining Sciences*, vol. 38, no. 4, pp. 569–576, 2001.

[104] R. Pabst and J. Weick, "Double-torsion measurements with and without a guiding notch," *Journal of Materials Science*, vol. 16, no. 3, pp. 836–838, 1981.

[105] A. Virkar and R. Gordon, "Crack Front Profiles in Double-Torsion Specimens," *Journal of the American Ceramic Society*, vol. 58, no. 11-12, p. 536, 1975.

[106] J. Pollet and S. Burns, "Crack velocity correction factor for the crack front shape in double torsion specimens," *Journal of the American Ceramic Society - Discussion and Notes*, vol. 62, no. 7-8, pp. 426–427, 1979.

[107] D. Biswas and V. Pujari, "Verification of the Double-Torsion Equation by Using Different Thickness Samples of a Machinable Glass-Ceramic," *Journal of the American Ceramic Society*, vol. 64, no. 7, pp. 98–99, 2006.

[108] B. Stalder and H. Kausch, "Some geometrical observations on crack front profiles in PMMA double torsion specimens," *Journal of Materials Science*, vol. 17, no. 9, pp. 2481–2485, 1982.

[109] P. Hine, R. Duckett, and I. Ward, "A double-torsion study of the fracture of polyethersulphone," *Journal of Materials Science*, vol. 19, no. 11, pp. 3796–3805, 1984.

[110] M. Madjoubi, M. Hamidouche, N. Bouaouadja, J. Chevalier, and G. Fantozzi, "Experimental evaluation of the double torsion analysis on soda-lime glass," *Journal of Materials Science*, vol. 41, no. 18, pp. 7872–7881, 2007.

[111] M. Ciccotti, "Realistic finite element model for the double torsion loading configuration," *Journal of the American Ceramic Society*, vol. 83, pp. 2737–2744, 2000.

[112] G. Kourtesis, G. Renwick, A. Fischer-Cripps, and M. Swain, "Mechanical property characterization of a number of polymers using uniaxial compression and spherical tipped indentation tests," *Journal of Materials Science*, vol. 32, no. 17, pp. 4493–4500, 1997.

[113] S. Suresh and R. Ritchie, "A geometric model for fatigue crack closure induced by fracture surface roughness," *Metallurgical and Materials Transactions A*, vol. 13, no. 9, pp. 1627–1631, 1982.

[114] J. Wasen, K. Hamberg, and B. Karlsson, "The influence of grain size and fracture surface geometry on the near-threshold fatigue crack growth in ferritic steels," *Materials Science and Engineering*, vol. 102, no. 2, pp. 217–226, 1988.

[115] N. Kamp, M. Parry, K. Singh, and I. Sinclair, "Analytical and finite element modelling of roughness induced crack closure," *Acta Materialia*, vol. 52, no. 2, pp. 343–353, 2004.

[116] F. Li, C. Shih, and A. Needleman, "A comparison of methods for calculating energy release rates," *Engineering Fracture Mechanics*, vol. 21, no. 2, pp. 405–421, 1985.

[117] M. Sutton, W. Wolters, W. Peters, W. Ranson, and S. McNeill, "Determination of displacements using an improved digital correlation method," *Image and Vision Computing*, vol. 1, no. 3, pp. 133–139, 1983.

[118] S. McKenna and W. McGillis, "Performance of digital image velocimetry processing techniques," *Experiments in fluids*, vol. 32, no. 1, pp. 106–115, 2002.

[119] DaVis, *DaVis, User's Manual*. LaVision GmbH, Gottingen, 2009.

[120] M. Sutton, S. McNeill, J. Helm, and Y. Chao, "Advances in two-dimensional and three-dimensional computer vision," *Photomechanics*, vol. 372, pp. 323–372, 2000.

[121] T. Ricco, R. Frassine, and A. Pavan, "Problems in Fracture mechanics characterisation of rubber-modified glassy polymers, using double torsion," *Journal of Material Science*, vol. 25, pp. 1517–1521, 1990.

[122] R. Jones, "Local strain approach to fatigue crack formation life at notches," *International Journal of Fatigue*, vol. 11, pp. 255–259, July 1989.

[123] T. Kreis and J. Geldmacher, "Evaluation of interference patterns: a comparison of methods," *Society of Photo*, vol. 1554, p. 718, 1991.

[124] J. Burke and H. Helmers, "Messung schnell veraenderlicher Verformungen mit raeumlich phasenschiebender elektronischer Specklemuster-Interferometrie (ESPI)," *Zeitschrift der Angewendeten Mathemtatic und Mechanic*, vol. 78, pp. 321–322, 1998.

[125] J. Gryzagoridis, "ESPI - a viable NDE tool for plant extension," *International Journal of Pressure Vessels and Piping*, vol. 73, pp. 25–32, Aug. 1997.

[126] D. Findeis, J. Gryzagoridis, and D. Rowland, "Vibration isolation techniques suitable for portable electronic speckle pattern interferometry," in *Non-destructive Evaluation and Health Monitoring of Aerospace Materials and Civil Infrastructures*, 2002.

[127] H. Puga, "General model to predict and correct errors in phase map interpretation and measurement for out-of-plane ESPI interferometers," *Optics & Laser Technology*, vol. 34, pp. 81–92, Feb. 2002.

[128] J. Da Fonseca, P. Mummery, and P. Withers, "Full-field strain mapping by optical correlation of micrographs acquired during deformation," *Journal of microscopy*, vol. 218, no. 1, pp. 9–21, 2005.

[129] H. Li, J. Duff, and T. Marrow, "In-situ observation of crack nucleation in nuclear graphite by digital image correlation," in *ASME Pressure Vessels and Piping Conference*, (Chicago, Illinois), American Society of Mechanical Engineers, 2008.

[130] A. Wells, "Unstable crack propagation in metals: cleavage and fast fracture," tech. rep., Naval Research Laboratory Washington, DC, Cracnfeild, UK, 1961.

[131] M. Williams, "On the stress distribution at the base of stationary crack," *Spie Milestone Series MS*, vol. 24, pp. 109–114, 1657.

[132] ASTM-E399, "ASTM-E399, Standard Method for Plane-Strain Fracture Toughness of Metallic Materials," 2004.

[133] ASTM-E1921, "ASTM-E192,1Standard Test Method for Determination of Reference Temperature, To, for Ferritic Steels in the Transition Range ," 2000.

[134] BS7910, "BS7910, Guide on methods for assessing the acceptability of flaws in metallic structures," 2000.

[135] V. Kumar, "An engineering approach for elastic-plastic fracture analysis (NP1931)," tech. rep., EPRI Report, 1981.

[136] R6, "R6 Assessment of the Integrity of Structures Containing Defects," 2001.

[137] G. Sinclair, "Some inherently unreliable practices in present day fracture mechanics," *International Journal of Fracture*, vol. 28, no. 1, pp. 3–16, 1985.

[138] F. Chiang and A. Asundi, "A white light speckle method applied to the determination of stress intensity factor and displacement field around a crack tip," *Engineering Fracture Mechanics*, vol. 15, pp. 115–121, 1981.

[139] J. Huntley and J. Field, "Measurement of crack tip displacement field using laser speckle photography," *Engineering fracture mechanics*, vol. 30, pp. 779–790, 1988.

[140] S. McNeill, W. Peters, and M. Sutton, "Estimation of stress intensity factor by digital image correlation," *Engineering fracture mechanics*, vol. 28, pp. 101–112, 1987.

[141] J. Abanto-Bueno and J. Lambros, "Investigation of crack growth in functionally graded materials using digital image correlation," *Engineering Fracture Mechanics*, vol. 69, pp. 1695–1711, 2002.

[142] J. Yau, S. Wang, and H. Corten, "A Mixed-Mode Crack Analysis of Isotropic Solids Using Conservation Laws of Elasticity," *Journal of Applied Mechanics*, vol. 47, no. 2, pp. 335–341, 1980.

[143] H. Chen and R. Shield, "Conservation laws in elasticity of the J-integral type," *Zeitschrift fuer Angewandte Mathematik und Physik*, vol. 28, pp. 1–22, 1977.

[144] J. Kim and G. Paulino, "T-stress, mixed-mode stress intensity factors and crack initiation angles in functionally graded materials: a unified approach using the interaction integral method," *Computer Methods in Applied Mechanics and Engineering*, vol. 192, pp. 1463–1494, 2003.

[145] J. Rethore, A. Gravouil, F. Morestin, and A. Combescure, "Estimation of mixed-mode stress intensity factors using digital image correlation and an interaction integral," *International journal of fracture*, vol. 132, pp. 65–79, 2005.

[146] J. Rethore, S. Roux, and F. Hild, "Noise-robust intensity factor determination from kinematic field measurements," *Engineering Fracture Mechanics*, vol. 75, pp. 3763–3781, 2008.

[147] J. Rethore, S. Roux, and F. Hild, "An extended and integrated digital image correlation technique applied to the analysis of fractured samples," *European Journal Computational Mechanics*, vol. 18, pp. 285–306, 2009.

[148] S. Yoneyama, Y. Morimoto, and M. Takashi, "Automatic evaluation of mixed-mode stress intensity factors utilizing digital image correlation," *Strain*, vol. 42, pp. 21–29, 2006.

[149] S. Yoneyama, T. Ogawa, and Y. Kobauashi, "Evaluating mixed-mode stress intensity factors from full-filed displacement by optical methods," *Engineering Fracture Mechanics*, vol. 74, pp. 1399–1412, 2007.

[150] S. Roux and F. Hild, "Stress intensity factor measurements from digital image correlation: post-processing and integrated approach," *International journal of fracture*, vol. 140, pp. 141–157, 2006.

[151] S. Roux, J. Rethore, and F. Hild, "Digital image correlation and fracture: an advanced technique for estimating stress intensity factors of 2D and 3D cracks," *Journal of Physics D: Applied Physics*, vol. 42, no. 21, pp. 1–21, 2009.

[152] R. Hamam, F. Hild, and S. Roux, "Stress intensity factor gauging by digital image correlation: Application in cyclic fatigue," *Strain*, vol. 43, pp. 181–192, 2007.

[153] P. Lopez-Crespo, A. Shterenlikht, E. Patterson, J. Yates, and P. Withers, "The stress intensity of mixed mode cracks determined by digital image correlation," *The Journal of Strain Analysis for Engineering Design*, vol. 43, pp. 769–780, 2008.

[154] F. Yusef and P. Withers, "Real-time acquisition of fatigue crack images for monitoring crack-tip stress intensity variations within fatigue cycles," *The*

Journal of Strain Analysis for Engineering Design, vol. 44, no. 2, pp. 149–158, 2009.

[155] J. Quinta Da Fonseca, P. Mummery, and P. Withers, "Full-field strain mapping by optical correlation of micrographs acquired during deformation.," *Journal of Microscopy*, vol. 218, pp. 9–21, Apr. 2005.

[156] M. Fagan, *Finite element analysis: Theory and practice*. Longman, 1992.

[157] J. Kugan and Y. Chen, "The values of J-integral within the plastic zone," *Engineering fracture mechanics*, vol. 55, no. 6, pp. 869–881, 1996.

[158] BS7448, "BS7448, Fracture mechanics toughness tests," 1997.

[159] F. Hild and S. Roux, "Digital Image Correlation: from Displacement Measurement to Identification of Elastic Properties - a Review," *Strain*, vol. 42, pp. 69–80, May 2006.

[160] A. Wasylyk and A. Sherry, "Evolution of plasticity in relation to ductile tearing in 304(L) stainless steel," in *University of Manchester*, (Bellevue, WA), 2010.

[161] G. Irwin, "Plastic zone near a crack and fracture toughness," *Society for Experimental Mechanics*, vol. 137, pp. 267–279, 1997.

[162] M. Mostafavi, J. Duff, and T. Marrow, "In-situ observation of damage nucleation in graphite under biaxial flexural loading," in *University of Manchester*, (Dresden, Germany), 2010.

[163] B. Allard, D. Rouby, G. Fantozzi, D. Dumas, and P. Lacroix, "Fracture behaviour of carbon materials," *Carbon*, vol. 29, no. 3, pp. 457–468, 1991.

[164] B. Rand, A. Hosty, and S. West, *Introduction to carbon science*. London: Stoneham, MA (USA); Butterworth Publishers, 1989.

[165] B. McEnaney and T. Mays, *Porosity in Carbons*. London: Stoneham, MA (USA); Butterworth Publishers, 1995.

[166] Z. Bazant, "Size Effect Aspects of Measurement of Fracture Characteristics of Quasibrittle Material," *Advanced Cement Based Materials*, vol. 4, pp. 128–137, Oct. 1996.

[167] R. Talreja, "Transverse Cracking and Stiffness Reduction in Composite Laminates," *Journal of Composite Materials*, vol. 19, pp. 355–375, Jan. 1985.

[168] S. Shah, *Toughening mechanisms in quasi-brittle materials*. Kluwer Academic Publishers, 1991.

[169] M. Thouless, "Bridging and Damage Zones in Crack Growth," *Journal of the American Ceramic Society*, vol. 71, pp. 408–413, June 1988.

[170] A. Castro-Montero, S. Shah, and R. Miller, "Strain Field Measurement in Fracture Process Zone," *Journal of Engineering Mechanics*, vol. 116, pp. 2463–2484, Nov. 1990.

[171] J. Homeny and W. Vaughn, "R-Curve Behavior in a Silicon Carbide Whisker/Alumina Matrix Composite," *Journal of the American Ceramic Society*, vol. 73, pp. 2060–2062, July 1990.

[172] P. Leevers, "Material and geometry effects on crack shape in double torsion testing," *Journal of Material Science*, vol. 20, pp. 77–84, 1985.

[173] J. Begley and J. Landes, "Serendtrity and the J integral," *International Journal of Fracture*, vol. 12, no. 5, pp. 764–766–766, 1976.

[174] C. Ouyang and S. Shah, "Geometry-Dependent R-Curve for Quasi-Brittle Materials," *Journal of the American Ceramic Society*, vol. 74, pp. 2831–2836, Nov. 1991.

[175] C. Shih and M. German, "Requirements for a one parameter characterization of crack tip fields by the HRR singularity," *International Journal of Fracture*, vol. 17, no. 1, pp. 27–43, 1981.

[176] K. Broberg, "Critical review of some methods in nonlinear fracture mechanics," *Engineering Fracture Mechanics*, vol. 50, pp. 157–164, Jan. 1995.

[177] Z. Bazant and M. Kazemi, "Determination of fracture energy, process zone length and brittleness number from size effect, with application to rock and concrete," *International Journal of Fracture*, vol. 44, no. 2, pp. 111–131, 1990.

[178] V. Saouma and D. Natekar, "Cohesive stresses and size effect in quasi-brittle materials," *Sadhana*, vol. 27, pp. 461–466, Aug. 2002.

[179] M. Srinivasan, "On estimating the fracture probability of nuclear graphite components," *Journal of Nuclear Materials*, vol. 381, pp. 185–198, Oct. 2008.

[180] Z. Zou, S. Fok, B. Marsden, and S. Oyadiji, "Numerical simulation of strength test on graphite moderator bricks using a continuum damage mechanics model," *Engineering Fracture Mechanics*, vol. 73, pp. 318–330, Feb. 2006.

[181] M. Pavier, C. Poussard, and D. Smith, "Effect of residual stress around cold worked holes on fracture under superimposed mechanical load," *Engineering Fracture Mechanics*, vol. 63, no. 6, pp. 751–773, 1999.

[182] D. Read, "Measurement of applied J-integral produced by residual stress," *Engineering Fracture Mechanics*, vol. 32, no. 1, pp. 147–153, 1989.

[183] W. Mitter, F. Rammerstorfer, O. Grundler, and G. Wiedner, "Discrepancies between calculated and measured residual stresses in quenched pure iron cylinder," *Materials Science and Technology*, vol. 1, no. 10, pp. 793–797, 1985.

[184] D. Smith, S. Hadidimoud, and H. Fowler, "The effects of warm pre-stressing on cleavage fracture. Part 2: finite element analysis," *Engineering Fracture Mechanics*, vol. 71, no. 13-14, pp. 2033–2051, 2004.

[185] T. Oku and M. Ishihara, "Lifetime evaluation of graphite components for htgrs," *Nuclear engineering and design*, vol. 227, no. 2, pp. 209–217, 2004.

[186] M. Pavier, D. Smith, N. Simandjuntak, and H. Alizadeh, "Predicting fatigue crack growth in aerospace alloys: Including the effect of plasticity induced closure," *Engineering Integrity*, vol. 21, no. 1, pp. 6–9, 2007.

[187] Y. Lei, N. O'dowd, and G. Webster, "Fracture mechanics analysis of a crack in a residual stress field," *International journal of fracture*, vol. 106, no. 3, pp. 195–216, 2000.

[188] D. Beardsmore and A. Sherry, "Allowance for residual stresses and materials interfaces when calculating J in and close to welded joints," in *ASME Conference Proceedings*, vol. 464, pp. 11–21, 2003.

[189] Z. Bazant, "Size Effect in Blunt Fracture: Concrete, Rock, Metal," *Journal of Engineering Mechanics*, vol. 110, no. 4, p. 518, 1984.

[190] Z. Bazant and L. Cedolin, *Stability of structures: elastic, inelastic, fracture and damage theories*. New York:: Oxford University Press, 1991.

[191] Z. Bazant and J. Planas, *Fracture and size effect in concrete and other quasibrittle materials*. Boca Raton: CRC Press, 1998.

[192] A. Hillerborg, M. Modeer, and P. Petersson, "Analysis of crack formation and crack growth in concrete by means of fracture mechanics and finite elements," *Cement and concrete research*, vol. 6, no. 6, pp. 773–781, 1976.

[193] P. Petersson, "Crack growth and development of fracture zones in plain concrete and similar materials, Report TVBM-1006," tech. rep., Division of Building Materials, Lund Institute of Technology, Lund, Sweden, 1981.

[194] J. Planas, G. Guinea, and M. Elices, "Report to ACI-SEM Joint Task Group on Fracture Testing of Concrete," tech. rep., Universidad Politecnica de Madrid, Madrid, 1994.

[195] G. Guinea, J. Planas, and M. Elices, "A general bilinear fit for the softening curve of concrete," *Materials and Structures*, vol. 27, no. 2, pp. 99–105, 1994.

[196] J. Planas, M. Elices, and G. Guinea, "Measurement of the fracture energy using three-point bend tests: Part 2 Influence of bulk energy dissipation," *Material Structures*, vol. 25, pp. 305–312, 1992.

[197] J. Lubliner, "A plastic-damage model for concrete," *International Journal of Solids and Structures*, vol. 25, no. 3, pp. 299–326, 1989.

[198] W. Chen, *Plasticity in Reinforced Concrete*. New York: McGraw-Hill, 1982.

[199] H. Kupfer and K. Gerstle, "Behavior of concrete under biaxial stresses," *Journal of Engineering Mechanics Division*, vol. 99, no. 4, pp. 853–866, 1969.

[200] J. Galvez, "A discrete crack approach to normal/shear cracking of concrete," *Cement and Concrete Research*, vol. 32, pp. 1567–1585, Oct. 2002.

[201] R. Malm, "Predicting shear type crack initiation and growth in concrete with non-linear finite element method," tech. rep., Royal Institute of Technology (KTH) Department of Civil and Architectural Engineering Division of Structural Design and Bridges, Stockholm, Sweden, 2009.

[202] R. Yu, G. Riuz, and E. Chaves, "A comparative study between discrete and continuum models to simulate concrete fracture," *Engineering Fracture Mechanics*, vol. 75, pp. 117–127, Jan. 2008.

[203] E. Seldin, "Stress-strain properties of polycrystalline graphites in tension and compression at room temperature," *Carbon*, vol. 4, pp. 177–191, July 1966.

[204] J. Lee and G. Fenves, "Plastic-Damage Model for Cyclic Loading of Concrete Structures," *Journal of Engineering Mechanics*, vol. 124, no. 8, p. 892, 1998.

[205] U. Cicekli, G. Voyiadjis, and R. Abualrub, "A plasticity and anisotropic damage model for plain concrete," *International Journal of Plasticity*, vol. 23, pp. 1874–1900, Oct. 2007.

[206] G. Voyiadjis, Z. Taqieddin, and P. Kattan, "Anisotropic damage plasticity model for concrete," *International Journal of Plasticity*, vol. 24, pp. 1946–1965, Oct. 2008.

[207] V. Gopalaratnam and S. Shah, "Softening Response of Plain Concrete in Direct Tension," *Journal Proceedings*, vol. 82, no. 3, pp. 310–323, 1985.

[208] J. Oliver, "A consistent characteristic length for smeared cracking models," *International Journal for Numerical Methods in Engineering*, vol. 28, pp. 461–474, Feb. 1989.

[209] M. Mostafavi, J. Duff, R. Delorme, and T. Marrow, "Damage Nucleation in Nuclear Graphite under Biaxial Flexural Loading," in *ICMFF9 Parma*, (Prama, Italy), 2010.

[210] B. Marsden, "Stresses and Deformations in Graphite Bricks," in *Graphite Symposium, University of Manchester*, (Pretoria), 2009.

[211] B. Kelly and J. Brocklehurst, "Irradiation damage in graphite.," *Journal of nuclear materials*, vol. 7, p. 3, 1966.

[212] B. Marsden, "Dimensional changes in GR graphite subject to fast neutron damage and radiolytic oxidation," in *University of Manchester*, 2002.

[213] J. Kies, A. Clark, and P. Pratt, "Fracture 1969," *Chapman and Hall Ltd, London*, pp. 483–491, 1969.

[214] O. Osano, "A review of the double torsion technique for brittle materials," *Journal of Material Science*, pp. 2505–2511, 1988.

[215] G. Irwin and J. Kies, "Critical Energy Release rate analysis to fracture strength," *Welding Journal*, vol. 33, p. 193, 1954.

[216] A. Evans and S. Wiederhorn, "Crack propagation and failure prediction in silicon nitride at elevated temperatures," *Journal of Materials Science*, vol. 9, no. 2, pp. 270–278, 1974.

[217] C. Martins, M. Steen, and L. Rosa, "Theoretical comparison of error in kic values determined by different testing methods of ceramics," *Journal of testing and evaluation*, vol. 19, no. 3, pp. 256–259, 1991.

[218] G. Quinn and J. Quinn, *Fracture Mechanics of Ceramics*. New York,: Plenum Press, 6, pg 603 ed., 1983.

[219] G. Quinn, "Delayed failure of a commercial vitreous bonded alumina," *Journal of materials science*, vol. 22, no. 7, pp. 2309–2318, 1987.

[220] H. McKinney and H. Smith, "Method of Studying Subcritical Cracking of Opaque Materials," *American Ceramics Society Bullitin*, vol. 58, pp. 536–536, 1975.

[221] P. Swanson, "Subcritical crack growth and other time- and environment-dependent behaviour in crustal rocks," *Journal of Geophysical Research*, vol. 89, no. B6, pp. 4137–4152, 1984.

[222] J. Gere and S. Timoshenko, *Mechanics of Materials*. PWS Publishing Company, Boston, MA, 1997.

[223] H. Adefashe, "Determining the Fracture Mechanics Properties of Sedimentary Rocks Using Double Torsion Testing," Master's thesis, University of Texas at Austin, 2006.

[224] M. Radovic and E. Lara-Curzio, "Mechanical properties of tape cast nickel-based anode materials for solid oxide fuel cells before and after reduction in hydrogen," *Acta Materialia*, vol. 52, no. 20, pp. 5747–5756, 2004.

[225] R. Roark and W. Young, "Formulas for stress and strain," 1975.

[226] P. Leevers and J. Williams, "Double torsion testing of high velocity crack resistance," *Journal of Materials Science*, vol. 22, no. 3, pp. 1097–1107, 1987.

[227] B. Whittaker, R. Singh, and G. Sun, *Rock Fracture Mechanics- Principles, Design and Applications*. Elsevier, 1992.

[228] B. Atkinson, *Fracture mechanics of rocks*. Academic Press, London, 1987.

[229] P. Rijken, *Modelling naturally fractured reservoirs: from experimental rock mechanics to flow simulation*. PhD thesis, The University of Texas at Austin, Department of Petroleum and Geosystems Engineering, 2005.

[230] F. Champomier, "Crack propagation measurements on glass: a comparison between double torsion and double cantilever beam specimens," *Fracture mechanics applied to brittle materials*, vol. 60, p. 72, 1979.

[231] T. Naidu, "Comparison of six fracture toughness test techniques applied to three alumina materials," Master's thesis, University of Cape Town, Cape Town,, 2002.

[232] K. Huebner, D. Dewhirst, D. Smith, and T. Byrom, *The finite element method for engineers*. Wiley, New York, 2009.

[233] O. Zienkiewicz and R. Taylor, *The finite element method for solid and structural mechanics*. Elsevier Butterworth-Heinemann, 2006.

Appendix A

The Double Torsion Technique

The Double Torsion (DT) specimen is generally used for the characterisation of fracture toughness, slow crack growth determination and fatigue properties of highly brittle materials. It has the unique ability to allow for stable controlled crack propagation irrespective of how brittle the material is. It thus proves useful in a number of application, including the fracture characterisation of nuclear grade graphite. This being said, the DT technique has not yet been standardised and there exists reported scatter of test data from different laboratories for the same materials considered.

This review analyses the major topics which concern the DT technique. Attempts to validate the technique are presented in Chapter 5 which uses an experimental analysis using Perspex (PMMA), a full Finite Element (FE) model and Digital Image Correlation (DIC) to measure out-of-plane deformations. The Experimental, FE and DIC investigations, presented in Chapter 5, have been submitted for publication to the Journal of Experimental Techniques.

A.1 Overview of the DT Technique

The DT testing methodology has been around for several decades, but is still relatively uncommon and unused as it has yet to be standardised. It was first introduced by Outwater and Gerry [90], and Kies and Clark [213] in the late 1960's and proved especially useful for fracture characterisation of highly brittle materials where common testing procedures such as the Compact Tension (CT) or Single Edge Notched Beam (SENB) may prove difficult. The DT technique

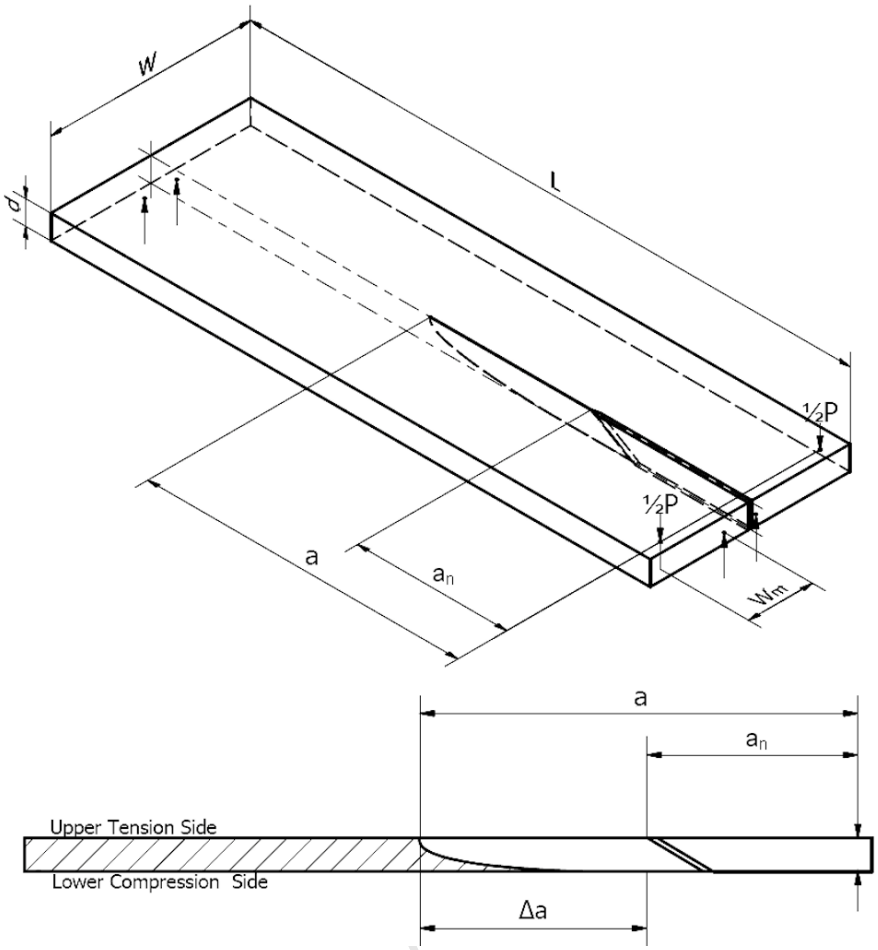

Figure A.1 – The DT specimen layout, loading configuration and corresponding dimensions: crack length a, notch length a_n, crack extension Δa, moment arm w_m , specimen length L, specimen width W, specimen thickness d and applied load P with displacement y at the load point in the y-direction (not shown).

has a unique and very attractive feature in that the Stress Intensity Factor (SIF), as a first approximation, is independent of the crack length over the middle half of the specimen. This allows for relatively long range over which a crack may be propagated in a highly controlled stable manner at a constant driving force. With this elegant feature it becomes clear that the DT technique is particularly useful for fracture characterisation of very brittle materials such as ceramics, cements and brittle polymers such as graphite.

The DT geometry also proves very useful in the investigation of slow crack growth rate dependent systems for the generation of crack velocity versus SIF data (VK data). Because the crack length does not enter into the equation of the SIF it provides a useful tool in facilitating testing situations which would be difficult with

the use of other techniques such as the evaluation of opaque and non-reflective materials where crack length measurements could prove difficult. This feature becomes especially desirable for high temperature and controlled environments where access for crack length measurements are difficult to make. The technique may also be used for fatigue investigations [89]. Due to the crack length independence of the SIF and the large crack propagation range the technique also proves useful to observe the direct effect of altered test parameters on crack velocity, where the user can "read off" the immediately effect of that parameter during testing [89].

The DT method provides many advantages and there are several good reviews available for the DT technique from both analytical and experimental standpoints [36, 32, 214]. Research has been done in the analytical, experimental and some practical aspects. Some FE studies were also carried out by Trantina [33] and Ciccotti et al [111, 102, 37, 103]. There is, as yet, no standardised DT test method and several investigators have expressed concerns over some factors involved. While the DT testing seems advantageous, a number of questions have arisen concerning several assumptions about the analysis which might influence the measured results. In recent years, several corrections have been proposed to the original work of the DT technique.

A.1.1 Specimen Geometry and Loading Configuration

The DT specimen comprises of a rectangular thin plate loaded in four point bending at one side. A diagram of the DT specimen is shown (Figure A.1), where usually the specimen is supported by four ball bearings. The load is applied so that each load point is subjected to exactly an equal force. The specimen is considered as two separate halves, which when loaded by load P will rotate through angle θ. The rotational elastic deformation or applied torque of each half if sufficiently large, results in a crack propagating between the considered halves. As mentioned earlier, the elegance of this method is that over a substantial section of the specimen the SIF is independent of the crack length. Thus the only dependence on the SIF is the driving force. Due to the nature of DT testing, alignment of the specimen to the fixture and the load actuator is critical. Slight misalignment results in "skewed" or non-symmetrical crack propagation which may yield invalid test data. This is discussed later.

A.1.2 Analysis of the DT Loading Geometry

There are two methodologies to determine a SIF from a DT specimen, the first derived from a theoretical compliance and referred to in this text as Evans' "theoretical approach" [91], the later based on the experimental compliance and referred to as William and Evans' "experimental approach" [92]. Essentially both use similar assumptions and in rely on the same principle. To calculate of the strain energy release rate G, the DT methodology makes use of Griffith energy criterion for a perfectly elastic material by assuming a linear compliance relationship C. This includes the following assumptions:

1. The specimen is considered as two separate independent beams. The propagating crack separates the two beams.
2. The applied load results in a torsional elastic deformation of each beam. The deformation of each half is assumed to be small.
3. The specimen is only subjected to torsional deformations and the unbroken section is assumed ridged.
4. There is no interaction between the two halves at the crack surface.
5. Crack front or crack profile may be characterised by a straight line though the specimen thickness.
6. The crack tip profile remains constant on crack extension.
7. Fracture is regarded as *Mode I* rupture.
8. Plane strain conditions are commonly assumed.

Theoretical Approach

Evans approach [91] is based on a theoretical calculated compliance relationship. For a bar with polar moment of inertia I_P and shear modulus μ subjected to a torsional moment T results in an angle of twist θ. This relationship is given as

$$\theta = \frac{y}{W_m} = \frac{Ta}{I_p \mu} \tag{A.1}$$

where T may be expressed as

$$T = \frac{P}{2} W_m \tag{A.2}$$

It can be shown that for small deflections and for a bar where the width is much greater than specimen thickness the second moment of area I_P may be expressed as [90]

$$I_P = \frac{Wd^3}{6} \tag{A.3}$$

and hence combining Equations A.1, A.2 and A.3 we obtain an equation for the compliance relationship based on the theoretical stiffness (noted as subscript A) of a rectangular torsion bar as

$$C_A(a) = \frac{y}{P} \approx \left(\frac{3{W_m}^2}{Wd^3\mu}\right) a = B_A a \tag{A.4}$$

The compliance relationship relates the load and displacement at the load points to the specimen crack length. A linear relationship exists between a load with its corresponding displacement to a crack length.

The SIF for a DT specimen is determined through standard fracture mechanics analysis of elastic strain energy release rate under the assumption of LEFM (Mode I). The strain energy release rate for crack extension is related to the specimen compliance by the Irwin expression [215]. If the crack tip shape is assumed independent of crack length, then the crack extension area remains constant ($dA = d \cdot da$) where d is the specimen thickness.

$$G_P = \frac{1}{2}P^2\frac{dC}{dA} = \frac{1}{2d}P^2\frac{dC}{da} \tag{A.5}$$

Note, d will be replaced by d_n for grooved specimens, where d_n the thickness without the groove depth.

By differentiating Equation A.4 with respect to a, and substituting into Equation A.5 we obtain

$$G_P(a) = \frac{3P^2{W_m}^2}{2Wd^4\mu} \tag{A.6}$$

With the application of the linear elastic fracture mechanics relationship (LEFM) [215] the fracture toughness K_I (for mode I) is given as

$$K_I = \sqrt{E'G} \tag{A.7}$$

where E', the Young's modulus, is related to the shear modulus μ (where ν is the Poisson's ratio) by $\mu = E'/2(1+\nu)$ and where $E' = E/(1-\nu^2)$ for plane strain

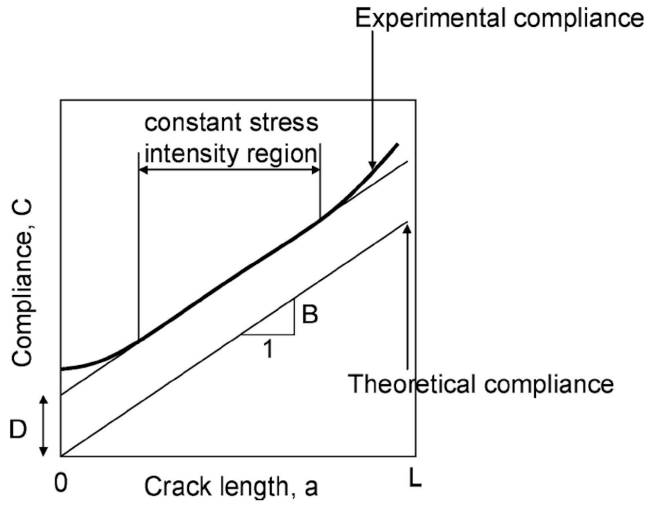

Figure A.2 – Schematic representation of the compliance relationship for the DT test configuration. The solid line represents ideal linear behaviour with the dashed line illustrating deviations from this behaviour that result from end influences *[31]*.

and $E' = E$ for plane stress. The expression for the SIF takes the form of

$$K_I(P) = \sqrt{\frac{2\mu G}{(1-\nu)}} = P\sqrt{\frac{B_A\mu}{d(1-\nu)}} = P\sqrt{\frac{3{W_m}^2}{Wd^4(1-\nu)}} \tag{A.8}$$

for plane strain and

$$K_I(P) = \sqrt{2\mu G(1+\nu)} = P\sqrt{\frac{B_A\mu(1+\nu)}{d}} = P\sqrt{\frac{3{W_m}^2(1+\nu)}{Wd^4}} \tag{A.9}$$

for plane stress conditions. Note, the SIF is a function of the applied load, the specimen geometry and Poisson's ratio only and is independent of crack length.

The validity of the model was tested experimentally by Williams and Evans [92] performing a compliance calibration on one specimen and comparing the empirical relationship with that of the analytical expression. They found that the data fits the linear relationship $C = B_A a$ with some discrepancies. These are discussed later.

Experimental Approach

Alternatively, Williams and Evans [92] amongst others [91, 31, 35] have found a compliance relationship experimentally. They have shown that generally the relationship between deflection and load varies linearly with the crack length as

measured by the longest extension of the cracked profile

$$C(a) = \frac{y}{P} \approx B_E a + D_E \tag{A.10}$$

where B_E and D_E (subscript E noting experimental derivation) are constants which depend on the elastic properties of the specimen and the specimen's dimensions, similar to the analytical approach. The linear relationship is illustrated schematically below. The parameters B_E and D_E are found to be independent of crack length. The exceptions to this are near the ends of the specimen. The intercept D_E is generally a non-zero constant [92].

Similar to the previous approach the strain energy release rate is found by substituting Equation A.10 into Equation A.5. And hence we obtain the fracture toughness with the use of Equation A.7 for plane strain

$$K_I(P) = \sqrt{\frac{2\mu G}{(1-\nu)}} = P\sqrt{\frac{B_E \mu}{d(1-\nu)}} \tag{A.11}$$

and for the plane stress assumption

$$K_I(P) = \sqrt{2\mu G(1+\nu)} = P\sqrt{\frac{B_E \mu(1+\nu)}{d}} \tag{A.12}$$

As before, the SIF given by the above equations is a function of the applied load, the test specimen compliance and geometry and Poisson's ratio but independent of crack length. The latter characteristic is one of the most attractive features of double-torsion testing.

Evans and Wiederhorn [216] showed that B_E may be obtained analytically as

$$B_E = \frac{3w_m^2}{W d^3 \mu} = B_A \tag{A.13}$$

Note, the fracture toughness is independent of D_E, the intercept of the experimental compliance curve C.

A.1.3 DT Technique for Fracture Toughness Determination

Fracture toughness can be determined in DT testing simply by loading a test specimen rapidly and recording the maximum load or plateau load P_c, during

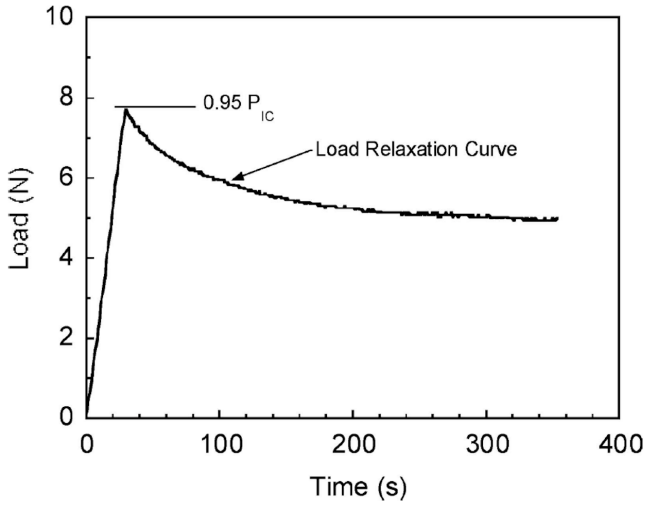

Figure A.3 – An illustration of temporal load variation obtained from a load relaxation test in a double-torsion test specimen of 3-YSZ *[32]*.

failure. The fracture toughness expression is obtained by substituting the failure load in Equation A.8 for plane strain or Equation A.9 for plane stress respectively

$$K_{Ic} = P_c \sqrt{\frac{3{W_m}^2}{Wd^4(1-\nu)\psi(t,W)}} \tag{A.14}$$

$$K_{Ic} = P_c \sqrt{\frac{3{W_m}^2(1+\nu)}{Wd^4\psi(t,W)}} \tag{A.15}$$

The factor $\psi(t,W)$ is a thickness correction factor which is discussed shortly. The experimental error in measuring the values of variables included in the formula for fracture toughness in DT is comparable to that of five other geometries (Chevron Notched (CN), SENB, Double Cantilever Beam (DCB), Single Edge Notched Tension (SENT) specimen and Three Point Bending (3BP)) [217].

A.1.4 Sub-Critical Crack Growth Studies

One of the most valuable characteristics of the DT technique is that crack growth data may be determined without having to monitor the crack length on a continuous basis. The DT beam has three methodologies for determining VK data, namely the load relaxation method, the constant rate of displacement method and the constant load method. In general, for quasi-static slow crack growth on

ceramic materials in a stress corroding medium is given by

$$v \equiv AK^n \tag{A.16}$$

where A is a constant and n is the sub critical crack growth index. The measured velocities are usually in the range of 10^{-3} to 10^{-8} mm/s, which are plotted on a log log scale to fit a linear log-log relationship.

Load Relaxation Method

The load relaxation method is commonly used indirectly to obtain the sub-critical crack propagation behaviour of brittle materials. According to this technique [91], a DT test specimen is loaded to below the expected fracture load $(0.9 - 0.95P_c)$. The cross head of the testing machine is then held at a fixed position and the increase in compliance of the test specimen from sub-critical crack growth leads to a relaxation of the load with time. A typical curve is shown in Figure A.3. Once the load relaxation curve has been found experimentally, it may be used to determine the corresponding VK curve.

Theoretical Approach

The theoretical approach to find the VK relationship is a continuation of the SIF derivation and is thus based on the same assumptions.To find the apparent crack velocity $\dot{a}$ we differentiate Equation A.4 with respect to time t. At fixed cross head $y = constant$ and hence $(dy/dt) = 0$. This yields the flowing equation for crack velocity (constant y denoted as subscript y)

$$\frac{da}{dt}_y (P,t) = \frac{Wd^3\mu}{3{W_m}^2} \frac{d}{dt}\left(\frac{1}{P^2}\right)_y \tag{A.17}$$

This may be rewritten as

$$\dot{a}_y(P,t) = -\frac{d}{dt}\left(\frac{B_A}{P^2}\right)_y \tag{A.18}$$

The crack growth rate may be found directly from the rate of load relaxation at a fixed displacement, simply from the slope of the load relaxation curve, if the displacement and the specimen dimensions are known. It is essential that precise material properties are known for the above approach.

Experimental Approach

An alternate method, which is based on the experimental compliance relationship, can also be manipulated to determine the crack growth rate. Similarly to the above methodology, the following equation for crack velocity is found as (constant y denoted as subscript y)

$$\dot{a}_y(P,t) = -\frac{(B_E a + D_E)}{B_E P}\left(\frac{dP}{dt}\right)_y \tag{A.19}$$

If the displacement remains constant and the tip of the crack remains in the crack length independent SIF region then

$$y = P(B_A a + D_E) = P_i(B_A a_i + D_E) = P_f(B_A a_f + D_E) \tag{A.20}$$

Where, the subscripts i and f denote the initial and final loads and crack lengths. The physical meaning of the above equation is that the increase in the compliance of the test specimen due to increase in crack length is exactly compensated by its temporal decrease in load. By setting the LHS of Equation A.19 equal to zero and rearranging it with Equation A.20, an expression for the crack growth velocity can be derived

$$\dot{a}_y(P,t) = -\frac{P_{i,f}}{P^2}\left(a_{i,f} + \frac{D_E}{B_E}\right)\left(\frac{dP}{dt}\right)_y \tag{A.21}$$

In some cases it may be assumed that $D/B << a_{i,f}$ and hence the above equation reduces to

$$\dot{a}_y(P,t) = -\frac{P_{i,f} a_{i,f}}{P^2}\left(\frac{dP}{dt}\right)_y \tag{A.22}$$

Even though Equation A.22 is popularly applied it is noted that in many cases the assumption that $a_{i,f}$ is much larger than D/B is not necessarily true. This is shown later.

In principle the entire VK curve can be obtained from a single load relaxation experiment. However, this methodology works better at relatively higher crack growth rates ($> 10^{-4} - 10^{-7} mm/s$ [35]) due to temperature fluctuations affecting load measurements at very low velocities. This method is also susceptible to spurious factors such as load train relaxation. It is for this reason that it has been recommended to generate complementary portions of the VK curve by combining the load relaxation technique with one of the two techniques discussed below [214].

Constant Rate of Displacement at Assumed Constant Load

The converse of the load relaxation technique at constant displacement for generating VK data employs a constant rate of displacement at assumed constant load. In this technique, the cross head is moved at a constant rate and the load value is allowed to reach a plateau where the increase in load from cross head movement is balanced by relaxation of the test specimen load from crack growth. If the plateau load value is given by P_c and is assumed to remain constant, then $dP/dt = 0$ (constant load is denoted a subscript P) and by differentiating Equation A.4 with respect to time t the crack velocity is found by

$$\dot{a}_P(y,t) = \frac{1}{P_p B_E}\left(\frac{dy}{dt}\right)_P = \frac{\dot{y}_P}{P_p B_E} \tag{A.23}$$

If the rate of change of deflection is known then it is possible to determine the crack growth rate. The disadvantage of this technique is that only one data point can be obtained per experimental run.

Wiederhorn [7] and later Quinn and co-workers [218, 219] successfully combined the constant displacement rate technique with the load relaxation technique to obtain slow crack growth information without having to make any crack length measurements. In this method, the cross head is moved at a slow, constant rate until the load decrease due to slow crack growth exactly offsets the load increase due to cross head movement. The peak load P_c and the cross head displacement rate can now be used to obtain the initial crack velocity $\dot{a}_i$ according to Equation A.23. The cross head is then arrested at the peak load and a load relaxation experiment is subsequently carried out. The initial crack velocity $\dot{a}_i$ from the load relaxation experiment can be obtained by substituting $P = P_i$ in Equation A.21. Assuming that the initial velocity obtained by application from Equation A.23 and Equation A.21 is the same, the following relationship is obtained

$$\dot{a}_i = \frac{\frac{dy}{dt}}{P_i B_E} = -\left(\frac{dP_i}{dt}\right)\frac{B_E a_i + D_E}{P B_E} \tag{A.24}$$

This relationship gives the expression of the compliance of the specimen at the beginning of the load relaxation experiment as [7]

$$B_E a_i + D_E = -\frac{dy}{dt}\,\frac{dP_i}{dt} \tag{A.25}$$

The initial compliance is related to the compliance at any other instant in the load relaxation experiment according to Equation A.20. Substitution of Equation A.24 in Equation A.25 therefore, allows the calculation of crack velocity according to

$$\dot{a}(P, y, t) = \left(\frac{\frac{dy}{dt}}{B_E}\right)\left(\frac{P_i}{\frac{dP_i}{dt}}\right)\left(\frac{\frac{dP}{dt}}{P^2}\right) \tag{A.26}$$

Since Equation A.26 does not involve any crack length term it is ideally suitable for applications such as elevated temperature and/or controlled environment testing.

Constant Load Technique

In one of the earliest application of the DT configuration the slow crack growth was measured through the constant load method [220]. This method is very simple; the average crack velocity corresponding to the SIF, which is calculated from the applied constant load can be obtained by measuring the crack length before and after the experiment and the elapsed time.

$$\dot{a}_P(a, t) = \frac{da}{dt} \tag{A.27}$$

By measuring crack length extension da over a time period Δt, an average crack velocity may be determined. The main disadvantage of the constant load technique is that only one data point can be obtained per experimental run. Additionally, relative crack length measurements are required. This technique, however, is suitable for the calculation of very low crack velocities where load relaxation measurements cannot be performed [35].

A.1.5 Implications and Considerations of the DT Method

The DT method seems simple, however, there are several important considerations which need to be considered. Often the data acquired shows large scatter and repeatability can be poor. Swanson [221] reported that for a given specimen geometry the values of the stress corrosion index n are repeatable to a degree, however there exist rather large differences in the mean values of n determined for the same material in different laboratories. These differences cannot be attributed to variations in material properties. There has been considerable recent discussion in the literature regarding the consistency of DT data and the validity

of the method. Various factors have been identified as possible sources of error. The following section discusses these concerns and intends to informs the reader about the assumptions the DT technique testing. Lets consider the assumptions the DT method is based upon given in section A.1.2:

Effect of Crack length on SIF K (note 1)

The derivation of the DT methodology assumes a crack length independent SIF (due to the linear compliance), however, this is not applicable over the entire length and is only valid through the middle section of the specimen. This has been discussed by various researchers [92, 31, 35, 33, 220, 222, 93, 90]. Trantina's [33] FE analysis showed that the SIF varies according to crack length to the theoretical assumed constant data. Figure A.4 illustrates this and indicates significant variation in the SIF near the ends of the specimen. The SIF remains nearly constant (to within 5 percent) in the range of crack lengths ranging from $a : W > 0.55$ and unbroken ligament lengths of $(L - a) : W > 0.65$. This implies that the range of crack lengths for which the SIF is independent of the crack length is a function of the length to width $(L : W)$ ratio of the test specimen. For $L/W = 3$ ratios the middle 60 percent of the test specimen displays this property $(0.18 < a : L < 0.78)$. This conclusion agrees well with experimental work done by Ebrahimi [93]. The specimen dimensions used by Trantina were of ratios $L : W = 2$ and $L : W = 3$ and were un-grooved DT specimens.

Similarly, the edge effects of a crack length independent SIF were discussed by Salem [34]. His experimental data is shown in Figure A.5. Table A.1 summarises some of the crack length ranges over which the SIF was found to remain reasonably constant.

Table A.1 provides details of researchers assumed constant SIF for the middle section of the specimen. Non-linearity in C may reasoned by the edge affects of the specimen. Chevalier and co-workers [95], however, have reported a crack length dependent SIF while studying the behaviour of zirconia and alumina. They have attributed a minor crack length dependence to the deflections of the unbroken ligament and proposed a correction for load relaxation tests which are a specimen geometry specific (dimensions and loading configuration). Their methodology is intended for tests using the load relaxation technique for VK investigations. According to them, the corrected expression for SIF ${K_I}^{Ch}$ in the DT testing

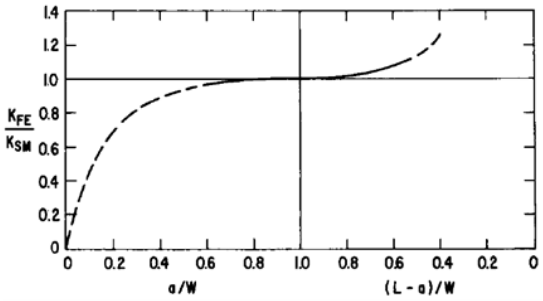

Figure A.4 – Trantina's constant K curve as a function of crack length [33]

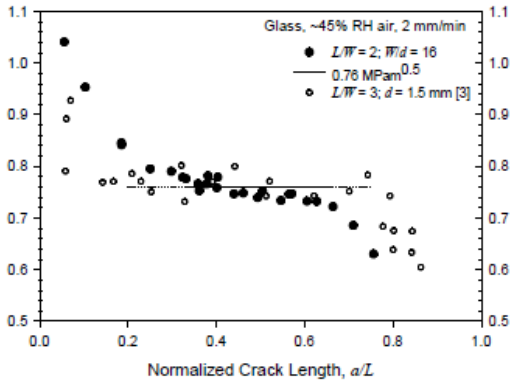

Figure A.5 – Salem's [34] plot of SIF readings as a function of normalized crack length in glass specimens tested at 2 mm/min in 45 percent RH air . For the plate, $L = 51mm$, $W = 23mm$, $d = 1.5mm$. Open symbols are data of Pletka et al [35] shown as reference [3] in the figure.

Length:Width $(L:W)$	a(lower limit)	a(upper limit)	Reference
1.5	$0.4W$	$L - 0.8W$	[222]
2.5	$0.5W$	$L - 1.0W$	[93]
2.6	$0.33L$	$0.67L$	[92]
3.5	$0.33L$	$0.83L$	[223]
3	$1/3L$	$2/3L$	[36]
3.9	$0.20L$	$0.7L$	[224]
4	W	$L - W$	[91]

Table A.1 – Summary of DT geometries utilised with corresponding assumed constant SIF range.

configuration can be given by

$$K_I^{Ch}(P,a) = K_I^E\left(\frac{a}{a_n}\right)^{\frac{m}{k}} \tag{A.28}$$

Here, K_I^E is Evans' derived SIF (where E denotes Evans' model) for plane strain, a_n is the notch length, m and k are constants for the test specimen geometry and material considered. The crack length may be estimated by

$$a(P) = \frac{\frac{P_{i,f}(B_E a_{i,f}+D_E)}{P} - D_E}{B_E} \tag{A.29}$$

The constant m is found by a series of constant load tests at various loads. Constant k is found from load relaxation tests at fixed cross head displacement. Chevalier found $m = 6$ and $k = 32$ for alumina and the loading configuration used. It is worth mentioning that Chevalier's correction is crack length dependent and thus requires a crack length estimate, obtained by employing Equation A.29. The SIF calculation for load relaxation tests becomes a function of load and crack length. The correction results in a shift of the VK curve and an increase of the stress corrosion index n. Chevalier and co-workers concluded in another paper [110], that their correction generally gives an overestimation of the SIF related to the exponent value.

Ciccotti and co-workers [111, 102, 37, 103] performed detailed three dimensional FE stress analysis for 'large' DT specimens ($L170mm$ and $W > 60mm$) and concluded that appreciable deviations occurred from the classical analytical solution predictions of strain energy release rate. They provided correction factors to account for experimental variables such as crack shape, groove width and depth, notch length and test specimen geometry and found deviations (up to 40%) in the value of strain energy release rate from the analytical solution. Of all the effects considered the effect of test specimen geometry on the calculated SIF was found to be the most significant and complex. A discussion on this follows in the next section.

Pure Torsional Analysis (note 2)

The 'Pure torsion' analysis assumes small deflections (the analysis assumes that $y = \theta W_m$). Under this condition the specimen compliance can be determined from expression $C = y/P$. When large deflections are reached however, this

relationship holds with approximation only and has to be corrected. Figure A.6 shown the reduction in W_m due to the torsional deformation at the loading points. Shown is one specimen half.

The issue of large deflections has been addressed by Hine et al [109] and later by Leevers [18], and experimentally [121] addressed by researchers investigating the behaviour and properties of polymers and polymer based composites. Leevers proposed a (most recent) correction for large deflections. Their analysis yielded the following expression for SIF, for the case of plane strain and plane stress respectively. R and r are the radii of supporting and loading balls and θ is the angle the torsional arm makes with the horizontal surface of the un-deformed specimen

$$K_I^{LDC}(P,\theta) = P_c\sqrt{\frac{3y(1+\nu)}{Wd^4\psi(t,W)}} * \sqrt{\left(\frac{W_m-(R+r+d)(sin\theta+\theta cos\theta)}{\theta}\right)}$$

$$K_I^{LDC}(P,\theta) = P_c\sqrt{\frac{3W_m^{LDC^2}(1+\nu)}{Wd^4\psi(t,W)}} \tag{A.30}$$

$$K_I^{LDC}(P,\theta) = P_c\sqrt{\frac{3y}{Wd^4(1-\nu)\psi(t,W)}}\sqrt{\left(\frac{W_m-(R+r+d)(sin\theta+\theta cos\theta)}{\theta}\right)}$$

$$K_I^{LDC}(P,\theta) = P_c\sqrt{\frac{3W_m^{LDC^2}}{Wd^4(1-\nu)\psi(t,W)}} \tag{A.31}$$

The function $\psi(d,W)$ is a thickness correction factor which is discuss in the next section.

Perfectly Rigid Crack Tip Front (note 3)

The assumption that the plate beyond the crack tip front is perfectly rigid imposes a few implications. The plate has the same torsional shear stresses applied to it as the independent beams. This results in a deformation of the assumed un-cracked plate. Fuller's analysis requires that this plate remains perfectly rigid and that the remaining ligament length $(L-a)$ is long. The above assumption was

addressed by various researchers, Ciccotti [111, 102, 37, 103], Chevalier [95] and Leevers[172, 101], but no generally accepted correction as been found. However, Fuller [31] states that the elastic deformation of the un-cracked portion of the DT specimen only becomes problematic when the boundaries and contact stresses affect the crack tip process zone.

Region of Overlap and Thickness Correction (note 4)

Specimen thickness plays an important role when it comes to the DT technique as there exists a region of interaction between the two sides of the cracked specimen seen in the diagram A.7. This is especially the case for thicker specimens, . It has been shown by Fuller [31] the two separate beams inter penetrate each other and the contact stresses which occur are ignored in the analysis. For thin specimens this is a good approximation [36] however, the interaction stresses for thicker specimens can generally not be disregarded as these affect the SIF.

Fuller has concluded, using polycrystalline alumina, that values for K_{Ic} are underestimated and that this is explained by the specimens thickness ratio of 0.25, whereas he had good agreement with other methods for a thickness ratio of 0.166 [216]. Fuller's analysis yielded a correction factor. The correction factor has been found and experimental tests have confirmed that $\psi(t, W)$ may be expressed with an accuracy of 0.1 percent as

$$\psi(t, W) = 1 - 0.6302\tau_1.20\tau e^{\frac{\pi}{\tau}} \tag{A.32}$$

where

$$\tau = \frac{2d}{W} \tag{A.33}$$

It is recommended that the use of thin specimens of thickness ratio $W : 0.1d - W : 0.83d$ by Evans [91] and Tait [36] amongst others. Many DT investigations though have been conducted on specimens between a quarter or half the minimum thickness and still yielded comparable data to CT specimens and DCB. Other thickness correction criterion's have been proposed [89] and [225]. Fuller's correction is most widely used by researchers. The thickness correction is included into the derivation and will change Equation A.8 for plain strain and Equation A.9 for

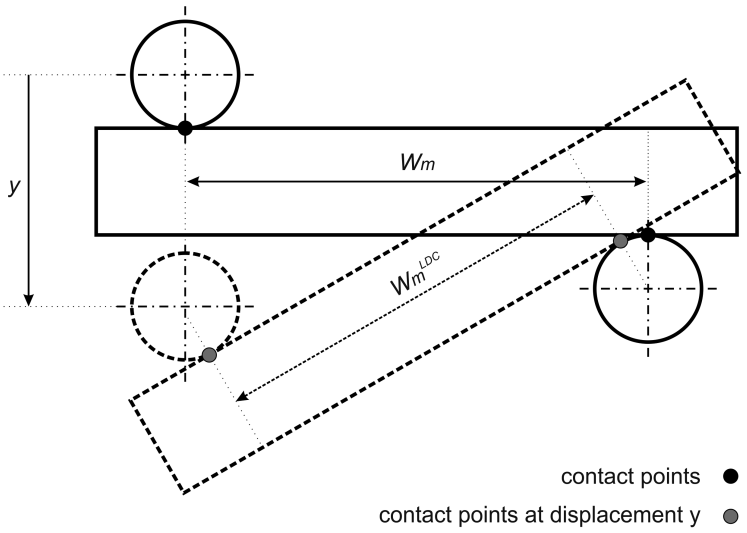

Figure A.6 – Illustration of the reduction in W_m due to large load point (P) deflections (Δy). Also shown is the crack surface interaction points which results in a shift of centre of rotation.

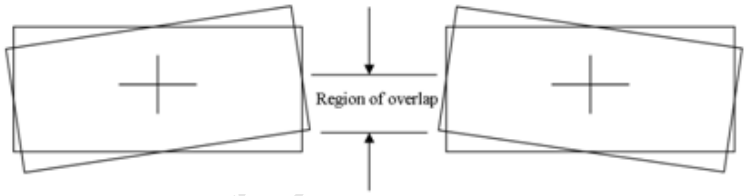

Figure A.7 – Showing the region of interaction of the two sides of cracked specimens (from Ref [36])

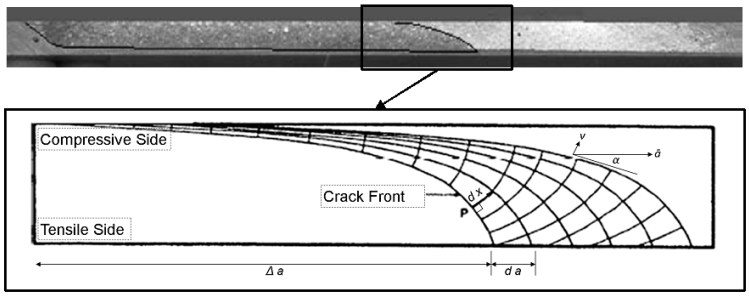

Figure A.8 – A schematic of the cross section of a crack profile in a DT specimen showing the curved crack front [9]. The crack opening is at the tensile surface of the specimen, where the compressive side remains closed.

plane stress to respectively.

$$K_I(P) = P\sqrt{\frac{3{W_m}^2}{Wd^4(1-\nu)\psi(t,W)}} \tag{A.34}$$

$$K_I(P) = P\sqrt{\frac{3{W_m}^2(1+\nu)}{Wd^4\psi(t,W)}} \tag{A.35}$$

Crack Tip Front Inclination (note 5 and 6)

The theoretical analysis assumes a straight crack profile front, perpendicular to the tensile surface. However, practical observation shows that the profile is curved as shown in Figure A.8. It should be noted that the term crack length a refers to the crack extension on the tensile surface of the DT specimen and refers to the longest part of the crack from the loading points.

Considering that the crack opening occurs at the tensile side of the specimen and that the compressive side remains closed, it follows that the crack grow faster on the tensile side of the specimen and the compressive side only follows once sufficient crack opening has occurred. It is also assumed that change in crack surface area with the increase in crack length is constant throughout the length of the specimen. It follows that $dA/da = constant$. This has been confirmed by Evans et al [91] [92], Fuller [31], Trantina [33] and Vikar et al [105], amongst others. The difference between the lower and upper crack extension of the DT specimen have been found empirically to be fixed and equal to five times the thickness d in the plane of the crack for glass and alumina [91]. Vikar and Gordon [105] have shown that the shape of the crack profile is dependent on the characteristics of sub-critical crack growth in any given material and environment.

Successive crack front positions as shown in Figure A.8. Notice that the crack velocity $\dot{a}$ is not the true crack velocity as it is not orthogonal to the crack front. The true crack velocity V varies along the crack front, the highest being at the tensile surface. Evans proposed an averaging factor to the crack velocity [91]

$$\phi = \frac{d}{\sqrt{\Delta a^2 + d^2}} \tag{A.36}$$

This correction simply assumes a straight crack front which is now at an acute angle. Hence the crack velocity in the plane of the specimen's tensile surface is

the fraction as shown in Equation A.36. The correction factor is multiplied by the former crack velocity.

Vikar and Gordon [105] have shown that the curvature of the crack front means that the true velocity of any crack element dx varies along the crack front implying that the local SIF also varies along the crack front. Since V is related to K_I in the form of $V = AK_I{}^n$ it implies that the SIF is also a function of the position along the crack front. Thus Equation A.36 becomes questionable. This problem was addressed by Pollet and Burns [106] who derived a better averaging process for the crack velocity. They assume that over a range of crack velocities encompassing those experienced by crack elements dx along the crack front, the VG relation may be described by

$$V = V_0(G - G_0)^m \tag{A.37}$$

where V_0, G_0 and m are constants. The average value of G, G_{av}, is related to the apparent crack velocity

$$\dot{a} = \frac{V0}{\phi}(G_{av} - G_0)^m \tag{A.38}$$

where ϕ is given by

$$\phi = \left(\frac{1}{d}\int_0^d sin\alpha(x)^{\frac{1}{m}}dx\right)^m \tag{A.39}$$

where α is the inclination of the fracture front relative to the specimen surface as a function of depth x along the thickness of the specimen and m has the same value as the stress-corrosion index n determined from conventional VK tests. They observed that the crack profiles and consequently ϕ was almost independent of $\dot{a}$ in PMMA. Consequently, providing DT data gives correct value for the stress corrosion index

$$V(G) = \phi\dot{a}G_{av} \tag{A.40}$$

The expression for the crack velocity correction reduces to the correction proposed by Evans if the crack front is approximated as a straight line with α remaining constant. The value of ϕ can be obtained from experimental measurements of the crack profile. Pollet and Burns also showed that ϕ does not vary significantly with $n > 4$. Thus ϕ can be accurately obtained even if n is not known precisely.

Leevers uses single crack shape parameter S to characterise the crack front. This shape factor can be predicted with accuracy adequate for general purposes from

specimen geometry only

$$S = 0.35Q'coth\left[\frac{(L-a)}{Q'd_n}\right] \tag{A.41}$$

where

$$Q' = 2\left(\frac{d}{d_n}\right)^2\left[\frac{ZW}{\pi(1+\nu)d}\right] \tag{A.42}$$

and

$$Z = \frac{1}{3} - 0.24\left(\frac{d}{W}\right) + 0.13\left(\frac{d}{W}\right)^2 \tag{A.43}$$

The curved crack shape may be theoretically derived with the hyperbolic shape function (with co-ordinate system x-axis and y-axis)

$$y = \frac{d_n S}{x} + K_0 \tag{A.44}$$

G_I^L against V data should be corrected by a factor derived from a measurement of crack front shape in order to achieve an adequate approximation to the underlying material property. This is particularly important for the rate-depended materials [226]. The strain energy release rate is found by solving for the change in area dA. This reduces to the term (G_I^L is the corrected strain energy release rate)

$$G_I^L(a) = G\left(\frac{a}{Sd_n + a}\right) \tag{A.45}$$

Similarly to Leevers model, Stadler and Kausch [108] have concluded that for alumina the crack front profile is independent of crack velocity but strongly on specimen thickness. Their factor M compromises the SIF, Poisson's ratio, crack opening displacement and shear modulus to predict crack front profile.

$$M = \frac{\zeta G}{K_I(1-v)^{1/2}} \tag{A.46}$$

where ζ is the local deformation parameter, which must be distinguished from a crack opening displacement (COD) in that it is the sum of the local plastic strain (COD) and the surrounding elastic strain. The equation of the crack profile is stated as: (with co-ordinate system x-axis and y-axis)

$$yx = M'F * f\left(\frac{dy}{dx}\right) \tag{A.47}$$

where M' is the derivative of M and $F = (2\mu W d^3)/d_n$.

Crack Opening Mode (note 7)

The DT test is not seen as pure mode I loading but rather a mixed mode I-III loading because of a minor existence of mode III SIF (K_{III}) at the crack tip [227]. A number of investigators [91] [216]have shown that K_{III} is extremely small in comparison with K_I in brittle materials. It is thus concluded that DT may be regarded as K_I.

Plane Strain or Plane Stress (note 8)

The appropriate choice between the two conditions is difficult to specify since the crack profile is curved or three dimensional. One assumption involves the choice of state of plane strain or stress to describe the SIF according to Equation A.14 for plane strain or Equation A.15 for plane stress. While earlier researchers favoured the plane strain expression for fracture toughness calculation [31] [36] recent calculations are based on the plane stress expression. Atkinson [59] reports that if the specimen thickness d is small compared to the non-linear process zone then the plane strain constraints are also small and plane strain stress analysis in applicable. The minimum thickness criterion $d \geq 2.5(K_{Ic}/\sigma_y)^2$ which is used for ductile materials is used to distinguish between plain strain and plain stress. The justification for the former is that plane strain fracture toughness is suitable for brittle materials [33].

A.1.6 Specimen Geometry Considerations

There is a large variation and debates about geometry aspects. These sections will discuss various geometry factors and consideration of DT specimen.

Length, Width and Thickness ratios ($L : W : d$)

There are no standardised dimensions to date for DT specimens. Tait et al published a paper [36] that reviewed DT specimens with the respective dimensions used by various researchers. His work recommends the following specimen proportions (Table A.2).

The FE work done by Trantina [33] uses a thickness of $0.1W$. Ciccotti's et al FE research [111, 102, 37, 103] used $0.117W$ thickness. They also reported in their analysis, where large specimens were used, that they found large discrepancies between the theoretical analysis and the FE analysis. Madjoubi et al [110] suggest that Evans model can be used uncorrected for specimen lengths more than $3W$ and a thickness of $0.075W$.

Grooved Specimens

DT specimen designs often included a groove along the length of the test specimen in order to guide the growth of the crack. Tests have been conducted on single or double grooved specimens. It has been shown that careful alignment of the test specimen and fixture eliminates the need of the machined groove [36]. Additionally, the presence of a groove leads to effects that are still not fully characterized and it also requires a modified analysis. Side grooves may cause significant stress concentrations and propagating cracks have been reported to deviate toward sharp edges caused by side grooves. Thus, more recently un-grooved specimens are preferred as it eliminates uncertainties. With careful alignment it becomes possible to grow straight crack.

Figure A.9 shows the effect of grooves on the SIF. This reflects work done by Ciccotti [102] in his FE analysis. His conclusion is that side groves, their depth and width greatly affects the strain energy release rate. Noticeable for no grooves are slight deviations from the analytical solution to the FE solution. The middle region of the specimen though for un-grooved specimens does not vary significantly. This may be explained by the slight deviations from the constant SIF, which was discussed earlier.

Starter Notch a_n

All DT specimens have a starter notch to facilitate crack initiation. A starter notch of length a_n is often recommended with a length such that any crack that initiates from the notch is in the constant SIF region. The effects of the length of the starter notches have been investigated by Ciccotti [102]. His results are summarised in the Figure A.10. Note that the graph does not only show the effects of the starter notch, but the deviations of the correction factor may also be due to the slight variations in the SIF. The only deviation between pre-notched and straight specimens is near the start of the specimen.

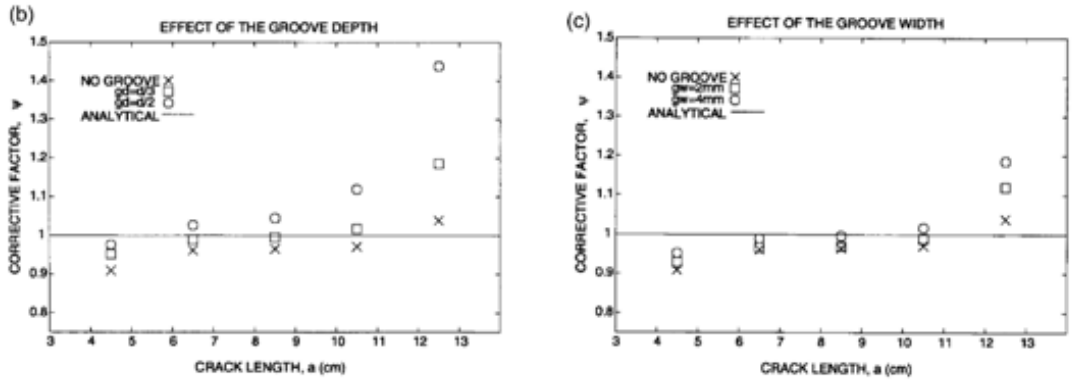

Figure A.9 – (b) Effect of groove depth on K (c) Effect of groove width on K. The graph shows the correction factor required to for K (from Ciccotti *[37]*).

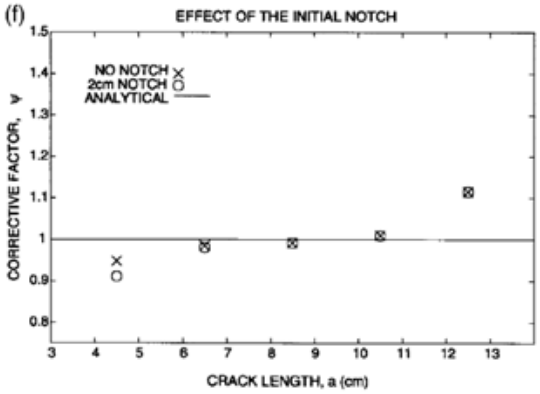

Figure A.10 – The effect a starter notch *[37]*

Length L	Width W	thickness d	Material	Reference
$3W$	W	$0.083W$	PMMA	[35]
$3W$	W	$0.120 - 0.10W$	Polymer	[91]
$2W$	W	$0.067W$	Rock	[8]

Table A.2 – Recommended specimen ratios by Tait et al [36]

If un-grooved specimens are used then alignment is critical and crack initiation needs to be precisely along the centre of the specimen. Any misalignment from the centre will cause the crack to deviate from its centre path and give invalid results. Salem reports valid K_{Ic} results for a crack initiation within 0.1 percent deviation off the centre line. A notch helps to form a crack at the centre of the specimen and provides a high stress concentration.

Pre-Cracking of Specimens

A number of investigators have commented on the importance of specimen pre-cracking and notching on fracture mechanics parameters. Pletka et al [35] argued that the absence of pre-cracking resulted in erroneously higher SIFs. Atkinson and Meredith [228] also asserted that specimen pre-cracking was essential to obtain a natural starting fracture from which a macro crack could extend during a test. The work of Rijken [229], however, suggested otherwise. In a test conducted on Travis Peak specimens, Rijken found no systematic relationship between pre-crack length and sub-critical fracture index or SIF for notched, un-notched and pre-cracked samples.

Generally specimens are pre-cracked for two reasons. Firstly; to have a sharp crack front identical to a real crack. Secondly; the DT technique requires a fully developed crack front. This can only be achieved by pre-cracking the specimens before commencing in any further testing.

Specimen Symmetry and Crack Propagation

Symmetry is crucial for the DT. The specimen needs to be aligned perfectly symmetrically about the crack propagation axis. In an ideal situation, the crack will propagate down the centreline of the specimen. Any misalignment can cause 'skewed' crack propagation as shown in Figure A.11. If the crack deviates significantly, as shown in Figure A.11b then the test data becomes invalid as the results will vary substantially to those of a straight crack, Figure A.11a. There are no significantly useful analysis or corrections available for variation of test data due to misalignment.

Correct alignment is always crucial, but not always achievable. Misalignment of the specimen with respect to the actuator and the fixture may result in inaccurate data. The effectiveness and alignment of the testing fixture will determine

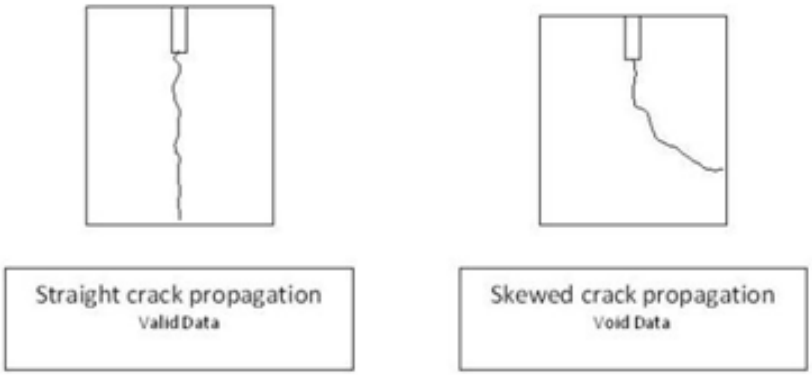

Figure A.11 – DT specimens showing (a) straight crack propagation and (b) skewed crack propagation, respectively.

the success of the DT testing. The fixture should allow for simple specimen fitting, alignment and the observation the specimen's crack. The fixture should be designed is such way that applied load is split equally to both halves of the specimen.

FE Analysis

The first comprehensive FE stress analysis of the DT geometry was performed by Trantina [33]. In the analysis Trantina used un-grooved specimens and the objectives were to determine crack front configurations, compare analytical SIF values to FE SIF values and to determine the variation of the SIF with crack length. The analysis concluded that most assumptions inherent in the derivation of the analytical expression are reasonable. The SIF calculation from the analytical analysis was shown to be nearly equal to the value obtained from the FE stress analysis. It was shown that the SIF remains nearly constant (to within five percent) in the range of crack lengths ranging from $a : W > 0.55$ and unbroken ligament lengths of $(L - a) : W > 0.65$. This implies that the range of crack lengths for which the SIF is independent of the crack length is a function of the length to width $L : W$ ratio of the test specimen. For $L : W = 3$ ratios the middle 60 percent of the test specimen displays this property ($0.18 < a : L < 0.78$). Their conclusion agrees well with experimental work done by Tait et al [36].

More recently, Ciccotti and co-workers [111, 102, 37, 103] performed detailed three-dimensional FE stress analysis for 'large' double-torsion test specimens ($L > 170mm$ and $W > 60mm$) and concluded that appreciable deviations occurred

from the classical analytical solution predictions of strain energy release rate. They provided correction factors to account for experimental variables such as crack shape, groove width and depth, notch length and test specimen geometry and found deviations (up to 30 percent) in the value of strain energy release rate from the analytical solution. Of all the different variables considered, the factor of test specimen geometry on the calculated SIF was found to be the most significant and complex.

Ciccotti provided two correction factors $\varphi(a)$ and $\xi(a)$ for calculation of the SIFs and for VK data. The correction factors are dependent on groove depth, groove width thickness, notch length and crack front inclination. Ciccotti analysed four different specimen sizes for width and length. Variations for the specimen thickness were not considered in his analysis. Both correction factors are function of crack lengths and thus deem the necessity of crack length measurements (Superscript E stands for Evans' model). Note that Ciccotti's corrections are functions of the crack length.

$$C^{Ci}(a) = \varphi(a) B_A a \tag{A.48}$$

$$K_I^{Ci}(P,a) = \sqrt{\varphi(a)} K_I^E(P) \tag{A.49}$$

$$V^{Ci}(P,t,a)_y = -\vartheta \frac{\xi(a_{i,f})}{\varphi(a)} \frac{a_{i,f} P_{i,f}}{P^2} \left(\frac{dP}{dt}\right)_y \tag{A.50}$$

where the crack length is estimated by

$$a(P) = C^{-1}\left(\frac{C(a_{i,f}) P_{i,f}}{P}\right) \tag{A.51}$$

The correction factors were derived from this analysis for five different crack lengths, covering a large interval. The variation curves of these coefficients with crack length can be obtained by a 3rd order polynomial fitted to the five data points.

It is important to underline that the direct use of the recorded values is conditioned by the type of dimensions ratios ($L : W : d$) of the samples used by the Ciccotti and co-workers. In the case where the sample geometry is different, it is possible to do linear interpolations between the values of the different geometries proposed. Examples were published by Ciccotti [102].

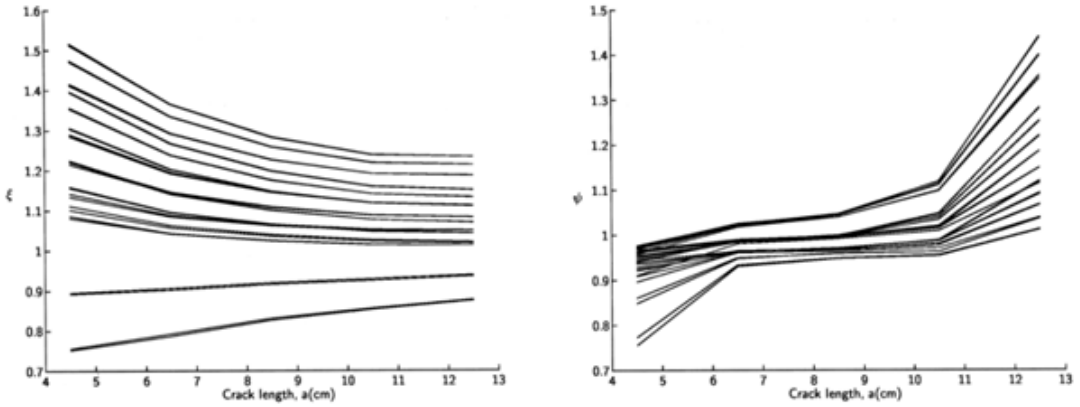

Figure A.12 – The corrective coefficients of the correction factors $\varphi(a)$ and $\xi(a)$ for specimens with length $L = 17cm$ and width $W = 6cm$. The different curves represent all combinations of the other geometric parameters *[37]*.

A.2 Summary

This Appendix presented a critical review of the DT technique. Discussed was the derivation of the technique for the measurement of the SIF and slow crack growth data. The author believes that the DT technique is a very powerful technique for the fracture investigations of highly brittle material. The technique offers a crack length independent SIF, which enables the ability of controlled crack propagation at constant driving force. In addition, Champomier [230] compared the DT to Double Cantilever Beam (DCB) favourably and states that reproducibility is excellent. Tait et al [231] also gives a good review of the DT test method compared to other fracture toughness test techniques for brittle materials. They conclude that the DT has good precision and gives reasonable values of K_{Ic}. Results for tests for a verity of materials show that the DT technique is generally acceptable [36].

This being said an evaluation of the DT technique, presented in Chapter 5, has shown a minimal but clear dependence of SIF on crack length for all specimen configurations, especially for the thicker $2.7W : W : 0.11W$ geometry. This can result in scatter of fracture toughness data and non-reproducibility of VK relationship data. These discrepancies are believed to be linked to marked non-linearity in the assumed linear compliance relationship, which has been linked to the large deflections at the load points and the out-of-plane deformations of the assumed ridged unbroken ligament. Since SIF is a function of the change in compliance, small deviations to the assumed linear compliance may results in

significant error in the SIF. If a linear compliance is achieved, by either correcting for these errors, or by an optimal loading and specimen geometry. The validity of the crack length independent DT technique thus depends on the loading configuration, the specimen geometry and material. The reader is referred to Chapter 5 for details on the investigation.

Appendix B

Design and Commission of the Double Torsion Testing Fixture

This project included the design and commission of a Double Torsion (DT) fixture which has been used for the evaluation of the DT technique and the graphite experimental work. Presented below is the design and commission report of this fixture.

B.1 Introduction

This appendix deals with a design and commission report of the design of a DT testing fixture. The DT technique, presented and evaluated in Chapter 5, was utilised to contribute to the understanding of the fracture mechanisms and characteristics of nuclear graphite. The aim of this appendix is to construct and commission a fixture that is simple, effective and favours repetitive testing. It is intended to help the user with the testing, the alignment of the specimen and measurements/observation of the propagating crack. The objectives are summarised below:

- Introduce the DT method,
- clarify the issues of correct alignment,
- review previous fixtures that have been used,
- design and construct the fixture (Follow the design process of conceptual design through to design and commission) and

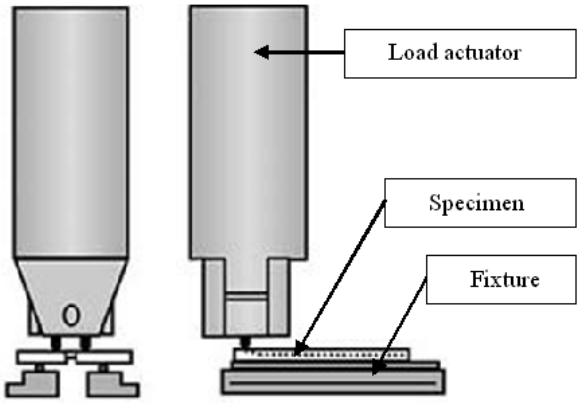

Figure B.1 – Simple layout with load actuator applying load to the specimen used by Zhu et al [38].

- summarise the achievements of this design report.

B.1.1 Design and Commission Procedure

This report follows the standard design procedure; discussing previously used designs, listing their advantages and disadvantages. First, the reader is introduced to several conceptual ideas from which the final design concept is drawn. Advantages and disadvantages are discussed. This leads to the detailed design where all aspects of the design are given (detailed drawings are attached in Appendix D). The designed fixture is then manufactured and tested. Last, conclusions are drawn on the validity of testing fixture. Some recommendations were made.

B.2 Background Information on the DT technique

The Double Torsion Beam technique is used for the characterisation of fracture toughness, slow crack growth determination and fatigue properties of highly brittle materials. This brief review analyses the major topics which revolve around the DT technique and summarises the technique and its testing procedure. Additionally the importance of alignment is discussed. A critical evaluation of the technique is provided in Chapter 5.

The DT methodology has been around for several decades, but remains relatively uncommon. It was first introduced by Outwater and Gerry [90], and Kies and

Clark [213] in the 1960's. The DT technique has a unique and very attractive feature that the Stress Intensity Factor (SIF), as a first approximation, is independent of the specimen's crack length over a central area of the specimen. Because the crack length does not enter into the equation of the SIF, it provides a useful tool in facilitating testing of opaque and non-reflective materials where crack length measurements could be difficult to make. The technique also facilitates for the investigation of slow crack growth rate investigations (VK) data. In addition, it may be used for fatigue investigations. Due to the independence to crack length and a large crack propagation range, the effects of alterations to test parameters can be "read off" immediately during the test.

Several good reviews available for the DT technique from both analytical and experimental standpoints. To this day though, there is no standardised test method and several investigators have expressed concerns over some factors involved with this fracture mechanics evaluation method. While DT testing seems advantageous, a number of questions have arisen concerning several assumptions which were made for the analysis which might influence the measured results.

B.2.1 Basic Layout of the DT Beam testing fixtures

The basic layout of any DT fixture, as shown in Figure B.1, is that the specimen is fixed to a fixture where the load is applied externally through a load cell. Due to the nature of the DT technique, alignment of the specimen to the fixture and the load actuator is critical. Slight misalignment results in non-symmetrical crack propagation which in turn can give void test results. Correct alignment thus becomes essential for valid and repeatable data (as discussed in Chapter 5).

The Specimen Layout

The specimen configuration essentially comprises of a rectangular thin beam supported in a four point bend configuration at one end where the crack propagates through the specimen's length. A schematic diagram of the DT specimen is shown in Figure 5.2 where: w_m the applied moment arm with applied load P. The specimen has dimensions: length L, width W and thickness d. Grooves, aligned along the specimen length, are sometimes used to constrain the crack path. The SIF

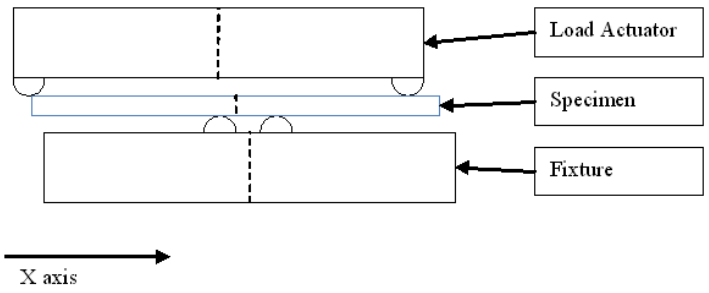

Figure B.2 – x-axis misalignment between the actuator, the specimen and the fixture (shown with exaggeration).

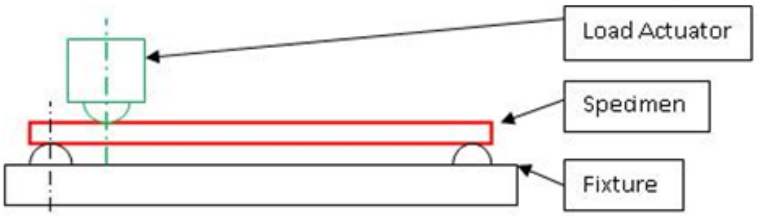

Figure B.3 – y-axis misalignment between the actuator, the specimen and the fixture (shown with exaggeration).

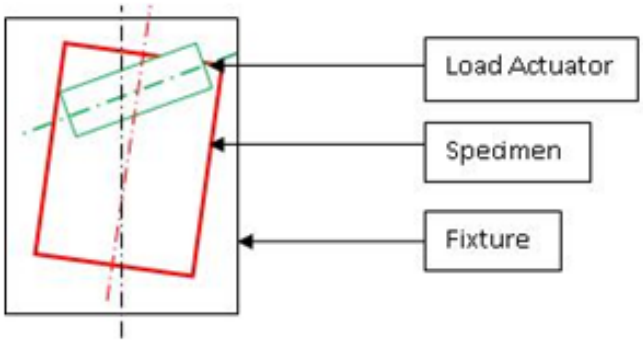

Figure B.4 – Angular misalignment between the actuator, the specimen and the fixture.

may be evaluated using

$$K_I = P\sqrt{\frac{3{W_m}^2}{Wd^4(1-\nu)\psi(t,W)}} \tag{B.1}$$

where v is the Poisson's ratio and $\psi(t, W)$ is a thickness correction. It is worth mentioning that no dependence of crack length on the SIF exists. This is what make the DT configuration favourable for the testing of highly brittle materials such as graphite.

In an ideal situation, the crack propagates down the centreline of the specimen. This, however, is usually not the case and often the crack deviates from the centreline. If crack propagation is such that the crack significantly deviates from the centreline, then the test data can be dubious.

B.2.2 Misalignment Possibilities

This section discusses the possible misalignment and assesses whether these are critical (i.e. if these effect symmetrical propagation). Its aim is to find the crucial aspects of the DT fixture to minimise the chance of misalignment and increase repeatability of experimental results.

The space, in which the DT is placed, can be considered to have Cartesian x y z coordinates. The z-axis being the height or along the thickness of the specimen, the x-axis along the width of the specimen and the y-axis along the length of the specimen (Figure 5.2). Hence, there are three identifiable reasons for misalignment which are categorised into x-axis misalignment, z-axis misalignment and angular misalignment:

1. "x-axis" misalignment

   This misalignment is between the actuator and the fixture. The centreline of the actuator ball bearings are not coincident with the supports of the DT fixture and the specimen is not centred correctly with the the fixture (Figure B.2). The consequence of such misalignment is that the applied torsional load is not equal and hence results in no-symmetrical crack propagation. This misalignment is seen as a critical one.

2. "y-axis" misalignment

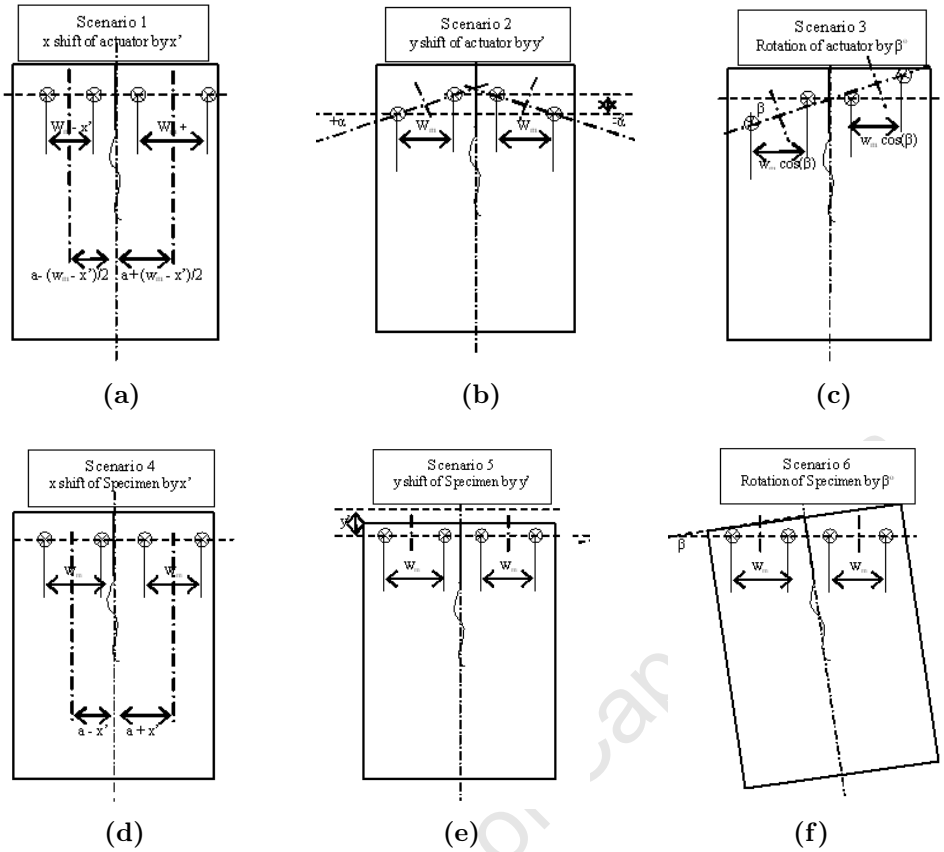

Figure B.5 – (a) to (c) Misalignment due to a shift of the load actuator and (d) to (f) Misalignment due to a shift of the specimen.

	Perfect	Scenario					
	Align.	1	2	3	4	5	6
a_1	a	$a-(w_m-x')/2$	a	a	$a-x$	a	a
a_2	a	$a+(w_m-x')/2$	a	a	$a+x$	a	a
W_{m1}	w_m	w_m-x'	0	$w_m cos(\beta)$	w_m-x'	0	$w_m+S_m cos(\beta)$
W_{m2}	w_m	w_m+x'	0	$w_m cos(\beta)$	w_m+x'	0	$w_m-S_m cos(\beta)$
y	0	0	y'	$\pm w_m sin(\beta)$	0	0	$S_m sin(\beta)$
α	0°	0	$\pm\alpha$	β	0	0	β
	ideal	critical	not critical	critical	critical	not critical	critical

Table B.1 – Quantification of misalignment

This misalignment is between the actuator and the fixture. The centres of the actuator ball bearings are not coincident with the supports of the DT fixture (Figure B.2). This results in an additional bending moment along the specimen length (y direction). The alignment of the specimen is not crucial for small errors.

3. "Angular" misalignment

   This misalignment between the actuator, the fixture and the specimen not being aligned properly in a co-linear sense. The components are not parallel to each other so that the specimen's and fixture's centreline are not parallel and the actuator is not perpendicular to the specimen and the fixture (Figure B.4). This effects are similar to the "x-axis" misalignment. The applied torsional load may not be balanced. This misalignment is seen as a critical one.

Fixture Evaluation Methodology

The above section established the overall relation of misalignment between the fixture, the specimen and the load actuator. The purpose of this exercise is to quantify misalignment to formulate an evaluation for various fixture designs. It is assumed that the specimen surface is always parallel to the load points as this type of misalignment was not considered.

Figures B.5 show the specimen with the considered misalignment scenarios where Table B.1 attempts to quantify the misalignment. Its purpose is the quantification of possible misalignment.. The dot ($\otimes$) indicates the loading points on the specimen.

B.2.3 Previously used Testing Fixtures

This section provides some of the previously, in literature, used DT fixtures. The aim is to identify and evaluate these concepts using the proposed evaluation provided in the previous section.

Example One

An example of a DT fixture design for a loading configuration is shown below in Figure B.6. The design shows two axes of rotation so that the load applied to the

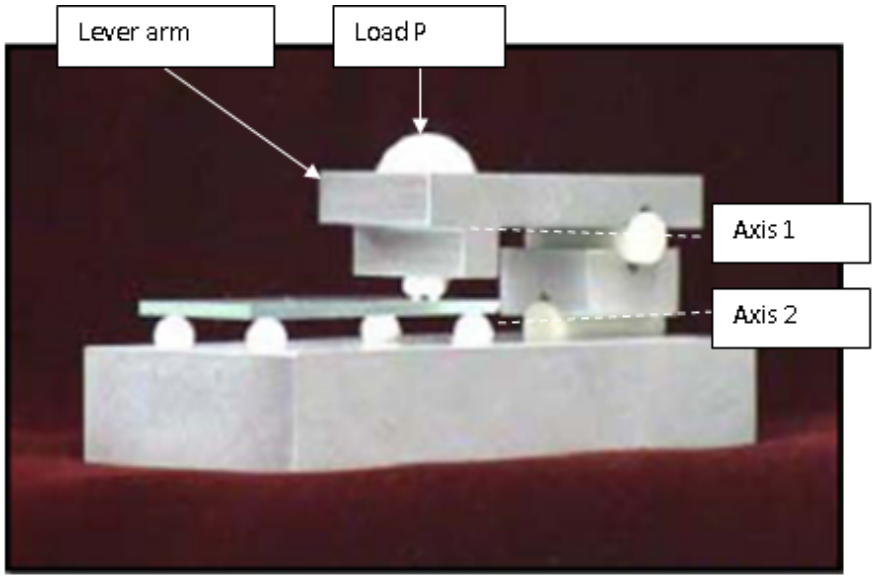

Figure B.6 – DT fixture as shown by Shyam et al [32]

	Scenario					
	1	2	3	4	5	6
a_1	a	a	a	$a-x$	a	a
a_2	a	a	a	$a+x$	a	a
W_{m1}	np	0	np	$w_m - x'$	0	$w_m + S_m cos(\beta)$
W_{m2}	np	0	np	$w_m + x'$	0	$w_m - S_m cos(\beta)$
y	0	np	np	0	0	$S_m sin(\beta)$
α	0	np	np	0	0	β

Table B.2 – Listing misalignment possibilities of example one. (np - not possible)

specimen is transmitted through a lever arm.. The advantage of this design is the loading configuration. The design entails a lever arm and the two axes (Axis 1 and Axis 2 in Figure B.6) of rotation by which the lever arm is supported. The load is applied through the lever arm to the specimen so that the loading points (if accurately manufactured) are always aligned to the support ball bearings. As such, little care has to be taken on the alignment of the testing fixture to the load actuator. In Addition, the two axes design ensures even loading, as slight misalignment of the lever arm is corrected through the two axis of rotation. This allows for easier straight crack propagation and repeatability of tests as summarised in Table B.2.

Example Two

Another example of a DT fixture is shown in Figure B.7 where the specimen is mounted in a movable platform. This has the advantage that the specimen's position may be adjusted perfectly to load cell. In Addition, the setup allows for different specimen sizes as the supporting ball bearings can be adjusted. However, the specimen is loaded via a single load point with a large radius. The advantage of this seems to be that alignment is enforced with the starter notch; the specimen centreline and the centreline of the load point. Because the actuator consists of one large radius, misalignment caused by rotation of the actuator are insignificant. Table B.3 list the possible misalignment possibilities. A concern of this layout is that the effects of only having one upper loading point are unknown.

Example Three

An additional example of a simple DT fixture is shown in Figure B.8. The load actuator and specimen are supported. This allows for simple specimen alignment, thus facilitating for repeatability of test data. Table B.4 lists the possible misalignment potential. It is noted that this setup has little misalignment possibilities and thus is very favourable. The actuator is supported and the specimen has guidelines for proper alignment. Table B.4 list the possible misalignment possibilities

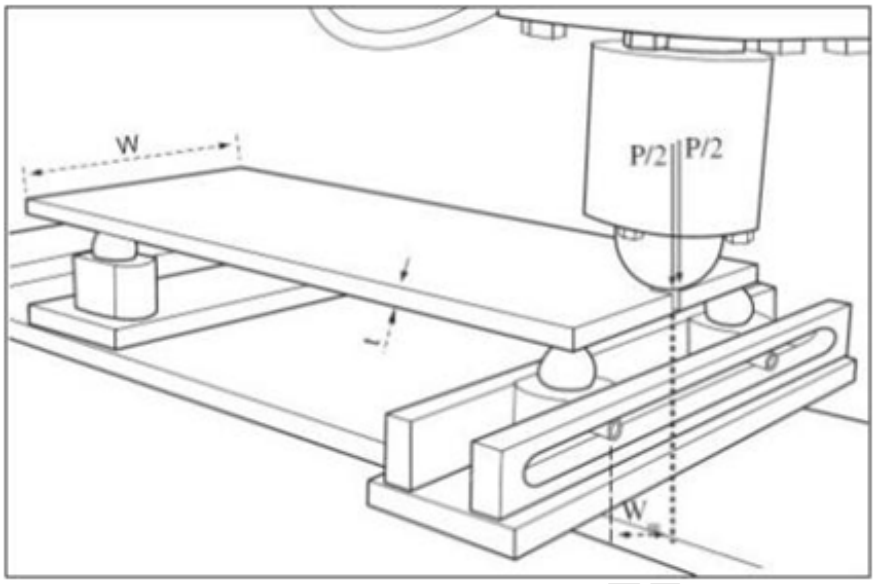

Figure B.7 – Double-torsion test arrangement by Albuquerqu et al [39].

	Scenario					
	1	2	3	4	5	6
a_1	$a-(w_m-x')/2$	a	a	a	a	a
a_2	$a+(w_m-x')/2$	a	a	a	a	a
W_{m1}	w_m-x'	0	np	np	0	np
W_{m2}	w_m+x'	0	np	np	0	np
y	0	y'	np	0	0	np
α	0	$\pm\alpha$	np	0	0	np

Table B.3 – Listing misalignment possibilities of example two. (np - not possible)

B.3 Design Specifications

The aim of the DT fixture is to hold the DT specimen during testing. It is essential that that the loading is evenly distributed and the fixture should favour repeatable testing conditions. The load is applied externally by a separate testing machine. The following list the "essential" and "desirable" requirements of the DT fixture:

Essential

- The fixture's purpose is for DT testing of specimen dimension 150 x 50 x 4 mm.
- Requires fitting onto the testing platform of the external testing machine at the University of Cape Town and the University of Manchester.
- Ensures proper alignment of the specimen to the load actuator and itself.
- Requires Specimen alignment to be simple.
- Facilitates for repeatability of tests.
- The design should be simple, inexpensive and easy to manufacture.

Desirable

- Allow for various specimen sizes.
- Allow for additional test environments to be added to the fixture. i.e. furnace, etc.

B.4 Fixture Design

Based on the literature review presented above, a DT fixture was designed and build as shown in Figure B.9. The most important purpose of the DT fixture is to hold and align the specimen correctly. As such, the fixture design is split into the following sections:

- Load actuator layout. This part applies the load to the specimen.

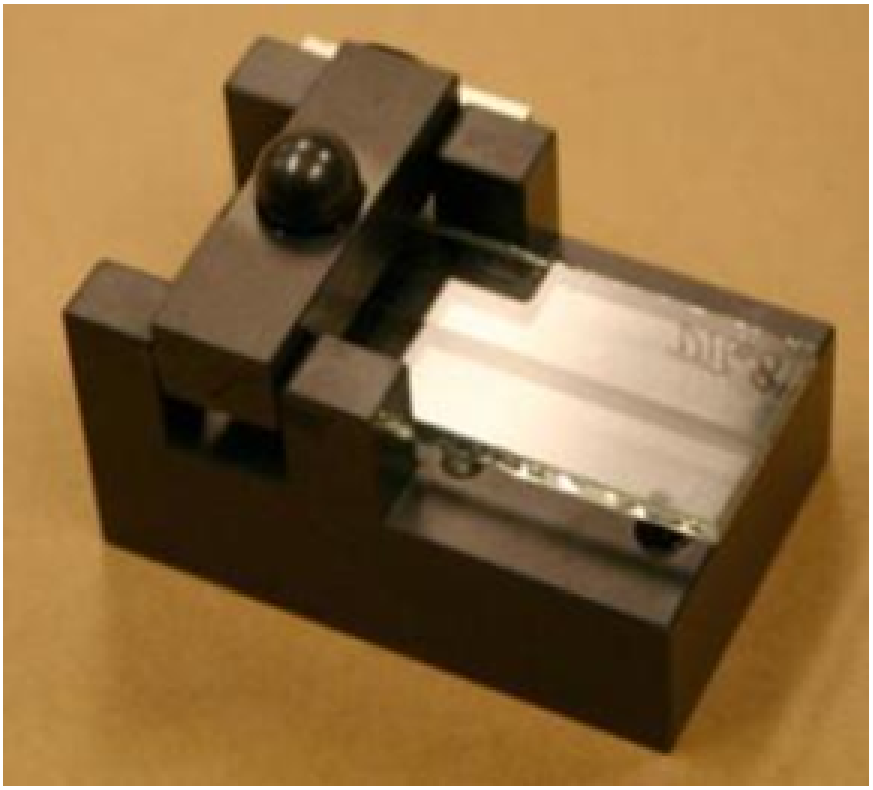

Figure B.8 – DT fixture with a simple layout with load actuator applying load to the specimen. The load actuator is guided by the base to ensure alignment (by Salem [34]).

	Scenario					
	1	2	3	4	5	6
a_1	a	a	a	a	a	a
a_2	a	a	a	a	a	a
W_{m1}	np	0	np	limited	0	np
W_{m2}	np	0	np	limited	0	np
y	0	y'	np	0	0	np
α	0	$\pm\alpha$	np	0	0	np

Table B.4 – Listing misalignment possibilities of example three. (np - not possible)

- The specimen support. The DT specimen has to be supported in a DT manner.
- The specimen alignment. This aligns the specimen to the load actuator and the base fixture.
- A base which holds all the components.

Of these, the following sections require conceptual ideas:

- The load actuator alignment.
- The specimen alignment.

It is assumed that the specimen is supported are ball bearings which positioned symmetrically around the specimens centreline. The supports are also located in such way that the specimen crack opening appears towards the top so that the crack may be easily observed.

B.4.1 Load Actuator Alignment

The load actuators function is to apply a load to the specimen. This may be done directly or indirectly (through a lever arm). One of the requirements is to insure proper alignment to the fixture and the specimen. For this, the design of Example One is chosen. A lever arm is used to guide the load actuator. The advantage of this concept is that the load actuator, in theory, is always aligned with the specimen. The load is applied directly in line with the load point to ensure a one to one load ratio. To ensure even loading a two axes setup is used. One disadvantage is that the loading point's arc and the position along the length of the specimen can vary, however, is said not to be crucial (the reader is referred to Table B.1. In addition, frictional effects are believed insignificant. Please refer to Appendix D for detailed drawings.

B.4.2 Specimen Alignment

To locate and align the specimen to the fixture four locating skews are used. The locating screws, which are fitted to the specimen supports, have the ability to adjust the specimen's position whilst allowing for variation in the specimen's width and allows the specimen to be aligned correctly. Please refer to Appendix D for detailed drawings.

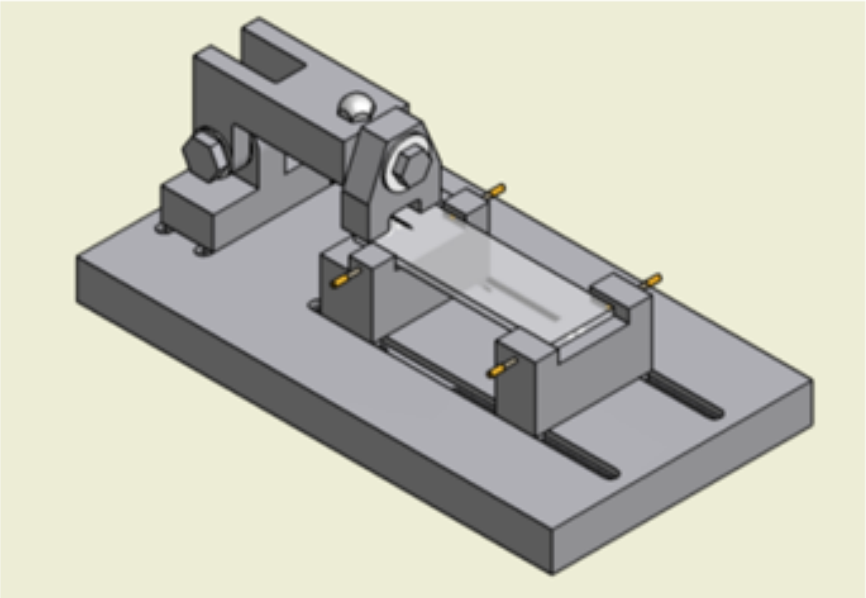

Figure B.9 – Layout of the designed and built DT fixture.

B.4.3 Base Plate

The function of the base is to hold the rest of the fixture's parts. The base has a unique feature which allows for once off adjustment of the fixtures parts for correct alignment. The main feature of the base plate are the side grooves where the lever arm and specimen supports are fitted. This enables for perfect, once off, positioning to ensure symmetry. As such it is believed that the base allows for easy alignment and repeatability of experimental conditions. Please refer to Appendix D for detailed drawings.

B.5 Evaluation and Commission of the Design

The evaluation and commission of the build DT fixture was undertaken experimentally. The test results were compared to a previous fixture. This included fracture toughness values and load relaxation curves. Since the DT methodology has no standardised test procedure the data results obtained in this evaluation may be questionable. This, however, was not in the scope of this design report. It was assumed that if comparable results were obtained that the fixture purpose's is adequate. For the commission of the DT fixture included five tests., which included three fracture toughness tests and two load relaxation tests.

B.5.1 Crack Propagation

The alignment of the specimen is critical to achieve straight crack propagation. Of the five test conducted, all tests achieved symmetrical crack propagation. The specimens are illustrated in Figure B.10. Table B.5 summarises the misalignment possibilities of the DT fixture. Correct alignment was easily achieved.

Fracture toughness test Three fracture toughness tests were conducted. The results obtained compare well to those obtained from previous fixture tests. It is worth mentioning that no corrections were used (the DT corrections are discussed Chapter 5). It may be concluded that the new fixture gives valid fracture toughness data.

Load Relaxation test Two Load relaxation tests were conducted. The results obtained compare well to those obtained from previous fixture tests. Similarly, no corrections were used (the DT corrections are discussed Chapter 5). It may be concluded that the new fixture obtains valid VK data.

B.6 Summary

The design and the commission of the fixture met all design specifications and hence it may be concluded that all design requirements were met. The experimental analysis yielded repeatable and comparable data with a previous DT fixture. The fixture design enables the generation of fracture toughness and VK data. As such the fixture is seen fit for further graphite testing. Recommendations include an improvement on the specimen support and locating screws. A movable platform would enable better control of the specimens alignment.

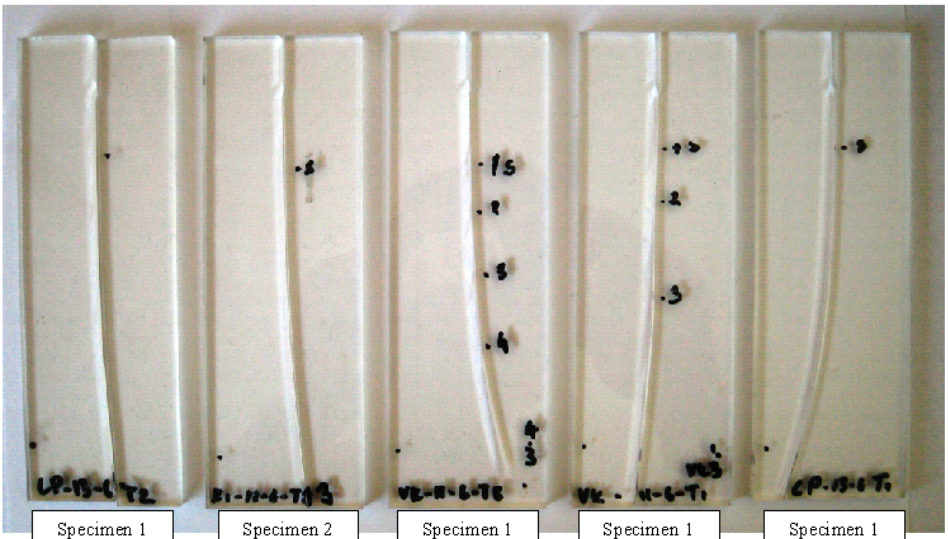

Figure B.10 – The five specimens tested. K_{Ic} abbreviates fracture toughness test and VK abbreviates slow crack growth analysis tests. All crack propagations were almost symmetrical.

	Scenario					
	1	2	3	4	5	6
a_1	a	a	a	a	a	a
a_2	a	a	a	a	a	a
W_{m1}	np	0	np	limited	0	np
W_{m2}	np	0	np	limited	0	np
y	0	np	np	0	0	np
α	0	np	np	0	0	np

Table B.5 – The misalignment possibilities of the designed fixture.

Appendix C

Finite Element Formulation of the JMAN Methodology

This appendix gives the mathematical Finite Element (FE) formulation of the JMAN methodology introduced in Chapter 6. The methodology was implemented using MATLAB ® code routine called JMAN. The input for JMAN is the location of points, their displacements as a function of load and the elastic material properties of Young's modulus and Poisson's ratio. The displacement data were obtained by Digital Image Correlation (DIC) analysis of observations during simple mechanical tests. The J-integral can be calculated by selecting any contour around a region that contains the crack tip, Theoretically, the J-integral should be path independent for any contour surrounding a singularity, and this can be exploited to verify the obtained J-integral.

The reader unfamiliar with the FE approach is referred to Uebner and Zienkiewicz [232, 233]. The derivation below assumes some basic knowledge of the FE methodology.

C.1 Elastic FE Method

The methodology assumes that displacements at certain points of a cracked body are known. This displacements were obtained from DIC. Assuming a 2D quadratic, iso-parametric four, eight or nine-node element, the displacement points can then be considered as nodes forming an element. The locations of these points in the global coordinates x_1 and x_2 are denoted by the appropriate

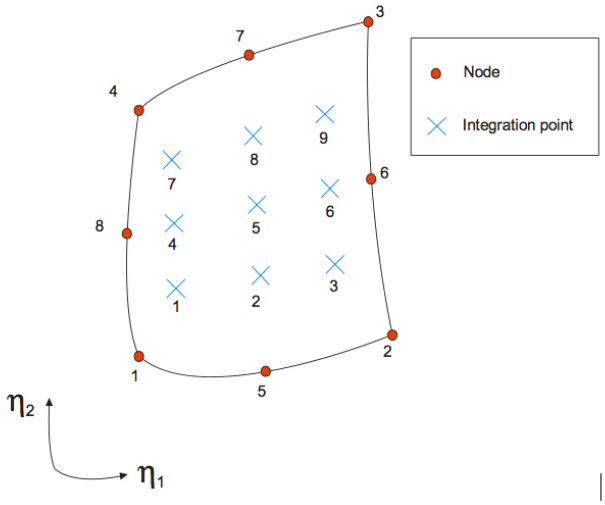

Figure C.1 – Quadratic element

order of elements pairs of $x_1(i)$ and $x_2(i)$, $i = 1...$number of element nodes. To calculate the J-integral from the known displacement field, stress and strains at each integration point need to be calculated first. Therefore, a brief review of the elastic FE method is given first.

For the classic stress based linear elastic approach, the FE domain is split into small elements, which in turn are approximate the strain distribution using continuous and smooth shape functions N. These shape functions, depending on the element order, are either linear, bi-linear or quadratic. Referring to Figure C.1, the shape functions for the eight node quadratic element in local coordinates, η_1 and η_2, are given by:

Element Node	Shape function:
1	$N_1 = -\frac{1}{4}(1-\eta_1)(1-\eta_2)(1+\eta_1+\eta_2)$
2	$N_2 = -\frac{1}{4}(1+\eta_1)(1-\eta_2)(1-\eta_1+\eta_2)$
3	$N_3 = -\frac{1}{4}(1+\eta_1)(1+\eta_2)(1-\eta_1-\eta_2)$
4	$N_4 = -\frac{1}{4}(1-\eta_1)(1+\eta_2)(1+\eta_1-\eta_2)$
5	$N_5 = -\frac{1}{4}(1-\eta_1^2)(1-\eta_2)$
6	$N_5 = -\frac{1}{4}(1+\eta_1)(1-\eta_2^2)$
7	$N_5 = -\frac{1}{4}(1-\eta_1^2)(1+\eta_2)$
8	$N_5 = -\frac{1}{4}(1-\eta_1)(1-\eta_2^2)$

It is worth mentioning that the JMAN methodology assumed four, eight or nine noded elements. An evaluation of the element order is given in Chapter 6. For

the completeness of this chapter the formulation of JMAN is given as the number of Gauss Points (GP), which is dependent on the element order.

Still assuming a eight noded element, the location (η_1, η_2) and weight functions (w_p) of the integration points in the eight node quadratic element are given as:

Integration point	η_1	η_2	w_p
1	$-\sqrt{\frac{3}{5}}$	$-\sqrt{\frac{3}{5}}$	$\frac{25}{81}$
2	0	$-\sqrt{\frac{3}{5}}$	$\frac{40}{81}$
3	$\sqrt{\frac{3}{5}}$	$-\sqrt{\frac{3}{5}}$	$\frac{25}{81}$
4	$-\sqrt{\frac{3}{5}}$	0	$\frac{40}{81}$
5	0	0	$\frac{64}{81}$
6	0	0	$\frac{40}{81}$
7	$-\sqrt{\frac{3}{5}}$	$\sqrt{\frac{3}{5}}$	$\frac{25}{81}$
8	0	$\sqrt{\frac{3}{5}}$	$\frac{40}{81}$
9	$\sqrt{\frac{3}{5}}$	$\sqrt{\frac{3}{5}}$	$\frac{25}{81}$

The shape functions are hard coded into the JMAN methodology for each element type (i.e linear or quadratic). The next step is to determine the strain and stress in each GP. This is done using the Jacobian matrix, J_P, which is defined by differentiating the shape functions with respect to the local coordinates and calculating the value of the resulting function at the local coordinate of that GP:

$$J_P = \begin{bmatrix} \frac{\partial N_1}{\partial \eta_1} x_1(1) + ... + \frac{\partial N_8}{\partial \eta_1} x_1(GP) & \frac{\partial N_1}{\partial \eta_1} x_2(1) + ... + \frac{\partial N_8}{\partial \eta_1} x_2(GP) \\ \frac{\partial N_1}{\partial \eta_2} x_1(1) + ... + \frac{\partial N_8}{\partial \eta_2} x_1(GP) & \frac{\partial N_1}{\partial \eta_2} x_2(1) + ... + \frac{\partial N_8}{\partial \eta_2} x_2(GP) \end{bmatrix}_P \tag{C.1}$$

$x_1(i)$ and $x_2(i)$ are the location of the nodes forming the said element in global coordinates. The local coordinates re mapped to the global coordinates with:

$$\begin{bmatrix} \frac{\partial N_i}{\partial x_1} \\ \frac{\partial N_i}{\partial x_2} \end{bmatrix}_P = [J_P]^{-1} \begin{bmatrix} \frac{\partial N_i}{\partial \eta_1} & \frac{\partial N_i}{\partial \eta_2} \end{bmatrix}_P \tag{C.2}$$

and **B** calculates the strains from the global displacements:

$$B_P = \begin{bmatrix} \frac{\partial N_1}{\partial x_1} & 0 & ... & \frac{\partial N_{GP}}{\partial x_1} & 0 \\ 0 & \frac{\partial N_1}{\partial x_2} & ... & 0 & \frac{\partial N_{GP}}{\partial x_2} \\ \frac{\partial N_1}{\partial x_1} & \frac{\partial N_1}{\partial x_2} & ... & \frac{\partial N_{GP}}{\partial x_1} & \frac{\partial N_{GP}}{\partial x_2} \end{bmatrix}_P \tag{C.3}$$

knowing the displacements at the nodes in global coordinates, $u_1(i)$ and $u_2(i)$, the strains at each integration point are given by:

$$\begin{bmatrix} \varepsilon_{11} \\ \varepsilon_{22} \\ \varepsilon_{12} \end{bmatrix} = B_P \begin{matrix} u_1(1) \\ u_2(1) \\ \vdots \\ u_1(GP) \\ u_2(GP) \end{matrix} \tag{C.4}$$

so that

$$\varepsilon_{ij,P} = \begin{bmatrix} \varepsilon_{11} & \varepsilon_{12} \\ \varepsilon_{12} & \varepsilon_{22} \end{bmatrix}_P \tag{C.5}$$

The linear elastic equivalent stress is determined from Hooke's law using

$$\begin{bmatrix} \sigma_{11} \\ \sigma_{22} \\ \sigma_{12} \end{bmatrix} = \frac{E}{1-v^2} \begin{bmatrix} 1 & v & 0 \\ v & 1 & 0 \\ 0 & 0 & \frac{1-v}{2} \end{bmatrix} \begin{bmatrix} \varepsilon_{11} \\ \varepsilon_{22} \\ \varepsilon_{12} \end{bmatrix} \tag{C.6}$$

so that

$$\sigma_{ij,P} = \begin{bmatrix} \sigma_{11} & \sigma_{12} \\ \sigma_{12} & \sigma_{22} \end{bmatrix}_P \tag{C.7}$$

The elastic energy can then be determined using

$$W_P = \frac{E}{2(1-v^2)} \begin{bmatrix} \varepsilon_{11} \\ \varepsilon_{22} \\ 2\varepsilon_{12} \end{bmatrix}^T \begin{bmatrix} 1 & v & 0 \\ v & 1 & 0 \\ 0 & 0 & \frac{1-v}{2} \end{bmatrix} \begin{bmatrix} \varepsilon_{11} \\ \varepsilon_{22} \\ 2\varepsilon_{12} \end{bmatrix} \tag{C.8}$$

C.2 J-integral Calculation

There are methods to calculate the J-integral, the crudest of which is to directly evaluate Rice's line integral [57]. Calculation of the line integrals is not accurate and is mathematically complex, and thus Li et al. [116] introduced an equivalent expression in terms of a volume integral using the divergence theorem. According

to Li a function Q is required which assumes, if the area surrounded by two contours encompassing the crack tip C_1, C_2, C_3 and C_4 is divided by a number of elements (Figure C.2), to be:

$$Q = \begin{cases} 1 & \text{on } C_1 \\ c & \text{on } C_3 \text{and } C_4 \\ 0 & \text{on } C_2 \end{cases} \tag{C.9}$$

where c is a number making the Q function sufficiently smooth. Q was assumed to be a linear function over the considered elements, ranging from 1 to 0 according to Equation C.9. Hence, the differentiation of Q at any GP with respect to the global coordinate is (assuming crack propagation is in the x_1 direction:

$$\frac{\partial q_P}{\partial x_1} = \begin{bmatrix} \frac{\partial N_1}{dx_1} & \cdots & \frac{\partial N_{GP}}{dx_1} \end{bmatrix} \begin{bmatrix} Q_1 \\ \vdots \\ Q_{GP} \end{bmatrix} \tag{C.10}$$

Similarly, the differentiation of the displacement is

$$\frac{\partial u_{i,P}}{\partial x_1} = \begin{bmatrix} \frac{\partial N_1}{dx_1} & \cdots & \frac{\partial N_{GP}}{dx_1} \end{bmatrix} \begin{bmatrix} u_i(1) \\ \vdots \\ u_i(GP) \end{bmatrix} \tag{C.11}$$

where Q_i is the value of the function Q at each GP. Finally, J-integral at each integration point is:

$$J_{GP} = \left(\sigma_{ij,P} \frac{\partial u_{i,P}}{\partial x_1} - W_p \delta_{1j} \right) \det\left(J_P\right) \frac{\partial q_P}{\partial x_j} \tag{C.12}$$

where δ is the Kronecker delta. The J-integral of an element is calculated by numerical integration of its value at each GP:

$$J_{El} = \sum_{P=1}^{GP} J_{GP} w_p \tag{C.13}$$

By summing the J-integrals of all the elements forming the ring around the crack tip, the J-integral associated with the crack is calculated. It should be noted that the crack is considered to be lying in the direction in this formulation.

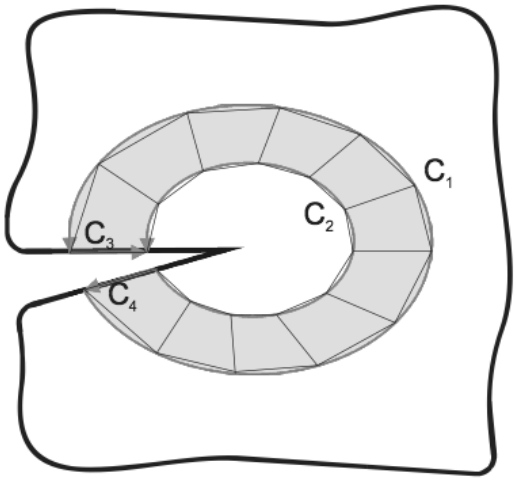

Figure C.2 – Area equivalent J-integral showing a ring of elements surrounding the crack tip.

Appendix D

Drawings

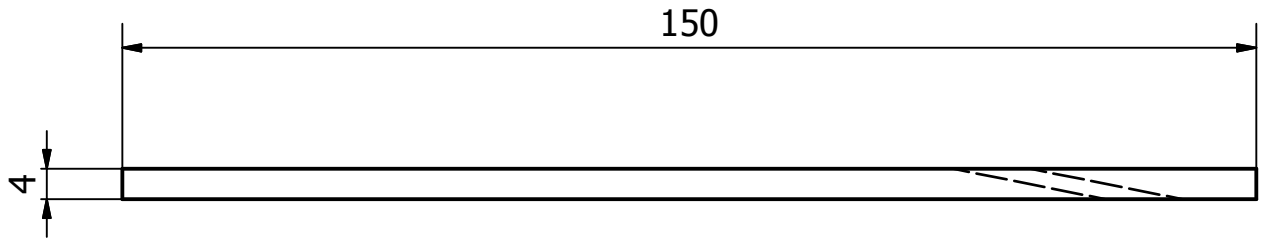

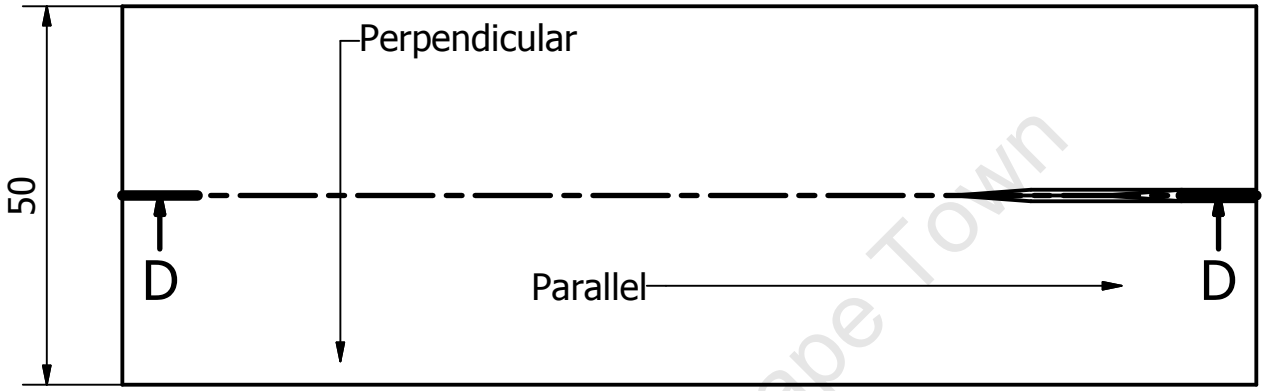

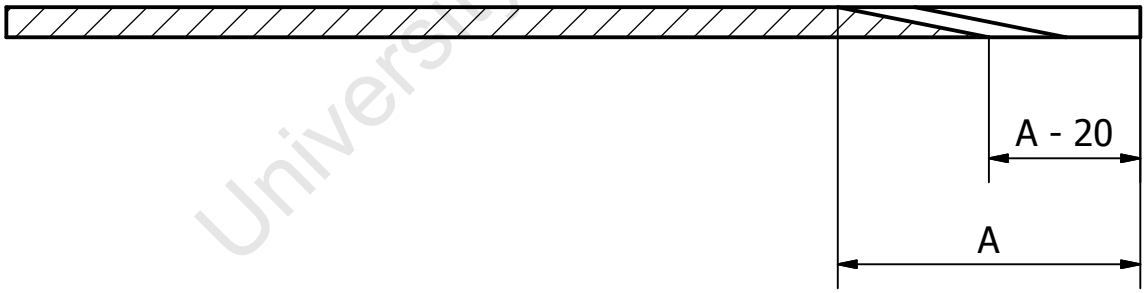

DT Specimen (30mm notch)	NBG10	40	20	5 perp. & 5 para.
DT Specimen (65mm notch)	NBG10	65	45	5 perp. & 5 para.
Part Name	Material	A	A-20	Quantity

Parts List

Designed by	Checked by	Approved by	Date		Date	
Thorsten	Tait				2009/09/01	

UCT/UM	Double Torsion Specimen		
	DT Specimen Modified	Edition	Sheet 1 / 1

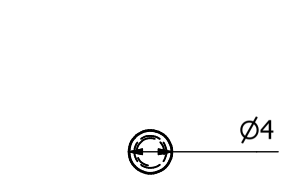

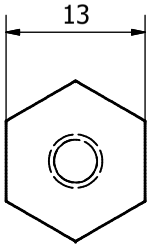

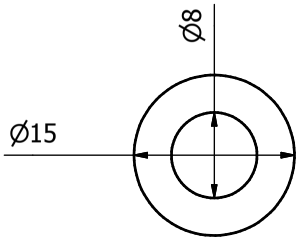

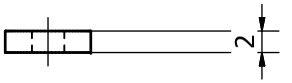

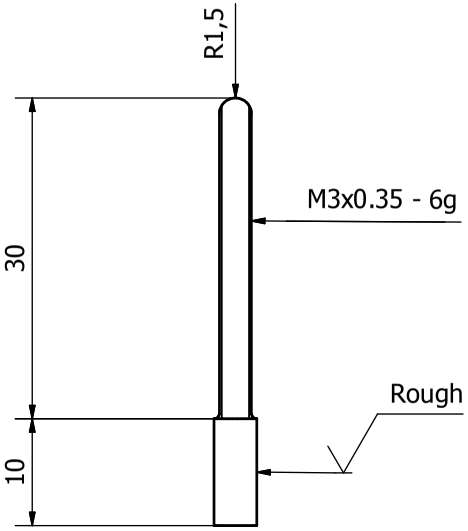

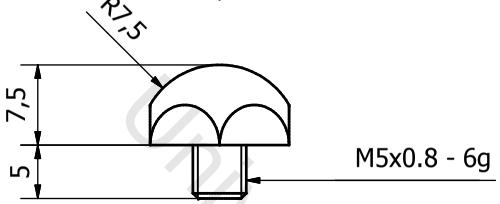

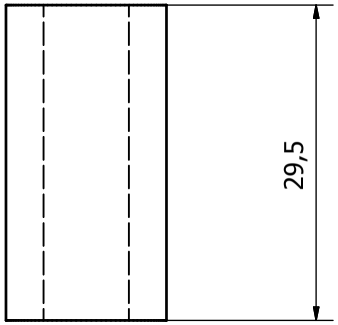

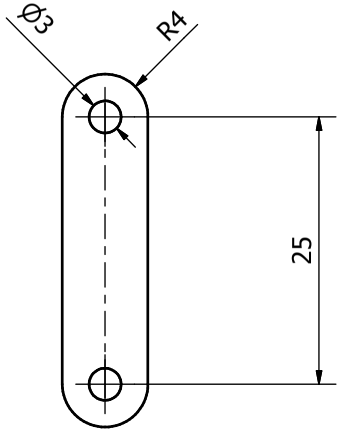

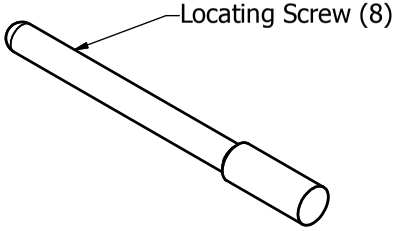

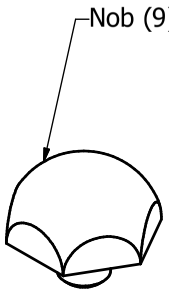

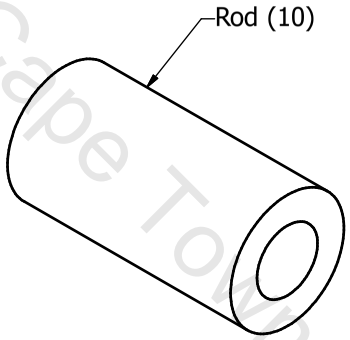

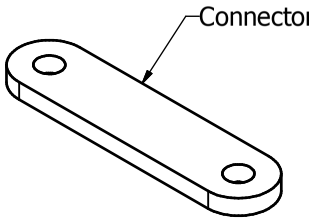

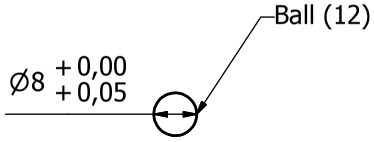

Part No.	Part Name	Quantity	Material
12	Ball	6	M303 Steel
11	Connector Plate	4	Aluminium
10	Rod	2	Brass
9	Nob	1	M303 Steel
8	Locating Screw	4	Brass

Parts List

Designed by	Checked by	Approved by	Date		Date	
Thorsten	Tait				2009/08/26	

UCT/UM	Double Torsion Fixture		
	PARTS (8)to(12)	Edition	Sheet 1 / 1

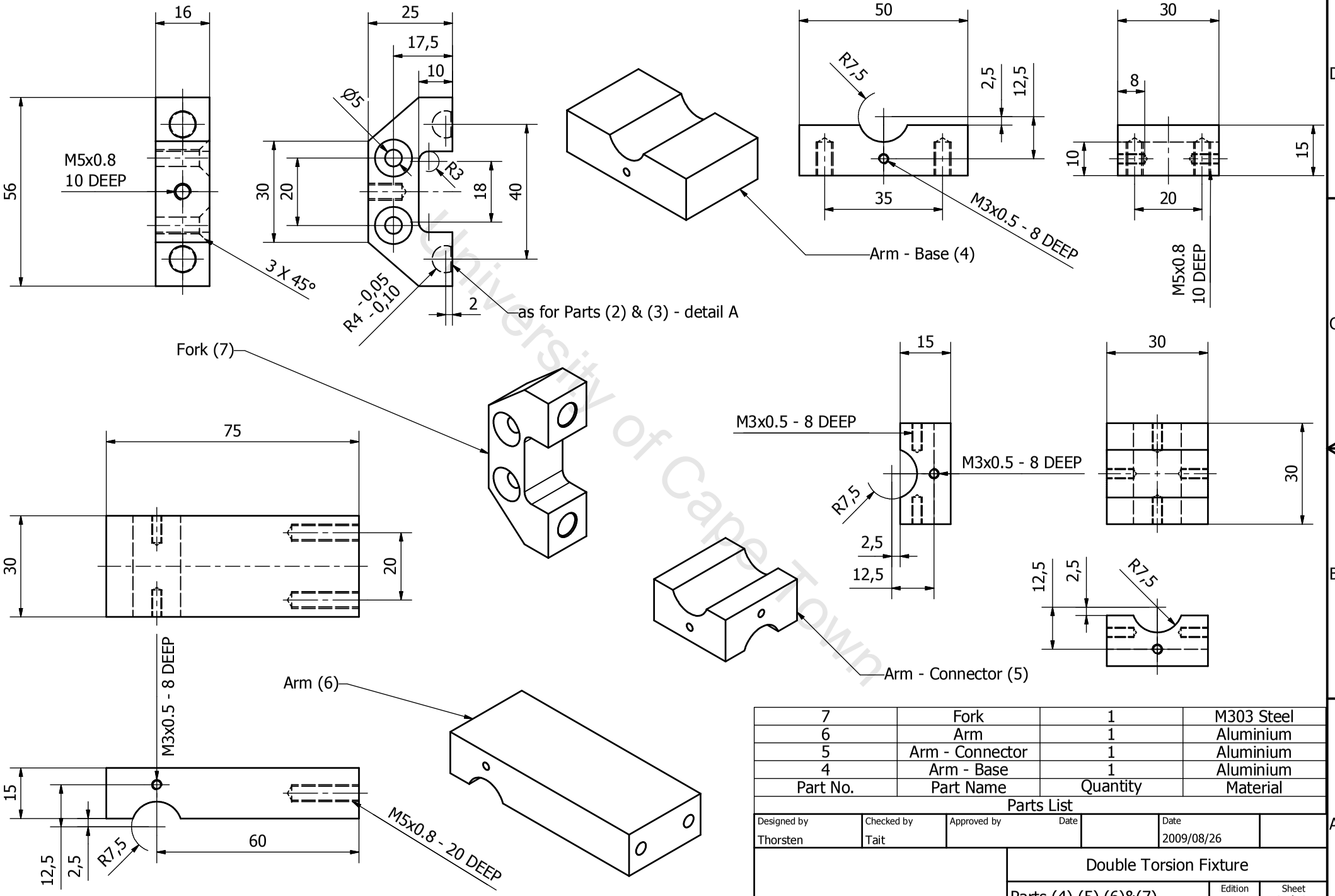

Part No.	Part Name	Quantity	Material
7	Fork	1	M303 Steel
6	Arm	1	Aluminium
5	Arm - Connector	1	Aluminium
4	Arm - Base	1	Aluminium

Parts List

Designed by	Checked by	Approved by	Date		Date
Thorsten	Tait				2009/08/26

Double Torsion Fixture

Parts (4),(5),(6)&(7) | Edition | Sheet 1 / 1

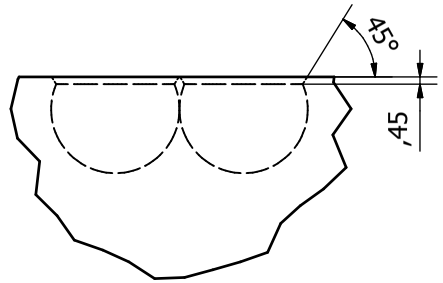

A (3 : 1)

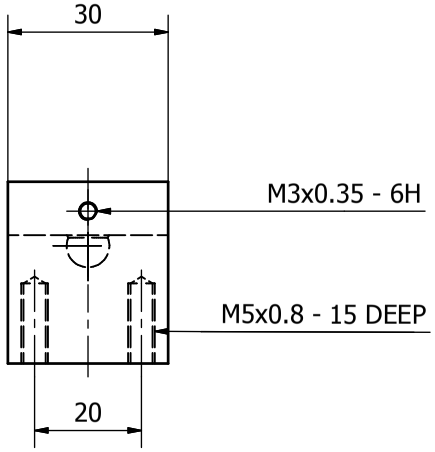

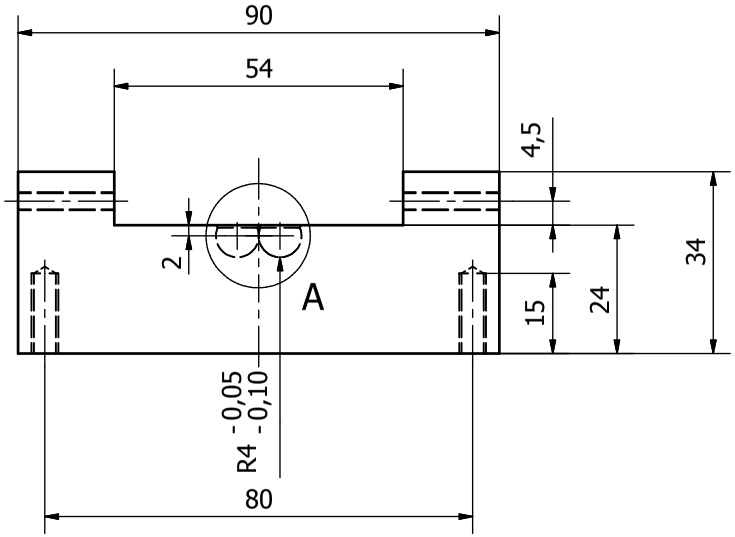

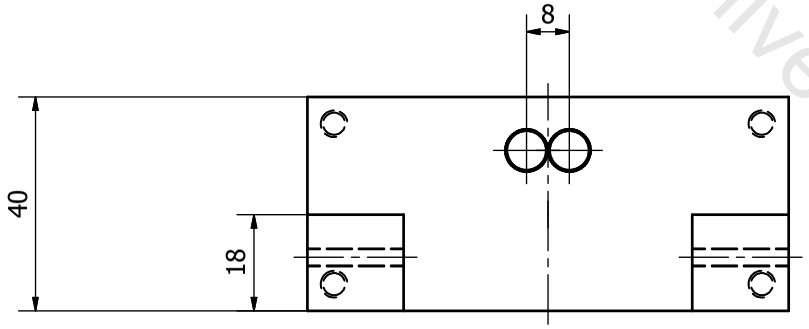

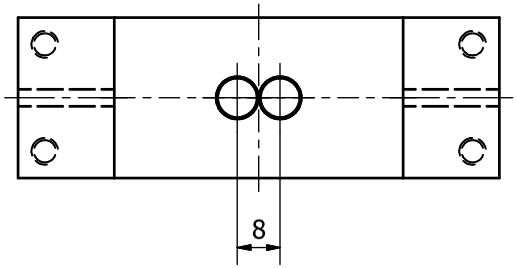

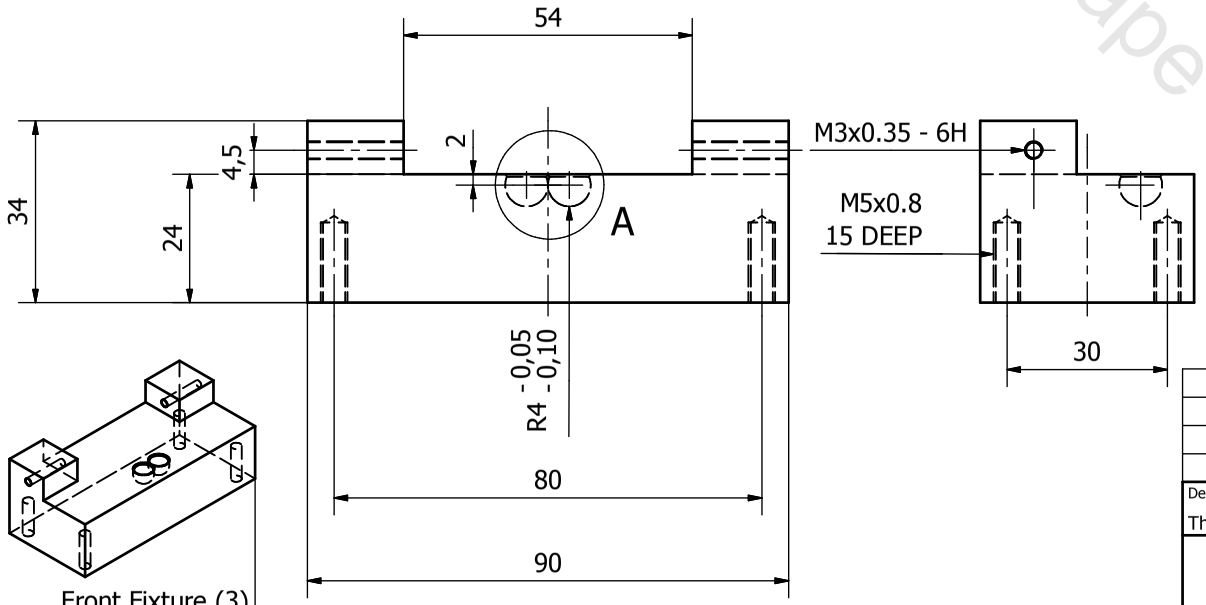

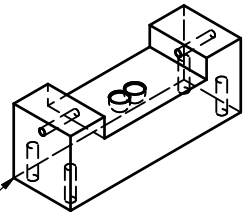

Part No.	Part Name	Quantity	Material
3	Front Fixture	1	M303 Steel
2	Rear Fixture	1	M303 Steel

Parts List

Designed by	Checked by	Approved by	Date	Date	
Thorsten	Tait			2009/08/26	

UCT/UM	Double Torsion Fixture		
	PARTS (2)&(3)	Edition	Sheet 1 / 1

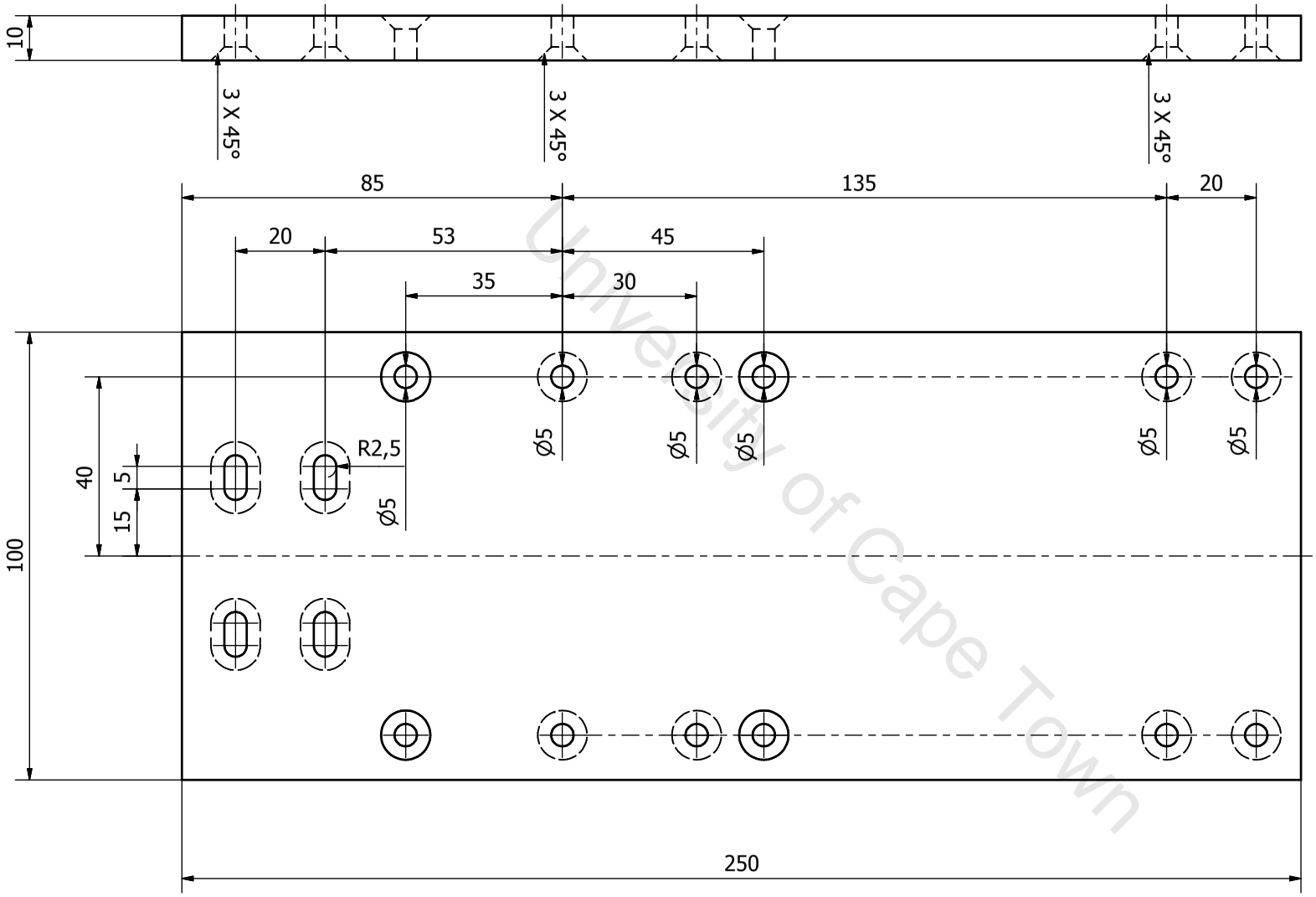

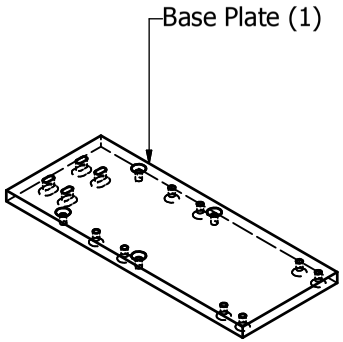

1	Base Plate	1	Aluminium
Part No.	Part Name	Quantity	Material

Parts List

Designed by	Checked by	Approved by	Date		Date	
Thorsten	Tait				2009/08/26	

UCT/UM	Double Torsion Fixture		
	PART (1)	Edition	Sheet 1 / 1

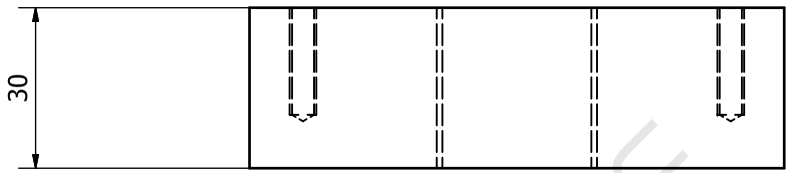

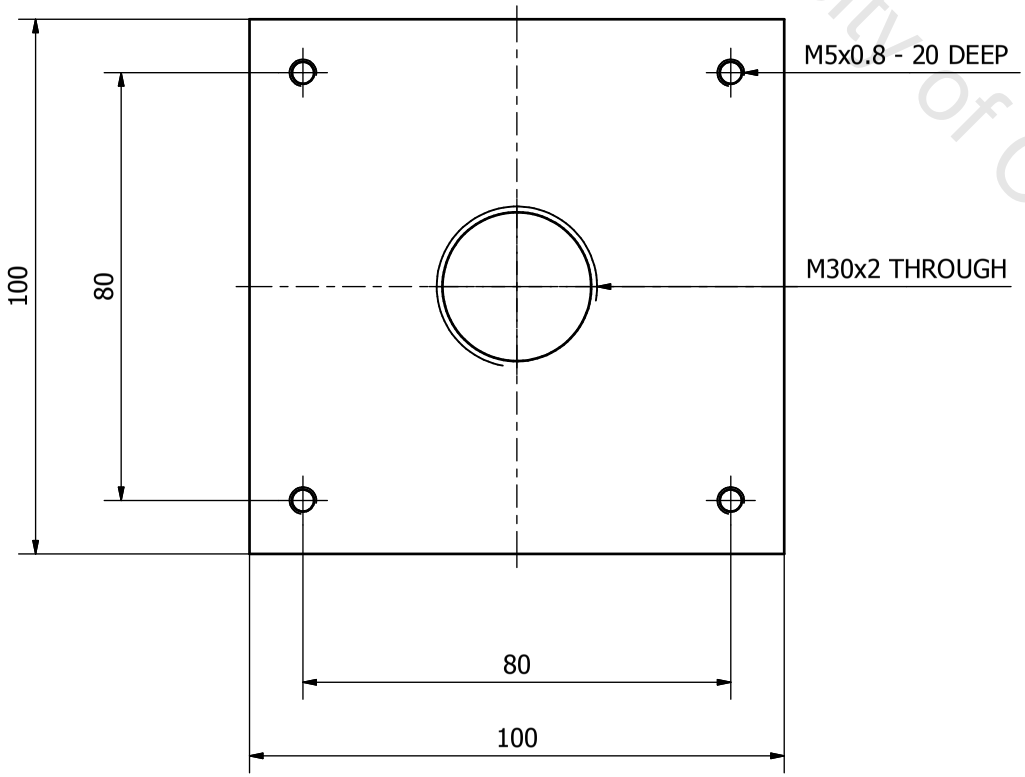

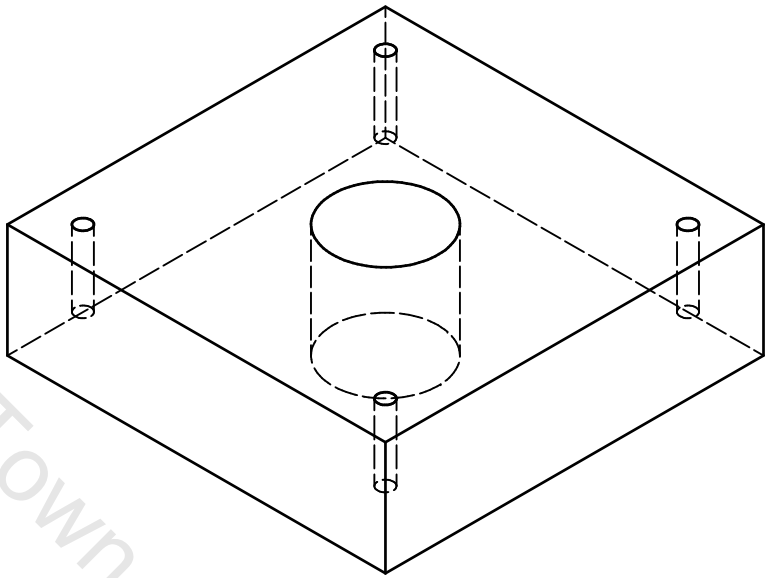

1	Mounting Plate	1	Aluminium
Part No.	Part Name	Quantity	Material
Parts List			

Designed by	Checked by	Approved by	Date	Date	
Thorsten	Tait			26/08/2009	

UCT/UM	Double Torsion Fixture		
	Mounting Plate	Edition	Sheet 1 / 1

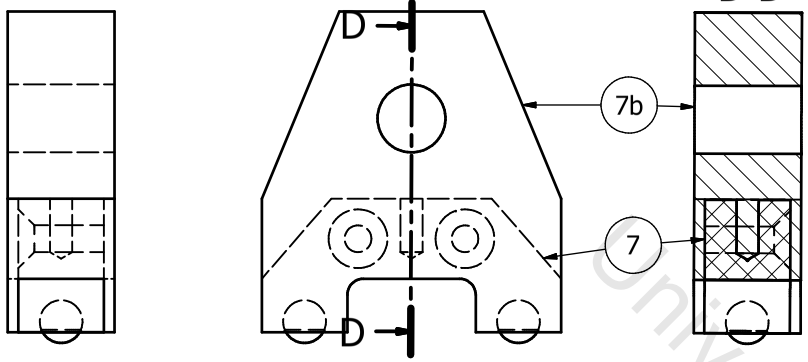

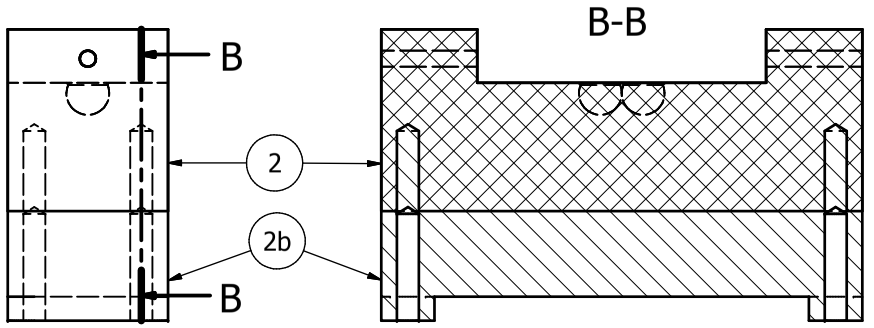

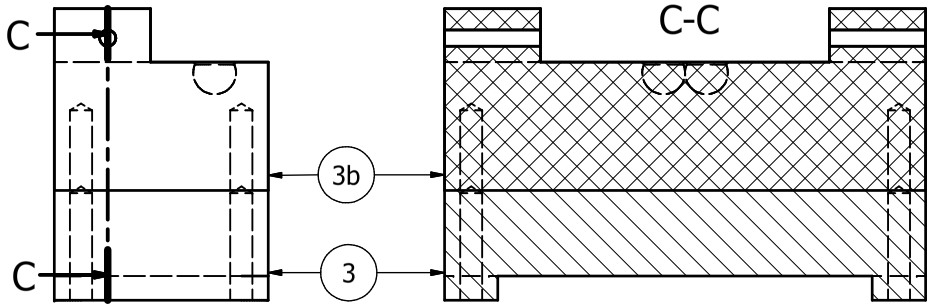

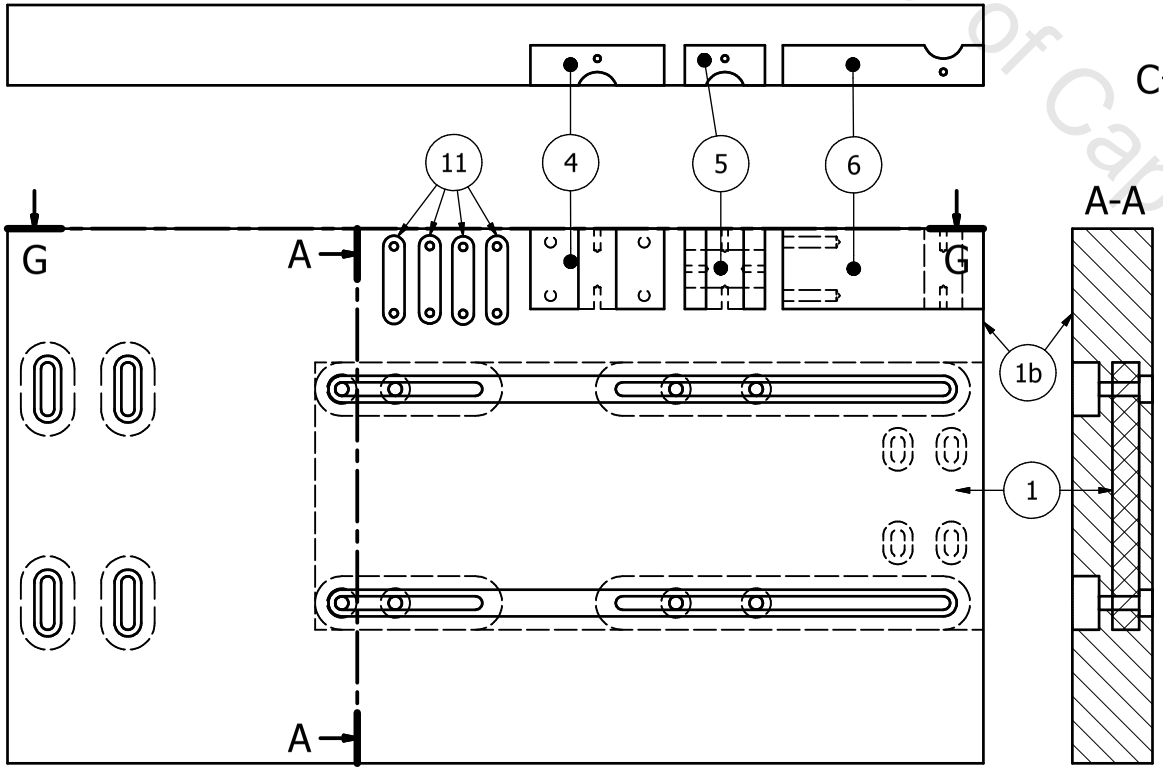

Part No.	Part Name	Quantity	Material
1	Base	1	Aluminium
1b	Previous Base	1	Aluminium
2	Rear Fixture	1	M303 Steel
2b	Previous Rear Fixture	1	M303 Steel
3	Front Fixture	1	M303 Steel
3b	Previous Front Frxture	1	M303 Steel
7	Frok	1	M303 Steel
7b	Previous Fork	1	M303 Steel
4	Arm Base	1	Aluminium
5	Arm Connector	1	Aluminium
6	Arm	1	Aluminium
11	Locator Plate	4	Aluminium

Parts List

Designed by	Checked by	Approved by	Date	Date	
Thorsten	Tait			2009/08/30	

UCT/UM	Double Torsion RIG		
	Layout w.r.t previous Rig	Edition	Sheet 1 / 1

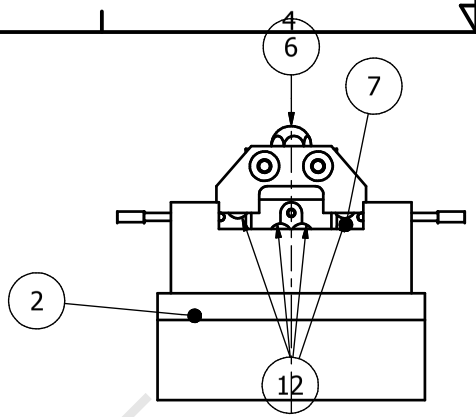

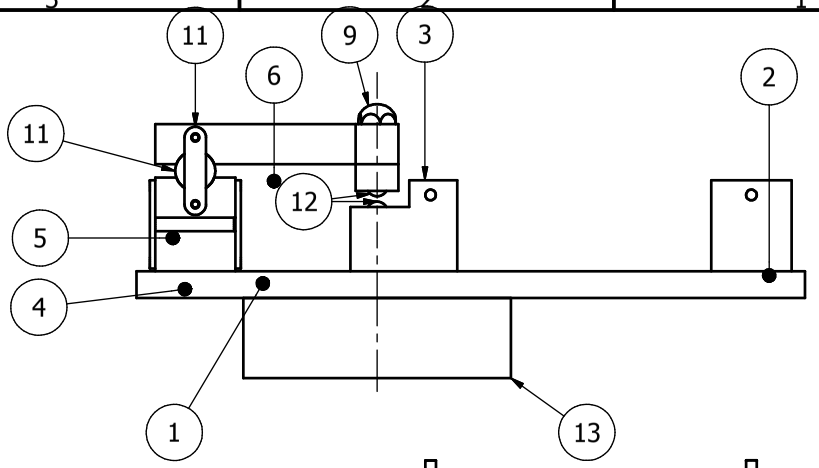

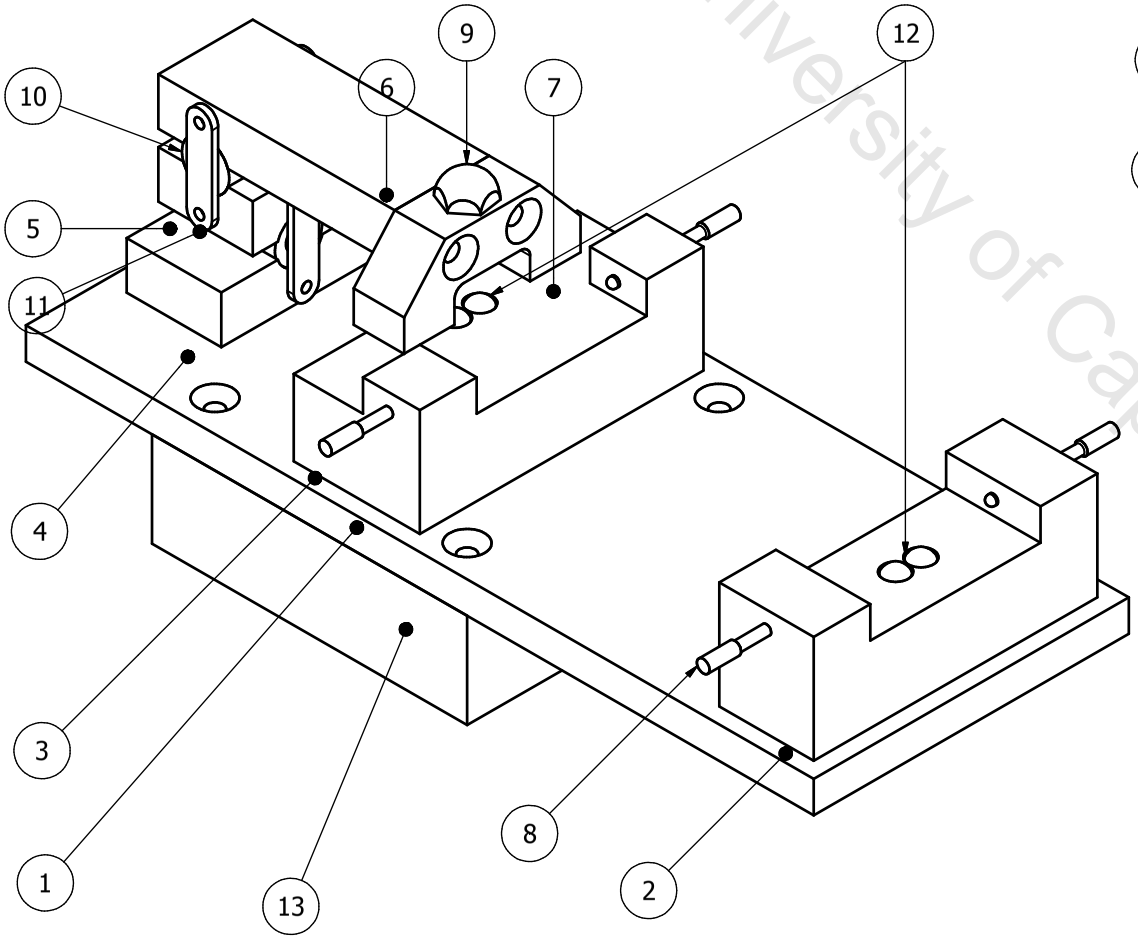

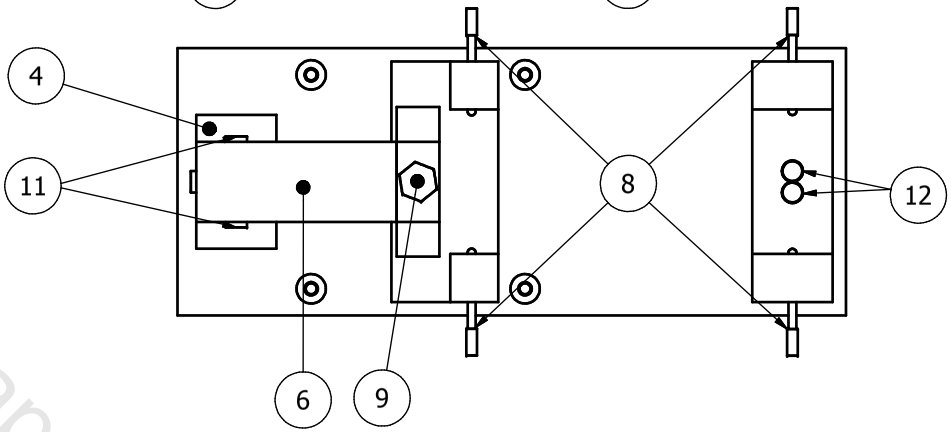

Part No.	Part Name	Quantity	Material
13	Mounting Plate	1	Alumimium
12	Ball	6	M303 Steel
11	Locator Plate	4	Aluminium
10	Rod	2	Brass
9	Nob	1	M303 Steel
8	Location Screw	4	Brass
7	Fork	1	M303 Steel
6	Arm	1	Aluminium
5	Arm - Connector	1	Aluminium
4	Arm - Base	1	Aluminium
3	Front Fixture	1	M303 Steel
2	Rear Fixture	1	M303 Steel
1	Base Plate	1	Aluminium

Parts List

Designed by	Checked by	Approved by	Date	Date	
Thorsten				2009/08/26	

Double Torsion RIG

Edition

Sheet 1 / 1